

The Pennsylvania State University
The Graduate School
Eberly College of Science

4 DEVELOPMENT OF SCALABLE APPROACHES TO NEUTRINO MASS 5 MEASUREMENT WITH THE PROJECT 8 EXPERIMENT

A Thesis in
The Physics Department
by
Andrew Douglas Ziegler

10 © 2023 Andrew Douglas Ziegler

Submitted in Partial Fulfillment
of the Requirements
for the Degree of

14 Doctor of Philosophy

15 December 2023

¹⁶ The thesis of Andrew Douglas Ziegler was reviewed and approved* by the following:

Luiz de Viveiros Souza
Assistant Professor of Physics
Thesis Advisor
Chair of Committee

Carmen Carmona
Assistant Professor of Physics

¹⁷ Doug Cowan
Professor of Physics and Astrophysics

Xingjie Ni
Associate Professor of Electrical Engineering

¹⁸ Stephanie Wissel
Associate Professor of Physics

¹⁹ *Signatures are on file in the Graduate School.

²⁰ Abstract

²¹ Neutrinos are fundamental particles in the standard model and play an important role
²² in the current understanding of the universe, however, the masses of the neutrinos, one
²³ of the most fundamental parameters for any particles, is currently unknown. This fact
²⁴ represents a gaping hole in our current knowledge of the universe that may provide clues
²⁵ to the energy scale of possible physics beyond the standard model. This dissertation
²⁶ summarizes research and development as a member of the Project 8 collaboration towards
²⁷ an experiment to measure the neutrino mass to a sensitivity below $50 \text{ meV}/c^2$, which
²⁸ is an order of magnitude below the most sensitive direct measurements of the neutrino
²⁹ mass to date. Project 8 will perform this measurement using Cyclotron Radiation
³⁰ Emission Spectroscopy (CRES) to measure the beta-decay endpoint spectrum of atomic
³¹ tritium. I present an analysis of the signal reconstruction performance of an antenna
³² array system designed to perform large-scale CRES measurements. Next, I discuss an
³³ approach to calibrating an antenna array CRES experiment using a unique probe antenna
³⁴ designed to mimic radiation from CRES events. Finally, I present design studies for a
³⁵ resonant cavity that could be used to perform a CRES experiment with atomic tritium
³⁶ at multi-cubic-meter scales.

Table of Contents

38	List of Figures	viii
39	List of Tables	xxvii
40	Chapter 1	
41	Introduction	1
42	1.1 Summary	1
43	1.2 Outline	4
44	Chapter 2	
45	Neutrinos and Neutrino Masses	6
46	2.1 Introduction	6
47	2.2 Neutrinos and Beta-decay	6
48	2.3 Neutrino Oscillations	8
49	2.4 Neutrino Masses in the Standard Model	11
50	2.5 Neutrino Absolute Mass Scale	13
51	2.5.1 Limits from Cosmology	13
52	2.5.2 Limits from Neutrinoless Double Beta-decay Searches	15
53	2.5.3 Limits from Beta-decay	17
54	Chapter 3	
55	Direct Measurement of the Neutrino Mass with Project 8	21
56	3.1 Introduction	21
57	3.2 Project 8 and Cyclotron Radiation Emission Spectroscopy	22
58	3.2.1 Cyclotron Radiation Emission Spectroscopy — CRES	22
59	3.2.2 Project 8	26
60	3.2.3 The Project 8 Phased Development Plan	30
61	3.3 Phase II: First Tritium Beta Decay Spectrum and Neutrino Mass Mea- 62 surement with CRES	34
63	3.3.1 The Phase II CRES Apparatus	34
64	3.3.2 CRES Track and Event Reconstruction	38
65	3.3.3 Results from Phase II	42
66	3.4 Phase III R&D: Antenna Array CRES	46
67	3.4.1 The Basic Approach	47

68	3.4.2 The FSCD: Free-space CRES Demonstrator	48
69	3.5 Pilot-scale Experiments	53
70	3.5.1 Choice of Frequency	54
71	3.5.2 Pilot-scale Experiment Concepts	56
72	3.6 Phase IV	59
73	Chapter 4	
74	Signal Reconstruction Techniques for Antenna Array CRES and the FSCD	61
75	4.1 Introduction	61
76	4.2 FSCD Simulations	62
77	4.2.1 Kassiopeia	62
78	4.2.2 Locust	67
79	4.2.3 CRESana	71
80	4.3 Signal Detection and Reconstruction Techniques for Antenna Array CRES	71
81	4.3.1 Digital Beamforming	76
82	4.3.2 Matched Filtering	85
83	4.3.3 Machine Learning	97
84	4.4 Analysis of Signal Detection Algorithms for the FSCD	102
85	4.4.1 Introduction	103
86	4.4.2 Signal Detection with Antenna Array CRES	104
87	4.4.2.1 Antenna Array and Data Rate Estimates	104
88	4.4.2.2 Real-time Signal Detection	107
89	4.5 Signal Detection Algorithms	110
90	4.5.0.1 Power Threshold	111
91	4.5.0.2 Matched Filtering	113
92	4.5.0.3 Machine Learning	117
93	4.5.1 Methods	118
94	4.5.1.1 Data Generation	118
95	4.5.1.2 Template Number and Match Estimation	119
96	4.5.1.3 CNN Training and Data Augmentation	120
97	4.5.2 Results and Discussion	122
98	4.5.2.1 Trigger Classification Performance	122
99	4.5.2.2 Computational Cost and Hardware Requirements	123
100	4.5.3 Conclusion	126
102	Chapter 5	
103	Antenna and Antenna Measurement System Development for the Project 8 Experiment	128
104	5.1 Introduction	128
105	5.2 Antenna Measurements for CRES experiments	129
106	5.2.1 Antenna Parameters	129
107	5.2.1.1 Radiation Patterns	129
108	5.2.1.2 Directivity and Gain	130

110	5.2.1.3	Far-field and Near-field	131
111	5.2.1.4	Polarization	132
112	5.2.1.5	Antenna Factor and Effective Aperture	133
113	5.2.2	Antenna Measurement Fundamentals	135
114	5.2.2.1	Friis Transmission Equation	135
115	5.2.2.2	S-Parameters and Network Analyzers	136
116	5.2.2.3	Antenna Array Commissioning and Calibration Measurements	137
117	5.2.3	The Penn State Antenna Measurement System	138
118	5.3	Development of a Synthetic Cyclotron Antenna (SYNCA) for Antenna Array Calibration	141
119	5.3.1	Introduction	142
120	5.3.2	Cyclotron Radiation Phenomenology	144
121	5.3.3	SYNCA Simulations and Design	150
122	5.3.4	Characterization of the SYNCA	154
123	5.3.5	Beamforming Measurements with the SYNCA	158
124	5.3.6	Conclusions	161
125	5.4	SYNCA Development Discussion	162
126	5.5	FSCD Antenna Array Measurements with the SYNCA	165
127	5.5.1	Introduction	165
128	5.5.2	Measurement Setups	166
129	5.5.2.1	FSCD Array Setup	166
130	5.5.2.2	Synthetic Array Setup	168
131	5.5.3	Simulations, Analysis, and Results	169
132	5.5.3.1	Simulations	169
133	5.5.3.2	Phase Analysis	170
134	5.5.3.3	Magnitude Analysis	175
135	5.5.3.4	Beamforming Characterization	177
136	5.5.4	Conclusions	180

139	Chapter 6		
140	Development of Resonant Cavities for Large Volume CRES Measurements		182
141	6.1	Introduction	182
142	6.2	Cylindrical Resonant Cavities	183
143	6.2.1	General Field Solutions	183
144	6.2.2	TE and TM Modes	184
145	6.2.3	Resonant Frequencies of a Cylindrical Cavity	186
146	6.2.4	Cavity Q-factors	188
147	6.3	The Cavity Approach to CRES	192
148	6.3.1	A Sketch of a Molecular Tritium Cavity CRES Experiment	192
149	6.3.2	Magnetic Field, Cavity Geometry, and Resonant Modes	194
150	6.3.3	Trade-offs Between the Antenna and Cavity Approaches	197
151	6.4	Single-mode Resonant Cavity Design and Simulations	199

153	6.4.1	Open Cylindrical Cavities with Coaxial Terminations	199
154	6.4.2	Mode Filtering	202
155	6.4.3	Simulations of Open, Mode-filtered Cavities	204
156	6.5	Single-mode Resonant Cavity Measurements	207
157	6.5.1	Cavities and Setup	207
158	6.5.2	Results and Discussion	210
159	Chapter 7		
160	Conclusion and Future Prospects		214
161	Bibliography		216

List of Figures

162	2.1	A diagram of two different neutrino mass ordering scenarios [1]. In the inverted hierarchy (inverted mass ordering) the lightest neutrino mass is m_3 , whereas, in the normal hierarchy (normal mass ordering) m_1 is the lightest neutrino. What cannot be measured by neutrino oscillations is the neutrino absolute mass scale, which is essentially the mass of the lightest neutrino mass eigenstate.	9
163	2.2	The masses of the neutrinos as a function of the lightest neutrino mass in both the normal (a) and inverted (b) mass ordering regimes.	10
164	2.3	The neutrino mass observable measured by cosmology as a function of the lightest neutrino mass eigenstate.	14
165	2.4	Feynman diagrams for double beta-decay (a) and $0\nu\beta\beta$ (b).	15
166	2.5	The discovery probabilities for the future generation of $0\nu\beta\beta$ experiments as a function of $m_{\beta\beta}$ and m_{least} . Figure from [2].	16
167	2.6	A Feynman diagram of beta decay	17
168	2.7	A figure from Fermi's 1934 paper on a theory of beta-decay depicting the kinetic energy spectrum of the emitted electron. The effect of the neutrino mass, written as μ , is to distort the shape of the spectrum near the endpoint from the zero-mass spectrum.	17
169	2.8	The tritium beta-decay spectrum. The effect of a massive neutrino on the spectrum is to change its shape near the endpoint by an amount proportional to the size of the neutrino mass. A sufficiently high-statistic and high-resolution measurement of the spectrum endpoint would be able to measure the neutrino mass.	19
170			
171			
172			
173			
174			
175			
176			
177			
178			
179			
180			
181			
182			
183			
184			
185			

186	3.1	A cartoon illustration of the CRES technique. An electron is contained in 187 a magnetic trap, which is a local minimum in the magnetic field, so that 188 its cyclotron radiation can be detected by an array of antennas. Detecting 189 the cyclotron radiation allows one to measure its cyclotron frequency and 190 determine its kinetic energy.	23
191	3.2	An illustration of an electron in a bathtub magnetic trap generated by 192 two well-separated coils.	24
193	3.3	A plot of the main components of an electron's trajectory in a cylindrically 194 symmetric trap.	25
195	3.4	A plot of the final state distributions of atomic and molecular tritium. The 196 final state distribution provides the primary contribution to the width of 197 the molecular spectrum whereas thermal doppler broadening is responsible 198 for the width of the atomic spectrum.	27
199	3.5	Neutrino mass exclusion plot including limits from cosmological measure- 200 ments and the KATRIN experiment. Allowed ranges for neutrino masses 201 under the normal and inverted hierarchies are shown as the blue and 202 orange lines respectively. The black dashed line shows Project 8's goal 203 neutrino mass sensitivity for the Phase IV experiment.	30
204	3.6	Sensitivity calculations for a cavity based CRES experiment that demon- 205 strate the neutrino mass measurement goals of Project 8 throughout the 206 phased development plan. The blue curves indicate molecular tritium 207 sources and the red curves indicate atomic tritium sources. In the current 208 plan, Phase III contains two tritium experiments. The first is the Low- 209 frequency Apparatus (LFA), which is a molecular tritium experiment, and 210 the second is the atomic tritium pilot-scale experiment that officially ends 211 Phase III. The sensitivity of these experiments is primarily a function 212 of statistics, however, there is a critical density beyond which CRES 213 electrons do not have enough time to radiate between collisions for a 214 high-resolution frequency measurement leading to worse sensitivity. . . .	31
215	3.7	The Phase II CRES apparatus used to perform the first measurement of 216 the tritium beta-decay spectrum using CRES.	35
217	3.8	Diagram of the CRES cell portion of the Phase II apparatus.	36
218	3.9	RF system diagram for the Phase II apparatus.	37

219	3.10 The time-frequency spectrogram of a tritium CRES event in the Phase II 220 apparatus.	39
221	3.11 The sparse spectrogram obtained by placing a power cut on the raw 222 spectrogram shown in Figure 3.10.	41
223	3.12 Fits to the measured 17.8-keV ^{83m}Kr conversion line using the deep and 224 shallow trap configurations.	43
225	3.13 Measurements of the 17.8-keV ^{83m}Kr line using the deep trap configuration 226 for different values of the magnetic field from the field shifting solenoid. .	44
227	3.14 The measured tritium spectrum from Phase II with Bayesian and frequen- 228 tist fits.	45
229	3.15 A cartoon illustration of the basics of the antenna array CRES technique.	47
230	3.16 An image of the MRI magnet installed in the Project 8 laboratory at the 231 University of Washington, Seattle.	49
232	3.17 (a) A model of the FSCD antenna array, magnetic trap, and tritium 233 containment vessel design.(b) A more detailed model of a prototype 234 design for the 5-slot waveguide antenna design.	50
235	3.18 (a) A plot of the decay rate for the two-body dipolar spin exchange 236 interaction for cc and dd state. (b) A plot of the decay rate of the dipolar 237 spin exchange interaction for d+d states as a function of magnetic field 238 magnitude. Lowering the magnetic field is key for reducing the losses 239 from this interaction.	55
240	3.19 A conceptual sketch of a large-volume antenna array based CRES experi- 241 ment to measure the neutrino mass.	56
242	3.20 A conceptual sketch of a pilot-scale cavity CRES experiment with an 243 atomic tritium beamline.	58

244	3.21 An illustration of a possible arrangement of ten pilot-scale cavity experiments for Phase IV. The experiments are arranged in a circle with an approximate diameter of 50 meters. Each atomic beamline connected to the bottom of each cavity is approximately 10 m in length. The cavities themselves are designed to operate at 325 MHz and are approximately 11 m tall. The circular arrangement of cavities has some advantages when it comes to cancellation of fringe fields from neighboring magnets, which is important due to the small magnetic field magnitudes consistent with these CRES frequencies. The advantage of ten independent atomic sources and cavities is that there is no single point of failure for the experiment. If an experiment goes down for repairs the other nine may continue running. Figure courtesy of Michael Huehn at UW-Seattle.	60
256	4.1 The geometry and parameters of the coils used to simulate the FSCD magnetic trap in Kassiopeia. Some axial profiles of the magnetic trap at different radial positions are show to demonstrate the shape of the magnetic field and trap depth as a function of position. Calulation of the magnetic field profiles was graciously done by René Reimann.	64
261	4.2 A map of the average ∇B -drift frequency for electrons trapped in the prototype FSCD trap shown in Figure 4.1. Negative drift frequencies indicate electrons that are drifting opposite to the standard direction, which means that they are close to escaping the magnetic trap.	66
265	4.3 The receiver chain used by Locust when simulating CRES events in the FSCD.	69
267	4.4 A high-level diagram depicting the process of CRES event reconstruction. The first step consists of identifying the presence of a signal in the data. This step is necessary to avoid the danger of performing a reconstruction of a false event, which would constitute a background contribution to the tritium spectrum measured by CRES.	73
272	4.5 An illustration of two PDFs associated a binary hypothesis test. The decision threshold is represented by the vertical line that partitions both distributions. The orange and red areas correspond to the true negative and false positive probabilities and the blue and green areas correspond to the false negative and true positive probabilities respectively. To decided between the two hypotheses the likelihood ratio test specified by the Neyman-Pearson theorem is applied. This approach achieves the highest true positive probability for a given false positive probability.	74

280	4.6 An example ROC curve formed by computing the P_{FP} and the P_{TP} for 281 a given likelihood ratio test. As the decision threshold is increased P_{FP} 282 decreases at the expense of a lower P_{TP} . The black dashed line indicates 283 the lower bound ROC curve obtained by randomly deciding between \mathcal{H}_0 284 and \mathcal{H}_1	75
285	4.7 An illustration of the constructive interference condition which is the 286 operating principle of digital beamforming using a uniform linear array 287 as an example.	76
288	4.8 A system level diagram of the laboratory setup used for beamforming 289 demonstrations at Penn State. For more information on this system see 290 Chapter 5. Signals near 26 GHz are fed to a dipole antenna using an 291 arbitrary waveform generator (AWG) and vector network analyzer (VNA), 292 which drive a mixer. The dipole radiation is collected by an array of 293 antennas connected to the digitizer data acquisition (DAQ) system.	78
294	4.9 Photographs of the beamforming demonstration setup. In (a) I show a 295 top-down view of the dipole antenna and the array of eight horn antennas. 296 Manual repositioning of the horn antennas allows one to synthesize a full- 297 circular antenna array. The dipole antenna is mounted on a camera tripod 298 mount that allows for manual position tuning. (b) is a close up image of 299 the dipole, which is manufactured from two segments of semi-rigid coaxial 300 cable. (c) is another image of the dipole and array.	79
301	4.10 An example of digital beamforming reconstruction of a dipole antenna 302 using a synthetic array of horn antennas. The beamforming image on 303 the right is constructed by computing the time-averaged power of the 304 summed signals for a two-dimensional grid of beamforming positions. In 305 the image, one can see a clear maximum that corresponds to the position 306 of the dipole antenna. On the left I show the frequency spectrum of the 307 time-series at the maximum power pixel. White Gaussian noise is added 308 to the signal to mimic a more realistic signal-to-noise-ratio. The signal 309 emitted by the dipole is clearly visible as the high power peak in the 310 frequency spectrum.	80
311	4.11 Beamforming images visualizing the reconstruction of an electron without 312 (a) and with (b) the cyclotron phase correction. The images were generated 313 using data from Locust simulations. The cyclotron phase refers to a phase 314 offset equal to the relative azimuthal position of an antenna in the array. 315 This phase offset is caused by the circular electron orbit and must be 316 corrected for during reconstruction.	81

317	4.12 Beamforming images visualizing the reconstruction of an electron located 318 off the central axis of the FSCD trap. In (a) beamforming is being 319 performed without the ∇B -drift correction, and in (b) it is included.	82
320	4.13 A plot of a typical frequency spectrum obtained by applying a Fourier 321 transform to the time-series obtained from beamforming. The frequency 322 spectra are plotted without noise on top of an example of a typical noise 323 spectrum to visualize a realistic signal-to-noise ratio. In the example, 324 without beamforming it would not be possible to detect anything since 325 the signal amplitudes would be reduced by a factor of sixty relative to 326 the noise. Additionally, it is clear the ∇B -drift correction is needed to 327 detect this electron in the presence of noise.	83
328	4.14 A plot of the total signal power received by the FSCD array from trapped 329 electrons with different radial positions and pitch angles generated using 330 Locust simulations. The lines on the plot indicate a 10 dB detection 331 threshold above the mean value of the noise in the frequency spectrum. 332 With static beamforming electrons with radial positions larger than about 333 two centimeters are undetectable due to the change in the electron's 334 position over time causing losses from beamforming phase mismatch. This 335 is corrected by including ∇B -drift frequencies in the beamforming phases. 336 Both beamforming techniques fail to detect electrons below $\approx 88.0^\circ$, since 337 these signals are composed of several relatively weak sidebands that are 338 comparable to the noise.	84
339	4.15 Example of a convolution of a CRES signal template with a segment of 340 noisy data. A simulated CRES signal was simulated using Locust and 341 normalized to create a matched filter template. When this template is 342 convolved with noisy data the convolution output increases dramatically compared to data with only noise. 343 The decreasing convolution output as the time offset of the convolution 344 increases is caused by zero-padding of the data and template.	86
345	4.16 An example two-dimensional parameter distribution of a matched filter 346 template bank and random test signals. θ refers to the pitch angle of the 347 electron and E is the kinetic energy. The template bank forms a regular 348 grid in pitch angle and energy, whereas, the test signals are uniformly 349 distributed in pitch angle and follow the tritium beta-decay kinetic energy 350 distribution. This is why there are fewer test signals at higher energies. 351 The need for high match across the full parameter space prevents one from 352 reducing the density of templates in this low activity region. A zoomed in 353 version of the template bank illustrates the relative density of templates 354 and signals needed for match $> 90\%$	89

356	4.17 The matched filter scores of a dense grid of templates in pitch angle energy 357 space. Dense template grids allow one to estimate the kinetic energy of 358 the electron by identifying the best matching template. The uncertainty 359 on this value is proportional to the space of templates that also match 360 the test signal well. In the worst case matched filter templates can be 361 completely degenerate where templates with different parameters match 362 a signal with equal likelihood.	90
363	4.18 The mean match of the dense template grid shown in Figure 4.17 for 364 different numbers of templates. Grids of different sizes were obtained by 365 decimating a dense grid of templates and the average match for each grid 366 was computed using the same set of randomly distributed test signals. 367 Plotting the mean match against the size of the grid allows one to visualize 368 the exponential relationship between match and template bank size. The 369 noise in each curve is caused by sampling effects from the decimation 370 algorithm. In general, longer templates are harder to match than shorter 371 templates.	90
372	4.19 Matched filter template bank ROC curves as a function of mean match. 373 One can see that for low match a matched filter is on average worse than 374 the more straight forward beamforming detection approach.	91
375	4.20 Boundaries of detectable electrons in pitch angle kinetic energy space 376 for a series of different signal detection algorithms. A detectable signal 377 is defined as a signal that is above a consistent decision with at least 378 50% probability. This non-rigorous treatment of detection probability is 379 primarily useful for the visualization the relative increases in detection 380 performance provided by the different algorithms. The static beamforming 381 (Static-BF) algorithm is the digital beamforming algorithm introduced 382 above without the ∇B -drift correction. The DNN algorithm refers to a 383 convolutional neural network classifier trained to detect CRES signals 384 (see Section 4.3.3).	92
385	4.21 Two example illustrations of the correlation between kinetic energy and 386 pitch angle imparted by the shape of the FSCD magnetic trap. The 387 correlations manifest themselves as degeneracies in the matched filter 388 score where multiple matched filter templates have the same matched filter 389 for a particular signal. These degeneracies are a sign that the magnetic 390 trap must be redesigned in order to break the correlation between pitch 391 angle and kinetic energy.	96

392	4.22 A visualization of the correlation between energy and pitch angle in the FSCD magnetic trap. The image is formed by computing the match of the best template from a grid consisting of pitch angles from 84 to 90 degrees in steps of 0.05 degrees, kinetic energies from 17574 to 18574 eV, located at 2 cm from the central axis, and simulated for a length of three FSCD time-slices. The signals used to compute the best matching template consisted of a grid from 84 to 90 degrees in steps of 0.05 degrees, kinetic energies from 18550 to 18575 eV in steps of 0.25 eV, located 2 cm from the central axis, and simulated for three FSCD time-slices. The colored regions of the plot show how well signals with lower energy can match those of higher energy for the FSCD magnetic trap, which is proportional to the achievable energy resolution of the FSCD design.	97
404	4.23 A representation of a matched filter template bank as a convolutional neural network. The network has a single layer composed of the templates, which act as convolutional filters. The activation of the neural network is an absolute value followed by a max operator.	100
408	4.24 A graphical depiction of CRES signal detection using a CNN. A noisy segment of data is converted to a frequency series using digital beamforming and a FFT. The complex-valued frequency series is input into a trained CNN model that classifies the data as signal or noise using a decision threshold on the CNN output.	101
413	4.25 The detection efficiency and false alarm rate (false positive rate) as a function of the decision threshold for different values of the noise temperature. The model is trained to output a value close to one for data that contains a signal and outputs a value near zero when the data contains only noise. One sees that a lower decision threshold will have a high detection efficiency at the cost of a high rate of false alarms.	102
419	4.26 ROC curves for a CNN model classifying CRES signals. One can see that the area under the curve, which is a figure of merit that describes the performance of the classifier, is roughly linearly dependent with the noise temperature.	102

423	4.27 An illustration of the conceptual design for an antenna array CRES	
424	tritium beta-decay spectrum measurement. The antenna array geometry	
425	consists of a 20 cm interior diameter with 60 independent antenna channels	
426	arranged evenly around the circumference. The nominal antenna design	
427	is sensitive to radiation in the frequency range of 25-26 GHz, which	
428	corresponds to the cyclotron frequency of electrons emitted near the	
429	tritium beta-spectrum endpoint in a 0.96 T magnetic field. The array is	
430	located at the center of the magnetic trap produced by a set of current-	
431	carrying coils. The nominal magnetic trap design is capable of trapping	
432	electrons up to 5 cm away from the central axis of the array and traps	
433	electrons within an approximately 6 cm long axial region centered on the	
434	antenna array.	105
435	4.28 A block diagram illustration of the real-time triggering algorithm proposed	
436	for antenna array CRES reconstruction.	106
437	4.29 An illustration of the digital beamforming procedure. The blue lines	
438	indicate the distances from the beamforming position to each antenna.	
439	In the situation depicted the actual position of the electron matches the	
440	beamforming position, therefore, one expects constructive interference	
441	when the phase shifted signals are summed. To prevent the electron's	
442	∇B -motion from moving the electron off of the beamforming position,	
443	the beamforming phases include time-dependence to follow the trajectory	
444	of the electron in the magnetic trap.	107
445	4.30 Frequency spectra of simulated CRES events in the FSCD magnetic	
446	trap after beamforming. The signal of a 90° electron consists of a single	
447	frequency component that is clearly detectable using a power threshold	
448	on the frequency spectrum. This power threshold remains effective for	
449	signals with relatively large pitch angles such as 89.0° and 88.75°, which	
450	are composed of a main carrier and a few small sidebands. Signals with	
451	smaller pitch angles, below about 88.5°, are dominated by sidebands such	
452	that no single frequency component can be reliably distinguished from	
453	the noise with a power threshold.	109
454	4.31 PDFs of the power threshold test statistic for CRES signals with various	
455	pitch angles as well as the PDF for the noise-only signal case. The average	
456	PDF computed for pitch angles ranging from 85.5 to 88.5° is also shown.	
457	As the pitch angle is decreased the signal PDF converges towards the	
458	noise PDF which indicates that the power threshold trigger is unable to	
459	distinguish between small pitch angle signals and noise.	112

460	4.32 Plots of PDFs that describe the matched filter template bank test statistic for CRES signals with various pitch angles, as well as the estimated PDF for the noise only case. 10^5 matched filter templates are used and perfect match between signal and template i.e. $\Gamma_{\text{best}} = 1$ is assumed. The mean PDF includes signals ranging from $85.5 - 88.5^\circ$ in pitch angle. There is a larger distinction between the signal PDFs at small pitch angles compared to the power threshold, which indicates a higher detection efficiency for these signals.	116
468	4.33 The mean match of the matched filter template bank to a test set of randomly parameterized signals as a function of the number or density of templates. The parameter space includes pitch angles from $85.5 - 88.5^\circ$ and energies from $18575 - 18580$ eV.	120
472	4.34 Histograms of the trained CNN model output from the test dataset. The blue histogram shows the model outputs for signal data. The oddly shaped peak near the end is the result of the softmax function mapping the long tail of the raw output distribution to the range $[0, 1]$	121
476	4.35 ROC curves describing the detection efficiency or true positive rates for the three signal classification algorithms examined in this paper. The matched filter (MF) and Power Threshold curves are computed analytically using the distribution functions introduced in Section 4.5, and the CNN curve is computed numerically using the classification results on the test dataset. The percent match indicated in the legend refers to the mean match of the classifier.	122
483	5.1 An example radiation pattern generated using HFSS simulations. The color and radial distance of the surface from the origin indicate the relative magnitude of radiation power emitted by the antenna in that direction. The primary goal of most antenna measurements is typically to measure the antenna pattern, which is used to derive many useful antenna performance parameters.	129

489	5.2 An illustration of the three field regions important for the analysis of 490 an antenna system. Very close to the antenna the electric fields are 491 primarily reactive so there is no radiation. If a receiving antenna were 492 placed in this region most of the energy would be reflected back to the 493 transmitter. Outside of the reactive near-field is the radiative near field. 494 At these distances the antenna does radiate, but the radiation pattern is 495 not well-defined since it changes based on the distance of the receiving 496 antenna. It is only in the far-field region where the radiation pattern 497 becomes constant as a function of distance, which is where the majority 498 of antenna engineering is assumed to take place. The antenna arrays 499 developed by Project 8 for CRES measurements operate in the radiative 500 near-field due to the importance of limiting power loss from free-space 501 propagation, which complicates the design of the antenna system.	131
502	5.3 An illustration of the Friis measurement technique commonly used for 503 antenna characterization measurements.	135
504	5.4 Illustration of a two-port S-parameter measurement setup. S-parameters 505 characterize how incoming waves of voltage or power scatter off of the RF 506 device under test. This allows you to measure important properties of the 507 device. In particular, this framework can be used to model a two antenna 508 radiation pattern measurement, which can be automated using a VNA. . .	136
509	5.5 Two measurement approaches to characterizing an antenna array for CRES 510 measurements. The full-array approach (a) requires a complete antenna 511 array with all the associated hardware. The synthetic array approach 512 (b) utilizes a single antenna and a set of rotation/translation stages to 513 reposition the transmitter or the receiving antenna to synthesize the signals 514 that would be received by the full-array. This approach reduces the cost 515 and complexity of array measurements. A down-side of the synthetic 516 array approach is that multi-channel effects such as reflections cannot 517 be measured. Utilizing both the full-array and the synthetic array is a 518 powerful way to quantify the impact of errors from the multi-channel array.	137
519	5.6 Illustration of the antenna measurement system developed for the Project 520 8 Collaboration. The reference and test antennas can be connected to 521 different data acquisition configurations depending on the measurement 522 goals. The reference antenna is typically a standard horn antenna and 523 the test antenna is mounted on a set of translation stages for positioning. 524 Automated translation stages allow for relatively painless data-taking enabling 525 synthetic antenna array measurements using only a single receiving 526 antenna. Anechoic form designed to mitigate RF reflections surrounds 527 the setup.	139

528	5.7	Diagrams of two measurement system configurations. Configuration (a) utilizes a VNA and is more suited to antenna characterization. Configuration (b) utilizes an AWG and VNA as a signal generation system and digitizer to collect measurement data, which is more suited to simulating CRES measurements. The transmission chain utilizes a quadrature hybrid and a pair of baluns to drive the cross-dipole variant test antenna developed for synthetic CRES measurements.	139
535	5.8	A sketch of an antenna array large-volume CRES experiment. Electrons from β -decays are confined in a magnetic field using a set of trap coils. The cyclotron radiation produced by the motion of the trapped electrons can be detected by a surrounding antenna array to determine the electron energies. Measuring the energies of many electrons produces a β -decay spectrum.	142
541	5.9	A schematic of the antenna array test stand. The circular antenna array has a radius of 10 cm with 60 independent channels (limited number shown for clarity). The test stand includes an arbitrary waveform generator (AWG), local oscillator (LO), and data acquisition (DAQ) hardware. Finally, a specialized Synthetic Cyclotron Antenna (SYNCA) is used to inject signals to test the antenna array.	143
547	5.10	An electron (red dot) performing cyclotron motion in the x-y plane. The resulting cyclotron radiation is observed by an antenna located at the field point of interest.	144
550	5.11	A plot of the numeric solution to Equation 5.30. The time-domain representation of the signal (a) is composed of a zero frequency term and a series of harmonics separated by the main cyclotron frequency as shown in the plot of the frequency spectrum (b). We can see that the relative amplitude of the harmonics beyond $k = 7$ are smaller than the main carrier by a factor of about 10^{-5} and are completely negligible.	147
556	5.12	The amplitude maxima of the cyclotron radiation form an Archimedean spiral as the radiation propagates outward from the cyclotron orbit center (a). A circular antenna array located at a fixed radius from the orbit center will receive electric fields with equal magnitude in each of its channels, but the phase of the electric field incident on each array channel will be linearly out of phase from its neighbor antennas by an amount equal to the angular separation of the two channels (b).	149

563	5.13 An idealized crossed-dipole antenna consists of two electric dipole antennas oriented perpendicular to each other and is fed with four signals with a quadrature phase relationship. An example antenna feed circuit is shown which is composed of a chained combination of a quadrature hybrid-coupler (Quad) and two baluns.	150
568	5.14 A model of the PCB crossed-dipole antenna with dimensions. The design has an inside diameter of 2.16 mm for the central circular trace, which is 0.13 mm wide. The dipole arms each have a width of 1.27 mm and protrude beyond the circular trace by 1.40 mm, which gives an overall width of 4.96 mm for the length of the antenna PCB trace from end-to-end. The overall size of the antenna is 20.0 mm the majority of which is the PCB dielectric material. This design was observed in simulation to maintain the field characteristics of the idealized crossed-dipole while being simpler to fabricate due to the increased size of the antenna.	151
577	5.15 A comparison of the electric field magnitudes, normalized by the maximum value of the electric field in each simulation, plotted on a 10 cm square to visualize the Archimedean spirals formed by the electron (a), the crossed-dipole antenna (b), and a PCB crossed-dipole antenna (c). The matching patterns indicate that the electric fields have similar phase characteristics. These images were generated using Locust simulations for the electron and ANSYS HFSS for both antennas.	152
584	5.16 A comparison of the normalized electric field magnitudes for the ideal crossed-dipole, PCB crossed-dipole, and a simulated electron as a function of the polar angle (θ). (a) Shows the total electric field, (b) shows the ϕ -polarized electric field component, and (c) shows the θ -polarized electric field component. These images were generated using Locust simulations for the electron and ANSYS HFSS for both antennas.	153
590	5.17 A comparison of the normalized electric field magnitudes for the crossed-dipole, PCB crossed-dipole, and a simulated electron as a function of the azimuthal angle (ϕ) evaluated at $\theta = 90^\circ$. This image was generated using Locust simulations for the electron and ANSYS HFSS for both antennas.	154

594	5.18 (a) A cartoon schematic which highlights the routing of the semi-rigid 595 coax transmission lines. (b) A photograph of a SYNCA constructed 596 using the modified crossed-dipole PCB antenna design. Visible in the 597 photograph of the SYNCA are four blobs of solder which are an artifact 598 of the SYNCA's hand-soldered construction. These solder blobs are the 599 most significant deviation from the SYNCA design shown in Figure 5.14 600 and are responsible for a significant fraction of the irregularities seen in 601 the antenna pattern.	155
602	603 5.19 A schematic of the VNA characterization measurements (a). This setup 604 allows for antenna gain and phase measurements across a full 360° of 605 azimuthal angles using a motorized rotation stage and control of the radial 606 position of the SYNCA using a translation stage. A photo of the setup in 607 the lab is shown in (b).	156
608	609 5.20 Linear interpolations of the measured electric field magnitude (a) and 610 phase (b). The data was acquired using a VNA at 120 points spaced 611 by 3 degrees from 0 to 357 degrees of azimuthal angle. The different 612 color lines indicate the vertical offset of the horn antenna relative to the 613 SYNCA PCB and the dashed line shows the expected shape from electron 614 simulations. No significant difference in the antenna pattern is observed 615 for the measured vertical offsets.	157
616	617 5.21 (a) A depiction of the relative phase differences for signals received by a 618 circular antenna array from an isotropic source. The phases correspond to 619 a unique spatial position. (b) A schematic of the setup used to perform 620 digital beamforming.	158
621	622 5.22 Digital beamforming maps generated using a simulated 60 channel array 623 and electron simulated using the Locust package. (a) and (b) show the 624 beamforming maps for simulated electrons without the cyclotron spiral 625 phases and with the cyclotron spiral phases respectively. (c) and (d) 626 show the beamforming maps produced from SYNCA measurements. We 627 observe good agreement between simulated electrons and the SYNCA 628 measurements.	160

625	5.23 A plot of the SYNCA's reconstructed position using the synthesized horn- 626 antenna array and digital beamforming. (a) Shows the reconstructed 627 position of the SYNCA compared with the target position indicated by 628 the positioning system readout. (b) Shows the reconstruction error, which 629 is the difference between the target and reconstructed positions. The error 630 bars in (b) are the uncertainty in the mean position of the 2D Gaussian 631 used to fit the digital beamforming reconstruction peak obtained from 632 the fit covariance matrix. The mean fit position uncertainty of 0.02 mm 633 is an order of magnitude smaller than the typical reconstruction error of 634 0.3 mm obtained by calculating the standard deviation of the difference 635 between the reconstructed and target position.	161
636	5.24 Images of an early prototype crossed-dipole antenna manufactured by 637 hand and the first measurement setup. The antenna was constructed 638 by hand using four stripped coaxial cables. The antenna was connected 639 to one port of the VNA, and the remaining three ports on the VNA 640 were connected to horn antenna arranged with 90 deg offsets around the 641 crossed-dipole. The measured unwrapped S-parameter phases exhibit the 642 desired relative phase behavior for a SYNCA. These early measurements 643 were the first laboratory proof-of-principle for the crossed-dipole SYNCA.	163
644	5.25 An early iteration of a crossed-dipole SYNCA antenna simulated in HFSS. 645 The antenna is electrically small at 26 GHz, which requires dipole arms on 646 the order of 1 mm long. This design is limited by the minimum achievable 647 distance between the dipole arms caused by the available diameters of 648 coaxial cables. The assumed termination scheme for the coaxial cables to 649 the antenna is hand-soldering, which introduces random variation in the 650 antenna pattern from the inevitable blobs of solder left on the surface of 651 the PCB.	164
652	5.26 A diagram of the array measurement system used to test the prototype 653 FSCD antenna array. A VNA is used as the primary measurement tool, 654 which is connected to the array through a series of switches. The other port 655 of the VNA connects to the SYNCA through the quad-balun chain used 656 to provide the SYNCA feed signals. During measurements the SYNCA 657 is positioned inside the center of the antenna array and translated to 658 different radial and axial positions using a 3-axis manual translation stage 659 setup.	165
660	5.27 Photos of the prototype FSCD antenna (a), the FSCD array and SYNCA 661 (b), and the translation stages and coordinate system used to position the 662 SYNCA (c).	167

663	5.28 A photo of the FSCD antenna and the SYNCA in the synthetic array 664 measurement setup at Penn State.	169
665	5.29 The unwrapped phases of signals received by the FSCD antenna array 666 from an electron with a 90° pitch angle located in the plane of the antenna 667 array. The data points indicated the phases extracted from simulation 668 and the dashed lines show the model predictions.	170
669	5.30 Plots of the measured unwrapped phases from the FSCD array (a) and the 670 synthetic array (b) compared to the model predictions for a series of radial 671 positions. The different phases of the sinusoidal phase oscillations in the 672 two plots reflects differences in the coordinate systems of the measurements.	172
673	5.31 The phase errors between the measurement and model for the synthetic 674 array (blue) and the FSCD array (orange) for a series of radial positions. 675 The label JUGAAD refers to an alternative name for the FSCD array 676 setup. As the SYNCA is translated off-axis phase errors with progressively 677 higher oscillation frequency enter into the measurements.	173
678	5.32 Two dimensional plots of the phase errors for the synthetic array (a) 679 and the FSCD (JUGAAD) array (b). In both plots there is evidence 680 of a similar diffraction pattern with bilateral symmetry, but the FSCD 681 array measurments have an additional phase error contribution from the 682 different antennas and paths through the switch network.	174
683	5.33 The amplitude of the signals from CRESana for the FSCD array from a 684 90° electron. As the electron is moved from $R = 0$ the signals begin to 685 have unequal amplitudes depending on the distance from the electron to 686 the antenna.	175
687	5.34 The normalized magnitudes of the S21 parameters measured in the FSCD 688 (orange) and synthetic array (blue) setups. The dominant observed 689 behavior as a function of radius is the increase in the number of magnitude 690 peaks, which was noted in the phase error curves. There does not appear 691 to be a strong change in the relative amplitude of a group of antennas as 692 predicted by CRESana.	176
693	5.35	177

694	5.36 Beamforming images from the synthetic array (a) and FSCD array (b) 695 setups with the SYNCA positioned 15 mm off the central axis. In both 696 images, there is a clear maxima that corresponds to the true SYNCA 697 position. However, in the FSCD array there is an additional faint peak 698 located at the opposite position of the beamforming maximum. This 699 additional peak is the mirror of the true peak and is the result of reflections 700 between antennas in the FSCD array.	178
701	5.37 A comparison of the maximum signal amplitude obtained by beamforming 702 to the signal amplitude obtained with an ideal summation as a function of 703 the radial position of the SYNCA. The amplitudes for the synthetic array 704 are shown in (a) and the FSCD array are shown in (b). In both setups, 705 the signal amplitudes obtained from beamforming are smaller than the 706 signal amplitude that could be attained with the ideal summation without 707 phase mismatch.	179
708	5.38 The ratio of the beamforming signal amplitude to the ideal signal amplitude 709 for the FSCD and synthetic arrays. The FSCD array has a larger 710 power loss from phase error compared to the synthetic array which indi- 711 cates that calibration errors associated with the multiple channels as well 712 as reflections are impacting the signal reconstruction.	180
713	6.1 Geometry of a cylindrical waveguide with radius b	183
714	6.2 The geometry of a cylindrical cavity with length L and radius b	186
715	6.3 Relation of mode frequency to cavity length for a cylindrical cavity with 716 a radius of 18.32 cm.	187
717	6.4 A series RLC circuit.	188
718	6.5 Illustration of the behavior of the input impedance of the series RLC 719 circuit as a function of the driving frequency. The BW is proportion to 720 the width of the resonance, which is inversely proportional to Q.	190
721	6.6 A series RLC circuit coupled to an external circuit with input impedance 722 R_L	191

723	6.7 A cartoon depiction of a cavity CRES experiment. A metallic cavity filled 724 with tritium gas is inserted into a uniform background magnetic field 725 to perform CRES measurements. Electrons from beta-decays inside the 726 cavity can be trapped and used to excite a resonant mode(s). By coupling 727 to the cavity mode with a suitable probe one can measure the cyclotron 728 frequency of the electron and perform CRES.	192
729	6.8 Examples of the resonant mode frequencies of a cylindrical cavity. This 730 cavity has a radius of 18.32 cm and a length to diameter ratio of 4.55.	196
731	6.9 An image of an open cavity with coaxial terminations used for dielectric 732 constant measurements. Figure from [3].	200
733	6.10 The simplified geometry of an open cavity with coaxial terminations. 734 Figure from [4].	201
735	6.11 Electric field regions for the open cavity boundary value problem. Figure 736 from [4].	201
737	6.12 Two mode filtering concepts to break the degeneracy of TE_{01} and TM_{11} 738 modes. The resistive approach uses dielectric materials to impede currents 739 that travel vertically along the cavity while leaving azimuthal currents 740 unperturbed. An alternative approach is to impede the currents using 741 grooves cut into the cavity wall, which achieve the same effect with an 742 inductive impedance.	204
743	6.13 Four cavity design variations. (a) is a standard sealed cylindrical cavity, 744 (b) is an open cavity with smooth walls, (c) is an open cavity with resistive 745 walls, and (d) is an open cavity with grooved walls. The main cavity and 746 coaxial terminator parameter are identical for all four cavities.	205
747	6.14 The frequencies and Q-factors of the resonant modes identified by HFSS 748 for the cavity variations shown in Figure 6.13. The fully-sealed cavity with 749 smooth walls has several high-Q modes near the TE_{011} resonance. Intro- 750 ducing the open-termination preserves the Q-factors of the $TE_{01\ell}$ modes 751 and suppresses the Q-factors of the modes whose boundary conditions do 752 not match the cylindrical partition. Both the resistive and grooved wall 753 perturbations shift the resonant frequencies of the TM modes away from 754 the TE_{011} mode. By properly tuning the geometry of the grooves or the 755 resistive spacers several MHz of frequency separation can be achieved.	206

756	6.15 A cartoon depicting the design of the open-ended cavity prototype designed 757 to operate at approximately 6 GHz. The main cavity wall was composed of 758 a single copper pipe. A mode-filtered version of this cavity was constructed 759 by	208
760	6.16 Images depicting the measurement of the filtered and non-filtered open 761 cavities using the VNA. The coupling loop in the figure is shown in the 762 TE orientation.	209
763	6.17 HFSS simulation results for a the as-built cavity with the coaxial termi- 764 nators removed. The TE_{011}/TM_{111} frequency is approximately 5.78 GHz.	210
765	6.18 Measurements of the filtered and non-filtered prototype cavities acquired 766 with the VNA.	211

List of Tables

768	4.1	A summary of the CNN model layers and parameters. The output of each 769 1D-Convolution and Fully Connected layer is passed through a LeakyReLU 770 activation function and re-normalized using batch normalization before 771 being passed to the next layer in the model. The output of the final 772 Fully Connected layer in the model is left without activation so that the 773 model outputs can be directly passed to the Binary Cross-entropy loss 774 function used during training. The first layer in the network has two 775 input channels for the real and imaginary components of the spectrum. . .	118
776	6.1	A table of the values of p'_{nm}	185
777	6.2	A table of the values of p_{nm}	186
778	6.3	A table of cavity design parameters used for HFSS simulations.	205
779	6.4	A table of parameters describing the cavity prototypes. Certain values 780 such as the cavity length and the distance between dielectric spacers are 781 approximate due to variation in the machining of the copper. In particular, 782 the filtered cavity was constructed from conducting copper segments that 783 varied in size from 1.50" to 1.85".	208

784 **Chapter 1** |
785 **Introduction**

786 **1.1 Summary**

787 Neutrinos are one of the fundamental particles that comprise the standard model of
788 particle physics and account for a significant fraction of the matter in the universe.
789 Neutrinos are the most abundant fermions in the universe, but due to their weak
790 interactions neutrinos seldom interact with other particles. Regardless, neutrinos play a
791 unique role in the evolution of the early-universe, and a detailed understanding of the
792 properties of the neutrino is key to understanding the universe at the cosmological scale
793 as well as the smallest particle physics regime.

794 It was uncertain that neutrinos had nonzero mass until vacuum neutrino flavor
795 oscillations were observed in the late 90's and early 00's. A simple relativistic argument
796 as to why oscillations are evidence for neutrino masses is that oscillations imply neutrinos
797 experience time, which means that they do not propagate at the speed of light, therefore
798 the masses of the neutrinos must be non-zero. Current neutrino oscillation data supports
799 that neutrino flavor states are actually a superposition of three separate neutrino states
800 with well-defined masses. Measurements of neutrino oscillations that have taken place
801 over the past couple of decades have measured the differences between neutrino mass
802 eigenstates with increasing precision. However, oscillation measurements cannot tell
803 us the mass scale of the neutrinos, which is required in order to measure the absolute
804 neutrino masses.

805 The neutrino mass scale remains an unknown quantity in the standard model of
806 particle physics. The value of the neutrino mass influences the evolution of the early
807 universe and is likely relevant to the energy-scale of new physics responsible for the factor
808 of 10^{-6} difference between the neutrino and electron masses. A model-independent way
809 to measure the neutrino mass is to measure the tritium beta-decay spectrum near its
810 endpoint. Energy conservation requires that the neutrino mass carry away some kinetic

811 energy from the beta-decay electron in the form of its mass, which causes a distortion in
812 the shape of the tritium beta-decay spectrum near the endpoint. The isotope tritium has
813 many advantages for this measurement, and has been used by the KATRIN collaboration
814 to perform the most sensitive direct neutrino mass measurement to date.

815 KATRIN represents the state-of-the-art in the current generation of neutrino mass
816 direct measurement experiments with a projected neutrino mass sensitivity of $m_\nu < 200$ meV.
817 This sensitivity does not fully exhaust the allowed parameter space of neutrino
818 masses under the normal and inverted neutrino mass ordering scenarios, which motivates
819 the development of a next generation of neutrino mass measurement experiments.

820 The Project 8 collaboration is developing a next-generation neutrino mass experiment
821 with a goal neutrino mass sensitivity of $m_\nu < 40$ meV. This sensitivity is sufficient to
822 exhaust the range of neutrino masses allowed under the inverted mass ordering regime.
823 Project 8 intends to achieve its sensitivity goal utilizing two technologies that are novel
824 to the space of direct neutrino mass measurements — atomic tritium and cyclotron
825 radiation emission spectroscopy (CRES). Atomic tritium is required in order to avoid
826 systematic broadening the tritium beta-decay spectrum caused by the final state of the
827 $^3\text{He}^+ \text{-T}$ molecule, and the CRES technique enables a differential measurement of the
828 tritium spectrum that is background-free and able to be directly integrated with the
829 atomic tritium source.

830 The Project 8 collaboration is currently engaged in a research and development
831 program intended to simultaneously develop the atomic tritium and CRES technologies
832 so that they can be combined in a next-generation experiment. This past year (2022)
833 Project 8 has used the CRES technique to measure the molecular tritium beta-decay
834 spectrum and place an upper limit on the neutrino mass: $m_\beta \leq 152$ eV. This measurement,
835 while not competitive scientifically, represents the first proof-of-principle that the CRES
836 technique can be used to measure the neutrino mass.

837 The future goals of the Project 8 collaboration are to develop the technologies
838 and techniques necessary to scale-up the volume in which CRES measurements can
839 be performed. Project 8's first neutrino mass measurement with CRES utilized a
840 measurement volume on the cubic-centimeter scale, however, sensitivity calculations
841 estimate that an experiment sensitive to neutrino masses of 40 meV will require several
842 tens of cubic-meters of experiment volume filled with atomic tritium. Developing a new
843 approach to performing CRES measurements that can be successfully scaled to these
844 volumes is a necessary step towards Project 8's neutrino mass measurement goal, and is
845 the primary topic of my dissertation research.

846 A parallel development is the technology necessary to produce, cool, trap, and
847 recirculate a supply of atomic tritium that is compatible with CRES measurements. The
848 atomic tritium system is equally important as the large-volume CRES measurement
849 technology, but will not be discussed at depth here.

850 The Project 8 collaboration has identified two scalable approaches to neutrino mass
851 measurement using the CRES technique. One approach is to use an array of antennas
852 that surrounds a volume of trapped atomic tritium that can perform CRES measurements
853 by collection the cyclotron radiation emitted by beta-decay electrons into free-space. The
854 other approach uses a resonant cavity filled with atomic tritium to perform CRES by
855 measuring the excitation of resonant cavity modes caused by the motion of electrons
856 trapped inside the cavity volume.

857 The cavity and antenna approaches to CRES have been studied in detail over the past
858 five years, and, while both approaches offer a physically viable path towards a 40 meV
859 neutrino mass measurement, the collaboration has elected to pursue the cavity approach
860 for the foreseeable future. The major advantage of the cavity approach is a significant
861 reduction in the cost and complexity of the experiment design and data analysis, which
862 provides a lower risk path to Project 8’s scientific goals.

863 In this dissertation I summarize my most impactful contributions to the research and
864 development of antenna array and cavity CRES. In short these contributions are

- 865 • the development and analysis of signal reconstruction algorithms for antenna array
866 CRES, which provide key inputs to sensitivity analyses of antenna array CRES
867 experiments.
- 868 • The development of a specialized antenna, designed to synthesize fake CRES
869 radiation, which enables bench-top testing and validation of the antenna array
870 CRES technique.
- 871 • The development of an open-cavity design for CRES measurement, whose mode
872 structure can be tuned using perturbations that modify the impedance of the cavity
873 walls. The development of this cavity concept was one of many developments that
874 eventually lead to the adoption of cavities as the CRES technology of choice for
875 the future of Project 8.

876 **1.2 Outline**

877 The outline of this dissertation is as follows. In Chapter 2 I provide an introduction to
878 the basic physics of neutrinos and beta-decay, which provides context for a discussion of
879 various methods to measure the neutrino absolute mass scale.

880 Chapter 3 is an overview of the CRES technique and the Project 8 collaboration.
881 Project 8's experimental program is organized into four phases. The first phase completed
882 in 2015 before I began my dissertation work, so begin by highlighting the Project 8's first
883 measurement of the tritium beta-decay spectrum with CRES. Next, I discuss the planned
884 research and development for an antenna array CRES experiment for the upcoming phase
885 of Project 8's experimental program. I end Chapter 3 with a discussion of Project 8's
886 pilot-scale and final phase experiments, that will combine a scalable CRES measurement
887 technology with atomic tritium and measure the neutrino mass with 40 meV sensitivity.

888 Chapter 4 discusses the first of my contributions mentioned above, which is the
889 development of signal reconstruction techniques for antenna array CRES and an antenna
890 array demonstrator experiment called the FSCD. I discuss the key tools that Project 8
891 uses to simulate antenna array CRES before introducing signal reconstruction algorithms
892 that can be used to detect CRES signals using the array. I end Chapter 4 with a
893 detailed analysis and comparison of the signal detection performance of each algorithm,
894 as reported in a paper I have authored.

895 Chapter 5 describes my contributions to the development of antennas and an antenna
896 measurement system for Project 8, which is the second major contribution of this
897 dissertation. I begin with a general overview of basic principle of antennas and antenna
898 measurements, and describe the development, as reported in another paper I have
899 authored, of unique antenna designed to mimic the cyclotron radiation emitted by
900 electrons in free-space. I call this antenna the synthetic cyclotron radiation antenna
901 (SYNCA) and its main purpose is to serve as a fake electron for laboratory validation
902 measurements of Project 8's antenna array CRES simulations. Chapter 5 ends with an
903 overview of laboratory measurements of a prototype antenna array using the SYNCA,
904 which were compared with simulations to provide upper bounds on reconstruction errors
905 caused by imperfections in real-life measurements.

906 Chapter 6 discusses the cavity approach to CRES, which was adopted as the preferred
907 CRES technology for Phase IV late into my dissertation work. The chapter starts by
908 discussing resonant cavities in general before introducing the operating principles of the
909 cavity approach to CRES. I end the chapter by discussing a study of and open-cavity

⁹¹⁰ design that could be used for CRES measurements and integrated with atomic tritium
⁹¹¹ and an electron gun calibration source for the pilot-scale and Phase IV experiments.

⁹¹² Finally, in Chapter 7 I conclude by briefly discussing the future directions of Project
⁹¹³ 8 as development proceeds towards a direct measurement of the neutrino mass.

914 **Chapter 2 |**

915 **Neutrinos and Neutrino Masses**

916 **2.1 Introduction**

917 In this chapter I provide a cursory overview of background information relevant to
918 neutrinos and neutrino mass measurements.

919 In Section 2.2 I provide background information on the history of neutrinos and beta-
920 decay. In Section 2.3 I describe the discovery of neutrino oscillations, which demonstrated
921 unambiguously that neutrinos have non-zero masses. In Section 2.4 I discuss the current
922 state of the theoretical understanding of neutrino masses in the standard model. Lastly,
923 in Section 2.5 I discuss a few methods for measuring the absolute scale of the neutrino
924 mass.

925 **2.2 Neutrinos and Beta-decay**

926 Late in the 19th century the phenomena of radioactivity was first observed in experiments
927 performed by Henri Becquerel with uranium, and further studied using thorium and
928 radium by Marie and Pierre Curie [5,6]. Early work in radioactivity classified different
929 forms of radiation based on it's ability to penetrate different materials. Rutherford was
930 the first to separate radioactive emissions into two types, alpha and beta radiation [7].
931 Alpha rays were easily stopped by a piece of paper or thin foil of metal, whereas beta
932 radiation could penetrate metal several millimeters thick. Later a third form of radiation
933 was identified by Villard [8], which was still more penetrating, later termed gamma
934 radiation by Rutherford.

935 When these forms of radioactivity were first discovered, it was unclear what physically
936 constituted an alpha, beta, or gamma particle. Experiments with radioactivity in magnetic
937 fields were eventually able to identify the charge composition of the different forms of

938 radiation. In particular, experiments by Becquerel identified [9] that beta radiation had
939 an identical charge-to-mass ratio to the electron. This was strongly suggestive that beta
940 particles were indeed electrons.

941 Studies of beta radiation lead to the discovery that radioactivity resulted in the
942 transmutation of elements [10] caused by the decay of a heavier nucleus to a lighter
943 species. A decay that produces beta-radiation is called a beta-decay. One feature of beta
944 radiation that differentiated it from alpha and gamma radiation is that the electrons
945 produced by beta-decay have a continuous spectrum of kinetic energies, whereas, alpha
946 and gamma particles are emitted with discrete energies. This feature of beta-decay was
947 first observed by Chadwick in 1914 [11], and was extremely puzzling at the time, since
948 the continuous spectrum apparently violates energy conservation [12].

949 Famously, in 1930 Pauli proposed the existence of a new neutral particle, which he
950 termed the "neutron", that was also produced during beta-decay to resolve the missing
951 energy problem posed by the beta-decay spectrum [13]. Because this particle carried
952 no charge, it was hypothesized that it had simply not been observed in any previous
953 experiments. This "neutron", which was initially estimated to have a mass no larger
954 than that of an electron, was eventually renamed the "neutrino" by Fermi [14] after the
955 discovery of the neutron by Chadwick in 1932 [15]. Later, in 1933, Fermi developed
956 a quantum mechanical theory for beta-decay in which an electron and neutrino are
957 produced by the decay of a neutron to a proton inside the radioactive nucleus [16].

958 Little more than a speculation when first introduced, indirect evidence for the existence
959 of neutrinos was obtained in 1938 by the simultaneous observation of the electron and
960 recoiling nucleus in cloud chambers by Crane and Halpern [17]. However, it wasn't
961 until the Cowan-Reines experiment [18] in 1956 that direct evidence for the existence
962 of neutrinos was observed through the observation of inverse beta-decays caused by
963 neutrinos from a nuclear reactor interacting with protons contained in water molecules.
964 The difficulty in detecting neutrinos is caused by their weak interactions with other
965 particles. Later experiments revealed the existence of different types or flavors of neutrinos
966 based on the nature of the leptons produced in neutrino charged-current interactions [19],
967 but the existence of a neutrino mass remained an open question that would take more
968 than 40 year to resolve.

969 2.3 Neutrino Oscillations

970 One of the first clues that neutrino flavor transitions or neutrino oscillations were occurring
 971 was the solar neutrino problem. The solar neutrino problem is a discrepancy between
 972 the measured and predicted flux of ν_e from the sum. The solar neutrino problem was
 973 famously observed by Ray Davis Jr. and collaborators in the 1960's [20] at the Homestake
 974 mine in South Dakota. In the early 2000's, the SNO experiment was able to resolve the
 975 solar neutrino problem by identifying neutrino oscillations as the cause of the observed
 976 deficit [21]. Furthermore, measurements of the atmospheric flux of neutrinos by the
 977 Super-Kamiokande experiment and others revealed that fewer muon-type neutrinos
 978 survived passage through the earth than expected providing strong evidence for neutrino
 979 oscillations for both flavors [22].

980 Neutrino oscillations occur because the neutrino flavor eigenstates are distinct from
 981 the mass eigenstates [23]. The neutrino mass eigenstates represent physical particles in
 982 that they are solutions to the free-particle Hamiltonian, whereas, the neutrino flavor
 983 eigenstates correspond to the neutrino states that interact via the weak charged-current
 984 interaction. The neutrino flavor eigenstates are a linear superposition of the neutrino
 985 mass eigenstates

$$986 \nu_\ell = \sum_i U_{\ell i} \nu_i, \quad (2.1)$$

986 where $\ell = e, \mu, \tau$ and $i = 1, 2, 3$. The matrix elements $U_{\ell i}$ are the elements of the
 987 Pontecorvo-Maki-Nakagawa-Sakata (PMNS) matrix that describes the mixing between
 988 the neutrino flavor and mass states.

989 A standard parameterization [24] of the PMNS matrix is

$$988 U_{PMNS} = \begin{bmatrix} U_{e1} & U_{e2} & U_{e3} \\ U_{\mu 1} & U_{\mu 2} & U_{\mu 3} \\ U_{\tau 1} & U_{\tau 2} & U_{\tau 3} \end{bmatrix} \\ = \begin{bmatrix} 1 & 0 & 0 \\ 0 & c_{23} & s_{23} \\ 0 & -s_{23} & c_{23} \end{bmatrix} \begin{bmatrix} c_{13} & 0 & s_{13}e^{-i\delta} \\ 0 & 1 & 0 \\ -s_{13}e^{i\delta} & 0 & c_{13} \end{bmatrix} \begin{bmatrix} c_{12} & s_{12} & 0 \\ -s_{12} & c_{12} & 0 \\ 0 & 0 & 1 \end{bmatrix} \quad (2.2) \\ \times \begin{bmatrix} e^{i\alpha_1/2} & 0 & 0 \\ 0 & e^{i\alpha_2/2} & 0 \\ 0 & 0 & 1 \end{bmatrix},$$

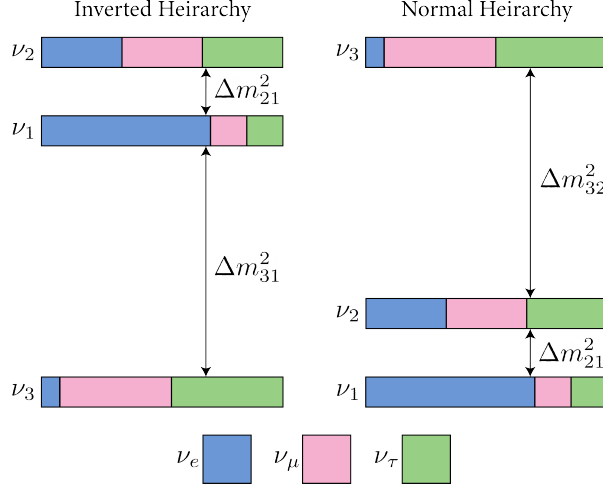


Figure 2.1. A diagram of two different neutrino mass ordering scenarios [1]. In the inverted hierarchy (inverted mass ordering) the lightest neutrino mass is m_3 , whereas, in the normal hierarchy (normal mass ordering) m_1 is the lightest neutrino. What cannot be measured by neutrino oscillations is the neutrino absolute mass scale, which is essentially the mass of the lightest neutrino mass eigenstate.

where $c_{ij} = \cos \theta_{ij}$ and $s_{ij} = \sin \theta_{ij}$. The parameters α_1 and α_2 are only included in the PNMS matrix if neutrinos are Majorana particles, something which represents a current area of research in neutrino physics. The phase δ quantifies the degree of CP-violation in the neutrino sector. Including the Majorana phases the PMNS matrix contains six independent parameters. Neutrino oscillation probabilities also depend on the squared mass differences between neutrino mass eigenstates

$$\Delta m_{ij}^2 = m_i^2 - m_j^2, \quad (2.3)$$

where $ij = 12, 32, 31$ respectively. Because $\Delta m_{32}^2 = \Delta m_{31}^2 - \Delta m_{21}^2$, this adds an additional two parameters that must be constrained by neutrino oscillations.

A large experimental effort over the past couple decades has greatly contained the majority of parameters in the PMNS matrix, many to relative uncertainties of only a few percent. However, certain ambiguities remain, which is the origin of the current uncertainty in the ordering of the neutrino masses (see Figure 2.1). The neutrino masses can be arranged by their relative masses. Current neutrino oscillation data supports that $m_2 > m_1$, however, the sign of Δm_{32}^2 is still unknown. Therefore, two mass-ordering scenarios are allowed, one where neutrino masses are arranged $m_3 > m_2 > m_1$, which is called the normal mass ordering (NMO), or alternatively neutrino masses may be ordered $m_2 > m_1 > m_3$, which is called the inverted mass ordering (IMO). Next-

1007 generation neutrino oscillation experiments such as JUNO [25], Hyper-Kamiokande [26],
1008 and DUNE [27] are poised to resolve this ambiguity in the coming years.

1009 Neutrino oscillation probabilities are sensitive to the neutrino masses via the squared
1010 mass differences. Therefore, oscillation probabilities are unaffected by the absolute scale
1011 of the neutrino mass. However, oscillations can be used to obtain a lower bound on the
1012 neutrino masses by setting the mass of the lightest neutrino mass state to zero. This
1013 results in different lower limits depending on the ordering of the neutrino mass states.
1014 Current best-fit values [24] with 1σ -uncertainties for the squared mass differences are

$$\Delta m_{21}^2 = (7.42^{+0.21}_{-0.20}) \times 10^{-5} \text{ eV}^2, \quad (2.4)$$

$$\Delta m_{31}^2 = (2.5176^{+0.026}_{-0.028}) \times 10^{-3} \text{ eV}^2 \text{ (NMO)}, \quad (2.5)$$

1015 for the normal mass ordering, and for the inverted ordering the limit is

$$\Delta m_{32}^2 = (-2.498^{+0.028}_{-0.028}) \times 10^{-3} \text{ eV}^2 \text{ (IMO).} \quad (2.6)$$

1016 The parameter Δm_{21}^2 is the same in the NMO and the IMO. Allowing the lightest neutrino
1017 mass in each ordering scenario (m_{least}) to take on a range of values, one can visualize the
1018 relative masses of the neutrinos as a function of m_{least} (see Figure 2.2). The absolute
1019 neutrino mass scale is effectively the value of this m_{least} parameter.

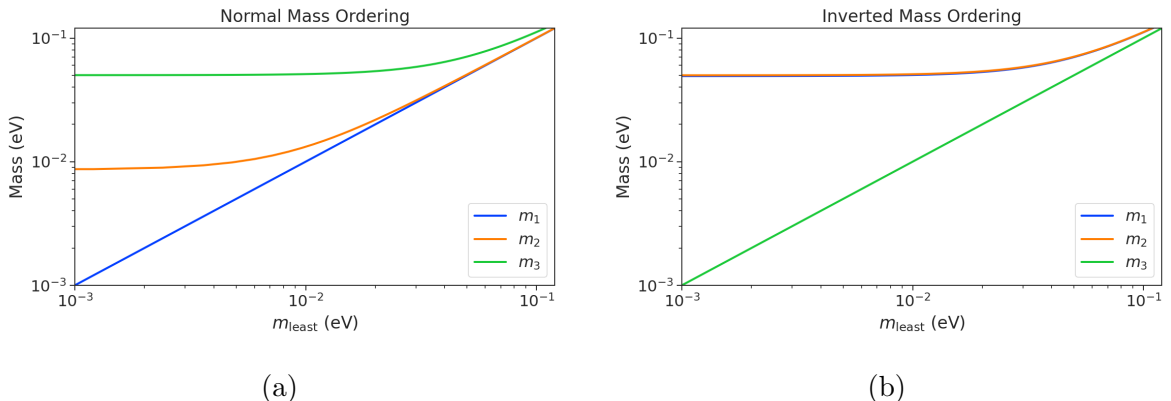


Figure 2.2. The masses of the neutrinos as a function of the lightest neutrino mass in both the normal (a) and inverted (b) mass ordering regimes.

2.4 Neutrino Masses in the Standard Model

In this section, I briefly summarize the current theoretical understanding of neutrino masses in the standard model [28–30]. Neutrinos are spin 1/2 particles, which are described using the Dirac equation.

$$(i\hbar\gamma^\mu\partial_\mu - mc)\psi(x) = 0, \quad (2.7)$$

where the field that describes the particle is denoted as $\psi(x)$. In the standard model fermions acquire mass through the Yukawa interaction, which add to the standard model Lagrangian terms of the form

$$\mathcal{L}_{\text{Yukawa}} = -Y_{ij}^\ell \bar{L}_{Li} \phi E_{Rj} + \text{h.c.}, \quad (2.8)$$

where Y_{ij}^ℓ is an element of the 3×3 Yukawa coupling matrix for leptons, L_{Li} is the left-handed lepton doublet for generation i , ϕ is the Higgs doublet, and E_{Rj} is the right-handed lepton field for generation j . Neutrinos are represented only as left-handed neutrinos and right-handed antineutrinos in the standard model, which is consistent with experimental observations. Since there are no right-handed neutrino singlet fields, there are no Yukawa interaction terms, thus neutrinos in the standard model are strictly massless. Therefore, non-zero neutrino mass is evidence for physics beyond the standard model.

For the charged leptons, the Yukawa interaction leads to masses of the form

$$m_{ij}^\ell = Y_{ij}^\ell \frac{v}{\sqrt{2}}, \quad (2.9)$$

where v is the Higgs vacuum expectation value. The observation of massive neutrinos motivates the extension of the standard model to explain the origin of neutrino masses, which can be approached in different ways, but all approaches add additional degrees of freedom to the standard model.

One approach is to introduce to the standard model a right-handed neutrino field that allows one to include Yukawa terms of the form

$$\mathcal{L}_{\nu \text{Yukawa}} = -Y_{ij}^\ell \bar{L}_{Li} \phi \nu_{Rj} + \text{h.c.} \quad (2.10)$$

where ν_{Rj} is the right-handed neutrino singlet. Because experimental evidence strongly

1043 predicts only three active neutrinos, these additional neutrinos are "sterile", in that they
1044 do not interact via the strong, weak, or electromagnetic interactions. After spontaneous
1045 symmetry breaking, the Yukawa interaction leads to mass terms given by

$$\mathcal{L}_D = -M_{Dij}\bar{\nu}_{Ri}\nu_{Lj} + \text{h.c.}, \quad (2.11)$$

1046 which is called a Dirac mass term. One of the issues with constructing neutrino masses
1047 in this way is that the required Yukawa couplings are at least a factor of 10^6 smaller than
1048 that of an electron, which begs the question: why are the Yukawa couplings so small for
1049 the neutrinos?

1050 An alternative approach is to allow the neutrinos to have a Majorana mass, which is
1051 possible because neutrinos are electrically neutral particles. The Majorana mass terms
1052 for neutrinos have the form

$$\mathcal{L}_M = -\frac{1}{2}(M_{Rij}\bar{\nu}_{Ri}\nu_{Rj}^c M_{Lij}\bar{\nu}_{Li}\nu_{Lj}^c) + \text{h.c.}, \quad (2.12)$$

1053 where M_{Rij} and M_{Lij} are right-handed and left-handed Majorana mass matrices. A
1054 consequence of neutrinos being Majorana particles is lepton number violation, which
1055 predicts the occurrence of neutrino-less double beta-decay at a rate proportional to the
1056 neutrino mass.

1057 In the most general case neutrinos have both Dirac and Majorana mass terms, which
1058 allows one to generate neutrino masses with Yukawa couplings similar to the rest of the
1059 standard model. Considering a single generation of neutrinos for demonstration, the
1060 combined neutrino mass Lagrangian can be written as

$$\mathcal{L}_{D+M} = -m_D\bar{\nu}_R\nu_L - \frac{1}{2}(m_L\bar{\nu}_L\nu_L^c + m_R\bar{\nu}_R\nu_R^c) + \text{h.c.}, \quad (2.13)$$

1061 or equivalently,

$$\mathcal{L}_{D+M} = -\frac{1}{2} \begin{bmatrix} \bar{\nu}_L & \bar{\nu}_R^c \end{bmatrix} \begin{bmatrix} m_L & m_D \\ m_D & m_R \end{bmatrix} \begin{bmatrix} \nu_L^c \\ \nu_R \end{bmatrix} + \text{h.c..} \quad (2.14)$$

1062 An example mass generation mechanism with this approach is the Type-I see-saw
1063 mechanism [31], in which one takes $m_L = 0$ and $m_R \gg m_D$. By diagonalizing Equation
1064 2.14 one obtains the mass eigenvalues that represent the physical masses of the neutrinos.
1065 The light neutrino mass eigenstate, which represents the observed neutrino mass, has a
1066 mass given by

$$m_1 \approx \frac{m_D^2}{m_R}, \quad (2.15)$$

1067 and the heavy neutrino mass eigenstate, which represents the unobserved sterile neutrino,
1068 has a mass

$$m_2 \approx m_R. \quad (2.16)$$

1069 For m_D similar to the other quark or lepton masses, one obtains physical neutrino masses
1070 consistent with observations from sterile neutrino masses of $m_R \approx O(10^{15})$ GeV. This
1071 mass scale is well beyond the capabilities of modern particle accelerators to probe.

1072 2.5 Neutrino Absolute Mass Scale

1073 The neutrino absolute mass scale or simply "neutrino mass" cannot be probed with
1074 neutrino oscillations, since oscillation probabilities are determined by the squared mass
1075 differences between neutrino mass eigenstates, therefore, alternative techniques are needed
1076 to perform an effective measurement of the neutrino mass.

1077 2.5.1 Limits from Cosmology

1078 The Λ CDM model summarizes the current cosmological understanding of the universe [24].
1079 Λ CDM predicts that the universe originated from a single expansion event colloquially
1080 called the "Big Bang". During the Big Bang, the universe originated as a hot spacetime
1081 singularity, which abruptly experienced rapid expansion in a process known as inflation.
1082 After expansion the inflationary field eventually decayed into a population of quarks,
1083 gluons, leptons, and photons, which were kept in thermal equilibrium by the high-
1084 temperatures of the early universe.

1085 As the universe continued to expand it's density and temperature decreased until
1086 the formation of neutral atoms, primarily hydrogen, was possible. At which point the
1087 population of photons produced during the Big Bang decoupled from the primordial
1088 universe and began to freely propagate. A direct prediction of the Λ CDM model is that
1089 this population of photons is still present, but with a significantly reduced temperature
1090 due to the subsequent expansion of the universe. This is consistent with the observation of
1091 the CMB (cosmic microwave background), which is a population of microwave radiation
1092 with a blackbody temperature of 2.7 K. The CMB is extremely uniform in all directions
1093 with slight anisotropies that can be analyzed to study the evolution of the early universe.
1094 A series of experiments have measured the CMB with increasing levels of precision, which
1095 has lead to a significant increase in our current understanding of cosmology.

1096 In addition to the CMB, inflation predicts the existence of a $C\nu B$ (cosmic neutrino

background) [32], which are the remnant neutrinos produced during the Big Bang. Since neutrinos only interact via the weak force, they decouple from the Big Bang plasma at an earlier time than the CMB photons. The temperature at which the C ν B decouples depends on the neutrino rest mass. Neutrinos play a unique role in the Λ CDM model, due to the fact that neutrinos act as radiation early in the universe but as matter in the late universe. This leads to specific signatures that impact the expected anisotropies of the CMB as well as the distribution of matter in the universe [33]. By combining measurements of the CMB with measurements of the large-scale structure (LSS) of the universe one can constrain the neutrino mass scale by fitting these datasets with the Λ CDM model. This analysis results in some of the most stringent constraints on the neutrino mass. Recent analyses [24] have been able to constrain the neutrino mass scale to

$$\Sigma_{m_\nu} \equiv \sum_i m_i < 0.11 \text{ eV}, \quad (2.17)$$

where m_i are the neutrino mass eigenstates.

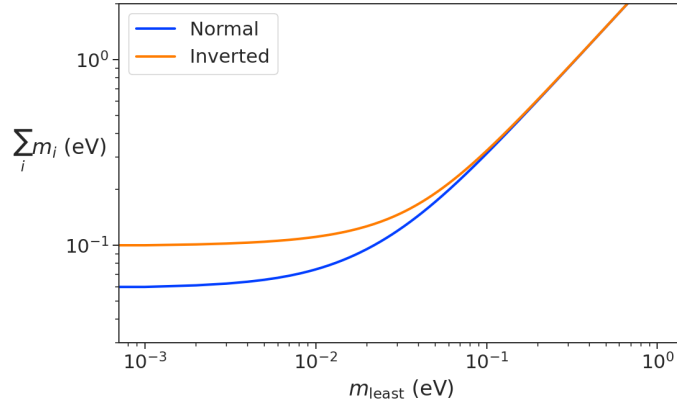


Figure 2.3. The neutrino mass observable measured by cosmology as a function of the lightest neutrino mass eigenstate.

The observable Σ_{m_ν} constrains the neutrino mass by setting the mass of the lightest neutrino mass eigenstate (m_{least}) (see Figure 2.3). In the normal mass ordering Σ_{m_ν} can be rewritten in the form

$$\Sigma_{m_\nu} = m_{\text{least}} + \sqrt{\Delta m_{21}^2 + m_{\text{least}}^2} + \sqrt{\Delta m_{32}^2 + m_{\text{least}}^2}, \quad (2.18)$$

where it is clear that a measurement of Σ_{m_ν} effectively sets the neutrino mass scale

1114 through m_{least} . The analogous formula for the inverted mass ordering is

$$\Sigma_{m_\nu} = m_{\text{least}} + \sqrt{-\Delta m_{32}^2 + m_{\text{least}}^2} + \sqrt{-\Delta m_{31}^2 + m_{\text{least}}^2}. \quad (2.19)$$

1115 Upcoming experiments [34] are planned to refine measurements of the CMB, LSS,
 1116 and other cosmological observables. With this additional data it is possible that in the
 1117 near future cosmological measurements will be able to positively constrain the neutrino
 1118 absolute mass scale. However, the strength of these limits strictly depend on the accuracy
 1119 of the Λ CDM model, which highlights the need for direct experimental measurements of
 1120 the neutrino mass to confirm the predictions of cosmology and to fix the neutrino mass
 1121 parameter in future cosmological analyses.

1122 2.5.2 Limits from Neutrinoless Double Beta-decay Searches

1123 If neutrinos are Majorana fermions, then the neutrino is equivalent to its own antiparticle
 1124 and lepton conservation is not an exact law of nature [35]. Limits on the rate of
 1125 neutrinoless double beta-decay ($0\nu\beta\beta$), are some of the most powerful current tests of
 1126 lepton number conservation [24]. If $0\nu\beta\beta$ were observed, it would be direct evidence that
 1127 neutrinos are Majorana fermions and provide a method for measuring the neutrino mass
 1128 scale.

1129 Standard double beta-decay occurs when two neutrons in an unstable nucleus spon-
 1130 taneously decay into two protons, which results in the production of two electrons and
 1131 two neutrinos (see Figure 2.4). Whereas, during $0\nu\beta\beta$ the two neutrinos self-annihilate

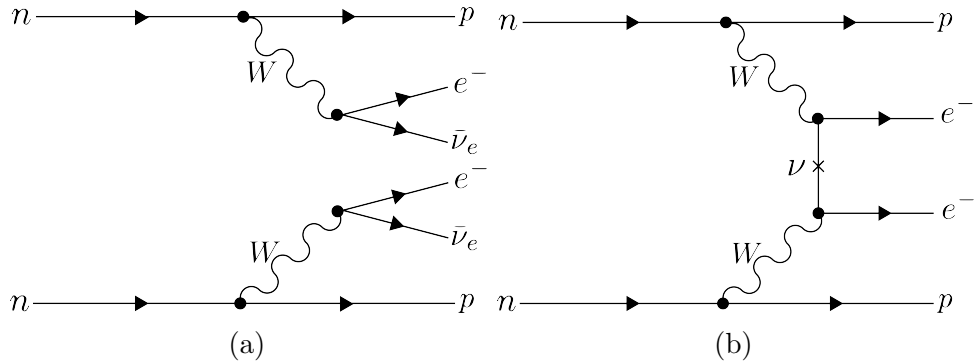


Figure 2.4. Feynman diagrams for double beta-decay (a) and $0\nu\beta\beta$ (b).

1131
 1132 producing only two electrons, which violates lepton number by two.

1133 Assuming that the exchange of two Majorana neutrinos is the dominant channel for
 1134 $0\nu\beta\beta$, then a measurement of the $0\nu\beta\beta$ half-life for a particular isotope can be used to

1135 set the neutrino absolute mass scale [36]. The half-life is written in terms of the effective
 1136 neutrino mass for $0\nu\beta\beta$ ($m_{\beta\beta}$) using the equation

$$T_{1/2}^{0\nu} = \frac{1}{G|\mathcal{M}|^2 m_{\beta\beta}^2}, \quad (2.20)$$

1137 where G is the phase-space factor for the decay and \mathcal{M} is the relevant nuclear matrix
 1138 element. $m_{\beta\beta}$ is given by an incoherent sum of the neutrino mass eigenstates weighted
 1139 by the PMNS mixing matrix parameters,

$$m_{\beta\beta} = \left| \sum_i U_{ei}^2 m_i \right|. \quad (2.21)$$

1140 The information provided from $0\nu\beta\beta$ on the neutrino mass scale can be visualized by
 1141 expressing the value of $m_{\beta\beta}$ in terms of m_{least} and two relative Majorana phases [2]. The
 1142 allowed regions for $m_{\beta\beta}$ as a function of m_{least} are shown in Figure 2.5 as the regions
 1143 bounded by the black curves overlayed with the discovery probabilities of future $0\nu\beta\beta$
 decay experiments based on current neutrino data.

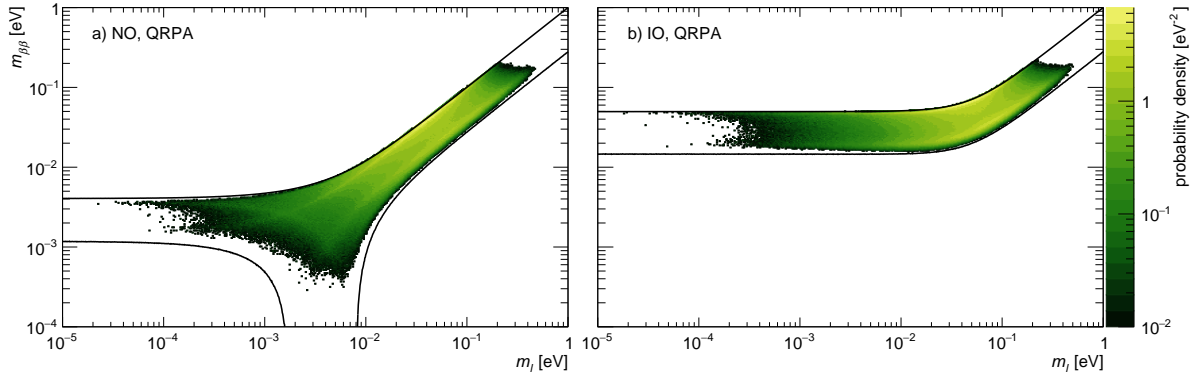


Figure 2.5. The discovery probabilities for the future generation of $0\nu\beta\beta$ experiments as a function of $m_{\beta\beta}$ and m_{least} . Figure from [2].

1144
 1145 Because of the possibility of cancellation due to the unknown Majorana phases included
 1146 in the sum specified by Equation 2.21, the neutrino mass information gained from $0\nu\beta\beta$
 1147 is necessarily imperfect. Additionally, theoretical uncertainties in the calculation of the
 1148 nuclear matrix elements complicates the calculation of $m_{\beta\beta}$ from a measurement of $0\nu\beta\beta$
 1149 half-life. Similar to cosmology, there is a high degree of complementarity between direct
 1150 measurements of the neutrino mass and $0\nu\beta\beta$. In particular, a measurement of m_{least} to
 1151 less than 0.1 eV sensitivity provides significant information for $0\nu\beta\beta$ searches based on
 1152 the discovery probabilities displayed in Figure 2.5.

2.5.3 Limits from Beta-decay

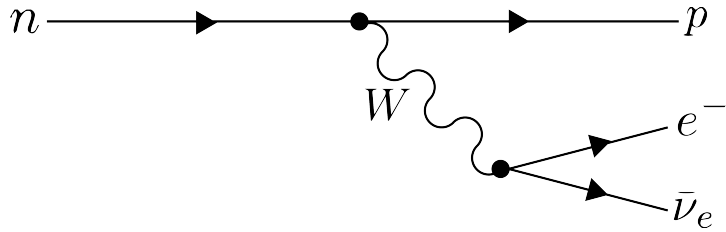


Figure 2.6. A Feynman diagram of beta decay

Certain processes involving neutrinos, in particular beta-decay (see Figure 2.6), have initial states with well-defined total energies and final states that can be measured with high accuracy and precision. Beta-decay involves the decay of an unstable isotope where a neutron spontaneously converts to a proton and emits an electron and anti-neutrino ("neutrino" for brevity) to conserve charge and lepton number [5]. Therefore, by applying the principles of energy and momentum conservation, a measurement of the kinematics of the final state can be used to constrain the neutrino mass [37].

Using beta-decay to measure the neutrino mass can be tied back to Fermi's original 1934 theory of nuclear beta-decay [16] (see Figure 2.7). Because the constraints on the

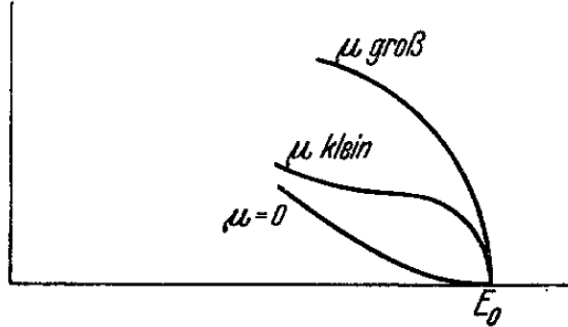


Figure 2.7. A figure from Fermi's 1934 paper on a theory of beta-decay depicting the kinetic energy spectrum of the emitted electron. The effect of the neutrino mass, written as μ , is to distort the shape of the spectrum near the endpoint from the zero-mass spectrum.

neutrino mass from beta-decay depend only on the final state measurement capabilities and the principles of energy and momentum conservation, neutrino mass measurements with beta-decay are called direct measurements. A direct measurement like beta-decay contrasts with other neutrino mass measurements approaches that are model-dependent such as cosmology and $0\nu\beta\beta$, which provide complementary ways to study the physics of massive neutrinos.

1169 The isotope of choice for direct neutrino mass measurements with beta-decay has
 1170 been tritium (3H_2) for many decades, because it conveniently fulfills many experimental
 1171 requirements. Of upmost importance is a decay with a low Q-value, which is the available
 1172 kinetic energy based on the mass difference between the initial and final states. The
 1173 effect of a massive neutrino on the shape of the spectrum is magnified for low Q-values
 1174 and tritium has an unusually low Q-value of 18.6 keV.

1175 Additionally, tritium beta-decay is super-allowed, which results in a relatively short
 1176 half-life of 12.3 years. Therefore, high source activity can be obtained with a relatively
 1177 small source mass. High-activity is desirable because of the low-activity near the tritium
 1178 spectrum endpoint. For tritium beta-decays, only a factor of 3×10^{-13} of the decays
 1179 occur in the last 1 eV of the spectrum. Isotopes with Q-values lower than tritium are
 1180 known [37], but this is outweighed by exceedingly long half-lives leading to unobtainable
 1181 source masses.

1182 The endpoint measurement approach involves quantifying the effect of the neutrino's
 1183 mass on shape of the electron's kinetic energy spectrum near the endpoint. The shape of
 1184 the kinetic energy spectrum (see Figure 2.8) is given by

$$\frac{d\Gamma}{dE} = \frac{G_F^2 |V_{ud}|^2}{2\pi^3} (G_V^2 + 3G_A^2) F(Z, \beta) \beta (E + m_e)^2 (E_0 - E) \\ \times \sum_{i=1,2,3} |U_{ei}|^2 [(E_0 - E)^2 - m_i^2]^{1/2} \Theta(E_0 - E - m_i), \quad (2.22)$$

1185 where G_F is the Fermi coupling constant, V_{ud} is an element of the CKM matrix, E
 1186 is the kinetic energy of the electron, β is the velocity of the electron divided by the
 1187 speed of light, E_0 is the endpoint energy assuming zero neutrino mass, $F(Z, \beta)$ is the
 1188 Fermi function, and $\Theta(E_0 - E - m_i)$ is the Heaviside function, which enforces energy
 1189 conservation. One can see that the decay spectrum is actually a combination of three
 1190 spectra with different endpoints based on the values of the neutrino mass eigenstates, m_i .
 1191 This produces "kinks" in the spectrum shape due to overlapping spectra with different
 1192 endpoint values, but such an effect would be nearly impossible to resolve given the finite
 1193 energy resolution of a real experiment.

1194 The neutrino mass scale variable measured by beta-decay is given by

$$m_\beta^2 = \sum_i |U_{ei}|^2 m_i^2, \quad (2.23)$$

1195 where m_β is the electron-weighted neutrino mass or simply "neutrino mass" for brevity.

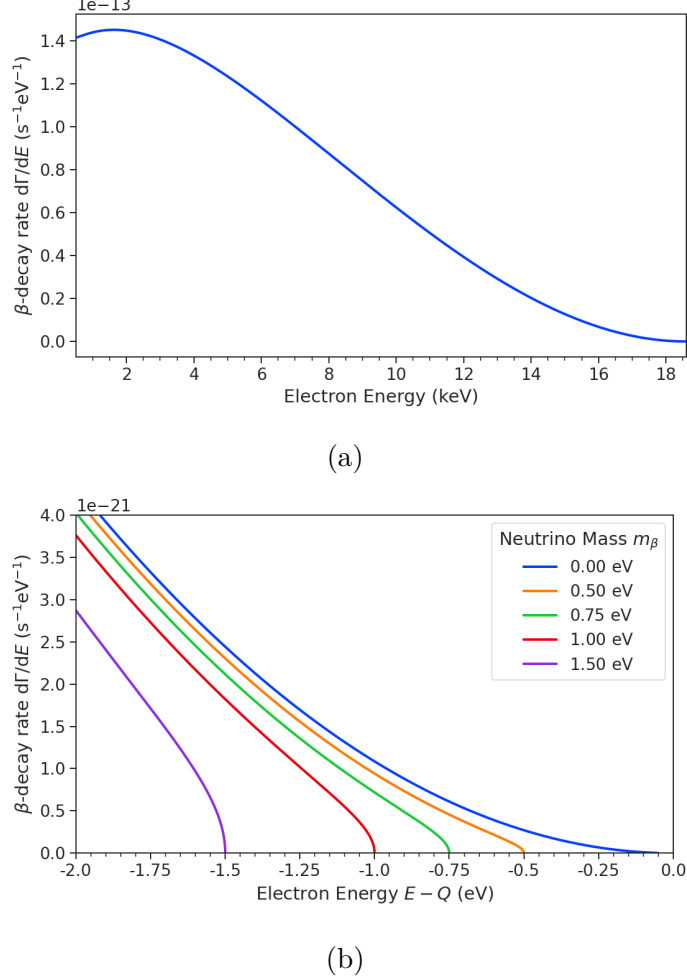


Figure 2.8. The tritium beta-decay spectrum. The effect of a massive neutrino on the spectrum is to change its shape near the endpoint by an amount proportional to the size of the neutrino mass. A sufficiently high-statistic and high-resolution measurement of the spectrum endpoint would be able to measure the neutrino mass.

The quantity m_β corresponds to a particular weighted sum of the neutrino masses, which is distinct from effective neutrino masses such as $m_{\beta\beta}$ [37]. Assuming unitarity, the neutrino mass can be expressed in terms of the PMNS matrix elements, squared mass differences, and the lightest neutrino mass eigenstate. For the normal mass ordering the equation is

$$m_\beta^2 = m_{\text{least}}^2 + |U_{e2}|^2 \Delta m_{21}^2 + |U_{e3}|^2 \Delta m_{31}^2, \quad (2.24)$$

and for the inverted ordering the equation is

$$m_\beta^2 = m_{\text{least}}^2 + |U_{e1}|^2 (-\Delta m_{32}^2 - \Delta m_{21}^2) + |U_{e2}|^2 (-\Delta m_{32}^2). \quad (2.25)$$

1202 Therefore, a measurement of the neutrino mass in combination with neutrino mixing
1203 parameters is effectively a measurement of m_{least} .

1204 Since the neutrino mass is small (< 1 eV), its effect on the spectrum is limited to the
1205 endpoint region. The affect of a non-zero neutrino mass on the endpoint spectrum is
1206 plotted for the reader in Figure 2.8. Resolving the small changes in the spectrum shape
1207 requires an experimental technique with high statistics, excellent energy resolution, and
1208 low background activity.

Chapter 3

Direct Measurement of the Neutrino Mass with Project 8

3.1 Introduction

A promising technique for direct measurements of the neutrino mass beyond the projected 200 meV limit of the KATRIN experiment [38] is tritium beta-decay spectroscopy with an atomic tritium source [39]. Atomic tritium, combined with a large-volume, high-resolution energy measurement technique, is capable of measuring the neutrino mass with sensitivity below the 50 meV, which exhausts the range of neutrino masses allowed under the inverted hierarchy.

Cyclotron Radiation Emission Spectroscopy (CRES) is a high-resolution energy measurement technique compatible with atomic tritium production and storage that can enable the next-generation of neutrino mass direct measurement experiments [40]. The Project 8 collaboration is currently engaged in a program of research and development (R&D) aimed at developing the technology necessary for a measurement of the neutrino mass using CRES and atomic tritium with a sensitivity of 40 meV [41].

In Section 3.2 I provide an introduction to the basics of the CRES technique as well as the goals of the Project 8 experiment. Additionally, I sketch out the phased experiment development plan being implemented by Project 8 to build towards a next-generation neutrino mass experiment.

In Section 3.3 I give an overview of Phase II of the Project 8 experiment [42,43], which completed early in 2023. Although the bulk of the work presented in this dissertation is relevant to designs of future Project 8 experiments, a description of the work in Phase II provides useful context.

In Section 3.4 I introduce a CRES measurement concept based on antenna arrays [44], which could be the basis for the ultimate Project 8 neutrino mass experiment. A

1235 significant portion of the R&D efforts of Project 8 in Phase III were directed towards
1236 simulating and modeling this experimental concept in order to understand the achievable
1237 sensitivity to the neutrino mass.

1238 Lastly, in Section 3.5 I introduce conceptual designs of pilot-scale experiments and
1239 Phase IV that combine atomic CRES with a large-volume CRES detection technique.
1240 This includes a design concept for an antenna array based experiment, but also a design
1241 for a resonant cavity based experiment. Resonant cavities are discussed in more depth in
1242 Chapter 6 and have become the default choice for the Phase IV experiment.

1243 **3.2 Project 8 and Cyclotron Radiation Emission Spectroscopy**

1244 **3.2.1 Cyclotron Radiation Emission Spectroscopy — CRES**

1245 Time and frequency are two of the most precisely measured quantities in physics. Atomic
1246 clocks, which operate by measuring the frequencies of various atomic transitions, have
1247 been used to measure time with astounding relative uncertainties of 10^{-18} seconds [45].
1248 The extreme precision possible with frequency measurements is often summarized using
1249 the a quote from the Physicist Arthur Schawlow who said advise his students to "Never
1250 measure anything but frequency!" [46].

1251 Neutrino mass measurements using tritium beta-decay require the measurement
1252 of perturbations to the 18.6-keV tritium endpoint with a precision as small as 0.1 eV.
1253 Therefore, a spectroscopic technique with extremely high resolution is required. Frequency
1254 measurements are capable of such high-resolutions for the intuitive reason that they are
1255 essentially digital counting measurements, which average the number of oscillations of a
1256 physical system over time. By observing a rapidly oscillating system over a sufficient
1257 length of time one can obtain essentially arbitrary precision on a frequency limited only
1258 by the measurement time and signal-to-noise ratio (SNR) of the system.

1259 A method is required for translating an electron kinetic energy measurement into a
1260 frequency measurement. A straightforward way to accomplish this is to place a gaseous
1261 supply of tritium into a magnetic field, therefore, when a beta-decay occurs the resulting
1262 electron will immediately begin to orbit around a magnetic field line at the cyclotron
1263 frequency, proportional to its kinetic energy (see Figure 3.1). The acceleration caused
1264 by the orbit leads to the emission of cyclotron radiation that can be detected using an
1265 array of antennas or resonant cavity. The starting frequency of the radiation gives the

1267 electron's initial kinetic energy, which is used to build the beta-decay spectrum and
 1268 measure the neutrino mass. The name for this measurement technique is Cyclotron
 1269 Radiation Emission Spectroscopy or CRES [40].

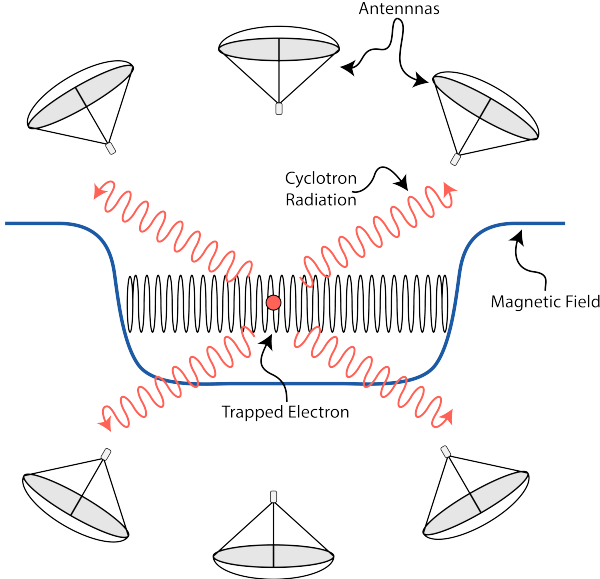


Figure 3.1. A cartoon illustration of the CRES technique. An electron is contained in a magnetic trap, which is a local minimum in the magnetic field, so that its cyclotron radiation can be detected by an array of antennas. Detecting the cyclotron radiation allows one to measure its cyclotron frequency and determine its kinetic energy.

1270 In the non-relativistic case, the cyclotron frequency is simply a function of the
 1271 charge-to-mass ratio of the particle, however, the relativistic correction to the cyclotron
 1272 frequency

$$f_c = \frac{qB}{2\pi m_e \gamma} = \frac{1}{2\pi} \frac{qB}{m_e + E_{\text{kin}}/c^2}, \quad (3.1)$$

1273 introduces a dependence of the kinetic energy (E_{kin}) to the inverse of the cyclotron
 1274 frequency (f_c). Electrons with kinetic energies of 18.6 keV are in the weakly relativistic
 1275 regime with $\beta = \frac{v}{c} = 0.263$ and $\gamma = 1.036$.

1276 The frequency resolution of a CRES measurement can be estimated by differentiating
 1277 Equation 3.1,

$$\frac{df_c}{dE_{\text{kin}}} = \frac{1}{2\pi} \frac{-qBc^2}{(m_e c^2 + E_{\text{kin}})^2}, \quad (3.2)$$

1278 from which one obtains the relationship between fractional differences in energy and
 1279 frequency,

$$\frac{df_c}{f_c} = \frac{1 - \gamma}{\gamma} \frac{dE_{\text{kin}}}{E_{\text{kin}}}. \quad (3.3)$$

1280 Therefore, an energy precision of 1 eV for an 18.6 keV electron can be achieved with a
 1281 frequency precision of approximately 2 ppm.

1282 The minimum observation time required to achieve this resolution can be estimated
 1283 using the uncertainty principle as formulated by Gabor [47]. Electrons from tritium
 1284 beta-decay experience random collisions with the background gas particles, which limits
 1285 the uninterrupted radiation lifetime. The time between collision events, referred to as
 1286 "track length", is an exponentially distributed variable. Differences in the track lengths
 1287 of a population of mono-energetic electrons leads to an uncertainty or broadening in the
 1288 distribution of measured frequencies, which is proportional to the mean track length, τ_λ .
 1289 The resulting frequency distribution has a Lorentzian profile, whose width is given by
 1290 the Gabor limit,

$$\tau_\lambda \Delta f_c = \frac{1}{2\pi} \implies \Delta f_c = \frac{1}{2\pi\tau_\lambda}. \quad (3.4)$$

1291 The cyclotron frequency for a 18.6-keV electron in a 1 T field is approximately
 1292 27 GHz, consequently, the minimum observation time for a frequency resolution of 2 ppm
 1293 is approximately 3 μ sec. The Gabor limit is not the true lower bound on the frequency
 1294 resolution for a CRES signal, since it derives from the Fourier representation of a fixed
 1295 length time-series using a basis of infinite duration sinusoids. If one takes the approach of
 1296 fitting the CRES signal in the time-domain, then the lower limit on frequency precision
 1297 is given by the Cramér-Rao lower bound (CRLB) [48], which depends on the track length
 1298 and SNR. The CRLB is the minimum variance achievable by an unbiased estimator
 1299 for an unknown but deterministic parameter. In general, the CRLB allows for better
 1300 precision on the cyclotron frequency.

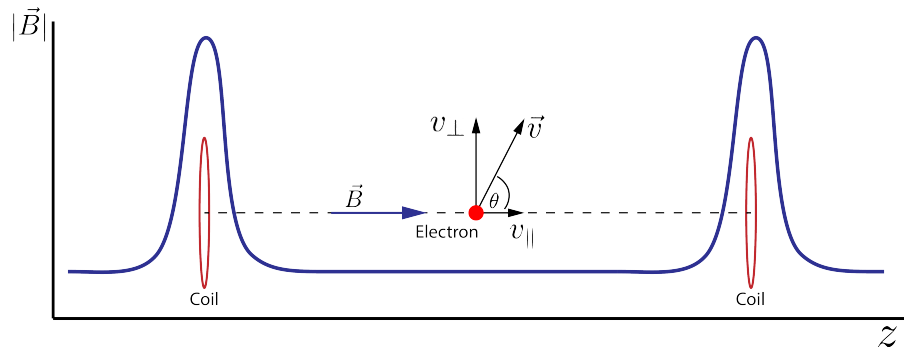


Figure 3.2. An illustration of an electron in a bathtub magnetic trap generated by two well-separated coils.

1301 Ensuring that an electron remains under observation long enough so that its frequency
 1302 can be precisely measured can be achieved using a magnetic trap. A magnetic trap is a

1303 local minimum in a background magnetic field generated an appropriate configuration of
 1304 electromagnetic coils. Since magnetic fields can do no work, there is no danger of the
 1305 magnetic trap affecting the kinetic energy of the electron after it is emitted from the
 1306 beta-decay. One common approach to creating a magnetic trap is the "bathtub" trap
 1307 configuration, which can be produced using two magnetic pinch coils aligned on a central
 1308 axis that are separated by a distance that is large compared to the coil radius (see Figure
 1309 3.2). This configuration produces a trap with a uniform bottom and relatively steep
 1310 walls, which is ideal for CRES measurements.

1311 The electron's pitch angle is a useful parameter for describing its motion in the
 1312 magnetic trap. Pitch angle is defined in terms of the ratio between the component of the
 1313 electron's velocity perpendicular to the magnetic field and the component parallel to the
 1314 magnetic field

$$\tan \theta_p = \frac{v_{\perp}}{v_{\parallel}}. \quad (3.5)$$

1315 Electrons with pitch angles less than 90° oscillate back and forth in the magnetic trap,
 1316 which leads to variations in the cyclotron frequency caused by the changing value of
 1317 the magnetic field along the electron's path. This leads to frequency modulation that
 1318 produces sidebands in the cyclotron radiation spectrum. Resolving these sideband
 1319 frequency components is necessary for a complete reconstruction of the CRES signal in
 1320 the experiment.

1321 Electrons trapped in a cylindrically symmetric trap have three primary components of
 motion (see Figure 3.3). The dominant component, typically with the highest frequency,

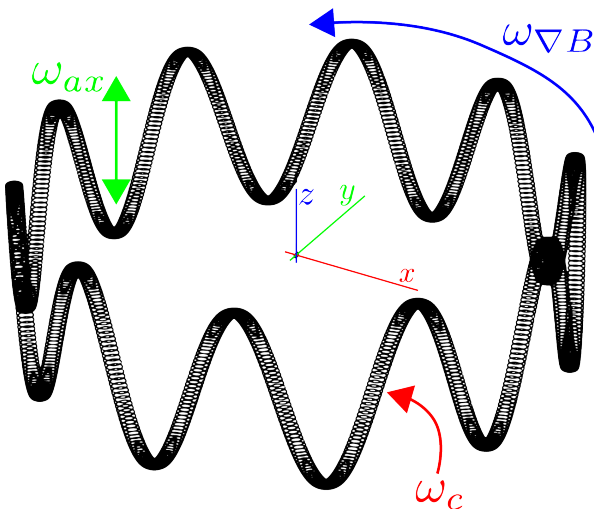


Figure 3.3. A plot of the main components of an electron's trajectory in a cylindrically symmetric trap.

1322

1323 is the electron's cyclotron orbit, which encodes information on the electron's kinetic
 1324 energy. Axial motion from the electron's pitch angle leads to frequency modulation,
 1325 and a shift in the average magnetic field experienced by an electron. This leads to a
 1326 correlation between the kinetic energy of the electron and the pitch angle depending on
 1327 the particular shape of the magnetic trap, which can negatively impact energy resolution.
 1328 Generally, more variation in the magnetic field along the electron's trajectory leads to
 1329 a worse energy resolution. The magnetic trap can be engineered to have a flat bottom
 1330 with very steep walls to mitigate this effect. A bathtub trap design, where the distance
 1331 between the coils is much greater than the coil radius, is the trap that best approximates
 1332 this ideal design. Radial gradients in the trap leads to a third component of motion
 1333 called grad-B drift [49]. The equation for the drift velocity is

$$\mathbf{v}_{\nabla B} = \frac{m_e v_{\perp}^2}{2qB} \frac{\mathbf{B} \times \nabla B}{B^2}. \quad (3.6)$$

1334 The total power of the radiation emitted by an electron in a free-space environment
 1335 is given by the Larmor equation [50]

$$P(\gamma, \theta_p) = \frac{1}{4\pi\epsilon_0} \frac{2}{3} \frac{q^2 \omega_c^2}{c} (\gamma^2 - 1) \sin^2 \theta_p, \quad (3.7)$$

1336 where ω_c is the cyclotron frequency multiplied by 2π and θ_p is the pitch angle to distinguish
 1337 it from the spherical angle coordinate. A single electron with a 90° pitch angle and
 1338 18.6 keV of kinetic energy in a 1 T magnetic field emits a total radiation power of 1.2 fW.
 1339 Furthermore, one is typically only able to receive a fraction of this total power with an
 1340 antenna or other detection system. Therefore, RF systems in CRES experiments must be
 1341 operated at cryogenic temperatures to limit the noise power such that adequate SNR can
 1342 be achieved for signal detection and reconstruction. Alternatively, longer tracks enable
 1343 detection of weaker signals due to the increase in the total signal energy available for the
 1344 detection algorithm.

1345 3.2.2 Project 8

1346 The Project 8 collaboration¹ is a group of institutions in the United States and Germany
 1347 building an experiment to measure the neutrino mass by developing a novel spectrometer
 1348 technology based on CRES. In the ultimate Project 8 experiment, the CRES technique
 1349 will be used to measure the beta-decay spectrum using a large source of atomic tritium

¹<https://www.project8.org/>

1350 sufficient to achieve the required statistics in the last $O(10)$ eV of the decay spectrum.
1351 Project 8 is targeting a neutrino mass sensitivity below 50 meV [51], which exhausts the
1352 range of possible neutrino masses under the inverted hierarchy and is a factor of four less
1353 than sensitivity projections for the ongoing KATRIN experiment.

1354 Project 8's proposed experiment requires the development of two novel technologies:
1355 the production and trapping of a source of atomic tritium on cubic-meter scales and
1356 technology to enable CRES measurements of individual electrons in the same volume.

1357 Atomic Tritium

1358 Previous measurements of the tritium beta-decay spectrum for neutrino mass measure-
1359 ments have relied on sources of molecular tritium for their measurements [38, 52, 53] due
1360 to the technical challenges associated with the production and storage of atomic tritium.

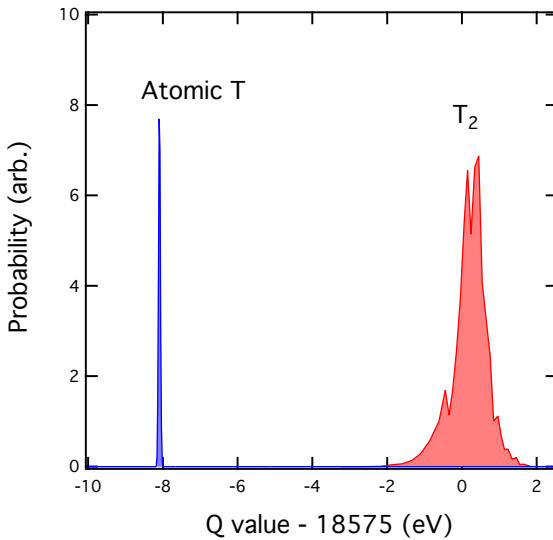


Figure 3.4. A plot of the final state distributions of atomic and molecular tritium. The final state distribution provides the primary contribution to the width of the molecular spectrum whereas thermal doppler broadening is responsible for the width of the atomic spectrum.

1361 One must supply sufficient energy to the tritium molecules to break the molecular
1362 bond and create atomic tritium. Common approaches include the use of hot coaxial
1363 filament atom crackers as well as plasma sources. Both involve heating the tritium atoms
1364 to temperatures of > 2500 K, which must then be cooled to temperatures on the order
1365 of a few mK so that the tritium atoms can be trapped. Cooling the atoms requires the
1366 construction of a large tritium infrastructure and cooling system that can supply a source
1367 of cold atoms to the trap.

1368 Once cold tritium atoms are produced they cannot make contact with any surfaces
1369 to avoid recombination of the atoms to molecules. Therefore, a magnetic trap is required
1370 to store the atoms for a sufficient length of time that they have a chance to decay before
1371 escaping the trap. Trapping the atoms requires the construction of a large and complex
1372 magnet system that must be cooled to cryogenic temperatures.

1373 The significant experimental complexity caused by atomic tritium makes a molecular
1374 source the obvious choice from practical considerations. However, the drawback of
1375 molecular tritium for neutrino mass measurement is the irreducible broadening in the
1376 electron's kinetic energy due to the final state spectrum of molecular tritium (see Figure
1377 3.4). The broadening of the final state spectra has a RMS amplitude of 436 meV [54, 55]
1378 caused by variation in the final vibrational state of the daughter molecule.

1379 For atomic tritium, the primary sources of broadening in the final state spectrum are
1380 magnetic hyperfine splittings (magnitude of $O(10^{-5})$ eV) and thermal Doppler broadening
1381 caused by the motion of the trapped atom. Atomic tritium at a temperature of 1 mK
1382 has a broadening which is dominated by thermal Doppler broadening, providing about
1383 1 meV RMS of broadening to the electron's kinetic energy.

1384 The larger energy broadening with molecular tritium leads to an irreducible statistical
1385 uncertainty that limits the achievable sensitivity to approximately 100 meV at 90%
1386 confidence. For previous direct measurements of the neutrino mass, this uncertainty is
1387 an insignificant contribution to the overall uncertainty budget. However, for experiments
1388 like Project 8 atomic tritium is a key component to the success of the experiment.

1389 **CRES for Neutrino Mass Measurement**

1390 Several features of the CRES technique make it an attractive choice for a next generation
1391 neutrino mass measurement experiment. Because CRES is a remote-sensing technique,
1392 it is possible to observe the kinetic energy of the electron without altering its trajectory
1393 or directly interacting with the particle, therefore, in a CRES experiment the source
1394 gas volume can be the same as the CRES spectrometer volume. Tritium gas is also
1395 transparent to cyclotron radiation, which means that the kinetic energies of electrons can
1396 be measured using a cavity or antenna array, located directly outside the atom trapping
1397 volume.

1398 Because source and spectrometer can be colocated, CRES experiments have an
1399 advantageous scaling law relative to the current state-of-the-art beta-decay spectroscopy
1400 experiment, KATRIN. KATRIN utilizes the magnetic adiabatic collimation with an
1401 electrostatic filter (MAC-E filter) technique to measure the beta-decay spectrum of

1402 molecular tritium. In this approach, a source of molecular tritium is located outside the
1403 spectrometer. When a beta-decay occurs the electron is guided out of the tritium source
1404 using a magnetic field and is transported through the MAC-E filter before it is detected
1405 on the other side of the filter using a charge sensor. The measurement statistics of the
1406 MAC-E filter are limited by the transverse area of the tritium source and filter due to the
1407 need to travel through the experiment without scattering. This scaling is less favorable
1408 than the volumetric scaling of CRES due to the ability to colocate source and detector.

1409 Another promising aspect of the CRES technique is the inherently high precision
1410 of frequency based measurements. The endpoint of the molecular tritium beta-decay
1411 spectrum is approximately 18.6 keV, which dwarfs the neutrino mass scale of $< 1 \text{ eV}/c^2$
1412 by at least a factor of 10^5 . Measuring the effect of such a small mass on a high energy
1413 electron requires excellent energy resolution. Since frequency measurements are essentially
1414 counting measurements they are intrinsically quite accurate due to the ability to measure
1415 the cyclotron frequency by effectively averaging over millions of cyclotron orbits. It
1416 is possible to achieve part-per-million accuracy on the kinetic energy with the CRES
1417 technique using the off-the-shelf RF components.

1418 CRES is also nearly immune to typical sources of backgrounds that can plague other
1419 experiments. Since CRES operates via a non-destructive measurement of the electron's
1420 cyclotron frequency, sources of background electrons are effectively filtered out by limiting
1421 the frequency bandwidth of the measurement. The fiducial volume of the experiment is
1422 free from any surfaces that could introduce stray electrons, and electrons from sources
1423 outside the fiducial volume can be prevented from entering the experiment.

1424 Neutrino Mass Sensitivity Goals

1425 Project 8's ultimate goal is to combine CRES with atomic tritium to measure the neutrino
1426 mass with 40 meV sensitivity at the 90% confidence level (see Figure 3.5). This sensitivity
1427 is sufficient to fully exhaust the range of allowable neutrino masses under the inverted
1428 neutrino mass ordering regime and is approximately an order of magnitude less than the
1429 projected final sensitivity of the KATRIN experiment. Excluding the full neutrino mass
1430 parameter space would require a sensitivity an order of magnitude lower than what is
1431 proposed by Project 8, which would require an experiment whose size and complexity
1432 are currently well beyond proposals for the next-generation of neutrino mass direct
1433 measurement experiments.

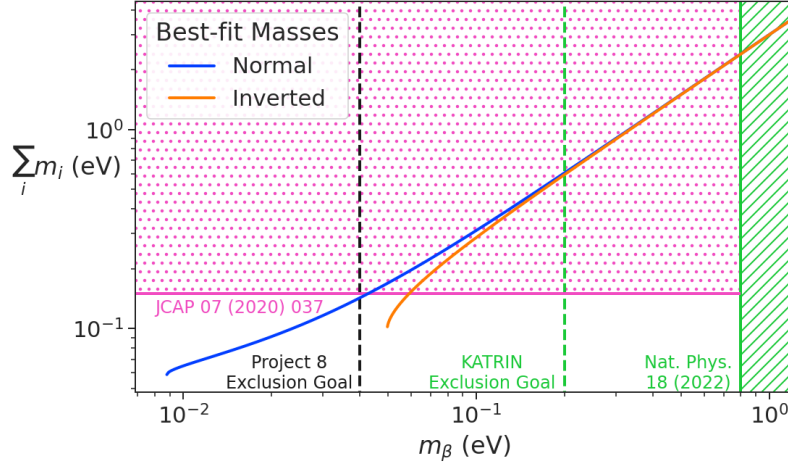


Figure 3.5. Neutrino mass exclusion plot including limits from cosmological measurements and the KATRIN experiment. Allowed ranges for neutrino masses under the normal and inverted hierarchies are shown as the blue and orange lines respectively. The black dashed line shows Project 8’s goal neutrino mass sensitivity for the Phase IV experiment.

1434 3.2.3 The Project 8 Phased Development Plan

1435 Reaching 40 meV sensitivity requires the simultaneous development and eventually
 1436 combination of CRES and atomic tritium. These technologies require a significant up-front
 1437 R&D investment to build-out the required capabilities for a 40 meV CRES experiment.
 1438 Therefore, Project 8 is following a phased experiment plan in which incremental progress
 1439 can be made towards the ultimate goal of a 40 meV neutrino mass measurement with
 1440 CRES.

1441 Project 8’s experiment plan is divided into four phases. The first phase, called Phase
 1442 I, consisted of a demonstration of the CRES technique and a measurement of the
 1443 internal conversion spectrum of ^{83m}Kr . Phase II was the first measurement of the tritium
 1444 beta-decay spectrum and neutrino mass measurement with CRES. Currently, Project 8
 1445 is engaged in Phase III, which is research and development towards a scalable CRES
 1446 measurement technique and atomic tritium source for the final Project 8 experiment in
 1447 Phase IV. Phase IV is the ultimate experiment by Project 8 that will combine CRES
 1448 with atomic tritium to measure the neutrino mass with a sensitivity of 40 meV.

1449 Phase I and II: Proof of Principle and First Tritium Measurements

1450 The earlier phases of the Project 8 experiment, Phase I and II, were focused on demon-
 1451 stration and development of the CRES technique itself as well as a proof-of-principle

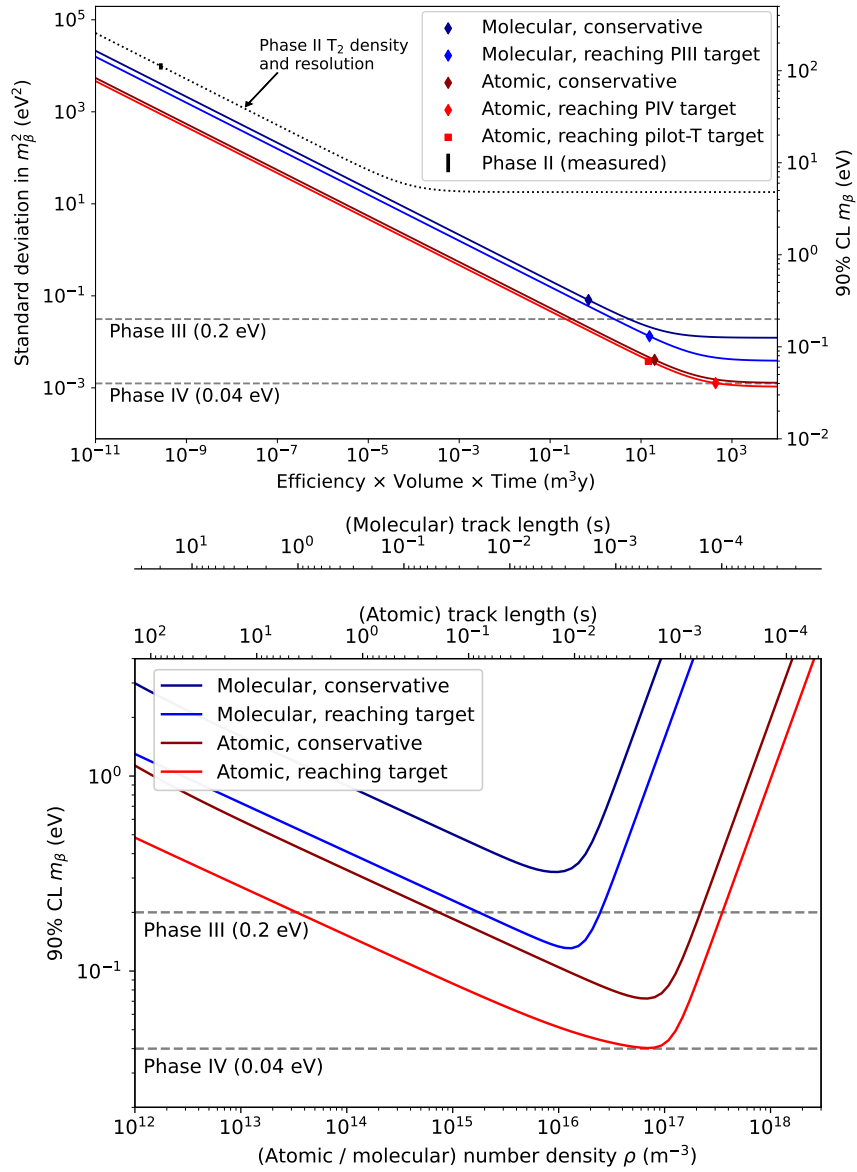


Figure 3.6. Sensitivity calculations for a cavity based CRES experiment that demonstrate the neutrino mass measurement goals of Project 8 throughout the phased development plan. The blue curves indicate molecular tritium sources and the red curves indicate atomic tritium sources. In the current plan, Phase III contains two tritium experiments. The first is the Low-frequency Apparatus (LFA), which is a molecular tritium experiment, and the second is the atomic tritium pilot-scale experiment that officially ends Phase III. The sensitivity of these experiments is primarily a function of statistics, however, there is a critical density beyond which CRES electrons do not have enough time to radiate between collisions for a high-resolution frequency measurement leading to worse sensitivity.

¹⁴⁵² measurement of the neutrino mass using the CRES technique.

¹⁴⁵³ In Phase I, Project 8 performed a proof-of-principle measurement of the ^{83m}Kr
¹⁴⁵⁴ spectrum using CRES, which marked the first ever kinetic energy spectrum measurement
¹⁴⁵⁵ with CRES. The experiment included all the components of a basic CRES experiment.
¹⁴⁵⁶ An electron source consisting of a gas of ^{83m}Kr was supplied to a waveguide gas cell
¹⁴⁵⁷ constructed out of a segment of WR-42 waveguide and sealed with Kapton windows at
¹⁴⁵⁸ the top and bottom. A magnetic trapping region was created in the waveguide cell using
¹⁴⁵⁹ a single electromagnetic coil wrapped around the waveguide which provided a trapping
¹⁴⁶⁰ volume on the order of a few cubic-millimeters. Detection of the cyclotron radiation was
¹⁴⁶¹ performed by connecting the waveguide cell to an additional segment of waveguide that
¹⁴⁶² transmitted the radiation to a cryogenic amplifier.

¹⁴⁶³ Success in Phase I was achieved with the 2014 publication of the measured ^{83m}Kr
¹⁴⁶⁴ conversion spectrum [56], which contains a mono-energetic 17.8-keV line as well as several
¹⁴⁶⁵ other conversion lines at higher energies. Publication of this result marked the official
¹⁴⁶⁶ end of Phase I and the start of Phase II, in which Project 8 shifted its focus to the
¹⁴⁶⁷ demonstration of the first tritium beta-decay spectrum using CRES. Phase II is described
¹⁴⁶⁸ below in Section 3.3.

¹⁴⁶⁹ **Phase III: Research and Development and a Pilot-scale Experiment**

¹⁴⁷⁰ After completing Phase II, Project 8 has shifted focus towards R&D aimed at the
¹⁴⁷¹ construction of an experiment that demonstrates all the technologies required for a
¹⁴⁷² 40 meV measurement of the neutrino mass. The culmination of Phase III is a pilot-scale
¹⁴⁷³ experiment that successfully retires all technological and engineering risks associated
¹⁴⁷⁴ with the Phase IV experiment, while also being a scientifically interesting experiment in
¹⁴⁷⁵ its own right. Sensitivity estimates of the pilot-scale experiment predict a neutrino mass
¹⁴⁷⁶ sensitivity on par with the projected sensitivity of the KATRIN experiment.

¹⁴⁷⁷ Phase III R&D is divided into two main efforts — atomic tritium and CRES detection
¹⁴⁷⁸ techniques. Atomic tritium development in Phase III must retire all risks associated
¹⁴⁷⁹ with the atomic tritium system. This includes the production of tritium atoms, atomic
¹⁴⁸⁰ cooling and recirculation systems, purity and isotope concentration monitoring, and
¹⁴⁸¹ atom trapping. Currently, Project 8 is operating small scale atom cracking demonstrator
¹⁴⁸² systems to show that atom production at the estimated rates needed for Phase IV is
¹⁴⁸³ achievable. Future efforts will continue the current developments on atom production
¹⁴⁸⁴ and expand to include demonstrations of atomic cooling with an evaporative beam line
¹⁴⁸⁵ as well as atom trapping using Halbach magnet arrays.

1486 The need for new CRES detection techniques is driven by the drastic increase in scale
1487 from Phase II to the pilot-scale experiments. The physical volume used for CRES in
1488 Phase II was on the order of a few cubic-centimeters, and achieving Project 8’s sensitivity
1489 target of 40 meV requires an experiment volume on the multi-cubic meter scale. Therefore,
1490 the waveguide gas cell CRES detection technique used in Phase II is not a feasible option
1491 for the future of Project 8 due to its inability to scale to the required size.

1492 Two alternative CRES detection techniques have been proposed for the pilot-scale
1493 experiment — antenna arrays and resonant cavities (see Section 3.4 and Chapter 6).
1494 Both approaches have relative advantages and disadvantages, however, the improved
1495 understanding of the antenna array and cavity approaches to CRES in the recent years
1496 has led to cavities being the preferred technology for the pilot-scale experiment and
1497 Phase IV due to the estimated reduced cost and complexity of this approach. Since
1498 a large degree of the work presented in this dissertation is focused specifically on the
1499 development of the antenna array CRES technique as well as the design of demonstrator
1500 experiments, I describe the proposed R&D plan for antenna array CRES in Section 3.4.
1501 A description of the cavity approach to CRES can be found in Chapter 6.

1502 Cavity CRES R&D consists of a series of demonstrator experiments intended to
1503 demonstrate cavity CRES at a variety of scales and magnetic fields. Radioactive sources
1504 gases include ^{83m}Kr and molecular tritium, as well as electrons produced by an electron-
1505 gun, which is a key calibration tool for future CRES experiments. The near-term cavity
1506 effort in Project 8 is the cavity CRES apparatus (CCA), which is a small-scale cavity
1507 experiment operating near 26 GHz. The CCA will perform the first CRES measurements
1508 using a small cavity, and will pave the way towards larger scale cavity experiments in
1509 preparation for the eventual pilot-scale tritium experiment.

1510 The pilot-scale experiment will be the first experiment to combine atomic tritium and
1511 large-volume CRES detection. It will directly demonstrate all the technologies required
1512 for Phase IV such that no technical risks remain for scaling the experiment to required
1513 scale. A robust approach to scaling the pilot-scale experiment is to simply build multiple
1514 copies of it for the Phase IV experiment.

1515 **Phase IV: Project 8’s Ultimate Neutrino Mass Experiment**

1516 The design of Phase IV should be a direct extension of the pilot-scale CRES experiment
1517 that marks the official end of Phase III (see Section 3.5). The Phase IV experiment
1518 represents the final experiment in the Project 8 neutrino mass measurement experiment
1519 plan and will have sensitivity to neutrino masses of 40 meV.

1520 3.3 Phase II: First Tritium Beta Decay Spectrum and 1521 Neutrino Mass Measurement with CRES

1522 In Phase II, Project 8 demonstrated the first ever measurement of the tritium beta-decay
1523 spectrum endpoint using the CRES technique, which lead to the first neutrino mass
1524 measurement by Project 8. This milestone was made possible by many improvements
1525 in the CRES technique and in the understanding of CRES systematics, which takes
1526 an important first step towards larger scale measurements of the tritium beta-decay
1527 spectrum with CRES. In this section, I briefly describe some important elements of the
1528 Phase II experiment, with the goal of contextualizing the research and development
1529 efforts for Phases III and IV of Project 8. For more complete descriptions of the work
1530 that lead to Project 8's Phase II results please refer to the relevant publications by the
1531 collaboration [42, 43].

1532 3.3.1 The Phase II CRES Apparatus

1533 Magnet and Cryogenics

1534 The magnetic field for the Phase II experiment is provided by a nuclear magnetic
1535 resonance (NMR) spectroscopy magnet with a central bore diameter of 52 mm (see
1536 Figure 3.7). The magnet produces a background magnetic field with an average value
1537 of 0.959 T with a 10 ppm variation across the bore diameter achieved using several
1538 shim coils built into the magnet. Using an external NMR field probe, the variation of
1539 the magnetic field along the vertical axis of the magnet bore was measured to obtain
1540 an accurate model of the magnetic field so that the CRES cell could be positioned for
1541 optimal magnetic field uniformity.

1542 An external solenoid magnet was installed inside the magnet bore to provide the
1543 ability to shift the magnitude of the background magnetic field by a few mT. The solenoid
1544 has inside diameter of 46 mm and a length of 350 mm, which terminates in a vacuum
1545 flange that allows it to be inserted into the NMR magnet bore from the bottom. By
1546 shifting the value of the magnetic field by a few mT, the cyclotron frequencies of electrons
1547 produced by the 17.8 keV ^{83m}Kr internal-conversion line [57] can be shifted by frequencies
1548 of ± 100 MHz. This allows one to study the frequency dependent behavior of several
1549 CRES systematics, such as detection efficiency, that directly affect the measured shape
1550 of the tritium spectrum.

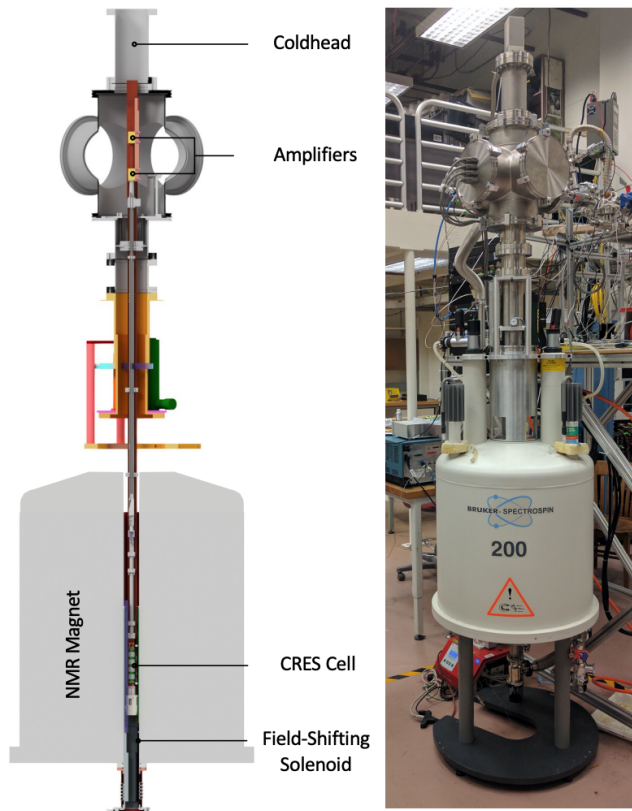


Figure 3.7. The Phase II CRES apparatus used to perform the first measurement of the tritium beta-decay spectrum using CRES.

1551 The inside of the magnet bore diameter was pumped down to a vacuum of less than
 1552 $10 \mu\text{torr}$ using a turbomolecular pump, which allows for cryogenic cooling of the CRES
 1553 cell and RF system. Cooling power was supplied to the Phase II apparatus using a
 1554 cryopump with its coldhead mounted above the primary magnet and CRES cell. This
 1555 arrangement allowed for sufficient cooling power to be delivered to the amplifiers to cool
 1556 them to a temperature of $\approx 40 \text{ K}$, while keeping the amplifiers far enough from the
 1557 magnet so as not to be damaged by the large field strength. Thermal contact between
 1558 the coldhead, amplifiers, RF system, and CRES cell is achieved using a copper bar that
 1559 runs the full length of the apparatus. To prevent freeze-out of ^{83m}Kr on the walls of the
 1560 CRES cell a separate heater was installed to keep the CRES cell near a temperature of
 1561 85 K during the operation of the experiment.

1562 **CRES Cell**

1563 Located in the most uniform region of the magnetic field is the CRES cell, which is
1564 the region of the apparatus where radioactive decays of ^{83m}Kr and T_2 produce electrons
that can be trapped and measured using CRES (see Figure 3.8). The CRES cell is

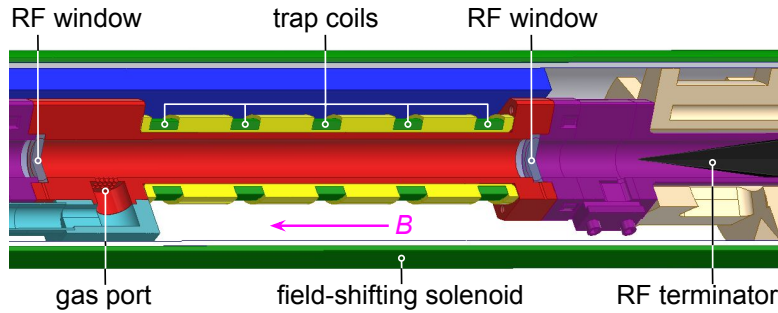


Figure 3.8. Diagram of the CRES cell portion of the Phase II apparatus.

1565
1566 manufactured from a segment of cylindrical waveguide designed to operate at K-band
1567 frequencies near 26 GHz. The diameter of the waveguide determines which resonant
1568 modes of the waveguide will couple to the electron and transmit its radiation to the
1569 amplifiers. For Phase II a waveguide diameter of 1 cm was selected, which allows electrons
1570 to couple to the TE_{11} and TM_{01} cylindrical waveguide modes. To reduce complexity in
1571 modeling and analyzing the CRES data, it is ideal to select a diameter that prevents
1572 electrons from coupling to higher-order waveguide modes beyond the fundamental TE
1573 and TM modes.

1574 Around the exterior of the cylindrical waveguide are several magnetic coils used to
1575 produce magnetic traps inside the CRES cell volume. Without a magnetic trap electrons
1576 produced from decays inside the CRES cell quickly impact the cell wall, which prevents
1577 a measurement of their cyclotron frequency using CRES. Each coil along the length of
1578 the waveguide produces a separate trap that is approximately harmonic in shape. By
1579 independently controlling the currents provided to each coil, the traps can be configured
1580 to have equal values of the magnetic field at the trap bottom despite a non-uniform field
1581 from the NMR magnet.

1582 Two primary magnetic trap configurations were used during the Phase II experiment.
1583 The first was a shallow trap configuration used primarily for its high energy resolution to
1584 study systematics using ^{83m}Kr decays, and the second was a deeper trap that could trap a
1585 higher percentage of pitch angles. The trade-off with this trap is that the higher trapping
1586 efficiency comes at the cost of lower energy resolution due to the greater variation in
1587 pitch angle (see Section 3.2.1). The deep trap was the trap used to measure the tritium

1588 beta-decay spectrum in Phase II.

1589 The source gases were delivered into the CRES cell through a gas port located near the
1590 top end of the cylindrical waveguide. To prevent the gases from escaping the cell, vacuum
1591 tight RF transparent windows are needed to contain the tritium and krypton source
1592 gas across a 1 atm pressure differential, while still transmitting the cyclotron radiation
1593 without distortion. The crystalline material, CaF₂, which has a thermal expansion
1594 coefficient similar to that of copper, was used for this purpose in the CRES cell. Two
1595 windows, each 2.4 mm thick, were used to seal off the ends of the CRES cell. The
1596 thickness of 2.4 mm corresponds to half of a cyclotron wavelength when one accounts for
1597 the permittivity of CaF₂.

1598 **RF System**

1599 The RF system in the Phase II apparatus propagates the cyclotron radiation from the
1600 CRES cell to the receiver chain. The receiver chain performs the down-conversion and
1601 digitization required to obtain signals that can be analyzed to determine the cyclotron
frequencies of electrons in the CRES cell (see Figure 3.9).

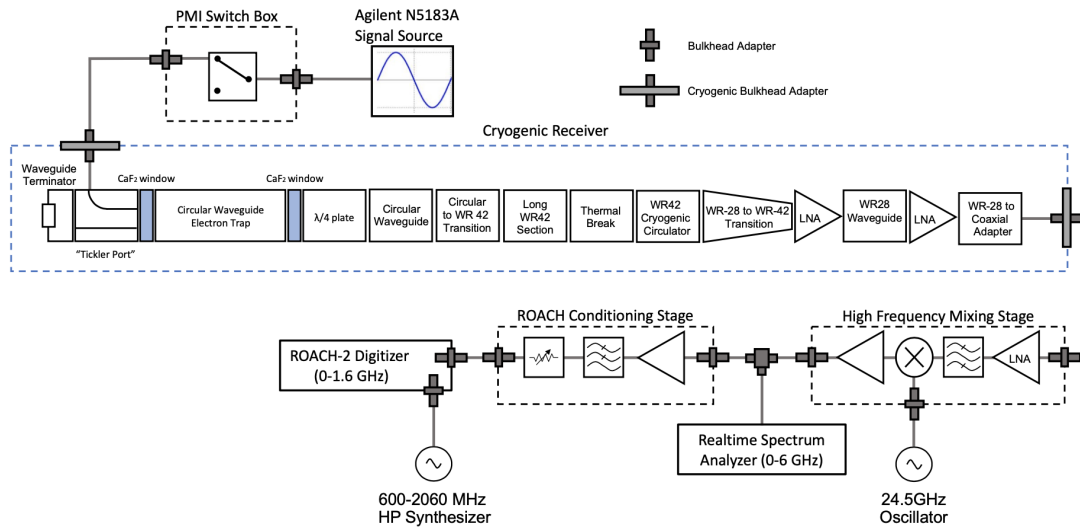


Figure 3.9. RF system diagram for the Phase II apparatus.

1602
1603 Below the CRES cell, at the bottom of the Phase II apparatus, is a tickler port and
1604 waveguide terminator. The tickler port is used to inject signals into the CRES cell and
1605 RF system for testing and calibration purposes. The waveguide terminator is designed to
1606 absorb cyclotron radiation emitted by electrons that transmits out of the bottom of the
1607 CRES cell. This lowers the total power received from electrons in the CRES cell, since all

1608 the energy radiated downwards is absorbed into the terminator. Earlier iterations of the
1609 Phase II apparatus used an RF short in this location that reflected this power up towards
1610 the amplifiers, however, interference between the upward traveling and reflected radiation
1611 led to a disappearance in the signal carrier that made reconstruction impossible.

1612 Radiation traveling upward passes through the CaF₂ window passes and a λ/4 plate,
1613 which transforms the circularly polarized cyclotron radiation into linear polarization.
1614 The linearly polarized fields next travel through a segment of circular waveguide that
1615 transitions into a long segment of WR-42 waveguide that carries the fields out of the
1616 high magnetic field region. A thermal break segment is included, which consists of a
1617 segment of gold-plated stainless steel WR-42 waveguide, to help thermally isolate the
1618 relatively warm CRES cell from the colder amplifiers. The radiation then passes through
1619 a cryogenic circulator, which prevents signals reflected from the amplifiers from interfering
1620 with the CRES cell before a WR-42 to WR-28 transition connects the waveguide to the
1621 first of the cyrogenic amplifiers. The radiation passes through two cyrogenic amplifiers
1622 before being coupled to a coaxial termination at the top of the Phase II apparatus.

1623 The coaxial cable transfers the cyclotron radiation signals to a high-frequency mixing
1624 stage that performs an analog frequency down-conversion using a 24.5 GHz LO. Two forms
1625 of digitization can be used at this stage to readout the CRES data. One is a real-time
1626 spectrum analyzer that digitizes the CRES signal data in time-domain and computes the
1627 frequency spectrum in real-time, which allows for direct visualization of CRES signal
1628 spectrograms as the experiment is running. The real-time spectrum analyzer is most
1629 useful for taking small amount of streamed data for debugging and analysis of the system.
1630 The other method, which was used to collect the majority of the CRES data in Phase II,
1631 is a ROACH-2 FPGA and digitizer system. The ROACH system consists of a fast ADC
1632 that samples the CRES signal data at 3.2 GSps. Internal digital down-conversion stages
1633 implemented in the FPGA perform a mixing operation that reduces the bandwidth of the
1634 CRES signals to 100 MHz. The FPGA implements a 4096 sample FFT and packetizes
1635 time and frequency domain records in parallel. The packetized data is then transferred
1636 from the ROACH to be analyzed by the data-processing pipeline.

1637 **3.3.2 CRES Track and Event Reconstruction**

1638 **Time-Frequency Spectrogram**

1639 The online data-processing software uses a real-time triggering algorithm that identifies
1640 interesting data that could contain CRES signals. Triggered data are collected into files

1641 that are transferred to a server for offline processing and analysis. The data files contain
1642 a continuous series of time-domain samples, broken into a set of records, which are 4096
1643 samples long. The time-series is made up of 8-bit IQ samples acquired at 100 MHz.

1644 Each time-series record is accompanied by an associated frequency spectrum consisting
1645 of 4096 frequency bins approximately 24.4 kHz wide, which is represented as a power
1646 spectral density. The individual frequency spectra can be organized temporally to create
1647 a time-frequency spectrogram that represents the evolution of the cyclotron frequency
spectrum over the course of the CRES event (see Figure 3.10). The time-frequency

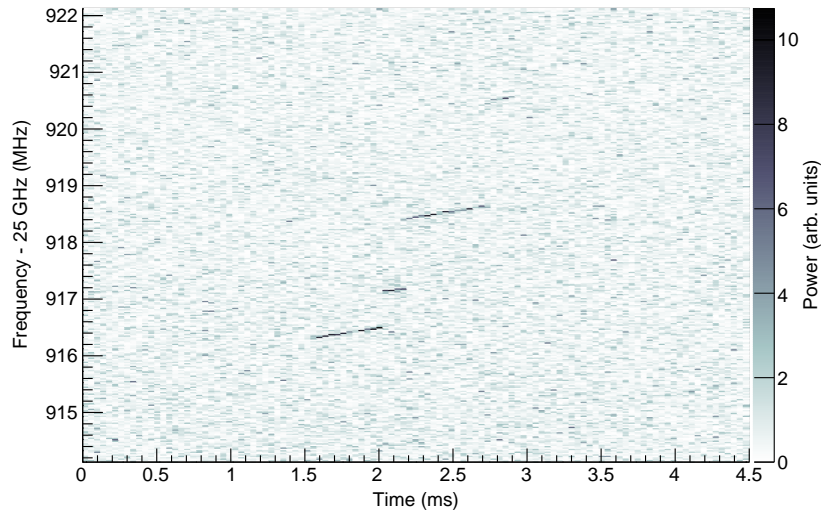


Figure 3.10. The time-frequency spectrogram of a tritium CRES event in the Phase II apparatus.

1648 spectrogram is represented as a two-dimensional image where the color of each pixel is
1649 proportional to the power spectral density. Each vertical slice of pixels in the image
1650 represents a frequency spectrum, therefore, each horizontal bin represents the data
1651 obtained over a duration of $4096 \times 0.01 \text{ MHz}^{-1} = 40.96 \mu\text{sec}$.

1653 CRES Event Data Features

1654 Phenomenologically, a CRES signal appears as a sinusoidal signal whose frequency slowly
1655 increases over time in what is called a frequency "chirp". Axial motion of the electron in
1656 the trap leads to the formation of frequency sidebands that surround the more powerful
1657 carrier frequency. The critical piece of information that must be extracted from the track
1658 and event reconstruction procedure is the carrier frequency, since it is this frequency that
1659 gives the cyclotron frequency and thus the kinetic energy. Axial motion from non-90°

1660 pitch angles changes the average magnetic field experienced by an electron, because
1661 the electron effectively samples the magnetic field along its trajectory. The change in
1662 the average magnetic field with pitch angle leads to different cyclotron frequencies that
1663 correspond to the same kinetic energy. However, because of the low-SNR in Phase
1664 II, sidebands were unable to be observed, so no attempt to correct for this effect was
1665 attempted. The effect of different pitch angles is to broaden the peak of a monoenergetic
1666 electron line, which can be quantified by measuring the instrumental resolution of the
1667 Phase II apparatus.

1668 In the time-frequency spectrogram representation, the chirping carrier frequency
1669 appears as a linear track of high-power frequency bins (see Figure 3.10). The vertical
1670 slope of the tracks is caused by the emission of energy from the electron in the form of
1671 cyclotron radiation, therefore, the size of the slope parameter is directly proportional
1672 to the Larmour power. The continuous track is periodically interrupted by random
1673 jumps to higher frequency (lower energy) caused by random inelastic collisions with
1674 background gas molecules. The length of a track is an exponentially distributed variable
1675 whose mean value is inversely proportional to the gas density. The size of the frequency
1676 discontinuities is directly proportional to the energies of the rotational and vibrational
1677 states of background gas molecules.

1678 A CRES event refers to the collection of tracks produced by a trapped electron until
1679 it inevitably scatters into a pitch angle that can no longer be trapped. The goal of track
1680 and event reconstruction is to identify the set of tracks in a time-frequency spectrogram
1681 that represents a segment of data acquired in the Phase II apparatus. These tracks must
1682 be clustered into events, from which one can determine the first track produced by the
1683 electron and thus estimate its starting cyclotron frequency and kinetic energy.

1684 **Track Reconstruction**

1685 The first step in CRES event reconstruction is the identification of tracks in the time-
1686 frequency spectrogram, which is essentially an image processing task. Track finding
1687 starts by normalizing the power spectral density based on the average noise power. Next
1688 a power threshold is applied to the normalized spectrogram where only bins that have a
1689 SNR ratio greater than five are selected to build tracks. In this case SNR is defined as the
1690 ratio between the normalized, unitless power of a bin divided by the average normalized
1691 power across the full frequency spectrum.

1692 The sparse spectrogram produced by this power cut consists only of a sparse collection
1693 of high-power frequency bins that could be part of a CRES signal track (see Figure

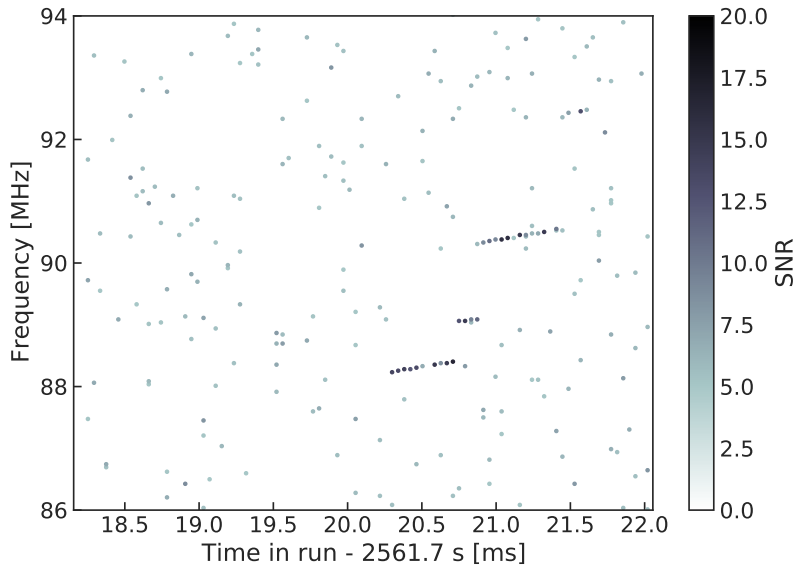


Figure 3.11. The sparse spectrogram obtained by placing a power cut on the raw spectrogram shown in Figure 3.10.

1694 3.11). In this form is it much easier to identify tracks "by eye", however, for the Phase II
 1695 analysis Project 8 developed its own custom-made track finding algorithm, called the
 1696 sequential track finder (STF).

1697 The STF algorithm processes the sparse spectrogram in sequential fashion, processing
 1698 each time-slice one-by-one until the end of the spectrogram is reached. Tracks are found
 1699 by searching for points in the sparse spectrogram that appear to fall on a straight line.
 1700 Multiple configurable parameters are built into the STF algorithm that allow the user to
 1701 tune the criteria for adding a point to an existing track or creating a new track. These
 1702 include parameters such as maximum time and frequency differences between subsequent
 1703 points in a track as well as minimum SNR values for the start and endpoints of the track.
 1704 Additionally, tracks are required to have a minimum length and slope to be considered
 1705 potential CRES tracks rather than random noise fluctuations.

1706 The resulting output of the STF is a collection of track objects that consist of the track
 1707 point objects and their properties. The final step is to calculate track-level properties and
 1708 apply cuts to reject false tracks found by the STF. This involves the fitting of a line to
 1709 the collection of track points as well as the total and average power of the track obtained
 1710 by computing the sum and mean of the points powers. The starting frequency of the
 1711 track is determined by calculating the time coordinate that intersects with the linear fit.
 1712 A cut is then performed to remove all tracks that do not have a specified average power
 1713 over their duration, which helps to remove the majority of noise fluctuations that have

¹⁷¹⁴ passed all previous cuts up to this point.

¹⁷¹⁵ Event Reconstruction

¹⁷¹⁶ After track reconstruction comes event reconstruction, where the identified tracks are
¹⁷¹⁷ grouped into events that correspond to the trajectory of a single electron in the trap.
¹⁷¹⁸ This procedure attempts to match tracks head to tail by checking if the start and end
¹⁷¹⁹ times of a pair of tracks falls within a certain tolerance. This tolerance is a configurable
¹⁷²⁰ parameter that can be tuned to an optimal value using Monte Carlo simulations of events
¹⁷²¹ in the Phase II apparatus.

¹⁷²² After the event building procedure has completed, there remains a small likelihood
¹⁷²³ that false tracks have made it through to the event reconstruction stage. Typically, cuts
¹⁷²⁴ at the track level are able to remove 95% of the false tracks identified by the STF, which
¹⁷²⁵ leads to a significant number of false tracks at the event building stage. However, the
¹⁷²⁶ additional event-level information makes it possible to reject events that contain these
¹⁷²⁷ false tracks with a high degree of confidence.

¹⁷²⁸ Two event level features are associated with events caused by real electrons — the
¹⁷²⁹ duration of the first track as well as the number of tracks in the event. Real electrons
¹⁷³⁰ tend to have event structures with longer first tracks and a higher number of total tracks.
¹⁷³¹ Based on the values of these two criteria, a minimum threshold on the average power in
¹⁷³² the first track was configured to reject false events. The average power in the first track
¹⁷³³ was chosen due to the critical nature of the starting frequency of the first track in an
¹⁷³⁴ event to the krypton and tritium spectrum analyses.

¹⁷³⁵ 3.3.3 Results from Phase II

¹⁷³⁶ The main result from Phase II was the measurement of the tritium beta-decay spectrum
¹⁷³⁷ using CRES, which lead to the first neutrino mass limit with CRES. However, Phase
¹⁷³⁸ II also included a significant ^{83m}Kr measurement campaign to understand important
¹⁷³⁹ systematics relevant to the tritium spectrum measurement and the fundamentals of
¹⁷⁴⁰ the CRES technique itself. This required high-resolution measurements of the ^{83m}Kr
¹⁷⁴¹ internal-conversion spectrum [57], which is an interesting science result in its own right.

¹⁷⁴² The results from Phase II represents a significant effort from entire Project 8 over
¹⁷⁴³ several years. Because the focus of my contributions to Project 8 is directed towards the
¹⁷⁴⁴ research and development efforts for the Phase III experiments, the goal in this section
¹⁷⁴⁵ is not to provide a detailed description of the analyses that lead to the Phase II results.

¹⁷⁴⁶ Rather, I will provide brief descriptions of a few plots representative of the main results
¹⁷⁴⁷ from Phase II as reported in [42, 43].

¹⁷⁴⁸ Measurements with Krypton

¹⁷⁴⁹ Measurements with krypton were a key calibration tool for Phase II of the experiment
¹⁷⁵⁰ and will continue to be useful in Phase III. Krypton measurements refers to CRES
¹⁷⁵¹ measurements of the internal-conversion spectrum of the metastable state of krypton-83,
¹⁷⁵² ^{83m}Kr , produced by electron capture decays of ^{83}Rb . A supply of ^{83}Rb was built into the
¹⁷⁵³ Phase II apparatus gas system that supplied the CRES cell with ^{83m}Kr via emanation.

¹⁷⁵⁴ The ^{83m}Kr internal-conversion spectrum consists of several lines based on the orbital
¹⁷⁵⁵ of the electron ejected during the decay. The conversion lines useful to Project 8 are
¹⁷⁵⁶ those that emit electrons with kinetic energies that fall inside the detectable frequency
¹⁷⁵⁷ bandwidth of the Phase II apparatus. These are the K; L2 and L3; M2 and M3; and N2
¹⁷⁵⁸ and N3 lines; with kinetic energies of 17.8 keV, \approx 30.4 keV, \approx 31.9 keV, and \approx 32.1 keV,
¹⁷⁵⁹ respectively. The different energies of the lines allows one to test the linearity of the
¹⁷⁶⁰ relationship between kinetic energy and frequency across the range of frequencies covered
¹⁷⁶¹ by the continuous tritium spectrum.

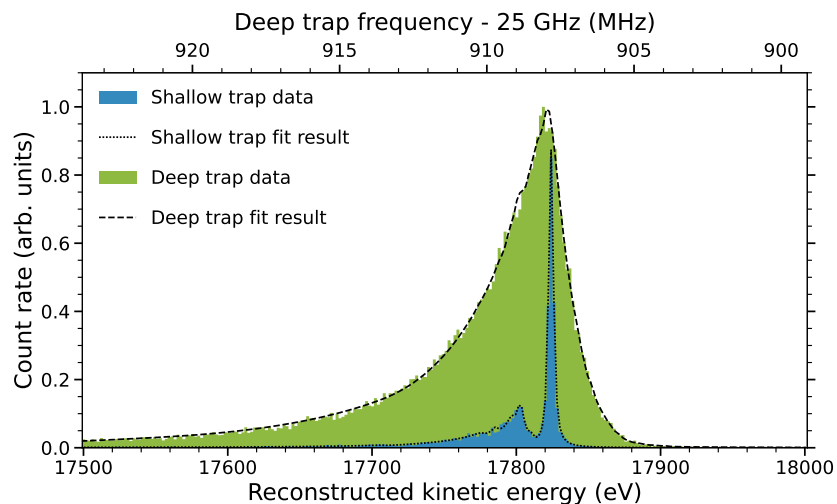


Figure 3.12. Fits to the measured 17.8-keV ^{83m}Kr conversion line using the deep and shallow trap configurations.

¹⁷⁶² Numerous detector-related effects relevant to the tritium analysis can be characterized
¹⁷⁶³ by measuring the shape of the krypton spectrum. Specific examples include variations
¹⁷⁶⁴ in the magnetic field as a function of the radial position of the electron, variation in
¹⁷⁶⁵ the magnetic field caused by the trap shape, variation in the average magnetic field for

1766 electrons with different pitch angles, and the effect of missing tracks due to scattering.
 1767 These spectrum shape measurements focused on the 17.8-keV krypton line and utilized
 1768 different trap geometries based on the particular goal of the dataset (see Figure 3.12).

1769 Krypton measurements with a shallow trap allow for high energy resolution, since
 1770 variation in frequency due to pitch angle differences is sharply reduced in the shallow
 1771 trap configuration. With this trap the main 17.8-keV peak of the conversion spectrum is
 1772 clearly visible along with additional satellite peaks at lower energy, which correspond to
 1773 the shakeup/shakeoff spectrum of the decay. The high accuracy of the fit demonstrates a
 1774 high degree of understanding of the CRES systematics.

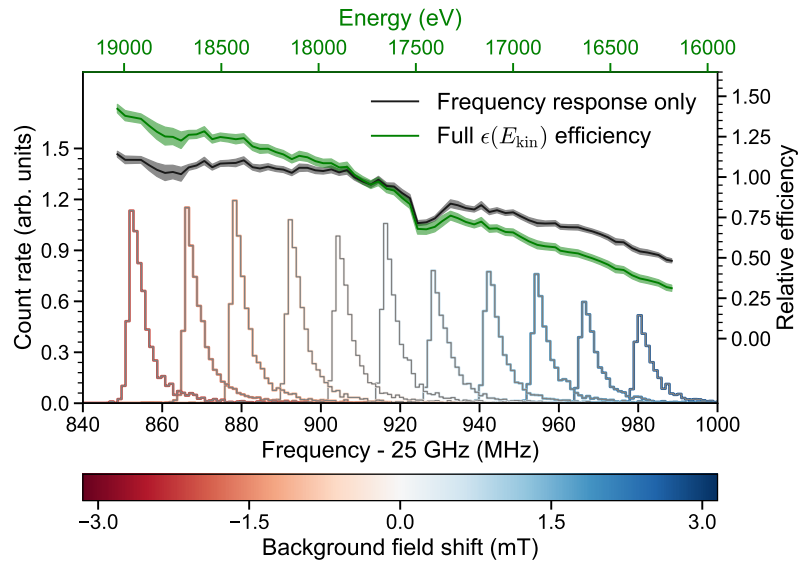


Figure 3.13. Measurements of the 17.8-keV ^{83m}Kr line using the deep trap configuration for different values of the magnetic field from the field shifting solenoid.

1775 The broadening of the krypton spectrum seen for the deeper track is due to the large
 1776 range of electron pitch angles that can be trapped. Furthermore, with a deeper trap
 1777 there is a larger parameter space of electron that could be produced with pitch angles
 1778 that are trappable but not visible in the time-frequency spectrogram. These electrons
 1779 remain in the trap and can scatter multiple times before randomly scattering to a visible
 1780 pitch angle. This leads to one or more missing tracks earlier in the event, which leads to
 1781 a misreconstruction of the true starting frequency. By measuring the krypton spectrum
 1782 shape in the same trap used to detect tritium events, the effect this has on the spectrum
 1783 shape can be characterized to mitigate its impact on the tritium measurements.

1784 Changes in the Krypton spectrum shape as a function of CRES frequency were

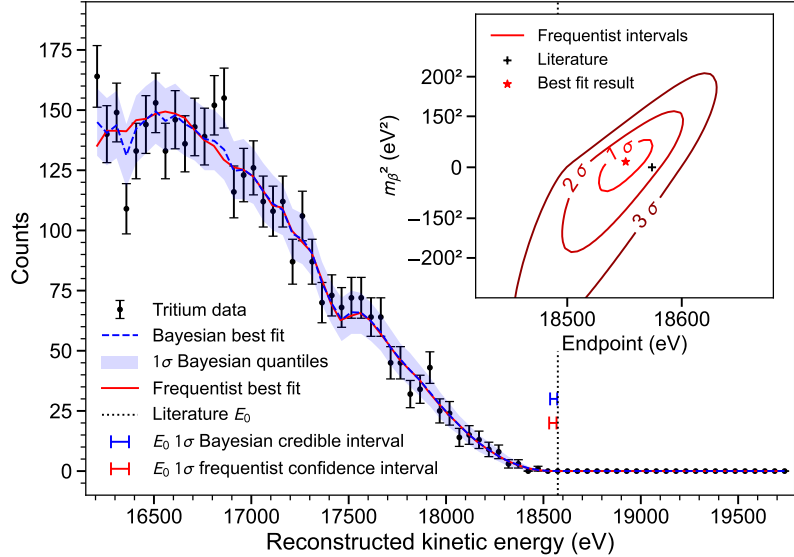


Figure 3.14. The measured tritium spectrum from Phase II with Bayesian and frequentist fits.

used to study the detection efficiency of the Phase II apparatus. Variations in the detection efficiency as a function of frequency directly influences the measured shape of the continuous tritium spectrum, which can lead to errors in the neutrino mass estimate if not modeled appropriately. Using the field-shifting solenoid (FSS) the cyclotron frequency of the krypton 17.83 keV line was shifted across the full frequency range of the tritium spectrum data (see Figure 3.13). The FSS is a wound copper solenoid magnet that surrounds the CRES cell. Controlling the current through this magnet allows one change the value of the background magnetic field and the frequency of the krypton conversion lines. Variations in the deep trap krypton spectrum shape can be used to infer the detection efficiency as a function of frequency and correct for this affect in the tritium measurements.

1796 Tritium Spectrum and Neutrino Mass Results

1797 The tritium measurement campaign resulted in the collection of 82 days of detector
 1798 live time during which 3770 total tritium events were detected. The track and event
 1799 reconstruction analysis extracted the starting frequencies of these tritium events, which
 1800 were used to build a frequency spectrum of tritium beta-decays. The resulting frequency
 1801 spectrum was then converted to an energy spectrum using the information gleaned from
 1802 the krypton measurement campaign to obtain the tritium beta-decay spectrum (see
 1803 Figure 3.14).

1804 CRES is inherently a very low background technique with the dominant source of noise
1805 being random RF fluctuations. Monte Carlo simulations, validated using measurements
1806 of the RF noise background, were used to set track and event cuts to guarantee that
1807 zero false events would occur over the duration of the experiment with 90% confidence.
1808 Notably, the measured spectrum has zero events beyond the tritium spectrum endpoint,
1809 which allows one to constrain the background rate in the Phase II apparatus to less than
1810 3×10^{-10} counts/ev/s. Achieving a low background is critical for future neutrino mass
1811 experiments that seek to measure the neutrino mass with less than 100 meV sensitivity.

1812 Bayesian and frequentist based fits to the measured tritium spectrum, incorporating
1813 information gained about CRES systematics from the krypton measurements, were
1814 performed to extract upper limits on the tritium beta-decay spectrum endpoint as well as
1815 the neutrino mass. The estimated spectrum endpoints are 18553^{+18}_{-19} eV for the Bayesian
1816 analysis and 18548^{+19}_{-19} eV for the frequentist analysis. The quoted uncertainties are
1817 $1-\sigma$, and both results are within $2-\sigma$ of the literature endpoint value of 18574 eV. The
1818 estimated neutrino mass for both results is consistent with $m_\beta^2 = 0$. The 90% confidence
1819 upper limits for the Bayesian analysis is $m_\beta < 155$ eV/c² and $m_\beta < 152$ eV/c for the
1820 frequentist analysis.

1821 Though the neutrino mass results from Phase II are not competitive with KATRIN,
1822 the experiment was a promising first step towards the development of more precise
1823 neutrino mass measurements using CRES. The low-background and high-resolution
1824 achievable with krypton measurements are promising features of the technique that were
1825 demonstrated with the Phase II apparatus. As new technologies are developed to enable
1826 CRES measurements in larger volume, many of the lessons learned from Phase II will
1827 continue to influence the operation and design of future experiments.

1828 **3.4 Phase III R&D: Antenna Array CRES**

1829 The goal of Phase III in the Project 8 experimental program is to develop the technologies
1830 and expertise required to build an experiment that uses CRES to measure the neutrino
1831 mass with a target sensitivity of 40 meV. One of the key technologies is a method for
1832 performing high resolution CRES measurements in a large volume, which allows one to
1833 observe a sufficient quantity of tritium to measure the low-activity endpoint region of
1834 the tritium spectrum.

3.4.1 The Basic Approach

1836 One possible approach, suggested in the original CRES publication [40], is to use many
1837 antennas to surround a volume of tritium gas in a magnetic field (see Figure 3.15). When
1838 a decay occurs the electron will emit cyclotron radiation that can be collected by the array
and used to perform CRES. Each antenna in the array collects only a small fraction of

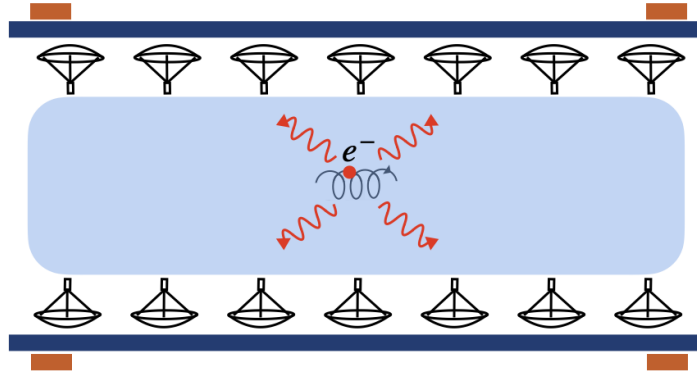


Figure 3.15. A cartoon illustration of the basics of the antenna array CRES technique.

1839
1840 the electron's signal power, which is less than 1 fW for a 18.6 keV kinetic energy electron
1841 in a 1 T magnetic field. Scaling to large volumes with the antenna array approach is
1842 accomplished by increasing the number of antennas in the array, which increases the
1843 volume available for CRES measurements.

1844 Several features of the antenna array approach make it an attractive candidate technol-
1845 ogy for a large volume experiment. One example is the accurate position reconstruc-
1846 tion possible with a multichannel antenna array. Using techniques like digital beamforming,
1847 it is possible to estimate the radial and azimuthal positions of the electron in the mag-
1848 netic trap with a precision significantly less than the size of the cyclotron wavelength.
1849 This capability allows one to perform event-by-event estimations of the magnetic fields
1850 experienced by an electron, which helps achieve high energy resolution with the CRES
1851 technique.

1852 The easy availability of position information with the antennas array approach
1853 is potentially a unique advantage that provides significant flexibility in the magnetic
1854 field uniformity requirements compared to other proposed approaches to large volume
1855 CRES (see Chapter 6). Spatial discrimination using digital beamforming leads to pileup
1856 reduction, which helps to reduce the potential of background events caused by missing
1857 tracks or by incorrectly clustering a group of tracks into an event. Limits on the
1858 background rate for a neutrino mass measurement with 40 meV sensitivity are stringent

1859 and the total activity of the tritium source is gigantic relative to the activity near the
1860 endpoint. Thus, pileup discrimination could be an important tool for a large scale CRES
1861 experiment.

1862 Another beneficial quality of antenna arrays is that the volume of the experiment can
1863 be scaled independent of frequency by simply adding more antennas to the array (see
1864 Figure 3.19). Resonant cavities, the proposed alternative large volume CRES technology,
1865 are ideally operated in magnetic fields that cause electrons to move with cyclotron
1866 frequencies near the fundamental cavity resonance, to avoid complex coupling of the
1867 electron to multiple cavity modes simultaneously. This leads to a coupling between the
1868 cavity volume and the magnetic field magnitude, which forces one to lower the magnetic
1869 field in order to increase the experiment scale. Whereas, for antenna arrays, in principle
1870 there is no physical limitation on the size of the antenna array that can be used at a
1871 particular magnetic field. However, this approach to scaling an antenna array experiment
1872 leads to rapidly increasing cost and complexity due to the large number of antennas,
1873 amplifiers, and data streams, which require substantial computer processing power to
1874 effectively utilize. The link between array size and computational cost will be explored
1875 in Section 4.3.

1876 **3.4.2 The FSCD: Free-space CRES Demonstrator**

1877 The complexity of the antenna array CRES technique requires the construction of a
1878 small scale demonstration experiment to develop an understanding of technique itself and
1879 relevant systematics. Without a demonstrator experiment it is not possible to sufficiently
1880 retire the technical risks associated with the full-scale experiment. Therefore, Phase
1881 III of the Project 8 experimental program is primarily focused on the development and
1882 operation of demonstrator experiments to inform the design of the Phase IV experiment.

1883 The Phase III demonstrator experiment for antenna array CRES is called the Free-
1884 space CRES Demonstrator or FSCD. The FSCD is also a capable neutrino mass mea-
1885 surement experiment in its own right, with a target neutrino mass sensitivity of a few
1886 eV using a molecular tritium source. The higher-costs associated with antenna-based
1887 CRES, which were identified over the course of the development of the FSCD, have lead
1888 to the adoption of resonant cavities as the technology of choice for Phase III. Therefore,
1889 all future development of the FSCD and antenna-based CRES in Project 8 has been
1890 suspended.

1891 **Magnetic Field**

1892 The background magnetic field for the FSCD is provided by a hospital-grade MRI magnet
1893 (see Figure 3.16). The magnet produces a magnetic field of approximately 0.958 T, which
corresponds to a tritium spectrum endpoint frequency of approximately 25.86 GHz. The



Figure 3.16. An image of the MRI magnet installed in the Project 8 laboratory at the University of Washington, Seattle.

1894
1895 magnet is installed in the Project 8 laboratory located at the University of Washington,
1896 Seattle, and is shimmed to produce a uniform magnetic field with variations on the
1897 ppm-level. Measurements of the magnetic field non-uniformities are performed using a
1898 NMR probe and rotational gantry to capture measurements of the magnetic field around
1899 an elliptical surface in the center of the MRI magnet. During the operation of the FSCD
1900 an array of Hall or NMR magnetometers would be used to periodically measure the
1901 magnetic field to monitor its time stability.

1902 Inside the field of the MRI additional electromagnets would be installed that provide
1903 the capability to shift the value of the background magnetic field and produce a magnetic
1904 trap. Shifting the background magnetic field by a few μ T lets one control the cyclotron
1905 frequencies of electrons with a fixed kinetic energy, which is key to an effective calibration
1906 of the FSCD. The preferred calibration method for the FSCD is a mono-energetic electron
1907 gun that can inject electrons into the magnetic trap with a known kinetic energy. In
1908 combination with the field shifting magnet, one can vary the cyclotron frequencies of the
1909 electrons to measure the response of the antenna array as a function of the radiation
1910 frequency and electron position. This procedure characterizes the response of the antenna

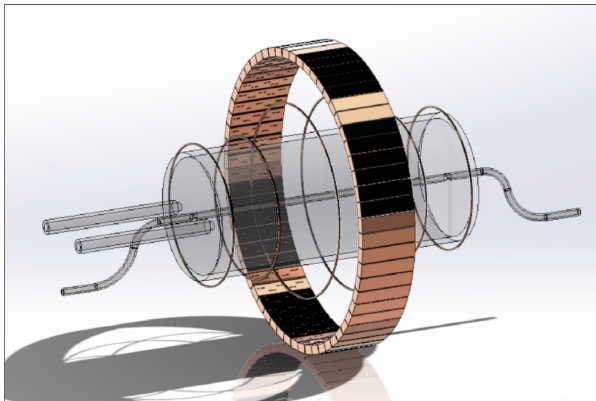
array and provides further information on magnetic field uniformity, which is important to achieving good energy resolution.

The design of the magnetic trap is absolutely critical to the success of a CRES experiment. The ideal shape is the perfect magnetic box, which has a flat bottom and step function walls. Any variation in the average magnetic field experienced by an electron leads to changes in the cyclotron frequency that can make determining the true starting kinetic energy more difficult. This includes changes in the magnetic field caused by the walls of the magnetic trap as well as radial magnetic field variations.

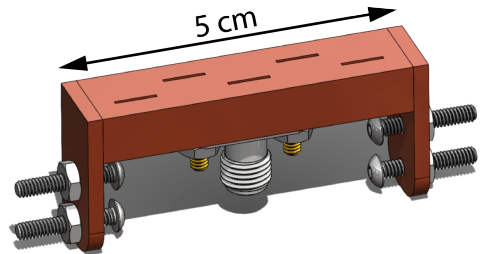
The ideal box trap is completely uniform and has infinitely steep walls that cause no change in the electron's cyclotron frequency as it is reflected from the trap wall. However, such a trap cannot be made from any combination of magnetic coils since it violates Maxwell's equations. One of the goals of magnetic trap design is to identify the configuration of coils that produces a trap that approximates the perfect box trap as closely as possible.

Antenna Array

The canonical antenna array design for CRES is a uniform cylindrical array of antennas that surrounds the magnetic trap volume. Since the FSCD is a demonstrator experiment, the antenna array design is the simplest form of the uniform cylindrical array, which is a single circular ring of antennas with a diameter of 20 cm (see Figure 3.17). Along



(a)



(b)

Figure 3.17. (a) A model of the FSCD antenna array, magnetic trap, and tritium containment vessel design.(b) A more detailed model of a prototype design for the 5-slot waveguide antenna design.

1929

1930 this circle are sixty slotted waveguide antennas that fully populate the available space

1931 around the array circumference. It is optimal to cover as large a fraction of the solid
1932 angle around the magnetic trap as possible in order to maximize the power collected
1933 from each electron .

1934 The distance between antennas around the circumference of the array is proportional
1935 to the wavelength of the cyclotron radiation. Therefore, maximizing the solid angle
1936 coverage of the array, while minimizing channel count to keep the hardware and data
1937 acquisition costs manageable, biases one towards smaller array diameters. Antenna
1938 near-field effects limit the minimum diameter of the array for a given antenna design,
1939 since the radiation from electrons that are too close to the array cannot be detected due
1940 to destructive interference.

1941 Slotted waveguide antennas are used in the FSCD antenna array due to their high
1942 efficiency and low loss, which comes from the lack of dielectric materials in the antenna
1943 structure. Coupling to the waveguide is performed with a coaxial cable connected at the
1944 center of the antenna. One of the drawbacks of waveguide antennas is the large amount
1945 of space required to fit them inside the limited MRI magnet volume. Alternative antenna
1946 designs, constructed from microstrip printed circuit boards require significantly less space
1947 at the cost of slightly higher energy losses in the antenna structure.

1948 The FSCD antenna design is a 5 cm long segment of WR-34 waveguide with 5 vertical
1949 slots cut into the side. The distance between slots along the length of the waveguide is
1950 a half wavelength for optimal power combination between the individual antenna slots.
1951 Each slot is offset from the center of the antenna face a small distance in order to most
1952 effectively couple the slot to waveguide modes inside the antenna.

1953 The passive power combination achieved by placing 5 slots in a single waveguide is a
1954 compromise intended to reduce the cost and complexity of the antenna array system.
1955 Each additional channel in the array requires its own cryogenic amplifier and also increase
1956 the required computer power to process the raw data collected by digitizing each channel.
1957 Passive summation, achieved by combining antennas into arrays axially, reduces the
1958 array channel count at the cost of losses from imperfect passive combination.

1959 Interference and re-radiation eventually limit the axial extent of passive power combi-
1960 nation. The 5-slot designed developed for the FSCD is optimized to minimize the impact
1961 of these losses while achieving the maximum amount of axial coverage with a single ring
1962 of antennas. Scaling beyond the volume covered by a single ring of antennas is achieved
1963 by stacking additional rings of antennas together to cover a larger trap volume. A likely
1964 scenario for the FSCD experiment involves a staged experiment approach, where first
1965 a series of measurements is performed using only a single ring of antennas followed by

¹⁹⁶⁶ experiments that add additional rings to the FSCD. The goal would be to first understand
¹⁹⁶⁷ the principles of antenna array CRES using the simplest possible experiment, before
¹⁹⁶⁸ attempting to scale the technique by expanding the antenna array size.

¹⁹⁶⁹ **Tritium Source**

¹⁹⁷⁰ While the primary purpose of the FSCD is as a technology demonstrator, it is impossible to
¹⁹⁷¹ retire all risks with the Phase IV experiment without an intermediate scale measurement
¹⁹⁷² of the neutrino mass. Therefore, the FSCD has the scientific goal of measuring the
¹⁹⁷³ neutrino mass with a rough sensitivity goal in the range of a few eV. This level of precision
¹⁹⁷⁴ is achievable using a molecular tritium source with a volume of approximately 1 L at a
¹⁹⁷⁵ density comparable to potential Phase IV scenarios.

¹⁹⁷⁶ Unlike previous CRES experiments, where the tritium source could be colocated
¹⁹⁷⁷ with the receiving antenna inside a waveguide transmission line, the tritium source
¹⁹⁷⁸ in the FSCD is thermally isolated from the antenna array to avoid freeze-out of the
¹⁹⁷⁹ tritium molecules. The tiny radiation power emitted by electrons requires a system noise
¹⁹⁸⁰ temperature of ≈ 10 K or less, in order to detect events at a high enough efficiency to
¹⁹⁸¹ reach the neutrino mass sensitivity goals of the experiment. Achieving a system noise of
¹⁹⁸² 10 K requires that the antenna array and amplifiers operate at liquid helium temperatures
¹⁹⁸³ of ≈ 4 K, which significantly lowers the vapor pressure of molecular tritium. By keeping
¹⁹⁸⁴ the molecular tritium isolated in an RF-transparent vessel the tritium gas can be kept
¹⁹⁸⁵ at a relatively warmer temperature in the range of 30 K to avoid the accumulation of
¹⁹⁸⁶ tritium on the experiment surfaces.

¹⁹⁸⁷ **Data Acquisition and Reconstruction**

¹⁹⁸⁸ A fundamental change in the data acquisition system for the FSCD is the shift from
¹⁹⁸⁹ single to multichannel reconstruction. This transition results in a significant increase in
¹⁹⁹⁰ the data-generation rate, which is linearly related to the number of independent channels
¹⁹⁹¹ in the array. The larger data volume coincides with an increased demand for computer
¹⁹⁹² processing power based on the need for more precise signal reconstruction algorithms
¹⁹⁹³ driven by the FSCD and Phase IV sensitivity goals. Therefore, the data acquisition
¹⁹⁹⁴ system for the FSCD is likely to represent a significantly larger fraction of the experiment
¹⁹⁹⁵ cost and complexity than in Phase II.

¹⁹⁹⁶ Each antenna is connected to a cryogenic amplifier and down-converted from the
¹⁹⁹⁷ 26 GHz CRES frequency using an IQ-mixer to reduce the size of the analysis window.
¹⁹⁹⁸ Using an LO with a frequency of approximately 25.80 GHz the antenna array signals can

1999 be digitized at a rate of 200 MHz, which is sufficient bandwidth to resolve the complete
2000 sideband spectrum produced by axial oscillations of electrons in the FSCD magnetic
2001 trap.

2002 Direct storage of the raw FSCD antenna array data is undesirable, since the estimated
2003 amount of raw data generated is $O(1)$ exabyte per year. The storage of such a large
2004 dataset is infeasible for a demonstrator experiment like the FSCD, since it would represent
2005 a disproportionate fraction of the total experiment budget in Phase III and Phase IV.
2006 Therefore, a goal of the FSCD experiment is the development of real-time reconstruction
2007 methods that could reduce the raw data volume by detecting and reconstructing CRES
2008 events in real-time. Ultimately, a real-time CRES reconstruction pipeline is desired, which
2009 takes raw voltages samples from the antenna array and converts them into measured
2010 starting kinetic energy values for electrons.

2011 The feasibility of a real-time reconstruction pipeline rests on the development of
2012 computationally efficient algorithms that can be implemented without the need for
2013 enormous computing resources. One challenge with the antenna array approach is that
2014 the small radiation power of a single electron is distributed among all channels in the array,
2015 such that reconstruction using only the information in a single channel is not possible.
2016 Therefore, simply performing the initial step in reconstruction — signal detection —
2017 requires orders of magnitude more computational power than previous CRES experiments.
2018 This operation will then be followed by other, potentially more expensive, reconstruction
2019 steps that are required in order to determine the kinetic energy of the electron.

2020 **3.5 Pilot-scale Experiments**

2021 The Project 8 pilot-scale experiment represents the experiment that retires all technical
2022 and engineering risks with Project 8’s neutrino mass measurement approach, by combining
2023 all the required components of Phase IV in a multi-cubic-meter experiment. The larger
2024 scope and complexity of the pilot-scale experiment requires a careful choice of magnetic
2025 field and cyclotron frequency since this directly affects the design of nearly all parts of
2026 the experiment. Currently, designs for the pilot-scale experiment are in the conceptual
2027 stage, but a goal of Phase III is to translate these design concepts into detailed technical
2028 designs and specifications.

2029 **3.5.1 Choice of Frequency**

2030 The optimal CRES frequency for Project 8 is that which reaches the target sensitivity of
2031 40 meV, while minimizing the cost and complexity of the overall experiment. The CRES
2032 frequency is directly linked to the magnetic field, which is coupled to nearly all aspects
2033 of the experiment design, therefore, an optimization of CRES frequency is effectively an
2034 optimization of the sensitivity of the overall experiment.

2035 **Frequency Scaling Laws**

2036 The Phase I and II experiments utilized a background magnetic field of 0.959 T provided
2037 by an NMR magnet. Since this magnet was already available, the 0.959 T background
2038 field was selected for convenience. However, one additional reason to use this background
2039 field is that the cyclotron frequencies for electrons near the tritium endpoint in a 0.959 T
2040 field are approximately 26 GHz, which is within the standard RF Ka-band. Therefore,
2041 microwave electronics specialized for these frequencies are obtainable for relatively low
2042 cost. The operating frequency for the large-scale experiments must be selected in a more
2043 rigorous manner due to the increased scale and complexity of the systems as well as the
2044 requirements of the 40 meV neutrino mass science goal.

2045 There is a bias towards lower frequencies in a large-volume experiment, due to the
2046 direct relationship between wavelength and the physical size of the compatible RF
2047 components like antennas and cavities. With a longer wavelength more volume can
2048 be surrounded by an array with fewer antennas, which reduces hardware and data-
2049 processing costs. Additionally, the size of a cavity experiment is directly proportional to
2050 the wavelength, since this sets the physical dimensions of the cavity. It is also simpler to
2051 engineer a magnet that provides a uniform magnetic field across several cubic-meters of
2052 space at lower magnetic fields, which provides advantages in terms of cost-reduction.

2053 A concern with lower magnetic fields and frequencies is the power scaling as described
2054 by the Larmour equation, in which power is proportional to the square of the frequency.
2055 Naively, one would predict that the SNR would decrease with lower fields, however, two
2056 additional scaling laws that affect the noise power also come into play. Noise power
2057 is directly proportional to the required bandwidth, which decreases linearly with the
2058 magnetic field. Furthermore, at lower frequencies it is possible to purchase amplifiers with
2059 lower noise temperatures until approximately 300 MHz, at which point this relationship
2060 tends to flatten. Therefore, it is expected that the SNR remains approximately constant
2061 as the frequency decreases.

2062 The facts that large-volume experiments are simpler to achieve at lower frequencies
 2063 and SNR is expected to be approximately the same together motivate the usage of lower
 2064 magnetic fields in the large-scale experiments. This is simply because a low-frequency
 2065 experiment is less costly than a high-frequency experiment and there is little to no penalty
 2066 in SNR or detection efficiency at these fields.

2067 One drawback of lower magnetic fields is the increased influence of external magnetic
 2068 fields on the experiment. This includes magnetic fields from the building materials as well
 2069 as variations in the earth's magnetic field. A suitable magnetic field correction system
 2070 will need to be devised to deal with these effects, which includes constant monitoring of
 2071 external fields.

2072 Atomic Tritium Considerations

2073 The pilot-scale experiments will be the first Project 8 experiments to combine CRES with
 2074 atomic tritium, therefore, the optimal frequency should take into account the affect of the
 background magnetic field on the atom trap. The primary influence of the background

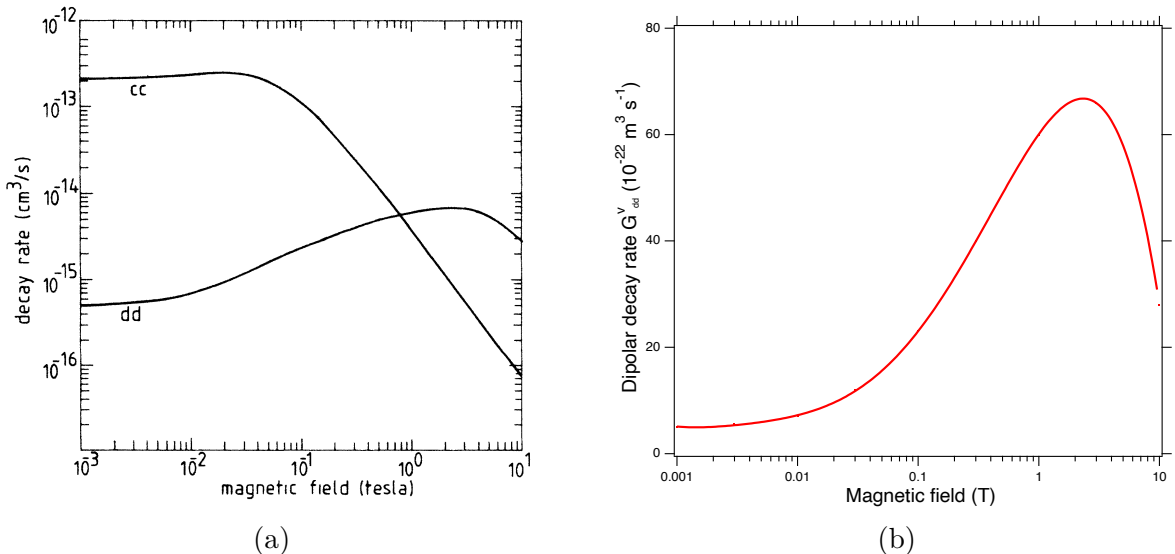


Figure 3.18. (a) A plot of the decay rate for the two-body dipolar spin exchange interaction for cc and dd state. (b) A plot of the decay rate of the dipolar spin exchange interaction for d+d states as a function of magnetic field magnitude. Lowering the magnetic field is key for reducing the losses from this interaction.

2075
 2076 field magnitude is through the rate of dipolar spin-flips caused by a spin exchange
 2077 interaction between trapped atoms [58].

2078 Atomic tritium is a simple quantum system with a hyperfine structure given by the
 2079 addition of the nuclear and atomic spins. The addition of two spins leads to a hyperfine

structure with four states in the (m_s, m_I) basis [59]. The states with atomic spins directed anti-parallel to the magnetic field have $m_s = -1/2$ and are labeled as the a and b states. The a and b states are colloquially known as high-field seeking states, since their energy is minimized when in regions of higher magnetic field. This leads to losses in the magnetic trap as these atoms are drawn to higher fields away from the trap center. Alternatively, the c and d states, with atomic spin $m_s = +1/2$, minimize their energy in low magnetic fields because of the parallel alignment between spin and the magnetic field. Therefore, these low-field seeking states tend to stay trapped significantly longer than the high-field seeking states.

It would be advantageous to prepare tritium atoms in purely c and d states before trapping, however, even in this case losses still occur due to dipolar interactions between pairs of c and d states leading to flipped atomic spins and subsequent losses from high-field seeking atoms. The rate of these interactions depends on the magnitude of the background magnetic field and is maximal for dd interactions around 1 T (see Figure 3.18). The rate of losses from these interactions at 1 T requires atomic tritium production at a rate two orders of magnitude larger than at 0.1 T, thus, requirements on the whole atomic tritium system are significantly relaxed at lower magnetic fields, which provides powerful argument for moving to lower frequencies with the pilot-scale experiments and Phase IV.

3.5.2 Pilot-scale Experiment Concepts

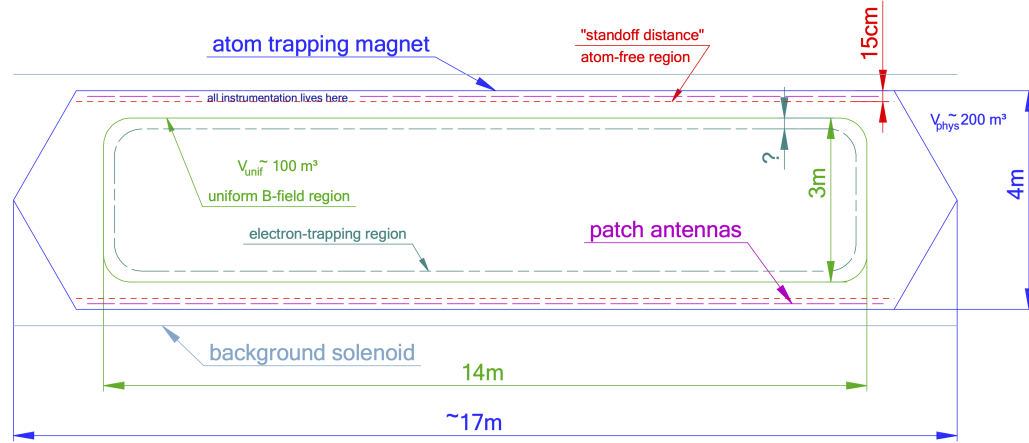


Figure 3.19. A conceptual sketch of a large-volume antenna array based CRES experiment to measure the neutrino mass.

While the pilot-scale experiments are still in the early stages, enough is known to

2101 sketch the general features of these experiments at the conceptual level. Development of
2102 the antenna-based experiment has been suspended in favor of the cavity-based experiment.

2103 **Pilot-scale Antenna Array CRES Experiment Concept**

2104 A conceptual design for an antenna-based CRES experiment is shown in Figure 3.19. A
2105 large solenoid magnet provides a uniform background magnetic field less than 0.1 T in
2106 magnitude. Inside this region is the atom trapping magnet that generates a high magnetic
2107 field at the walls, which decays exponentially towards the central region. Known magnet
2108 designs that produce suitable atom trapping fields include Ioffe-Pritchard traps [60],
2109 which use conducting coils, as well as a Halbach array [61] made from permanent magnets.
2110 Either magnet choice produces a region of high magnetic fields, which excludes atoms
2111 and allows for the placement of antennas inside the experiment.

2112 Inside this region an array of microstrip patch antennas is inserted to collect the
2113 cyclotron radiation without providing a surface for atomic tritium recombination. Due
2114 to the lower frequency of cyclotron radiation antennas of a larger size can be used,
2115 which lowers the total number of antennas required to observe the experiment volume.
2116 Because of this scaling, the lower frequency experiment uses a similar number of antennas
2117 compared to a much smaller demonstrator experiment with a 1 T magnetic field.

2118 The atomic tritium beamline that supplies fresh tritium atoms to the experiment is
2119 not shown in the figure. The general configuration would matches the one shown for the
2120 pilot-scale cavity experiment (see Figure 3.20).

2121 **Pilot-scale Cavity CRES Experiment Concept**

2122 The pilot-scale cavity experiment includes both an atomic tritium system and cavity
2123 CRES system. The atomic system consists of a thermal atom cracker located at the
2124 start of an evaporatively cooled atomic beamline. The atomic tritium system provides a
2125 supply of tritium atoms to the trap with temperatures on the order of a few mK. Atoms
2126 at this temperature can be trapped magneto-gravitationally, which is the reason for the
2127 vertical orientation of the cavity. At these low magnetic fields the trapping requirements
2128 for electrons and atoms differ enough such that it is advantageous to decouple the the
2129 trapping potentials to avoid radioactive heating of the tritium atoms from excess trapped
2130 electrons. Electron trapping is provided by a set of magnetic pinch coils at the top and
2131 bottom of the cavity and a multi-pole Ioffe or Halbach magnet serves to contain the
2132 atoms.

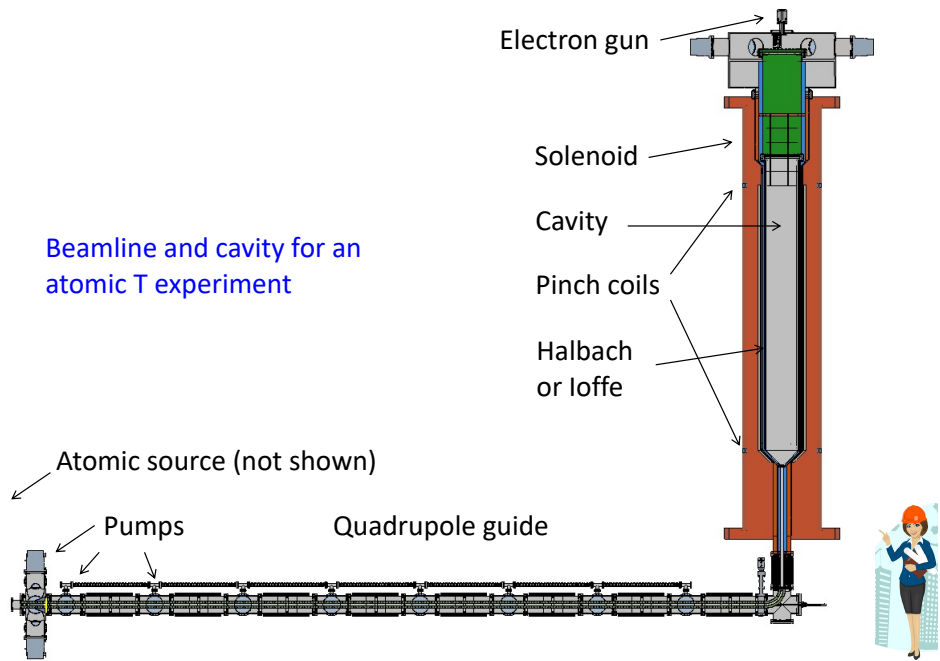


Figure 3.20. A conceptual sketch of a pilot-scale cavity CRES experiment with an atomic tritium beamline.

2133 The cavity design for the pilot-scale experiment consists of a large cylindrical cavity
 2134 with a TE011 resonance of 325 MHz. Such a cavity is truly enormous, with a diameter of
 2135 approximately 1.2 m and a height of 11 m. When an electron is produced inside the cavity
 2136 with a cyclotron frequency that matches the TE011 resonant frequency, its cyclotron
 2137 orbit couples the electron to the TE011 mode, which drives a resonance in the cavity.
 2138 These resonant fields can be read-out using an appropriate cavity coupling mechanism
 2139 located at the center of the cavity. For more information on the cavity approach to
 2140 CRES see Chapter 6.

2141 The bottom of the cavity has a cone termination to match the contour of the atom
 2142 trapping magnet. This shape still allows for TE011 resonances with high internal Qs,
 2143 which are required for good SNR in the cavity experiment. A small opening in the bottom
 2144 of the cone serves as an entry point for the tritium atoms. To allow for calibration of
 2145 the magnetic field inhomogeneities with an electron gun, the top of the cavity is left
 2146 nearly completely open. Normally, this would drastically lower the Q-factor of the TE011
 2147 mode, but a specially configured coaxial partition is inserted at the top. This termination
 2148 scheme is designed to act as a perfect short for the TE011 mode since the circular shape
 2149 of the partition matches the electric field boundary conditions for the TE011 mode.
 2150 Simulations with HFSS have confirmed that this design results in a high quality TE011

2151 resonance despite the nearly completely open end.

2152 3.6 Phase IV

2153 The baseline CRES technology being pursued by Project 8 are resonant cavities, which,
2154 due to their geometric properties, simple CRES signal structure, and low channel
2155 count, appear to be the better option for Phase IV. The current knowledge of the
2156 antenna array CRES approach reveals no technical obstacles that would preclude it
2157 as a baseline technology for Phase IV, though it would certainly be significantly more
2158 expensive. Therefore, antenna arrays represent a fallback approach if resonant cavities
2159 prove infeasible.

2160 The sensitivity of the pilot-scale atomic tritium experiment is estimated to be on
2161 the order of 0.1 eV, which means that increasing the sensitivity to reach the Phase IV
2162 goal will require an even larger experiment. Because of the direct coupling between the
2163 RF characteristics of a cavity and its geometry, the baseline plan is to build multiple
2164 copies of the pilot-scale experiment (see Figure 3.21) to obtain the required amount of
2165 volume rather than increase the size of the cavity beyond the pilot-scale. The built-in
2166 redundancy of this approach is useful in the sense that the experiment has no single
2167 point of failure, additionally, building several copies of the a pilot-scale experiment will
2168 minimize new engineering and design effort.

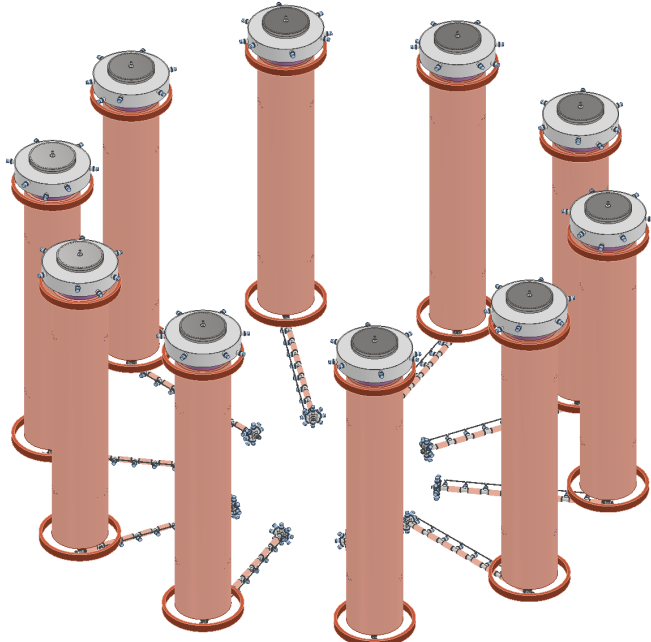


Figure 3.21. An illustration of a possible arrangement of ten pilot-scale cavity experiments for Phase IV. The experiments are arranged in a circle with an approximate diameter of 50 meters. Each atomic beamline connected to the bottom of each cavity is approximately 10 m in length. The cavities themselves are designed to operate at 325 MHz and are approximately 11 m tall. The circular arrangement of cavities has some advantages when it comes to cancellation of fringe fields from neighboring magnets, which is important due to the small magnetic field magnitudes consistent with these CRES frequencies. The advantage of ten independent atomic sources and cavities is that there is no single point of failure for the experiment. If an experiment goes down for repairs the other nine may continue running. Figure courtesy of Michael Huehn at UW-Seattle.

Chapter 4

Signal Reconstruction Techniques for Antenna Array CRES and the FSCD

4.1 Introduction

An antenna array CRES experiment introduces new challenges related to data acquisition, signal detection, and signal reconstruction caused by the multi-channel nature of the data. The development of signal reconstruction algorithms is crucial to the design of antenna array based experiments like the FSCD, because these algorithms directly influence the detection efficiency and energy resolution of the CRES experiment. In this Chapter I summarize my contributions to the development and analysis of signal reconstruction and detection algorithms for the FSCD experiment.

In Section 4.2 I discuss the primary tool for this work, which is the Locust simulations package developed by the Project 8 experiment. Locust is used to simulate CRES events in the detector, which begins with calling a second software package — Kassiopeia — to calculate particle trajectory solutions for electrons in the magnetic trap. The trajectories are subsequently used to calculate the response of the antenna array to the cyclotron radiation produced by the electron, which results in signals that can be used to analyze the performance of different signal reconstruction algorithms. More recently, Project 8 has developed CREsana, which is a new simulations package that takes a more analytical approach to CRES signal simulations for antenna arrays. Although CREsana signals were not used for the signal reconstruction algorithm development detailed here, I introduce the software as it is the simulation software used to model the antenna array measurements presented in Section 5.5.

In Section 4.3 I discuss the signal reconstruction and detection approaches analyzed for the FSCD experiment. In general there are two steps to signal reconstruction — detection and parameter estimation. With signal detection one is concerned with distinguishing

2195 between data that contains a signal versus data that contains only noise, whereas, with
2196 parameter estimation one extracts the kinematic parameters of the electron encoded in
2197 the cyclotron radiation signal shape. Due to the low signal power of electrons near the
2198 spectrum endpoint in the FSCD experiment, signal detection is a non-trivial problem.
2199 This is magnified by the need to maximize the detection efficiency of the experiment
2200 in order to achieve the neutrino mass sensitivity goals. My contributions to signal
2201 reconstruction analyses for the FSCD are focused on the signal detection component of
2202 reconstruction.

2203 After discussing various signal detection approaches, in Section 4.4 I present a
2204 detailed analysis of the detection performance of three algorithms, which could be used
2205 to signal detection in the FSCD. This section was prepared for publication in JINST as
2206 a separate paper. The algorithms include a digital beamforming algorithm, a matched
2207 filter algorithm, and a neural network algorithm, which I analyze in terms of classification
2208 accuracy and estimated computational cost.

2209 **4.2 FSCD Simulations**

2210 Antenna array CRES and the FSCD require a combination of different capabilities
2211 not often found in a single simulation tool. In particular, accurate calculations of the
2212 magneto-static fields produced by current-carrying coils are needed to accurately model
2213 the magnetic trap and background magnets. The resulting magnetic fields must then be
2214 used to calculate the exact relativistic trajectory of electrons. The electron trajectories
2215 are required to calculate the electro-magnetic (EM) fields produced by the acceleration
2216 of the electron. Finally, the simulation must model the interaction of the antenna and
2217 RF receiver chain with the EM-fields in order to yield the simulated voltage signals from
2218 the antenna array. No available simulation tools adequately perform these combined
2219 functions, therefore, Project 8 developed a custom simulation framework to simulate the
2220 FSCD and CRES. This simulation framework includes custom simulation tools developed
2221 by Project 8, as well as open-source and proprietary software developed by third-parties.

2222 **4.2.1 Kassiopeia**

2223 Kassiopeia¹ is a particle tracking and static EM-field solver developed by the KATRIN
2224 collaboration for simulations of their spectrometer based on the MAC-E filter technique

¹<https://github.com/KATRIN-Experiment/Kassiopeia>

[62]. Unfortunately, Kassiopeia is not designed to solve for the EM-fields radiated by electrons in magnetic fields. However, it does provide efficient solvers for static electric and magnetic fields and charged particle trajectory solvers. Because of this, Project 8 has incorporated parts of Kassiopeia into the Locust simulation framework.

Magnetostatic Field Solutions

The solutions to the electric and magnetic fields generated by a static configuration of charges and currents is given by Maxwell's equations in the limit where the time-dependent terms go to zero. In their static form Maxwell's equations [49] are

$$\nabla \cdot \mathbf{E} = \frac{\rho}{\epsilon_0} \quad (4.1)$$

$$\nabla \times \mathbf{E} = 0 \quad (4.2)$$

$$\nabla \cdot \mathbf{B} = 0 \quad (4.3)$$

$$\nabla \times \mathbf{B} = \mu_0 \mathbf{J}, \quad (4.4)$$

where it can be seen that the electric and magnetic fields are completely decoupled from one another. The solution for the magnetic field in this boundary value problem is given by the Biot-Savart law

$$\mathbf{B}(\mathbf{r}) = \frac{\mu_0}{4\pi} \int dr'^3 \frac{\mathbf{J}(\mathbf{r}') \times (\mathbf{r} - \mathbf{r}')}{|\mathbf{r}' - \mathbf{r}|^3}, \quad (4.5)$$

which Kassiopeia can use a variety of numeric integration techniques to solve for a particular current distribution.

Kassiopeia Simulation of the FSCD Magnetic Trap

The trap developed for the FSCD experiment utilizes six current carrying coils, which surround a cylindrical tritium containment vessel (see Figure 4.1). Some critical aspects of the trap design include the total trapping volume, the maximum trap depth, the steepness of the trap walls, as well as the radial and azimuthal uniformity of the magnetic fields.

The volume of the FSCD trap is a cylindrically shaped region with a radius of 5 cm and a length of 15 cm resulting in a roughly 1 L total trap volume. The trap volume is an important design feature, because it sets the volume of the experiment that is potentially usable for CRES measurements. Trapping a larger volume allows one to observe a larger

number of tritium atoms, which increases the statistical power and sensitivity of the neutrino mass measurement. Due to the cost of constructing magnets with large and uniform magnetic fields it is important that the trap use as much of the available volume as possible to limit the overall cost of the experiment.

Coil	Radius (mm)	Z Pos. (mm)	Current (Amp.×Turns)
1	50.0	-92.3	750.0
2	50.1	-56.9	-220.3
3	68.5	-19.5	-250.0
4	68.5	19.5	-250.0
5	50.1	56.9	-220.3
6	50.0	92.3	750.0

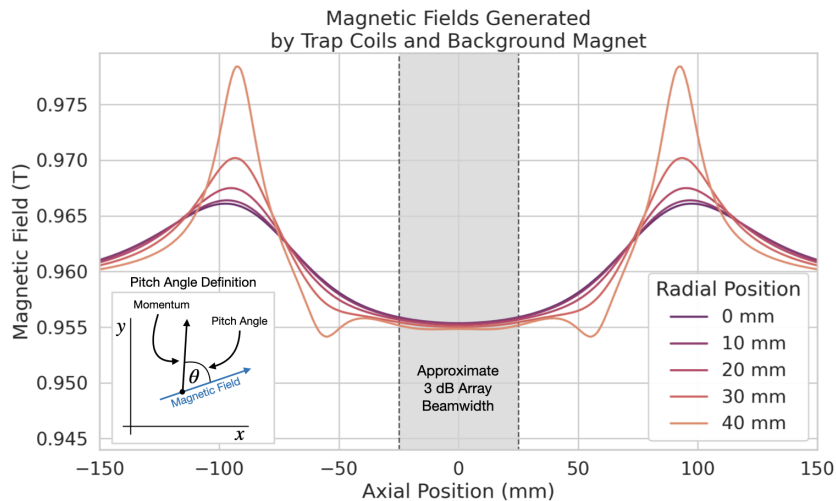
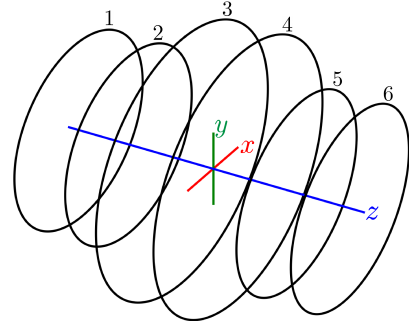


Figure 4.1. The geometry and parameters of the coils used to simulate the FSCD magnetic trap in Kassiopeia. Some axial profiles of the magnetic trap at different radial positions are shown to demonstrate the shape of the magnetic field and trap depth as a function of position. Calculation of the magnetic field profiles was graciously done by René Reimann.

The depth of the FSCD trap is approximately 10 mT when measured along the central axis, which is sufficient to trap electrons with pitch angles as small as 84° . The trap depth influences the efficiency of the experiment by directly controlling the range of electron pitch angles that can be trapped. If a higher fraction of pitch angles are trapped, in principle, more decay events can be observed. However, the signals from electrons with small pitch angles are significantly harder to detect in the FSCD than large pitch angles, which increases the likelihood of not detecting the first track of the CRES event and harms the energy resolution of the experiment.

The steepness of the trap walls as well as non-uniformities in the magnetic field

2261 contribute to the total energy resolution of the CRES measurement by causing uncertainty
 2262 in the relationship between an electron's kinetic energy and its cyclotron frequency. When
 2263 an electron is trapped, it oscillates back and forth along the trap z-axis (see Figure 4.1)
 2264 unless it has a pitch angle of exactly 90° [63]. As the electron is reflected from the trap
 2265 walls it experiences a change in the total magnetic field, which causes a modulation in the
 2266 cyclotron frequency. This change in magnetic field from the trap introduces a correlation
 2267 between the pitch angle and kinetic energy parameters of the electron that can reduce
 2268 energy resolution. In order to mitigate this effect it is important to make the trap walls
 2269 as steep as possible.

2270 Particle Trajectory Solutions

2271 The magnetic fields solved by direct integration of the coil current densities are used to
 2272 calculate the trajectories of electrons based on user specified initial conditions. Various
 2273 statistical distributions are available, which can be sampled to replicate realistic event
 2274 statistics. These include uniform, Gaussian, and Lorentzian distributions among others.
 2275 In general, an electron has six kinematic parameters that define its trajectory, which are
 2276 the three-dimensional coordinates of the initial position and the three components of the
 2277 electron's momentum vector. However, when simulating CRES events it is common to
 2278 parameterize the electron's trajectory in terms of the initial position, kinetic energy, pitch
 2279 angle, and initial direction of the component of the electron's momentum perpendicular
 2280 to the magnetic field. This parameterization is completely equivalent to specifying the
 2281 starting position and momentum vectors.

2282 From the initial parameters of the electron and the magnetic field, Kassiopeia solves
 2283 for the trajectory of the electron. The direct approach proceeds by solving the motion of
 2284 the electron using the Lorentz force equation, which takes the form of a set of differential
 2285 equations

$$\frac{d\mathbf{r}}{dt} = \frac{\mathbf{p}}{\gamma m} \quad (4.6)$$

$$\frac{d\mathbf{p}}{dt} = e(\mathbf{E} + \frac{\mathbf{p} \times \mathbf{B}}{\gamma m}), \quad (4.7)$$

2286 where \mathbf{r} is the position of the electron, \mathbf{p} is the electron's momentum, e is the charge of
 2287 the electron, m is the electron's mass, and γ is the relativistic Lorentz term. Kassiopeia
 2288 solves this pair of differential equations using numerical integration, however, the exact
 2289 trajectory can be computationally intensive to solve. If the adiabatic approximation can

2290 be applied, then Kassiopeia can make use of a simpler set of equations that can be more
2291 readily solved numerically.

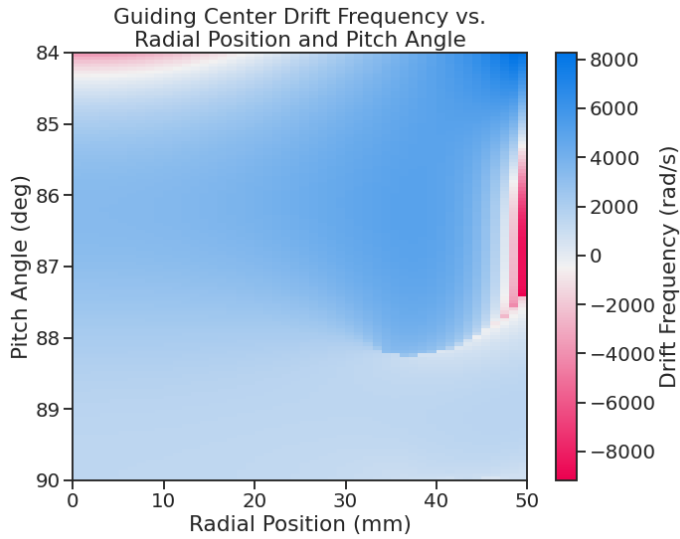


Figure 4.2. A map of the average ∇B -drift frequency for electrons trapped in the prototype FSCD trap shown in Figure 4.1. Negative drift frequencies indicate electrons that are drifting opposite to the standard direction, which means that they are close to escaping the magnetic trap.

2292 Though Kassiopeia is not directly capable of simulating the cyclotron radiation, it is
2293 an invaluable CRES simulation tool. With Kassiopeia it is possible to test the efficiency
2294 of a particular trap design, and analyze features of the electron trajectories that are
2295 important to the position, track, and event reconstruction (see Section 4.3). An example
2296 is the analysis of the average ∇B -drift frequency as a function of the electrons radial
2297 position and pitch angle in the FSCD trap (see Figure 4.2). Radial gradients in the trap
2298 cause the guiding center of the electron to drift around the center of the magnetic trap
2299 with an average frequency on the order of 10^3 rad/s. This frequency, while slow compared
2300 to the length of a typical CRES time-slice, is large enough to cause a significant loss in
2301 efficiency of certain signal reconstruction algorithms. Therefore, it is important to model
2302 the drift of the electron in the reconstruction algorithm in order to mitigate the effects
2303 of this motion on the reconstruction.

4.2.2 Locust

The Locust² software package [64] is the primary simulation tool developed and used by the Project 8 collaboration for CRES experiments. Locust simulates the responses of antennas and receiver electronics chain to rapidly time-varying electric fields using a flexible approach that allows one to choose from a variety of electric field sources and antennas. Similarly, one can simulate the receiver chain using a series of modular generators that include standard signal processing operations such as down-mixing and fast Fourier transforms (FFT). Since the primary focus of this chapter is the application of Locust to analyses of the FSCD, I shall describe only the most relevant aspects of the software rather than provide a comprehensive description.

Cyclotron Radiation Field Solutions

Simulating CRES events in the FSCD requires one to calculate the electric fields produced by the acceleration of the electron. In the general case, this can be a complicated computation, due to back-reaction forces on the electron. However, in the case of the FSCD it is possible to ignore such effects and approximate the electron as radiating into a free-space environment.

The equations that describe the EM fields from a relativistic moving point particle are the Liénard-Wiechert equations [65, 66], which are obtained by differentiating the Liénard-Wiechert potentials. In their full form, the Liénard-Wiechert field equations are

$$\mathbf{E} = e \left[\frac{\hat{n} - \boldsymbol{\beta}}{\gamma^2(1 - \boldsymbol{\beta} \cdot \hat{n})^3 |\mathbf{R}|^2} \right]_{t_r} + \frac{e}{c} \left[\frac{\hat{n} \times [(\hat{n} - \boldsymbol{\beta}) \times \dot{\boldsymbol{\beta}}]}{(1 - \boldsymbol{\beta} \cdot \hat{n})^3 |\mathbf{R}|} \right]_{t_r} \quad (4.8)$$

$$\mathbf{B} = [\hat{n} \times \mathbf{E}]_{t_r}, \quad (4.9)$$

where e is the charge of the particle, \hat{n} is the unit vector pointing from the particle to the position where the fields are calculated, $\boldsymbol{\beta}$ and $\dot{\boldsymbol{\beta}}$ are the velocity and acceleration of the particle divided by the speed of light (c), \mathbf{R} is the distance from the particle to the field calculation position, and γ is the relativistic Lorentz term. The subscript t_r indicates that the equations are evaluated at the retarded time so that the time-delay from the travel time of the electromagnetic radiation is taken into account.

The only required input to calculate the electric field at the position of an FSCD antenna is the velocity and acceleration of the electron, which can be obtained from Kassiopeia simulations. Therefore, when simulating a CRES event Locust first runs

²https://github.com/project8/locust_mc/tree/master

2332 a Kassiopeia simulation of the electron and subsequently calculates the electric field
 2333 incident on the antenna. This requires one to calculate the retarded time. The retarded
 2334 time corresponds to the time that a photon, which has just arrived at an antenna at
 2335 the space-time position (t, \mathbf{r}) , was actually emitted by the electron at the space-time
 2336 position of $(t_r, \mathbf{r}_e(t_r))$. To calculate the retarded time one solves

$$c(t - t_r) = |\mathbf{r} - \mathbf{r}_e(t_r)|, \quad (4.10)$$

2337 where the distance traveled by the photon between the measurement and retarded times
 2338 is equal to the distance between the antenna and the electron at the retarded time.
 2339 Locust solves Equation 4.10 using root finding algorithm to calculate the retarded time,
 2340 which yields the electric field emitted by the electron, at the position of each antenna in
 2341 the FSCD array.

2342 Antenna Response Modeling

2343 The electric field solutions are used to calculate the resulting voltages produced in the
 2344 antenna. However, direct simulation of the antenna itself is computationally expensive,
 2345 since it requires modeling the complex interactions of the electron's electric fields with
 2346 charge carriers in the antenna. Direct simulation of the antenna in Locust is avoided by
 2347 modeling the antenna response using the antenna factor, or antenna transfer function.
 2348 The antenna factor defines the voltage produced in the antenna terminal for an incident
 2349 electric field [67],

$$A_F = \frac{V}{|\mathbf{E}|}, \quad (4.11)$$

2350 where V is the voltage and $|\mathbf{E}|$ is the magnitude of the incident electric field. To obtain the
 2351 antenna factor for the antennas developed for the FSCD Project 8 employs Ansys HFSS.
 2352 HFSS is a commercially available finite element method electromagnetic solver widely
 2353 used throughout the antenna engineering industry [68]. HFSS is capable of calculating
 2354 the antenna factor and gain patterns for complex antenna designs and outputting the
 2355 resulting quantities in the form of a text file that can be used as a configuration input to
 2356 Locust.

2357 The antenna factor defines the steady-state response of the antenna to electromagnetic
 2358 plane waves in the frequency-domain. Since the antenna response is calculated in the
 2359 time-domain Locust models the antenna as a linear time-invariant system [69]. In this

2360 formalism the response of the system to the driving force is given by

$$y[n] = h * x = \sum_k h[k]x[n - k], \quad (4.12)$$

2361 where $y[n]$ is the discretely sampled response, x is the driving force stimulus, and h is
 2362 the finite impulse response (FIR) filter. When applied to the FSCD array, this formalism
 2363 calculates the voltage time-series produced in each antenna by convolving the electric
 2364 field time-series with the antenna FIR filter, which is obtained by performing an inverse
 2365 Fourier transform on the transfer function from HFSS.

2366 Radio-frequency Receiver and Signal Processing

2367 After obtaining the voltage time-series by computing the electron trajectory and antenna
 2368 response, Locust simulates the signal processing performed by the radio-frequency (RF)
 2369 receiver chain. The simulated Locust receiver chain includes all operations that would
 2370 be performed by the RF hardware (see Figure 4.3).

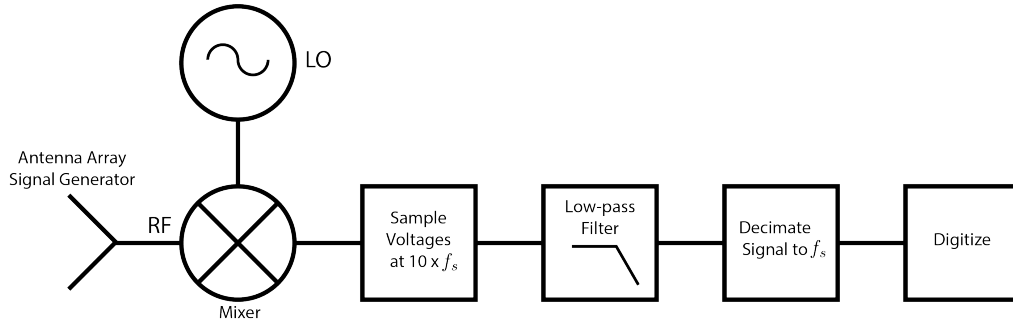


Figure 4.3. The receiver chain used by Locust when simulating CRES events in the FSCD.

2371 Frequency down-conversion reduces the digitization bandwidth required to read-out
 2372 CRES data. According to the Nyquist sampling theorem [70], the minimal sampling rate
 2373 that guarantees no information loss for a signal with a bandwidth Δf is given by

$$f_{\text{Nyq}} = 2\Delta f. \quad (4.13)$$

2374 The total bandwidth for CRES events ranges from 0 to 26 GHz in a 0.95 T magnetic field,
 2375 therefore, direct digitization of CRES signals from the FSCD would require sampling
 2376 frequencies greater than 50 GHz, which is infeasible for a real experiment. However, one
 2377 need only measure the shape of the spectrum in the last 100 eV, which corresponds to a
 2378 frequency bandwidth of 5 MHz, to effectively measure the neutrino mass.

2379 Down-conversion is a technique for reducing the base frequencies of signals in a
2380 bandwidth given by $[f_{\text{LO}}, f_{\text{LO}} + \Delta f]$ to the bandwidth $[0, \Delta f]$, by performing the following
2381 multiplication

$$x(t) \rightarrow x(t)e^{-2\pi f_{\text{LO}} t}. \quad (4.14)$$

2382 The signal, $(x(t))$, is multiplied by a sinusoidal signal with frequency f_{LO} to reduce the
2383 absolute frequencies of the signals in the bandwidth. In the FSCD, this allows one to
2384 detect events in the last 100 eV of the tritium spectrum, while sampling the data far
2385 below 50 GHz. The standard bandwidth used in the FSCD is 200 MHz, which allows for
2386 higher frequency resolution than the minimum sampling frequency for 100 eV of energy
2387 bandwidth.

2388 Directly simulating down-conversion with a frequency multiplication in Locust requires
2389 sampling the electric fields at each antenna in the FSCD array with a period of ≈ 20 ps,
2390 which is extremely slow computationally. To avoid this, Locust performs the down-
2391 conversion by intentionally under-sampling the electric fields with a frequency of 2 GHz.
2392 Sampling below the Nyquist limit causes the higher frequency components of the CRES
2393 signal to alias, however, Locust can remove these aliased frequency peaks using a
2394 combination of low-pass filtering and decimation to recreate frequency down-conversion.
2395 After filtering and decimation, Locust simulates digitization by an 8-bit digitizer at a
2396 sampling frequency of 200 MHz to recreate the conditions of the FSCD. The voltage
2397 offset and digitizer range must be configured by the user based on the characteristics of
2398 the simulation.

2399 Data

2400 The output of Locust simulations for the FSCD primarily consists of two data files. The
2401 first is the electron trajectory information calculated by Kassiopiea, which is output in
2402 the form of a `.root` file [71]. This file contains important kinematic information about
2403 the electron such as its position and pitch angle as a function of time. The other file
2404 is produced by Locust and contains the digitized signals acquired from each antenna
2405 in the array. The Locust output files conform to the Monarch specification developed
2406 by Project 8, which is based on the commonly used HDF5 file format, and matches the
2407 format of the files produced by the Project 8 data acquisition software. This makes it
2408 possible to use the same data analysis code to analyze both simulated and real data.

2409 **4.2.3 CRESana**

2410 Locust is the primary simulation tool used by Project 8 in the development and simulation
2411 of the FSCD. However, simulations of CRES events in larger antenna arrays (≥ 100
2412 antennas) can take several hours to complete, which is prohibitively long when one is
2413 performing a sensitivity analysis and optimization. One reason for Locust's slow operation
2414 is that the electric fields from the electron must be solved numerically for each time-step
2415 for all antennas in the array. These numerical solutions allow Locust to accurately
2416 simulate the electric fields from arbitrarily complicated electron trajectories at the cost
2417 of more computations and slower simulations. Therefore, an additional simulation tool
2418 that sacrifices the accuracy of numerical approaches for computational efficiency is a
2419 useful tool for studying large antenna array experiments.

2420 Recently, Project 8 has developed a new simulations package called CRESana³,
2421 specifically designed to perform analytical simulations of antenna array based CRES
2422 experiments. CRESana provides a significant increase in simulation speed by using
2423 well-justified analytical approximations of the electrons motion and electric fields in a
2424 magnetic trap. The electric fields and signals generated by CRESana are consistent with
2425 theoretical calculations of the electron's radiation, and are tested for accuracy using
2426 well-known test-case simulations and consistency checks.

2427 **4.3 Signal Detection and Reconstruction Techniques for**
2428 **Antenna Array CRES**

2429 **Antenna Array CRES Signal Reconstruction**

2430 Antenna array CRES requires one to use the multichannel time-series obtained by
2431 digitizing the array to estimate the starting kinetic energies of electrons produced in
2432 the magnetic trap using CRES signal reconstruction algorithm. This procedure consists
2433 of a multi-stage process of detecting a CRES signal followed by an estimation of the
2434 electron's parameters.

2435 Antenna array CRES requires a significantly different approach to signal reconstruction
2436 than previous Project 8 experiments. In Phases I and II, CRES was performed using a
2437 waveguide gas cell directly integrated into a waveguide transmission line. The transmission
2438 line efficiently propagates the cyclotron radiation along its length to an antenna at the

3<https://github.com/MCflowMace/CRESana>

2439 ends of the waveguide. However, with an antenna array the electron is radiating into
2440 free-space, therefore, the cyclotron radiation power collected by the array is directly
2441 proportional to the solid angle surrounding the electron that is covered with antennas.
2442 Because it is not practical to fully surround the magnetic trap with antennas, some of the
2443 cyclotron radiation power that would have been collected by the waveguide escapes into
2444 free-space. Furthermore, the power that is collected by the antenna array is split between
2445 every channel in the antenna array, which significantly lowers the signal-to-noise ratio
2446 (SNR) of CRES signals in a single antenna channel compared to a waveguide apparatus.
2447 Therefore, a suite of completely new signal reconstruction techniques are needed in order
2448 to perform CRES in the FSCD.

2449 Changes to the approach to CRES signal reconstruction are also motivated by the
2450 more ambitious scientific goals of the FSCD experiment. A measurement of the tritium
2451 beta-decay spectrum that is sensitive to neutrino masses as small as 40 meV requires that
2452 we measure the kinetic energies of individual electrons with a total energy broadening of
2453 115 meV [72]. This resolution includes all sources of uncertainty in the electron's kinetic
2454 energy such as magnetic field inhomogeneities. This precise energy resolution is only
2455 achieved by an event-by-event signal reconstruction approach where the kinetic energies,
2456 pitch angles, and other parameters of the CRES events are estimated for individual
2457 electrons before constructing the beta-decay spectrum.

2458 The event-by-event approach is distinct from the analysis done for the Phase I and
2459 Phase II experiments where only the starting cyclotron frequency of the event was
2460 measured by analyzing the tracks formed by the carrier frequency. These frequencies
2461 were then combined into a frequency spectrogram, which was converted to the beta-
2462 decay energy spectrum using an ensemble approach that averaged over all other event
2463 parameters. The ensemble approach to signal reconstruction results in poor energy
2464 resolution because other kinematic parameters such as pitch angle change the cyclotron
2465 carrier frequency due to changes in the average magnetic field experience by the electron.

2466 Components of Reconstruction: Signal Detection and Parameter Estimation

2467 CRES signal reconstruction is a two-step procedure consisting of signal detection followed
2468 by parameter estimation. In the former, one is concerned with identifying CRES signals
2469 in the data regardless of the signal parameters, whereas, in the latter one operates under
2470 the assumption that a signal is present and then estimates its parameters.

2471 More formally, signal detection can be posed as a binary hypothesis test between
2472 the signal and noise data classes, and parameter estimation is a process of fitting a

2473 signal model to the observed data. While both of these are required for a complete
 2474 reconstruction (see Figure 4.4), the focus of my work and this chapter is on the signal
 2475 detection aspect of antenna array CRES signal reconstruction.

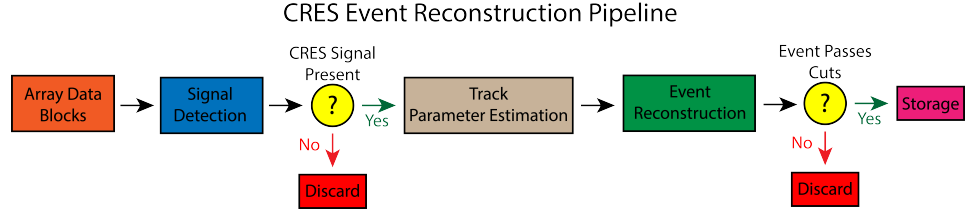


Figure 4.4. A high-level diagram depicting the process of CRES event reconstruction. The first step consists of identifying the presence of a signal in the data. This step is necessary to avoid the danger of performing a reconstruction of a false event, which would constitute a background contribution to the tritium spectrum measured by CRES.

2476 Detection Theory

2477 Signal detection is the process of deciding whether noisy data contains signal or noise,
 2478 which can be posed as a statistical hypothesis test [73]. For CRES signals, which are
 2479 essentially vectors with added white Gaussian noise (WGN), one needs to choose between

$$\mathcal{H}_0 : \mathbf{y} = \boldsymbol{\nu} \quad (4.15)$$

$$\mathcal{H}_1 : \mathbf{y} = \mathbf{x} + \boldsymbol{\nu}, \quad (4.16)$$

2480 where \mathbf{y} is the CRES data vector, $\boldsymbol{\nu}$ is a sample of WGN, and \mathbf{x} represents the CRES
 2481 signal. The hypothesis that the data contains only noise is labeled \mathcal{H}_0 and the hypothesis
 2482 that the data contains a signal is labeled \mathcal{H}_1 .

2483 For illustrative purposes, it is useful to study the case where only the first sample of
 2484 data is used to distinguish between \mathcal{H}_0 and \mathcal{H}_1 . The value of the first data sample is
 2485 distributed according to two possible Gaussian distributions (see Figure 4.5). By setting a
 2486 decision threshold on the value of this sample, one can choose the correct hypothesis with
 2487 a probability given by the area underneath the probability distribution curves. A true
 2488 positive corresponds to correctly identifying that the data contains signal, whereas, a true
 2489 negative means that one has correctly identified the data as noise. The rate at which the
 2490 detector performs a true positive classification is given by the green region underneath
 2491 $p(\mathbf{y}[0]; \mathcal{H}_0)$, and the rate at which the detector performs a true negative classification
 2492 is given by the orange region underneath $p(\mathbf{y}[0]; \mathcal{H}_1)$. Two types of misclassifications
 2493 are possible. Either one declares noise data as signal, which is called a false positive, or

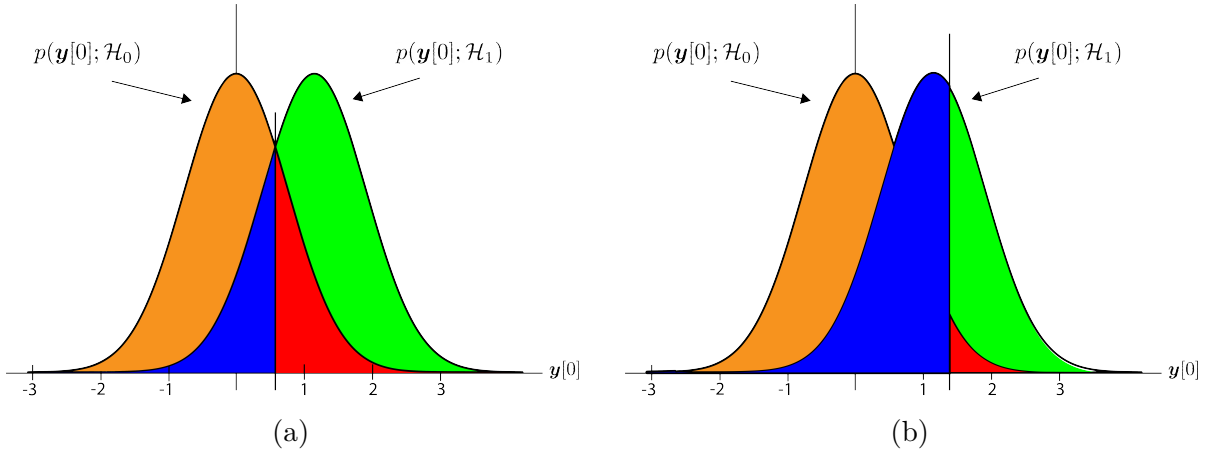


Figure 4.5. An illustration of two PDFs associated with a binary hypothesis test. The decision threshold is represented by the vertical line that partitions both distributions. The orange and red areas correspond to the true negative and false positive probabilities and the blue and green areas correspond to the false negative and true positive probabilities respectively. To decide between the two hypotheses the likelihood ratio test specified by the Neyman-Pearson theorem is applied. This approach achieves the highest true positive probability for a given false positive probability.

2494 one declares signal data as noise, which is a false negative. Note that it is only possible
 2495 to trade off these two types of errors by tuning the detection threshold. One cannot
 2496 simultaneously reduce the rate of false positives without also increasing the rate of false
 2497 negatives.

2498 The approach taken with CRES signals is to fix the rate of false positives by setting
 2499 a minimum decision threshold value. The rate of false positives that is acceptable at the
 2500 detection stage depends upon the total rate of background events compatible with the
 2501 sensitivity goals of the experiment. The ultimate goal of a neutrino mass measurement
 2502 with 40 meV sensitivity in general has strict requirements on the number of background
 2503 events, which requires a relatively high detection threshold to achieve. Consequently,
 2504 the ideal signal detection algorithm is the one that achieves the maximum rate of true
 2505 positives for a fixed rate of false positives, so that the detection efficiency of the experiment
 2506 is maximized and potential sources of background are kept to a minimum.

2507 According to the Neyman-Pearson theorem [74], the statistical hypothesis test that
 2508 maximizes the probability of detection for a fixed rate of false positives is the likelihood
 2509 ratio test, which is formed by computing the ratio of the signal likelihood to the noise
 2510 likelihood,

$$L(x) = \frac{P(\mathbf{y}; \mathcal{H}_1)}{P(\mathbf{y}; \mathcal{H}_0)} > \gamma. \quad (4.17)$$

2511 Here, the likelihood of the hypotheses \mathcal{H}_0 and \mathcal{H}_1 are described by the probability
 2512 distributions $P(\mathbf{y}; \mathcal{H}_0)$ and $P(\mathbf{y}; \mathcal{H}_1)$ respectively, and γ is the threshold for deciding \mathcal{H}_1 .
 2513 The decision threshold is determined by integrating $P(\mathbf{y}; \mathcal{H}_0)$ such that

$$P_{\text{FP}} = \int_{\gamma}^{\infty} P(\tilde{\mathbf{y}}; \mathcal{H}_0) d\tilde{\mathbf{y}} = \alpha, \quad (4.18)$$

2514 where α is the desired false positive detection rate given by the red colored areas shown
 2515 in Figure 4.5. The true positive detection rate is given by the similar integral

$$P_{\text{TP}} = \int_{\gamma}^{\infty} P(\tilde{\mathbf{y}}; \mathcal{H}_1) d\tilde{\mathbf{y}}, \quad (4.19)$$

2516 which corresponds to the green areas in Figure 4.5.

2517 Changing the decision threshold allows one to trade-off between P_{TP} and P_{FP} as
 2518 appropriate for the given situation. It is standard to summarize the relationship between
 2519 P_{TP} and P_{FP} using the receiver operating characteristic (ROC) curve, which is obtained
 2520 by evaluating the true positive and false positive probabilities as a function of the decision
 threshold value (see Figure 4.6). The ROC curve provides a convenient way to compare

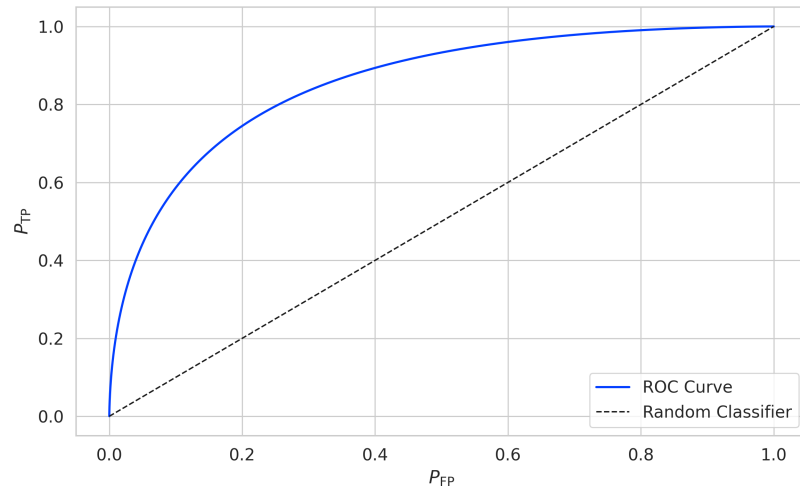


Figure 4.6. An example ROC curve formed by computing the P_{FP} and the P_{TP} for a given likelihood ratio test. As the decision threshold is increased P_{FP} decreases at the expense of a lower P_{TP} . The black dashed line indicates the lower bound ROC curve obtained by randomly deciding between \mathcal{H}_0 and \mathcal{H}_1 .

2521
 2522 the performance of different signal detection algorithms. In general, a classifier with
 2523 a higher the P_{TP} as a function of P_{FP} is desirable, which corresponds to a larger area
 2524 underneath the respective ROC curve. A perfect classifier has an area underneath the

2525 curve of 1.0, however, such a classifier is never achieved in practice.

2526 4.3.1 Digital Beamforming

2527 Introduction to Beamforming

2528 Beamforming is an antenna array signal processing technique designed to enhance the
2529 radiation of the array in a particular direction and suppress it in other directions [67].
2530 Beamforming is of interest to Project 8 as a first level of signal reconstruction for the
2531 FSCD and other antenna array CRES experiments, which operates at the signal detection
2532 stage of reconstruction.

2533 Beamforming is performed using a phased summation of the signals received by the
2534 antenna array. The beamforming phases are selected such that the signals emitted by
2535 the array will constructively interfere at the point of interest (see Figure 4.7). As a
2536 consequence of the principle of reciprocity [75], when the array is operating in receive
2537 mode, the signals emitted from a source at the same point will constructively interfere
when summed. The origin of the phase delays in beamforming is the path-length difference

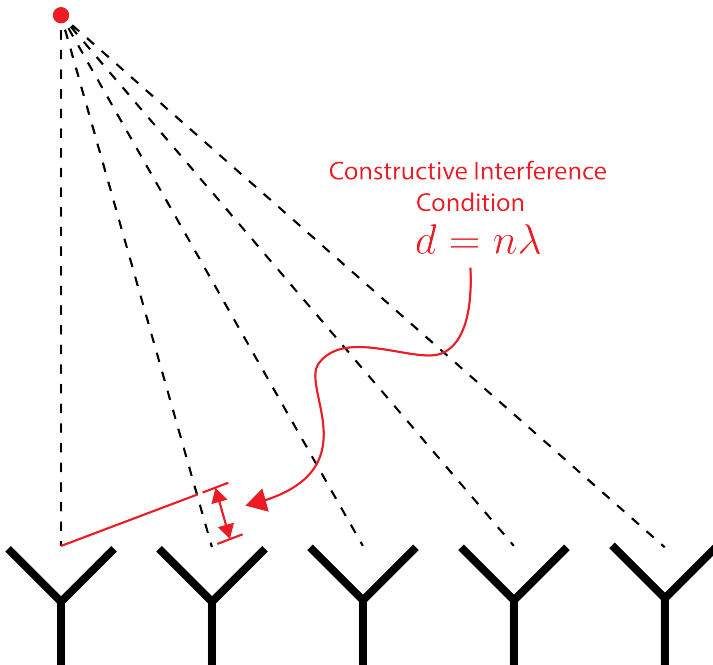


Figure 4.7. An illustration of the constructive interference condition which is the operating principle of digital beamforming using a uniform linear array as an example.

2538
2539 to the beamforming point between different antennas in the array. The relationship

2540 between the phase delay and the path-length difference is given by the familiar equation

$$\phi = \frac{2\pi d}{\lambda}, \quad (4.20)$$

2541 where ϕ is the phase delay, d is the path-length difference, and λ is the wavelength of
2542 the radiation. In practice, one chooses the values of d by specifying the beamforming
2543 positions of interest and then calculates the beamforming phases using Equation 4.20,
2544 which is guaranteed to follow the constructive interference condition shown in Figure 4.7.

2545 Beamforming can be neatly expressed mathematically using the vector equation

$$y[n] = \Phi^T[n] \mathbf{x}[n], \quad (4.21)$$

2546 where $\mathbf{x}[n]$ is the array snapshot vector, $\Phi[n]$ is a vector of beamforming shifts, and
2547 $y[n]$ is the resulting summed signal. The beamforming shifts consist of a set of complex
2548 numbers that contain the beamforming phase shift and an amplitude weighting factor,

$$\Phi[n] = [A_0[n]e^{-2\pi i\phi_0[n]}, A_1[n]e^{-2\pi i\phi_1[n]}, \dots, A_{N-1}[n]e^{-2\pi i\phi_{N-1}[n]}], \quad (4.22)$$

2549 where the set of magnitudes $A_i[n]$ are amplitude weighting factors and $\phi_i[n]$ are the
2550 phase shifts from the path-length differences. The index i is used to denote the antenna
2551 channel number. The amplitude weighting factor is the relative magnitude of the signal
2552 received by a particular antenna in the array. This factor properly accounts for antennas
2553 that are closer to the radiating source. In general, the beamforming phases can also be
2554 functions of time to track the motion of a non-stationary source.

2555 Digital beamforming specifically is the type of beamforming algorithm of interest to
2556 Project 8 for CRES. With digital beamforming, the phase shifts are applied to the array
2557 signals in software rather than employing fixed beamforming phase shifts in the receiver
2558 chain hardware. The advantage of digital beamforming is that for any given series of
2559 array data one can specify an arbitrarily large number of beamforming positions and
2560 search for electrons using a flexible and easily configurable beamforming grid.

2561 Digital beamforming can be viewed as the spatial filtering, which is a direct conse-
2562 quence of the constructive interference condition used to define the beamforming phases.
2563 Digital beamforming causes signals from multiple electrons at different positions in the
2564 trap to be separated, because the interference condition will cause the signals from
2565 electrons at other position to cancel out. This spatial filtering effect reduces pile-up that
2566 could become an issue for large scale CRES experiments using a dense tritium source.

2567 Beamforming positions can be specified with arbitrary densities limited only by
 2568 the available computational resources. This provides a very straight-forward way to
 2569 estimate the position of the electron in the trap by using a dense grid of beamforming
 2570 positions and maximizing the output power of the beamforming summation over this
 2571 grid. This approach to position reconstruction is attractive due the requirements of an
 2572 event-by-event signal reconstruction, which needs an accurate estimation of the exact
 2573 magnetic field experienced by the electron in order to correctly estimate its kinetic
 2574 energy. Combined with an accurate map of the magnetic field inhomogeneities of the
 2575 trap obtained from calibrations, beamforming allows one to apply this magnetic field
 2576 correction with a spatial resolution that is a fraction of the cyclotron wavelength.

2577 **Laboratory Beamforming Demonstrations**

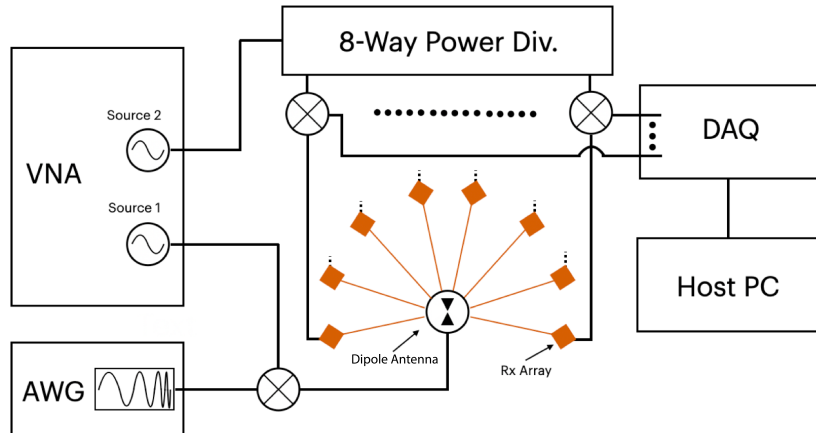


Figure 4.8. A system level diagram of the laboratory setup used for beamforming demonstrations at Penn State. For more information on this system see Chapter 5. Signals near 26 GHz are fed to a dipole antenna using and arbitrary waveform generator (AWG) and vector network analyzer (VNA), which drive a mixer. The dipole radiation is collected by an array of antennas connected to the digitizer data acquisition (DAQ) system.

2578 An antenna measurement setup was constructed at Penn State to serve as a testbed
 2579 for antenna prototypes and to perform laboratory validations of array simulations for
 2580 the FSCD. This system is discussed in more detail in Chapter 5. Early versions of
 2581 the antenna measurement system (see Figure 4.8 and Figure 4.9) were used to perform
 2582 beamforming reconstruction studies of a simple probe antenna.

2583 Signals from an arbitrary waveform generator were up-converted to 26 GHz using a
 2584 mixer and a high-frequency source from a vector network analyzer and fed to a dipole

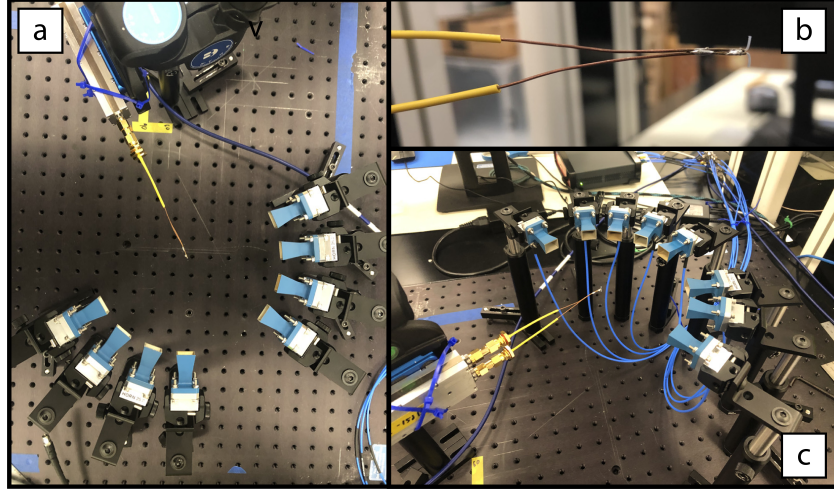


Figure 4.9. Photographs of the beamforming demonstration setup. In (a) I show a top-down view of the dipole antenna and the array of eight horn antennas. Manual repositioning of the horn antennas allows one to synthesize a full-circular antenna array. The dipole antenna is mounted on a camera tripod mount that allows for manual position tuning. (b) is a close up image of the dipole, which is manufactured from two segments of semi-rigid coaxial cable. (c) is another image of the dipole and array.

2585 antenna through a balun. The radiation from the dipole antenna was received by an
 2586 array of horn antennas. The signals from the horn antennas were down-converted to
 2587 baseband using a collection of mixers and an 8-way power divider. The signals were then
 2588 digitized and saved to a host computer for analysis.

2589 The data collected using the dipole and horn antenna array is reconstructed using the
 2590 beamforming reconstruction approach specified in Section 4.3.1. A two-dimensional grid
 2591 of xy-positions is defined and the beamforming phase shifts for each of these positions
 2592 is calculated. The phased summation can be visualized by plotting the time-averaged
 2593 power for each of the summations as a pixel in the resulting beamforming image (see
 2594 Figure 4.10). White Gaussian noise (WGN) can be added to the data at this stage
 2595 to simulate more realistic SNR if desired. The beamforming peak maxima is expected
 2596 to have a Bessel function shape due to the circular symmetry of the array, and by
 2597 analyzing the size of the beamforming maxima one can confirm that the beamforming
 2598 reconstruction measurement has similar position resolution as expected from Locust
 2599 simulations. Additionally, signal detection rates can be estimated from the data by
 2600 comparing the magnitude of the beamforming signal peak in the frequency spectra to
 2601 simulation.

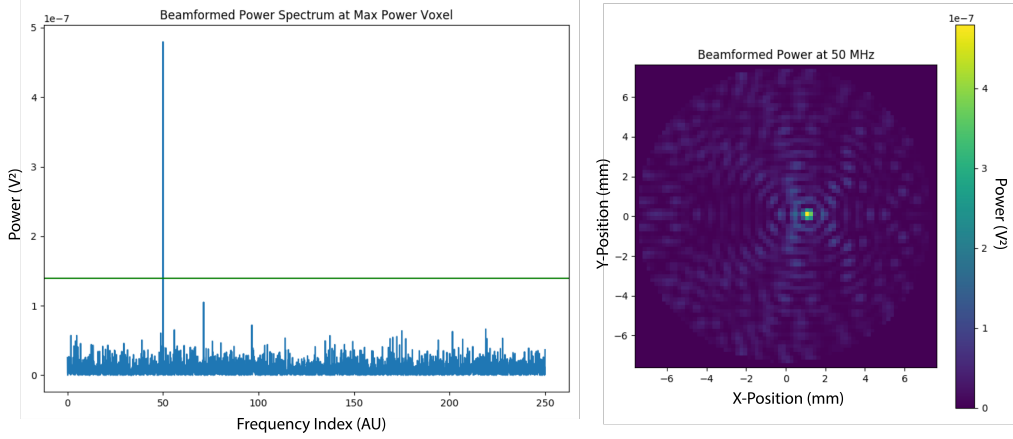


Figure 4.10. An example of digital beamforming reconstruction of a dipole antenna using a synthetic array of horn antennas. The beamforming image on the right is constructed by computing the time-averaged power of the summed signals for a two-dimensional grid of beamforming positions. In the image, one can see a clear maximum that corresponds to the position of the dipole antenna. On the left I show the frequency spectrum of the time-series at the maximum power pixel. White Gaussian noise is added to the signal to mimic a more realistic signal-to-noise-ratio. The signal emitted by the dipole is clearly visible as the high power peak in the frequency spectrum.

2602 FSCD Beamforming Simulations

2603 Locust simulations of the FSCD are used to generate simulated CRES signal data to
 2604 perform beamforming reconstruction studies. As mentioned in the previous section,
 2605 the beamforming procedure beings by specifying a set of beamforming positions and
 2606 corresponding beamforming shifts. The beamforming positions form a grid that covers
 2607 the region of interest. There are effectively an infinite number of ways to specify the
 2608 grid positions, however, uniform square grids are the most commonly used due to their
 2609 simplicity. In the actual experiment the number and pattern of beamforming positions
 2610 would be optimized to cover the most important regions of the trap volume, which
 2611 maximizes detection efficiency and minimizes superfluous calculations.

2612 The beamforming grids used for signal reconstruction with the FSCD consist of a set
 2613 of points that cover the two-dimensional plane formed by the perimeter of the antenna
 2614 array. The axial dimension is left out because electrons are treated as if they occupy only
 2615 their average axial position, which corresponds to the center of the magnetic trap. This
 2616 treatment is valid since it is impossible to resolve the axial position of the electron as a
 2617 function of time due to the rapid oscillation frequencies of trapped electrons.

2618 After beamforming, a summed time-series is obtained for each beamforming position
 2619 that can be check for a signal using a detection algorithm. A beamforming image is

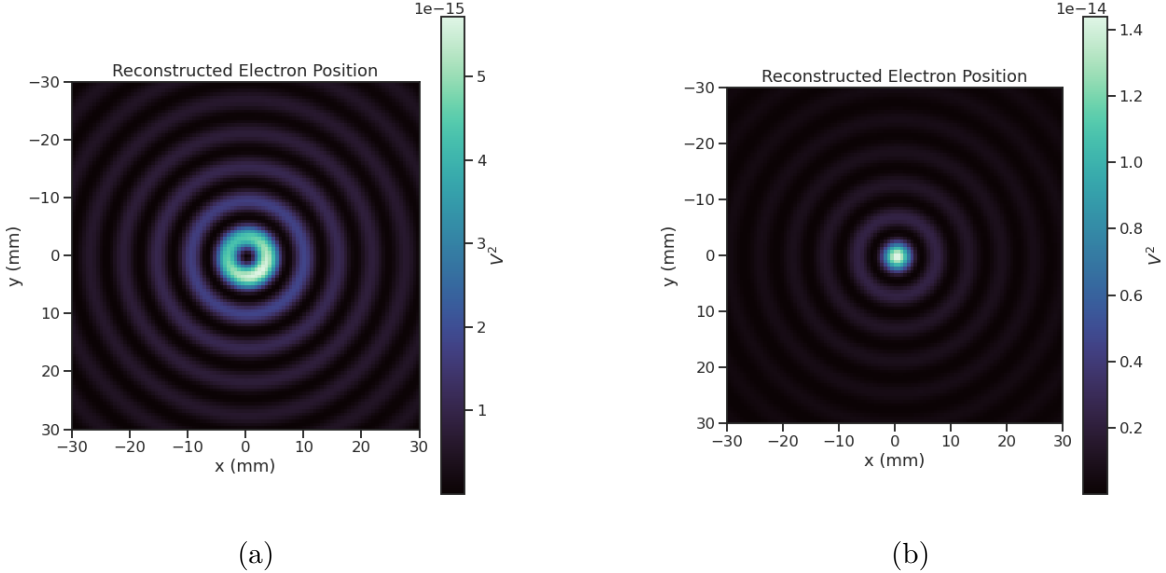


Figure 4.11. Beamforming images visualizing the reconstruction of an electron without (a) and with (b) the cyclotron phase correction. The images were generated using data from Locust simulations. The cyclotron phase refers to a phase offset equal to the relative azimuthal position of an antenna in the array. This phase offset is caused by the circular electron orbit and must be corrected for during reconstruction.

2620 a visualization method that is equivalent to arranging the beamforming grid points
 2621 according to their physical locations. Each pixel in the image corresponds to a summed
 2622 time-series obtained for a digital beamforming position, and the image is obtained taking
 2623 the time-averaged power at every pixel(see Figure 4.11).

2624 If only of the spatial beamforming phase component from Equation 4.20 is used, then
 2625 the resulting image contains a ring-shaped feature centered on the position of the electron
 2626 (see Figure 4.11a). The origin of this shape is an additional phase offset particular to
 2627 a cyclotron radiation source. The circular cyclotron orbitm introduces a relative phase
 2628 offset to the electric fields equal to the azimuthal position of the field measurement point.
 2629 Therefore, two antennas, one located at an azimuthal position of 0° and another located
 2630 at an azimuthal position of 90° , will recieve CRES signals out of phase by 90° , which is
 2631 the difference in their azimuthal positions. This phase offset can be corrected by adding
 2632 an additional term to the beamforming phase equation that is equal to the azimuthal
 2633 position of the antenna relative to the electron,

$$\phi_i[n] = \frac{2\pi d_i[n]}{\lambda} + \Delta\varphi_i[n], \quad (4.23)$$

2634 where $\Delta\varphi_i$ is difference between the azimuthal position of the electron and the i -th

2635 antenna channel. Using the updated beamforming phases changes the ring feature into
 2636 the expected Bessel peak whose maximum corresponds to the position of the electron.
 2637 Including this cyclotron phase correction significantly improves the signal detection and
 2638 reconstruction capabilities of beamforming by more than doubling the summed signal
 2639 power and shrinking the beamforming maxima feature size.

2640 The beamforming image examples in Figure 4.11 were produced using an electron
 2641 located on the central axis of the magnetic trap, which do not experience ∇B -drifts.
 2642 However, electrons produced at non-zero radial position the beamforming phases must
 2643 be made time-dependent to track the position of the electron's guiding center over
 2644 time. Without this correction the ∇B -drift causes the electron to move away from the
 2645 beamforming position, which effectively spreads the cyclotron radiation power over a
 wider area in the beamforming image (see Figure 4.12). This effect significantly reduces

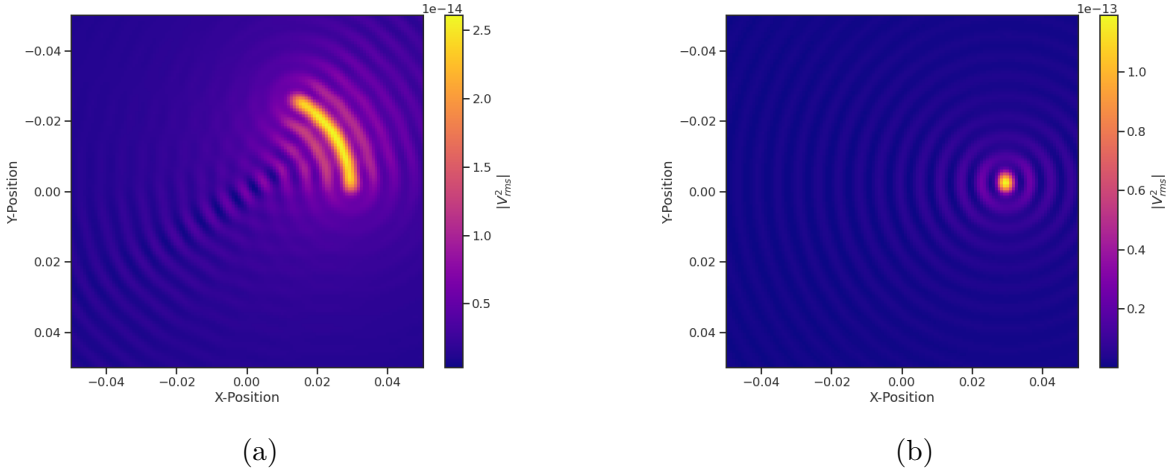


Figure 4.12. Beamforming images visualizing the reconstruction of an electron located off the central axis of the FSCD trap. In (a) beamforming is being performed without the ∇B -drift correction, and in (b) it is included.

2646
 2647 the power of the beamforming maxima and increases the size of the beamforming features,
 2648 simultaneously harming detection efficiency and position reconstruction.

2649 The ∇B -drift correction simply adds a circular time-dependence to the beamforming
 2650 positions as a function of time,

$$r[n] = r_0 \quad (4.24)$$

$$\varphi[n] = \varphi_0 + \omega_{\nabla B} t[n], \quad (4.25)$$

2651 where $\omega_{\nabla B}$ is the drift frequency and $t[n]$ is the time vector. In the ideal case the ∇B -drift

frequencies from Figure 4.2 for the correct pitch angle and radial position would be used,
 however, it is not possible to know the electron's pitch angle a priori. In principle, one
 could perform multiple beamforming summations for a given beamforming position using
 different drift frequencies and choose the one that maximizes the summed power, but
 this approach leads to a huge computational burden that would be impractical for a
 real FSCD experiment. A compromise is to use an average value of $\omega_{\nabla B}$ obtained by
 averaging over the drift frequencies for electrons of different pitch angle at a particular
 radius. This approach keeps the computational cost of time-dependent beamforming to a
 minimum while still providing a significant increase in the detection efficiency of digital
 beamforming.

Signal Detection with Beamforming and a Power Threshold

Up to this point I have neglected a specific discussion of how digital beamforming is used
 for signal detection and reconstruction. Because, strictly speaking, digital beamforming
 consists only of the phased summation of the array signals and cannot be used alone for
 signal detection. The example beamforming images shown in Figure 4.11 and Figure 4.12
 were produced using simulated data that contained no noise, which significantly degrades
 the utility of analyzing the beamforming images for signal detection and reconstruction.

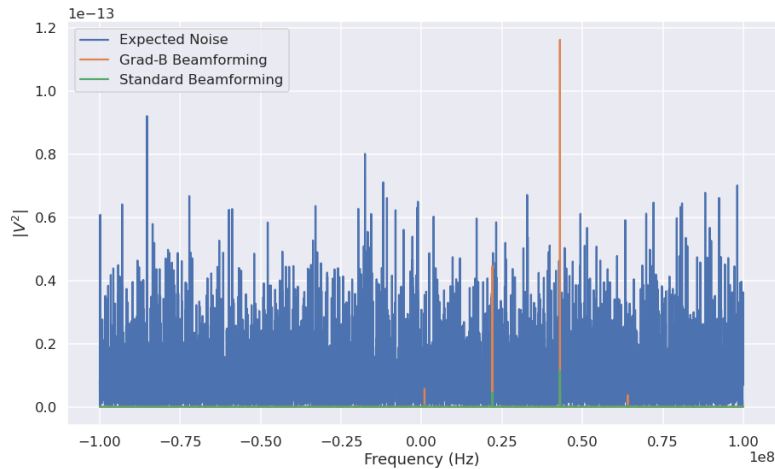


Figure 4.13. A plot of a typical frequency spectrum obtained by applying a Fourier transform to the time-series obtained from beamforming. The frequency spectra are plotted without noise on top of an example of a typical noise spectrum to visualize a realistic signal-to-noise ratio. In the example, without beamforming it would not be possible to detect anything since the signal amplitudes would be reduced by a factor of sixty relative to the noise. Additionally, it is clear the ∇B -drift correction is needed to detect this electron in the presence of noise.

2669 In Project 8, digital beamforming as a detection algorithm is understood to mean
 2670 digital beamforming plus a power or amplitude threshold placed on the frequency
 2671 spectrum obtained by applying a fast Fourier transform (FFT) to the summed time-series
 2672 (see Figure 4.13). This approach is similar to the time-frequency spectrogram analysis
 2673 employed in Phase I and II. However, it is possible to use any signal detection algorithm
 2674 after beamforming. In Section 4.4 I analyze the signal detection performance of the
 2675 power threshold approach in detail.

2676 Without a reconstruction technique that coherently combines the signals from the
 2677 full antenna the ability to detect CRES signals is drastically reduced (see Figure 4.13).
 2678 Because the CRES signals are in-phase at the correct beamforming position the summed
 2679 power increases as a function of N^2 compared to a single antenna channel, where N is
 2680 the number of antennas. It is true that the noise power is also increased by beamforming,
 2681 but, because the noise is incoherent, its power only increases linearly. Consequently, the
 2682 SNR of the CRES signal increases linearly with the number of antennas, which greatly
 2683 improves detection efficiency compared to using only the information in a single antenna.

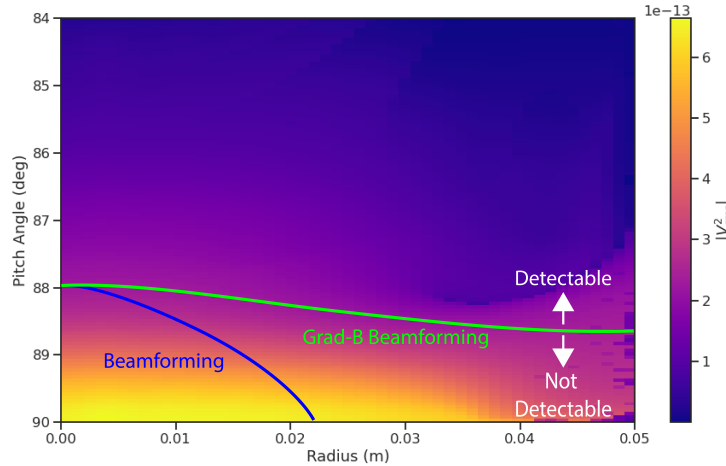


Figure 4.14. A plot of the total signal power received by the FSCD array from trapped electrons with different radial positions and pitch angles generated using Locust simulations. The lines on the plot indicate a 10 dB detection threshold above the mean value of the noise in the frequency spectrum. With static beamforming electrons with radial positions larger than about two centimeters are undetectable due to the change in the electron's position over time causing losses from beamforming phase mismatch. This is corrected by including ∇B -drift frequencies in the beamforming phases. Both beamforming techniques fail to detect electrons below $\approx 88.0^\circ$, since these signals are composed of several relatively weak sidebands that are comparable to the noise.

2684 The power threshold detection algorithm searches for high-power frequency bins that

2685 should correspond to a frequency component of the CRES signal. In order to prevent
 2686 random noise fluctuations from being mistaken as CRES signals the power threshold
 2687 must be set high enough so that it is unlikely that random noise could be responsible. A
 2688 consequence of this is that many electrons that can be trapped will go undetected because
 2689 the modulation caused by axial oscillations leads to the cyclotron carrier power to falling
 2690 below the decision threshold. The time-dependent beamforming used to correct for the
 2691 ∇B -drift increases the volume of the magnetic trap where electrons can be detected,
 2692 but it is ineffective at increasing the range of detectable pitch angles (see Figure 4.14).
 2693 Fundamentally, this is because the power threshold only uses a fraction of the signal
 2694 power to detect electrons and ignores the power present in the frequency sidebands. In
 2695 the subsequent sections I examine two other signal detection algorithms that seek to
 2696 improve the detection efficiency of the FSCD by utilizing the more of the signal shape to
 2697 compute the detection test statistics.

2698 **4.3.2 Matched Filtering**

2699 **Introduction to Matched Filtering**

2700 The problem of CRES signal detection is the problem of detecting a signal buried in
 2701 WGN, which has been examined at great depth in the signal processing literature [73].
 2702 For a fully known signal in WGN the optimal detector is the matched filter, which means
 2703 that it achieves the highest true positive rate for a fixed rate of false positives.

2704 The matched filter test statistic is calculated by taking the inner product of the data
 2705 with the matched filter template

$$\mathcal{T} = \left| \sum_n h^\dagger[n] y[n] \right|, \quad (4.26)$$

2706 where $h[n]$ is the matched filter template and $y[n]$ is the data. The matched filter test
 2707 statistic defines a binary hypothesis test in which the data vector is assumed to be an
 2708 instance of two possible data classes. By setting a decision threshold on the value of \mathcal{T} ,
 2709 one can classify a given data vector as belonging to two distinct hypotheses. Under the
 2710 first hypothesis the data is composed of pure WGN, and under the second hypothesis
 2711 the data is composed of the known signal with additive WGN.

2712 The matched filter template is obtained by rescaling the known signal in the following

2713 way

$$h[n] = \frac{x[n]}{\sqrt{\tau \sum_n x^\dagger[n]x[n]}}, \quad (4.27)$$

2714 where τ is the variance of the WGN and $x[n]$ is the known signal. Strictly speaking,
2715 Equation 4.27 is only true for noise with a diagonal covariance matrix, which is assumed
2716 to be true for the FSCD. Defining the matched filter templates in this way guarantees
2717 that the expectation value of \mathcal{T} is equal to one when the data contains only noise, which
2718 is the standard matched filter normalization.

2719 Although matched filters are canonically formulated in terms of a perfectly known
2720 signal, it is possible to apply the matched filter technique with imperfect information
2721 provided the signal is deterministic. From the discussion of CRES simulation tools (see
2722 Section 4.2) it was shown that the shape of CRES signals are completely determined
2723 by the initial parameters of the electron. The random collisions with background gas
2724 molecules, which cause the formation of signal tracks, are the only stochastic component
2725 of the CRES event after the initial beta-decay. Therefore, a matched filter can be used for
2726 the detection of CRES signal tracks between scattering events, which are fully determined
2727 by the initial parameters of the electron.

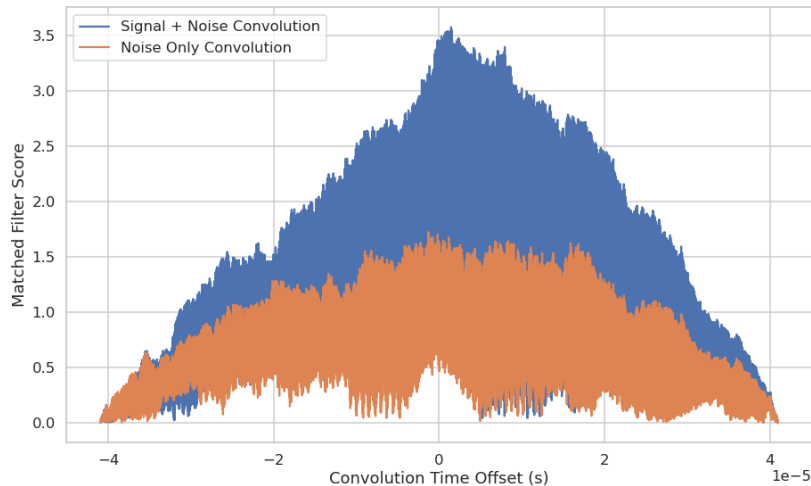


Figure 4.15. Example of a convolution of a CRES signal template with a segment of noisy data. A simulated CRES signal was simulated using Locust and normalized to create a matched filter template. When this template is convolved with noisy data the contains the matching signal the convolution output increases dramatically compared to data with only noise. The decreasing convolution output as the time offset of the convolution increases is caused by zero-padding of the data and template.

2728 The matched filter test statistic for CRES signals is a modified version of Equation

2729 4.26

$$\mathcal{T} = \max_{\mathbf{h}, m} |\mathbf{h} * \mathbf{y}| = \max_{\mathbf{h}, m} \left| \sum_k h^\dagger[k] x[m - k] \right|, \quad (4.28)$$

2730 where the matched filter inner product has been replaced with a convolution operation
2731 and a maximization over the template and convolution delay (m). Replacing the inner
2732 product with a convolution accounts for the fact that the start time of the CRES signal is
2733 now an unknown parameter, in addition, a maximization of the matched filter convolution
2734 is performed over a number of different templates. Because the shape of the signal is
2735 unknown, a range of different signal shapes, called a template bank, must be checked
2736 using an exhaustive search.

2737 The template bank approach, while powerful, can become computationally intractable.
2738 Specifically, the time-domain convolution specified by Equation 4.28 is particularly
2739 computationally intensive and is a major barrier towards the implementation of a
2740 matched filter for signal detection in an experiment like the FSCD. This can be avoided
2741 by using the convolution theorem to replace the time-domain convolution with an inner
2742 product in the frequency domain.

2743 The convolution theorem states that

$$\mathbf{f} * \mathbf{g} = \mathcal{F}^{-1}(\mathbf{F} \cdot \mathbf{G}) \quad (4.29)$$

2744 where \mathbf{f} and \mathbf{g} are discretely sampled time-series, \mathbf{F} and \mathbf{G} are the respective discrete
2745 Fourier transforms, and \mathcal{F}^{-1} is the inverse discrete Fourier transform operator. The
2746 convolution theorem allows us to perform the matched filter convolution by first com-
2747 puting the Fourier transform of the template and data, then performing a point-wise
2748 multiplication of the two frequency series, and finally performing the inverse Fourier
2749 transform to obtain the convolution output. Because discrete Fourier transforms can be
2750 performed extremely efficiently, the convolution theorem is almost always used in lieu of
2751 directly computing the convolution.

2752 One thing to note here is that the convolution theorem for discrete sequences shown
2753 here, is technically valid only for circular convolutions, which is not directly specified
2754 in Equation 4.28. However, because typical CRES track lengths are much longer than
2755 the Fourier analysis window and the frequency chirp rates are small compared to the
2756 time-slice duration, it is safe to use circular convolutions to evaluate matched filter scores
2757 for CRES signals, which allows one to apply the convolution theorem to compute matched
2758 filter scores for the FSCD.

2759 **Matched Filter Analysis of the FSCD**

2760 Since the matched filter is the optimal signal detection approach, it provides the ultimate
2761 upper bounds on signal detection. This makes it a useful algorithm for assessing the
2762 upper bounds on neutrino mass sensitivity for the FSCD, since it indicates the best
2763 possible detection efficiency achievable for that experiment configuration. The standard
2764 approach to performing these studies involves generating numerous simulated electron
2765 signals that span the kinematic parameter space of electrons.

2766 To limit the number of simulations required to evaluate the detection efficiency,
2767 the standard approach is to fix the starting axial position, starting azimuthal position,
2768 starting direction of the perpendicular component of the electron’s momentum, and event
2769 start time. This reduces the dimensionality of the simulated parameter space to three
2770 parameters — the starting radial position, starting kinetic energy, and starting pitch
2771 angle. The fixed variables are nuisance parameters, which do not affect the detection
2772 efficiency estimates for the FSCD design, because they simply introduce overall phase
2773 offsets that can be marginalized during the calculation of the matched filter score. Across
2774 radial position, kinetic energy, and pitch angle one defines a regular grid of parameters
2775 and uses Locust to simulate the corresponding signals (see Figure 4.16). This grid of
2776 simulated signals is used to estimate detection efficiency by calculating the detection
2777 probability of a randomly parameterized signal using the grid as a set of matched filter
2778 templates (see Section 4.4).

2779 The matched filter approach can also be used to estimate the achievable energy
2780 resolution of the experiment by using a dense grid of templates generated with parameters
2781 close to the unknown signal (see figure 4.17). Because matched filter templates with similar
2782 parameters have closely matching signal shapes, templates with incorrect parameters can
2783 have nearly identical matched filter scores as the correct template. Since only one sample
2784 of noise is included in a sample of real data, one cannot guarantee that the template
2785 with the maximum score corresponds to the ground truth parameters of the signal. This
2786 introduces uncertainty into the signal parameter estimation that manifests as an energy
2787 broadening. Dense grids of matched filter templates allow one to quantify this broadening
2788 by analyzing the parameter space of templates with matched filter scores close to the
2789 ground truth. This approach is analogous to maximum likelihood estimation and is one
2790 key component of a complete sensitivity analysis for an antenna array CRES experiment.

2791 A figure of merit that summarizes the performance of a matched filter template
2792 bank at signal detection is the mean match, which is defined as the average ratio of the
2793 highest matched filter score for a random signal to the matched filter score for a perfectly

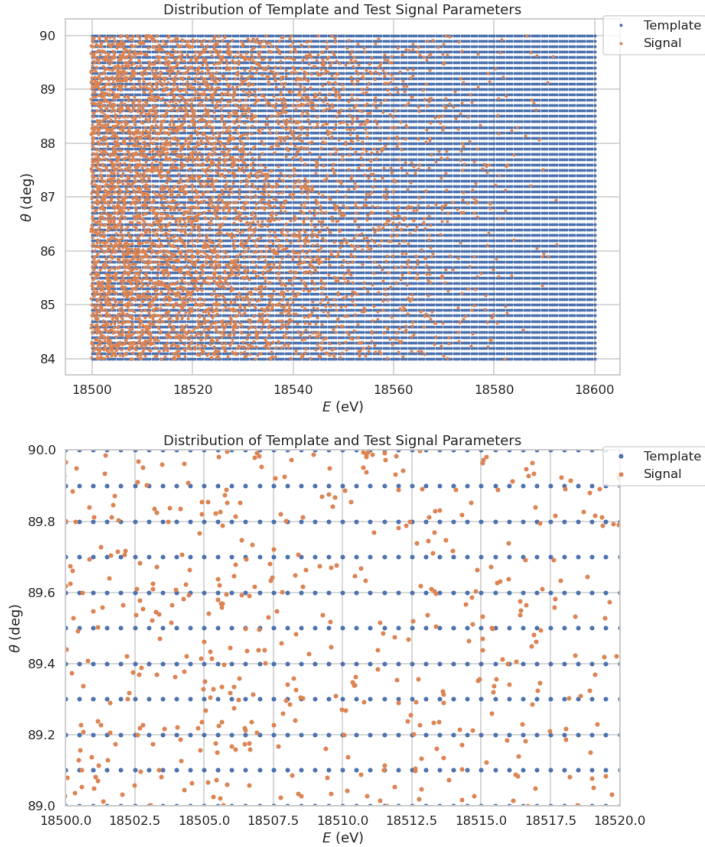


Figure 4.16. An example two-dimensional parameter distribution of a matched filter template bank and random test signals. θ refers to the pitch angle of the electron and E is the kinetic energy. The template bank forms a regular grid of in pitch angle and energy, whereas, the test signals are uniformly distributed in pitch angle and follow the tritium beta-decay kinetic energy distribution. This is why there are fewer test signals at higher energies. The need for high match across the full parameter space prevents one from reducing the density of templates in this low activity region. A zoomed in version of the template bank illustrates the relative density of templates and signals needed for match $> 90\%$.

2794 matching template. In equation form this is

$$\text{Match} \equiv \Gamma = \frac{\mathcal{T}_{\text{best}}}{\mathcal{T}_{\text{ideal}}}, \quad (4.30)$$

2795 where $\mathcal{T}_{\text{best}}$ is the matched filter score of the best fitting template in the bank and $\mathcal{T}_{\text{ideal}}$
 2796 is the hypothetical score one would measure if the signal perfectly matched the template.
 2797 Generally, one desires an average match as close to unity as possible. The mean match is
 2798 typically an exponential function of the number of templates in the template bank (see
 2799 Figure 4.18)..

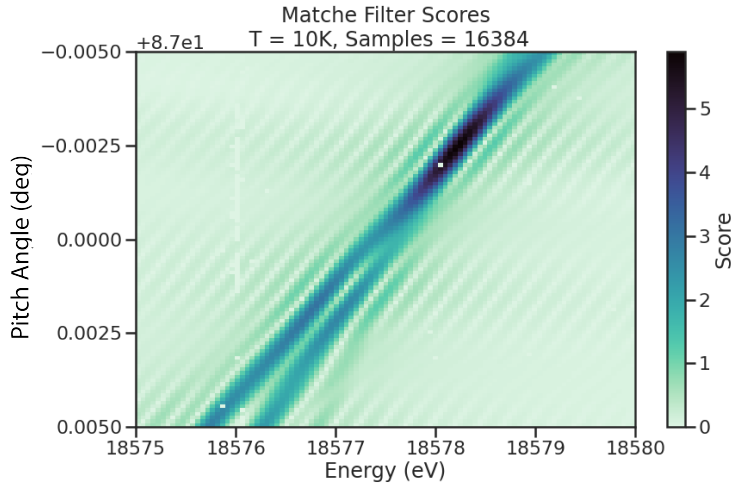


Figure 4.17. The matched filter scores of a dense grid of templates in pitch angle energy space. Dense template grids allow one to estimate the kinetic energy of the electron by identifying the best matching template. The uncertainty on this value is proportional to the space of templates that also match the test signal well. In the worst case matched filter templates can be completely degenerate where templates with different parameters match a signal with equal likelihood.

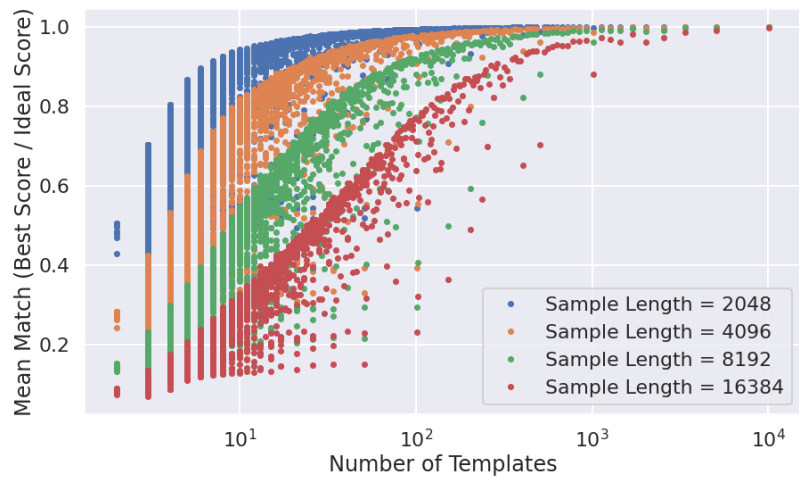


Figure 4.18. The mean match of the dense template grid shown in Figure 4.17 for different numbers of templates. Grids of different sizes were obtained by decimating a dense grid of templates and the average match for each grid was computed using the same set of randomly distributed test signals. Plotting the mean match against the size of the grid allows one to visualize the exponential relationship between match and template bank size. The noise in each curve is caused by sampling effects from the decimation algorithm. In general, longer templates are harder to match than shorter templates.

2800 The exponential relationship between match and template bank size manifests for
 2801 dense and sparse template grids. Sparse template grids are used for signal detection when
 2802 no prior information on the signal is available, whereas, dense templates grids are more
 2803 useful for parameter estimation. The mean match value directly influences the detection
 2804 efficiency of the template bank, but due to the exponential scaling, achieving a high
 2805 average match at the detection stage can easily overwhelm the available computational
 2806 resources.

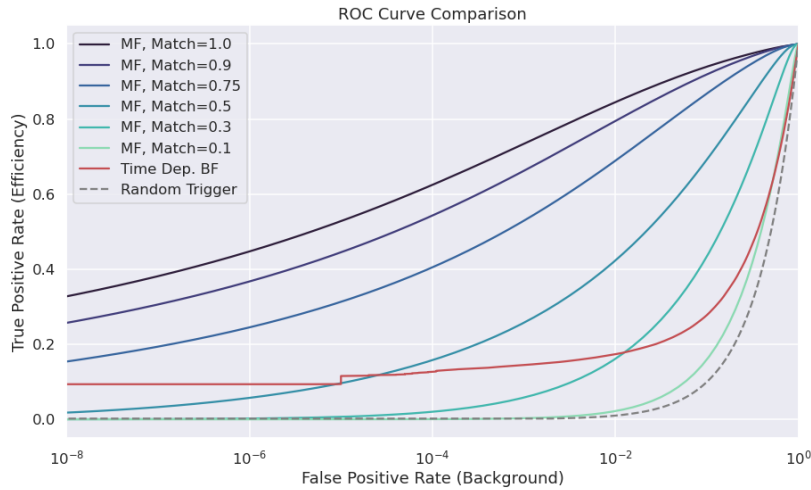


Figure 4.19. Matched filter template bank ROC curves as a function of mean match. One can see that for low match a matched filter is on average worse than the more straight forward beamforming detection approach.

2807 The effect of match on the detection efficiency of the matched filter template bank can
 2808 be summarized using the ROC curve (see Figure 4.19). A single ROC curve is obtained
 2809 by averaging over the PDFs that describe the detection probabilities of each individual
 2810 template.

2811 The distribution that describes the matched filter score under the signal hypothesis is
 2812 a Rician distribution, which has a mean value equal to the matched filter score multiplied
 2813 by the match ratio (see Section 4.4). Alternatively, the distribution of the matched
 2814 filter score when there is no signal in the data follows a Rayleigh distribution, which is
 2815 equivalent to a Rician distribution with zero mean. The matched filter score for each
 2816 template in the template bank is described by a separate Rician distribution. Therefore,
 2817 one way to model detection probability for a given signal is to average across all matched
 2818 filter distributions in the template bank to obtain a single distribution that describes the
 2819 statistical behavior of the matched filter score.

2820 A different way to visualize the detection performance for each algorithm is to specify
 2821 a minimum acceptable false positive rate at the trigger level. This is equivalent to
 2822 specifying a minimum threshold on the value of the matched filter score or the size of a
 2823 frequency peak for a beamforming power threshold trigger. One can then draw regions
 2824 of detectable signals as a function of the electron's pitch angle and radial position (see
 Figure 4.20). A kinetic energy shift is equivalent to an overall frequency shift of the

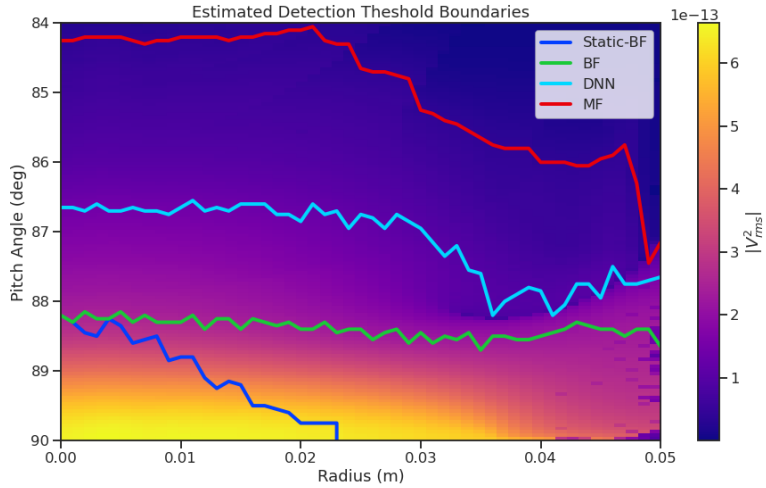


Figure 4.20. Boundaries of detectable electrons in pitch angle kinetic energy space for a series of different signal detection algorithms. A detectable signal is defined as a signal that is above a consistent decision with at least 50% probability. This non-rigorous treatment of detection probability is primarily useful for the visualization the relative increases in detection performance provided by the different algorithms. The static beamforming (Static-BF) algorithm is the digital beamforming algorithm introduced above without the ∇B -drift correction. The DNN algorithm refers to a convolutional neural network classifier trained to detect CRES signals (see Section 4.3.3).

2825
 2826 signal and should have no effect on the detection probability assuming sufficient density
 2827 of matched filter templates in the energy dimension. A electron is declared "detectable"
 2828 for the regions in Figure 4.20 if the signal has at least 50% probability of falling above the
 2829 decision threshold of the respective classifier. One can see that the parameter space of
 2830 detectable signals is greatly expanded beyond the beamforming power threshold trigger
 2831 with a matched filter (MF) or deep neural network (DNN) (see Section 4.3.3). Plots such
 2832 as Figure 4.20 are useful for visualization, but, since the handling of detection likelihood
 2833 is not sufficiently rigorous, the detection probability boundaries are not well-suited to
 2834 sensitivity estimates.

2835 **Optimized Matched Filtering Implementation for the FSCD**

2836 The biggest practical obstacle to the implementation of a matched filter template bank is
2837 the computational cost associated with exhaustively calculating the matched filter scores,
2838 therefore, one must employ several optimizations in a practical setting.

2839 Computing a matched filter score requires the convolution of two vectors, which can
2840 be performed very efficiently by computers if the convolution theorem and fast Fourier
2841 transforms (FFT) are utilized. Furthermore, one can apply digital beamforming as a
2842 pre-processing step to reduce the dimensionality of the data before the matched filter.
2843 In order to understand the relative gain in computational efficiency offered by these
2844 optimizations I analyze the total number of floating-point operations (FLOP) of several
2845 matched filter implementations in big O notation that utilize different combinations of
2846 optimizations.

2847 A direct implementation of a matched filter as specified by Equation 4.28 involves
2848 the convolution of N_{ch} signals of length N_s with template signals of length N_t . The
2849 FLOPs of the various matched filter implementations on a per-template basis will be
2850 used as a consistent metric, since each implementation scales linearly with the number of
2851 templates. The direct convolution approach to matched filtering costs

$$O(N_{\text{ch}}) \times O(N_s \times N_t) \quad (4.31)$$

2852 FLOP per-template, whose cost is dominated by the $O(M \times N)$ convolution operation.

2853 The computational cost of the direct matched filter approach can be significantly
2854 reduced by exploiting the convolution theorem and FFT algorithms. By restricting oneself
2855 to signals and templates that contain equal numbers of samples, the convolution can be
2856 calculated by Fourier transforming both vectors, performing the point-wise multiplication,
2857 and taking the inverse Fourier transform to obtain the convolution result. The FFT
2858 algorithm is able to compute the Fourier transform utilizing only $O(N \log N)$ operations.
2859 This optimization results in a computational cost per-template of

$$O(N_{\text{ch}}) \times O(N_s \log N_s) \quad (4.32)$$

2860 A typical signal vector in the FSCD contains $O(10^4)$ samples in which case the FFT
2861 reduces the computational cost of the matched filter by a factor of $O(10^3)$. This large
2862 reduction in computational cost implies that a direct implementation of a matched filter
2863 is completely infeasible in the FSCD due to resource constraints.

2864 Rather than relying solely on the matched filter it is tempting to consider using
 2865 digital beamforming as an initial step in the signal reconstruction for the purposes of
 2866 data reduction. The primary motivation is to reduce the dimensionality of the data by
 2867 a factor of N_{ch} by combining the array outputs coherently into a single channel. One
 2868 can view the beamforming operation as a partial matched filter, in the sense that the
 2869 matched filter convolution contains the beamforming phased summation along with a
 2870 prediction of the signal shape. By separating beamforming from the signal shape one
 2871 hopes to reduce the overall computational cost by effectively shrinking the number of
 2872 templates and reducing the number of operations required to check each one.

2873 The nature of this optimization requires that one account for the number of templates
 2874 used for pure matched filtering versus the hybrid approach. To first order, the total
 2875 number of templates at the trigger stage is a product of the number of guesses for each
 2876 of the electron's parameters

$$N_T = N_E \times N_\theta \times N_r \times N_\varphi, \quad (4.33)$$

2877 where N_E is the number of kinetic energies, N_θ is the number of pitch angles, N_r is the
 2878 number of starting radial positions, and N_φ is the number of starting azimuthal positions.
 2879 The starting axial position and cyclotron motion phase are not necessary to include in
 2880 the template bank, since these parameters manifest themselves as the starting phase of
 2881 the signal, which is effectively marginalized when using a FFT to compute the matched
 2882 filter convolution. Therefore, the total number of operations required by a matched filter
 2883 to detect a signal in a segment of array data is on the order of

$$O(N_T) \times O(N_{\text{ch}}) \times O(N_s \log N_s) \quad (4.34)$$

2884 With the hybrid approach one removes spatial parameters from the template bank
 2885 by using beamforming to combine the array signals into a single channel. Beamforming
 2886 explicitly assumes a starting position, which allows one to use matched filter templates
 2887 that span the two-dimensional space of kinetic energy and pitch angle. The total
 2888 computational cost of the hybrid method is directly proportional to the number of
 2889 beamforming positions. For the time-dependent beamforming defined in Section 4.3.1,
 2890 the number of beamforming positions is given by

$$N_{\text{BF}} = N_r \times N_\varphi \times N_{\omega_{\nabla B}}, \quad (4.35)$$

2891 where N_r and N_φ are the same spatial parameters encountered in the pure matched
 2892 filter template bank and $N_{\omega_{\nabla B}}$ is the number of ∇B -drift frequency assumptions. If a
 2893 unique drift frequency is used for each pitch angle then the hybrid approach is effectively
 2894 equivalent to a pure matched filter in the number of operations. The key efficiency gain
 2895 of the hybrid approach is to exploit the relatively small differences in $\omega_{\nabla B}$ for electrons
 2896 of different pitch angles by using only a few average drift frequencies.

2897 The total number of operations for the hybrid approach can be expressed as a sum of
 2898 the operations required by the beamforming and matched filtering steps,

$$O(N_{BF}) \times O(N_{ch}N_s) + O(N_{BF}) \times O(N_E N_\theta) \times O(N_s \log N_s). \quad (4.36)$$

2900 The first product in the sum is the number of operations required by beamforming,
 2901 which is simply the number of beamforming points times the computational cost of the
 2902 beamforming matrix multiplication, and the second product is the computational cost
 2903 of matched filtering the summed signal generated by each beamforming position. To
 2904 compare this to pure matched filtering, one takes the ratio of Equations 4.34 and 4.36 to
 obtain

$$\Gamma_{BFMF} = \frac{O(N_{\omega_{\nabla B}})}{O(N_E N_\theta) \times O(\log N_s)} + \frac{O(N_{\omega_{\nabla B}})}{O(N_{ch})}. \quad (4.37)$$

2905 This expression can be simplified by observing that $O(N_E N_\theta) \times O(\log N_s) \gg O(N_{ch})$,
 2906 which means that the ratio of computational cost for the two methods can be reduced to

$$\Gamma_{BFMF} \approx \frac{O(N_{\omega_{\nabla B}})}{O(N_{ch})}. \quad (4.38)$$

2907 Limiting oneself to a number of estimated drift frequencies of $O(1)$, then it can be seen
 2908 that the estimated computational cost reduction of the hybrid approach is of $O(N_{ch})$.
 2909 This is a large reduction considering that the FSCD antenna array contains sixty antennas
 2910 in the baseline design.

2911 The main drawback of the hybrid approach is that the limited number of allowed
 2912 drift frequency guesses can lead to detection efficiency loss due to phase mismatch. The
 2913 degree of phase error from an incorrect drift frequency is proportional to the length of
 2914 the array data vector used by the signal detection algorithm. For signals with lengths
 2915 equal to the baseline FSCD Fourier analysis window of 8192 samples, typical phase errors
 2916 from using an average versus the exact ∇B -drift frequency are on the order of a few
 2917 percent in terms of the signal energy. This has a relatively small impact on the overall
 2918 detection efficiency, however, future experiments with antenna array CRES will want to

balance optimizations such as these during the design phase to keep experiment costs to a minimum while still achieving scientific goals.

Kinetic Energy and Pitch Angle Degeneracy

Accurate modeling of a matched filter requires one to consider the effects of mismatched signals and template, since this more accurately reflects the real-world usage of a matched filter. One way to study this is to use a signal grid to compute the matched filter scores between mismatched signals and templates and evaluate the matched filter scores under this scenario. What one finds when performing this analysis is that templates for signals with incorrect parameters can have matched filter scores that are indistinguishable from the matched filter score of the correct template (see Figure 4.21 and Figure 4.21).

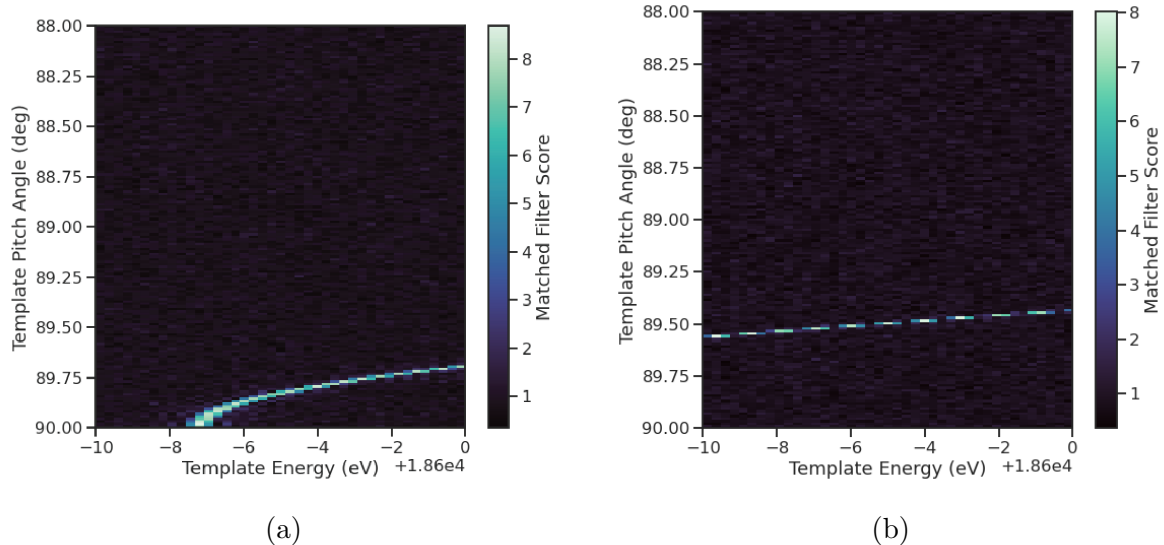


Figure 4.21. Two example illustrations of the correlation between kinetic energy and pitch angle imparted by the shape of the FSCD magnetic trap. The correlations manifest themselves as degeneracies in the matched filter score where multiple matched filter templates have the same matched filter for a particular signal. These degeneracies are a sign that the magnetic trap must be redesigned in order to break the correlation between pitch angle and kinetic energy.

This degeneracy in matched filter score is the result of correlations between the kinetic energy and pitch angle of the electron caused by the magnetic trap. These correlations are unacceptable since they greatly reduce the energy resolution of the experiment by causing electrons with specific kinetic energy to templates across a wide range of energies. It is important to emphasize that this degeneracy cannot be fixed by implementing a different signal reconstruction algorithm. As revealed by the matched filter scores the shapes of the signals for different parameters are identical. Resolving this degeneracy

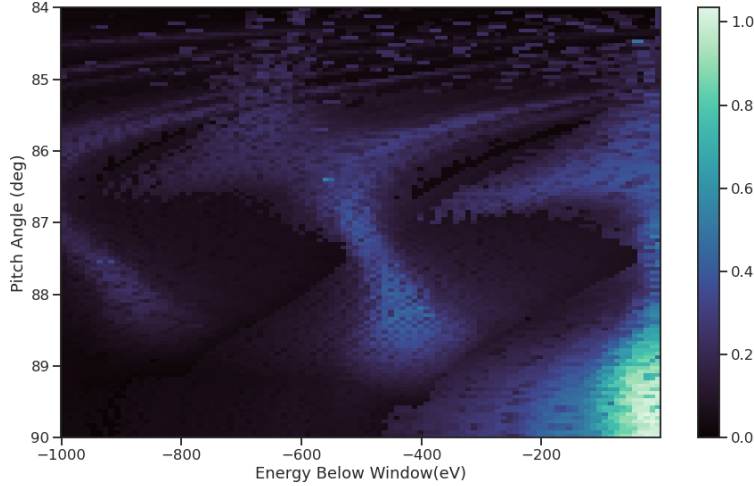


Figure 4.22. A visualization of the correlation between energy and pitch angle in the FSCD magnetic trap. The image is formed by computing the match of the best template from a grid consisting of pitch angles from 84 to 90 degrees in steps of 0.05 degrees, kinetic energies from 17574 to 18574 eV, located at 2 cm from the central axis, and simulated for a length of three FSCD time-slices. The signals used to compute the best matching template consisted of a grid from 84 to 90 degrees in steps of 0.05 degrees, kinetic energies from 18550 to 18575 eV in steps of 0.25 eV, located 2 cm from the central axis, and simulated for three FSCD time-slices. The colored regions of the plot show how well signals with lower energy can match those of higher energy for the FSCD magnetic trap, which is proportional to the achievable energy resolution of the FSCD design.

2936 between pitch angle and energy requires the design of a new magnetic trap with steeper
 2937 walls so that the average magnetic field experienced by an electron is less dependent on
 2938 pitch angle.

2939 **4.3.3 Machine Learning**

2940 Machine learning is a broad field of research [76] that has been particularly transformative
 2941 in the recent past. In this Section I provide a brief introduction to some concepts and
 2942 techniques of machine learning that were applied to CRES signal detection in my
 2943 dissertation.

2944 **Introduction to Machine Learning**

2945 Digitization of the FSCD antenna array generates large amounts of data that must
 2946 be rapidly processed for real-time signal detection and reconstruction. While digital
 2947 beamforming combined with a power threshold is relatively computationally inexpensive,

it is ineffective at detecting CRES signal with small pitch angles, since it relies on a visible frequency peak above the noise. On the other hand, a matched filter is able to detect signals with a significantly larger range of parameters, however, the exhaustive search of matched filter templates can be computationally expensive. Machine learning based triggering algorithms have been used successfully in many high-energy physics experiments [77], and recently have shown success in the detection of gravitational wave signals [78, 79] in place of more traditional matched filtering methods. The success of machine learning in these domains motivates the exploration of machine learning as a potential CRES signal detection algorithm.

Various approaches to machine learning are possible, but the one most important to the discussion here is the supervised learning approach. In supervised learning, one uses a differentiable model or function that is designed to map the input data to the appropriate label [76]. The data is represented as a multidimensional matrix of floating point values such as an image or a time-series, and the label is typically a class name such as signal or noise for classification problems, or a continuous value like kinetic energy for regression problems.

In supervised learning the model is trained to map from the data to the correct label by evaluating the output of the model using a training dataset consisting of a set of paired data and labels. To evaluate the difference between the model output and the correct label a loss function is used to quantify the error between the model prediction and the ground truth. For example, a common loss function in regression problems is the squared error loss function, which quantifies error using the squared difference between the model output and label.

Using the outputs of the loss function the next step in supervised learning is to compute the gradient of error with respect to the model parameters in a process called backpropagation. The gradients are used to update the model parameter values in order to minimize errors in the model predictions across the whole dataset. This loop is performed many times while randomly shuffling the dataset until the error converges to a minimum value at which point the training procedure has finished. It is standard practice to monitor the training procedure by evaluating the performance of the model using a separate validation dataset that matches the statistical distribution of the training data and to check the performance of the model after training using yet another dataset called the test dataset. These practices help to guard against overtraining which is a concern for models with many parameters.

2982 **Convolutional Neural Networks**

2983 A popular class of machine learning models are neural networks. A neural network is
2984 a function composed of a series of linear operations called layers, which take a piece of
2985 data typically represented as a matrix, multiply the elements of the data by a weight,
2986 and then sums these products to produce an output matrix. Neural networks composed
2987 of purely linear operations are unable to model complex non-linear behavior, therefore,
2988 non-linear activation functions are applied to the outputs of each of the layers to increase
2989 the ability of the neural network to model complex relationships between the data.

2990 Neural networks are typically composed of at least three layers, but with the present
2991 capabilities of computer hardware they typically contain much more than this. The first
2992 layer in a neural network is called the input layer, because it takes the data objects as
2993 input, and the last layer in a neural network is known as the output layer. The output
2994 layer is trained by machine learning to map the data an output label using the supervised
2995 learning procedure described in Section 4.3.3. Between the input and the output layer
2996 are typically several hidden layers that receive inputs from and transmit outputs to other
2997 layers in the neural network model. The term deep neural network (DNN) refers to those
2998 neural networks that have at least one hidden layer, which have proven to be extremely
2999 powerful tools for pattern recognition and function approximation.

3000 An important type of DNN are convolutional neural networks (CNN) that typically
3001 contain several layers which perform a convolution of the input with a set of filters. These
3002 convolution operations are typically accompanied by layers that attempt to down-sample
3003 the data along with the standard neural network activation functions. A standard CNN
3004 is composed of several convolutional layers at the beginning of the network and ends
3005 with a series of fully-connected neural network layers at the output. Intuitively, one
3006 can imagine that the convolutional layers are extracting features from the data that
3007 fully-connected layers use to perform the classification or regression task.

3008 **Deep Filtering for Signal Detection in the FSCD**

3009 CNNs have been extremely influential in the field of computer vision, particularly tasks
3010 such as image segmentation and classification, but have also been applied in numerous
3011 experimental physics contexts. Given the particular challenge posed by signal detection
3012 and reconstruction in the FSCD CNNs are an interesting choice for real-time signal
3013 detection, since this application requires both high efficiency and fast evaluation.

3014 In the machine learning paradigm, signal detection is a binary classification problem

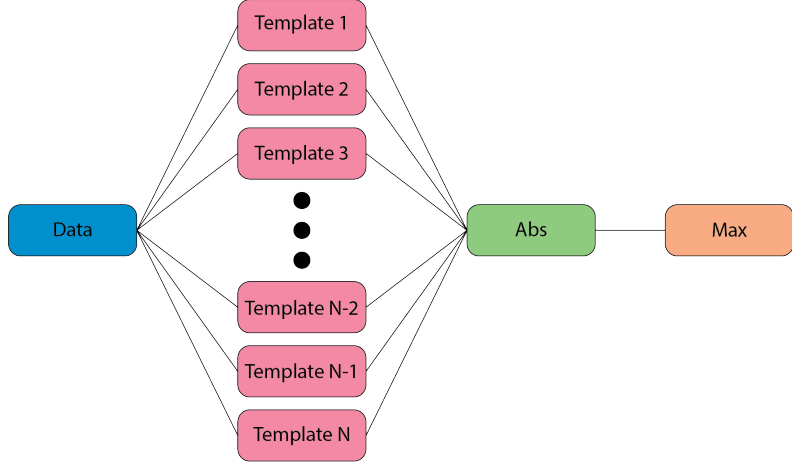


Figure 4.23. A representation of a matched filter template bank as a convolutional neural network. The network has a single layer composed of the templates, which act as convolutional filters. The activation of the neural network is an absolute value followed by a max operator.

3015 between the signal and noise data classes. My investigation focuses specifically on the
 3016 application of CNNs to signal detection in the FSCD, which is motivated by relatively
 3017 recent demonstrations of CNNs achieving classification accuracies for gravitational wave
 3018 time-series signals comparable to a matched filter template bank. In this framework
 3019 it is possible to interpret the matched filter as a type of CNN composed of a single
 3020 convolutional layer with the templates making up the layer filters (see Figure 4.23).
 3021 Since this neural network has no hidden layers, it is not a DNN, but one can attempt to
 3022 construct a proper CNN that attempts to reproduce the classification performance of the
 3023 matched filter network, which can be referred to as "deep filtering".

3024 The reason why deep filtering can be effective is that it may be possible to exploit
 3025 redundancies and correlations between templates, which allows one to perform signal
 3026 detection with similar accuracy but with fewer computations. This is relevant to real-time
 3027 detection scenarios like the FSCD experiment. In Section 4.4 I perform a detailed
 3028 comparison of the signal detection performance of a CNN to beamforming and a matched
 3029 filter template bank.

3030 Deep filtering is conceptually a simple technique. Similar to a matched filter template
 3031 bank, many simulated CRES signals are generated and used to train a model to distinguish
 3032 between signal and noise data (see Figure 4.24). To reduce the dimensionality of the
 3033 input FSCD data, a digital beamforming summation is applied to the raw time-series
 3034 data generated by Locust to compress the 60-channel data to a single time-series. CRES
 3035 signals have a sparse frequency representation and experiments training CNN's on time-
 3036 series and frequency-series data found that models trained on frequency spectrum data

3037 performed significantly better. Therefore, an FFT is applied to the summed time-series
 3038 before being normalized and fed to the classification model.

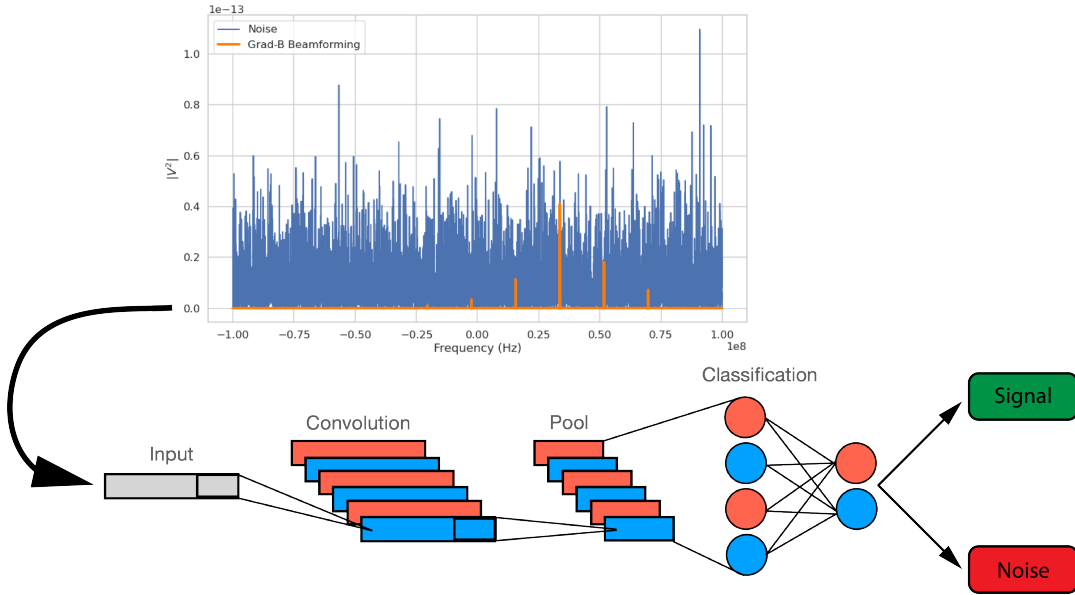


Figure 4.24. A graphical depiction of CRES signal detection using a CNN. A noisy segment of data is converted to a frequency series using digital beamforming and a FFT. The complex-valued frequency series is input into a trained CNN model that classifies the data as signal or noise using a decision threshold on the CNN output.

3039 The data used to train the model consists of an equal proportion of signal and noise
 3040 frequency spectra. Unique samples of WGN are generated and added to the signals during
 3041 training time to avoid have to pre-generate and store large samples of noise data. The
 3042 binary cross-entropy loss function combined with the ADAM optimizer proved effective
 3043 at training the models to classify CRES data. A simple hyperparameter optimization
 3044 was performed by manually tuning model, loss function, and optimizer parameters. The
 3045 model and training loops was implemented in python using the PyTorch deep learning
 3046 framework. Standard machine learning practices were followed when training the models,
 3047 such as overtraining monitoring using a validation dataset. Models were trained until the
 3048 training loss and accuracy converged and then evaluated using a separate test data set.

3049 The classification results of the test dataset are used to quantify the relationship
 3050 between the true positive rate and the false positive rate for the model. The true positive
 3051 rate is analogous to detection efficiency and the false positive rate is a potential source of
 3052 background in the detector. One can limit the rate of false positives using a sufficiently
 3053 high threshold on the model output at the cost of a lower detection efficiency (see Figure
 3054 4.25 and Figure 4.26). As expected, the performance of the model at signal classification

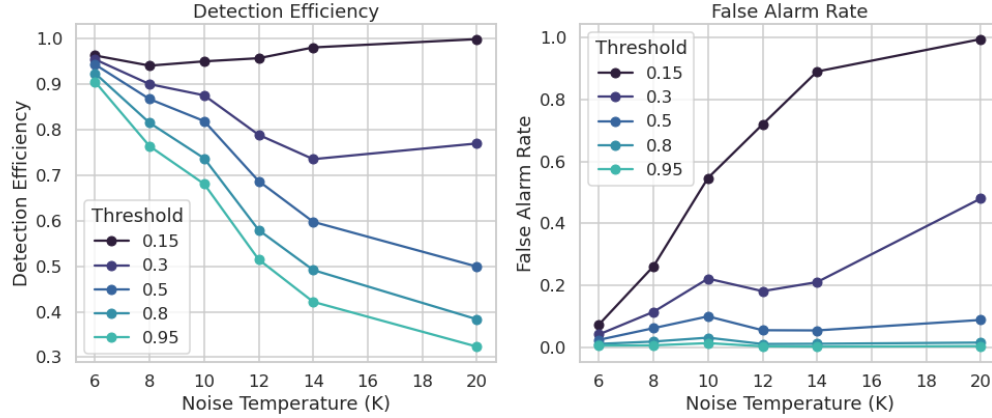


Figure 4.25. The detection efficiency and false alarm rate (false positive rate) as a function of the decision threshold for different values of the noise temperature. The model is trained to output a value close to one for data that contains a signal and outputs a value near zero when the data contains only noise. One sees that a lower decision threshold will have a high detection efficiency at the cost of a high rate of false alarms.

3055 is negatively effected the noise power, which is quantified by the noise temperature.

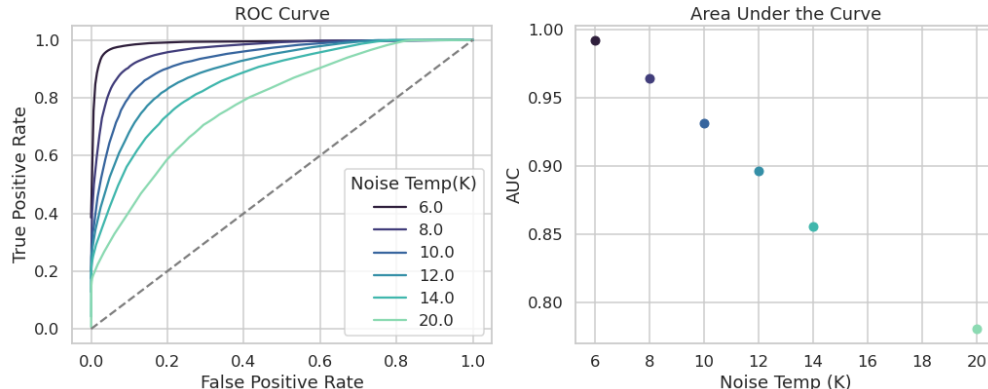


Figure 4.26. ROC curves for a CNN model classifying CRES signals. One can see that the area under the curve, which is a figure of merit that describes the performance of the classifier, is roughly linearly dependent with the noise temperature.

3056 4.4 Analysis of Signal Detection Algorithms for the FSCD

3057 This section contains an early version of the manuscript for the triggering paper prepared
 3058 for publication in JINST. I present a detailed analysis of the signal detection performance
 3059 of the three signal detection approaches discussed so far using a population of simulated

3060 CRES signals generated with Locust. The focus of the paper is on the performance of the
3061 signal detection algorithms for pitch angles below 88.5° where the beamforming power
3062 threshold is least effective.

3063 **4.4.1 Introduction**

3064 Cyclotron Radiation Emission Spectroscopy (CRES) is a technique for measuring the
3065 kinetic energies of charged particles by observing the frequency of the cyclotron radiation
3066 that is emitted as they travel through a magnetic field [40]. The Project 8 Collaboration
3067 is developing the CRES technique as a next-generation approach to tritium beta-decay
3068 endpoint spectroscopy for neutrino mass measurement. Recently, Project 8 has used
3069 CRES to perform the first ever tritium beta-decay energy spectrum and neutrino mass
3070 measurement [42, 43].

3071 Previous CRES measurements have utilized relatively small volumes of radiation source
3072 gas that are directly integrated with a waveguide transmission line, which propagates the
3073 cyclotron radiation emitted by magnetically trapped electrons to a cryogenic amplifier.
3074 While this technology has had demonstrable success, it is not a feasible option for scaling
3075 up to larger measurement volumes. In particular, the goal of the Project 8 Collaboration
3076 is to use CRES combined with atomic tritium to measure the neutrino mass with a
3077 40 meV sensitivity. Achieving this sensitivity goal will require a multi-cubic-meter scale
3078 measurement volume in order to obtain the required event statistics in the tritium
3079 beta-spectrum endpoint region; hence, there is a need for new techniques to enable large
3080 volume CRES measurements for future experiments.

3081 One approach is to surround a large volume with an array of antennas that together
3082 collect a portion of the cyclotron radiation emitted by trapped electrons [41, 80]. A
3083 promising design is an inward-facing uniform cylindrical array that surrounds the tritium
3084 containment volume. Increasing the size of the antenna array, by adding additional rings
3085 of antennas along the vertical axis, allows one to grow the experiment volume until a
3086 sufficient amount of tritium gas can be observed by the array. A challenging aspect of
3087 this approach is that the total radiated power emitted by an electron near the tritium
3088 spectrum endpoint is on the order of 1 fW or less in a 1 T magnetic field, which is then
3089 distributed among all antennas in the array. Because the CRES signal information is
3090 spread across the antenna array, detecting the presence of a CRES signal and determining
3091 the electron's kinetic energy requires reconstructing the entire array output over the
3092 course of the CRES event, posing a significant data acquisition and signal reconstruction
3093 challenge.

3094 Previous measurements with the CRES technique have utilized a threshold on the fre-
3095 quency spectrum formed from a segment of CRES time-series data. This algorithm relies
3096 on the detection of a frequency peak above the thermal noise background, which limits
3097 the kinematic parameter space of detectable electrons (see Section 4.4.2.2). Although a
3098 power threshold based classification was adequate for smaller detectors, improvements
3099 in detection efficiency are needed for better sensitivity to the neutrino mass. Better
3100 detection efficiency is possible by taking advantage of the deterministic CRES signal
3101 structure with a matched filter or machine learning based classifier [?]. In order to eval-
3102 uate the relative gains in detection efficiency that come from utilizing these algorithms for
3103 antennas, analytical models that describe the detection performance a power threshold
3104 and matched filter classifier are developed. In addition, a basic convolutional neural
3105 network (CNN) is implemented and tested as a first step towards the development of
3106 neural-network based classifiers for antenna array based CRES measurements. These
3107 results allow for a comparison between the estimated detection efficiencies of each of these
3108 methods, which are weighed against the associated computational costs for real-time
3109 applications.

3110 The outline of this paper is as follows. Section 4.4.2 is an overview of a prototyp-
3111 ical antenna array CRES experiment, and describes the approach to real-time signal
3112 identification. Section 4.5 develops models for the power threshold and matched filter
3113 algorithms and introduces the machine learning approach and CNN architecture. Section
3114 4.5.1 describes the process for generating simulated CRES signal data and the details of
3115 training the CNN. Finally, Section 4.5.2 compares the signal classification accuracy for
3116 the three approaches and discusses the relevant trade-offs in terms of detection efficiency
3117 and computational cost.

3118 **4.4.2 Signal Detection with Antenna Array CRES**

3119 **4.4.2.1 Antenna Array and Data Rate Estimates**

3120 In order to explore the potential of antenna array CRES for neutrino mass measurement,
3121 the Project 8 Collaboration has developed a conceptual design for a prototype antenna
3122 array CRES experiment [41, 80], called the Free-space CRES Demonstrator or FSCD (see
3123 Figure 4.27). The FSCD utilizes a single ring of antennas, which is the simplest form of a
3124 uniform cylindrical array configuration, to surround a radio-frequency (RF) transparent
3125 tritium gas vessel. A prototype version of this antenna array has been built and tested
3126 by the Project 8 collaboration [44] to validate simulations of the array radiation pattern

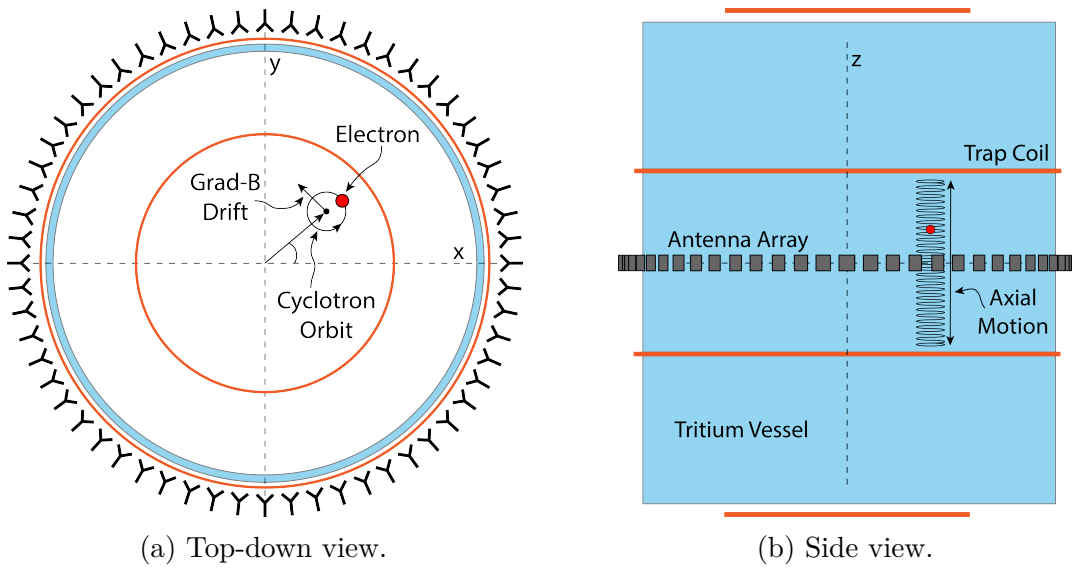


Figure 4.27. An illustration of the conceptual design for an antenna array CRES tritium beta-decay spectrum measurement. The antenna array geometry consists of a 20 cm interior diameter with 60 independent antenna channels arranged evenly around the circumference. The nominal antenna design is sensitive to radiation in the frequency range of 25-26 GHz, which corresponds to the cyclotron frequency of electrons emitted near the tritium beta-spectrum endpoint in a 0.96 T magnetic field. The array is located at the center of the magnetic trap produced by a set of current-carrying coils. The nominal magnetic trap design is capable of trapping electrons up to 5 cm away from the central axis of the array and traps electrons within an approximately 6 cm long axial region centered on the antenna array.

3127 and beamforming algorithms [?]. In the FSCD the antenna array is positioned at the
 3128 center of the magnetic trap formed by a set of electromagnetic coils, which create a local
 3129 minimum in the magnetic field with flat central region and steep walls in the radial and
 3130 axial directions.

3131 When an electron is trapped its motion consists of three primary components. The
 3132 component with the highest frequency is the cyclotron orbit whose frequency is determined
 3133 by the size of the background magnetic field. The FSCD design assumes a background
 3134 magnetic field value of approximately 0.96 T, which results in cyclotron frequencies
 3135 for electrons with kinetic energies near the tritium beta-spectrum endpoint of 26 GHz.
 3136 The component with the next highest frequency is the axial oscillation experienced by
 3137 electrons with pitch angles⁴ of less than 90° [63]. The flat region of the FSCD magnetic
 3138 trap extends approximately 3 cm above and below the antenna array plane causing
 3139 electrons to move back and forth as they are reflected from the trap walls. Typical

⁴Pitch angle is defined as the angle of the particle's total momentum with respect to the local magnetic field.

3140 oscillation frequencies are on the order of 10's of MHz, which results in an oscillation
 3141 period that is $O(10^3)$ smaller than the duration of a typical CRES event. Therefore, the
 3142 axial extent of the electron's motion is generally ignored for the purposes of reconstruction,
 3143 since the electron can be treated as if it is located in the average axial position at the
 3144 bottom of the magnetic trap. The component of motion with the smallest frequency
 3145 is the ∇B -drift caused by radial field gradients in the trap, producing an orbit of the
 3146 electron around the central axis of the trap with a frequency on the order of a few kHz,
 3147 dependent on the pitch angle and the radial position of the electron.

3148 Each component of motion influences the shape of the cyclotron radiation signals
 3149 received by the antenna array, therefore, the data acquisition (DAQ) system must be
 3150 properly designed in order to resolve the effects of the cyclotron motion, pitch angle, and
 3151 ∇B drift on the signal shape. Frequency down-conversion allows for intentional under-
 3152 sampling of the CRES signals at a nominal bandwidth of 200 MHz. The bandwidth is
 3153 required to be large enough to contain all sidebands produced by pitch angle modulation,
 3154 but must be limited to reduce the Nyquist-Johnson noise power for adequate signal-to-
 3155 noise ratio. The estimated noise temperature for the FSCD is ≈ 10 K, achievable with
 3156 low-noise HEMT amplifiers and cryogenic temperatures.

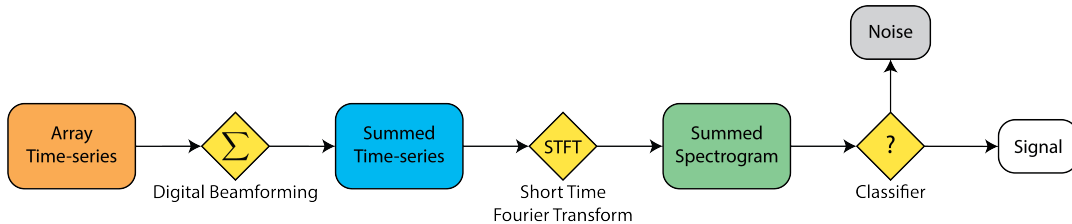


Figure 4.28. A block diagram illustration of the real-time triggering algorithm proposed for antenna array CRES reconstruction.

3157 A design goal for the FSCD DAQ system is to enable a significant portion of the
 3158 CRES event reconstruction to occur in real-time. The estimated data volume generated
 3159 by the FSCD is 1 exabyte of raw data per year of operation, with the nominal array size
 3160 of 60 antennas sampled at 200 MHz, which would be too expensive to store for offline
 3161 processing. Therefore, it is ideal to perform some CRES event reconstruction in real-time
 3162 so that it is possible to save a reduced form of the data for offline analysis. The first step
 3163 of the real-time reconstruction would be a real-time signal detection algorithm, which is
 3164 the focus of this paper. The basic approach consists of three operations performed on the
 3165 time-series data blocks including digital beamforming, a short time Fourier transform
 3166 (STFT), and a binary classification algorithm to distinguish between signal and noise

³¹⁶⁷ data (see Figure 4.28).

³¹⁶⁸ 4.4.2.2 Real-time Signal Detection

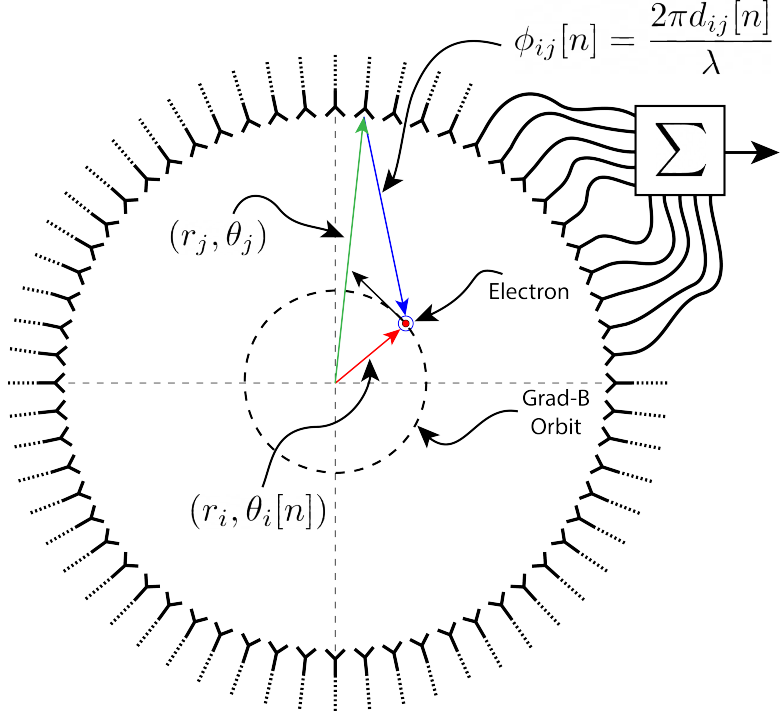


Figure 4.29. An illustration of the digital beamforming procedure. The blue lines indicate the distances from the beamforming position to each antenna. In the situation depicted the actual position of the electron matches the beamforming position, therefore, one expects constructive interference when the phase shifted signals are summed. To prevent the electron's ∇B -motion from moving the electron off of the beamforming position, the beamforming phases include time-dependence to follow the trajectory of the electron in the magnetic trap.

³¹⁶⁹ The first step in the real-time detection algorithm is digital beamforming, which is a
³¹⁷⁰ phased summation of the signals received by the array (see Figure 5.21). The phase shifts
³¹⁷¹ correspond to the path length differences between a spatial position and the antennas
³¹⁷² such that, when there is an electron located at the beamforming position, all the signals
³¹⁷³ received by the array constructively interfere. Since one does not know a priori where an
³¹⁷⁴ electron will be produced in the detector, a grid of beamforming positions is designed to
³¹⁷⁵ cover the entire azimuthal plane where electrons can be trapped. A beamforming phased
³¹⁷⁶ summation is performed for all points in the grid at each time-step. As shown in Section
³¹⁷⁷ 4.4.2.1, the axial oscillation of the electrons prevents one from resolving its position along
³¹⁷⁸ the z-axis, therefore, the beamforming grid need only cover the possible positions of the
³¹⁷⁹ electron in the two-dimensional plane defined by the antenna array.

3180 Digital beamforming can be expressed as

$$\mathbf{y}[n] = \Phi^T[n]\mathbf{x}[n], \quad (4.39)$$

3181 where $\mathbf{x}[n]$ is the array snapshot vector at the sampled time n , $\Phi[n]$ is the matrix of
3182 beamforming phase shifts, and $\mathbf{y}[n]$ is the summed output vector that contains the
3183 voltages for each of the summed channels corresponding to a particular beamforming
3184 position. The elements of the beamforming phase shift matrix can be expressed as a
3185 weighted complex exponential

$$\Phi_{ij}[n] = A_{ij}[n] \exp(2\pi i \phi_{ij}[n]), \quad (4.40)$$

3186 where the indices i and j label the beamforming and antenna positions respectively. The
3187 weight A_{ij} accounts for the relative power increase for antennas that are closer to the
3188 position of the electron, and ϕ_{ij} is the total beamforming phase shift for the j -th antenna
3189 at the i -th beamforming position.

3190 The beamforming phase shift is a sum of two terms

$$\phi_{ij}[n] = \frac{2\pi d_{ij}[n]}{\lambda} + \theta_{ij}[n], \quad (4.41)$$

3191 where the first term is the phase shift originating from the path length difference ($d_{ij}[n]$)
3192 between the beamforming and antenna positions, which are represented by the vectors
3193 (r_j, θ_j) and $(r_i, \theta_i[n])$, and the second term is the angular separation ($\theta_{ij}[n]$) of the two
3194 positions. The angular separation enters into the beamforming phase due to an effect
3195 caused by the circular cyclotron orbit of the electron that produces radiation whose
3196 phase is linearly dependent on the relative azimuthal position of the antenna [81, 82].
3197 The time-dependence of the beamforming phases corrects for the effects of the ∇B -drift,
3198 which cause the guiding centers of electrons to orbit the center of the magnetic trap. The
3199 correction adds a linear time-dependence to the azimuthal beamforming position,

$$\theta_i[n] = \omega_{\nabla B} t[n] + \theta_{i,0}, \quad (4.42)$$

3200 where $\omega_{\nabla B}$ is the azimuthal grad-B drift frequency, $t[n]$ is the time vector and, $\theta_{i,0}$
3201 is the starting azimuthal position, which allows the beamforming phases to track the
3202 XY-position of the guiding center. Predicting accurate values of $\omega_{\nabla B}$ for a specific trap
3203 and set of kinematic parameters can be done with simulations, which are performed

3204 using the Locust software package [64] developed by Project 8.

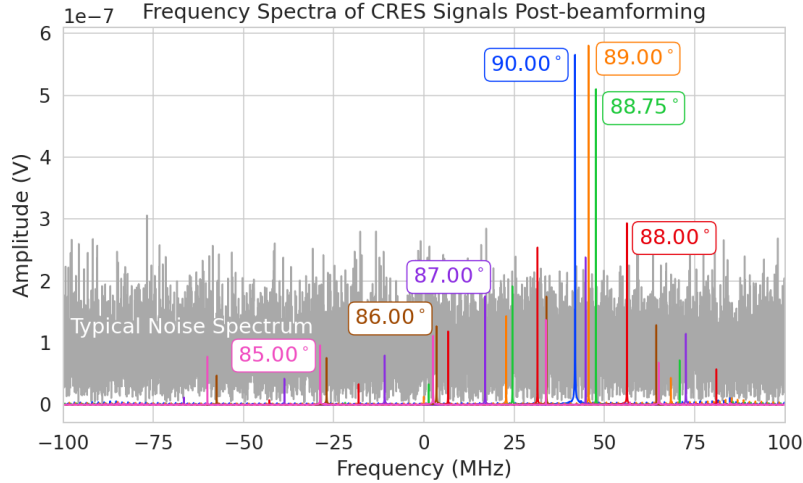


Figure 4.30. Frequency spectra of simulated CRES events in the FSCD magnetic trap after beamforming. The signal of a 90° electron consists of a single frequency component that is clearly detectable using a power threshold on the frequency spectrum. This power threshold remains effective for signals with relatively large pitch angles such as 89.0° and 88.75° , which are composed of a main carrier and a few small sidebands. Signals with smaller pitch angles, below about 88.5° , are dominated by sidebands such that no single frequency component can be reliably distinguished from the noise with a power threshold.

3205 After digital beamforming, a short-time Fourier transform (STFT) is applied to the
3206 summed time-series to obtain the signal frequency spectrum (see Figure 4.30). From the
3207 detection perspective, the frequency representation of the CRES data is advantageous
3208 compared to the time domain, due to the sparseness of CRES signals in the frequency
3209 domain. The frequency spectra of CRES signals are well-approximated by a frequency and
3210 amplitude modulated sinusoidal whose carrier frequency increases as a linear chirp [63].
3211 The modulation is caused by the axial oscillation of the electron in the magnetic trap,
3212 and the linear chirp is caused by the energy loss due to cyclotron radiation, which results
3213 in a relatively slow increase in the frequency components of the CRES signal over time.
3214 A typical CRES signal increases in frequency by approximately 15 kHz during the
3215 standard Fourier analysis window of $40.96 \mu\text{sec}$, which is smaller than the frequency
3216 bin width for a 200 MHz sample rate. Therefore, when considering a single frequency
3217 spectrum it is justifiable to neglect the effects of the linear frequency chirp.

3218 The majority of the CRES signal power for electrons in the FSCD trap is contained in
3219 a single frequency component when the electron has a pitch angle $\gtrsim 88.5^\circ$. The remain-
3220 ing signal power is distributed between a small number of sidebands with amplitudes

proportional to the electron's axial modulation (see Figure 4.30). Signal detection for these pitch angles is straightforward using a simple power threshold on the STFT, since the amplitude of the main signal peak is well above the thermal noise spectrum. However, as the pitch angle of the electron is decreased below 88.5° , the maximum amplitude of the frequency spectrum becomes comparable to typical noise fluctuations. At this point, the power threshold trigger is no longer able to distinguish between signal and noise leading to a reduction in detection efficiency, which is directly linked to the neutrino mass sensitivity of the FSCD. Because the distribution of electron pitch angles is effectively uniform, utilizing a signal detection algorithm that can improve efficiency for pitch angles less than 88.5° will lead to improvements in the neutrino mass sensitivity of the FSCD.

4.5 Signal Detection Algorithms

Modeling detection performance requires one to pose the signal detection problem in a consistent manner. The approach studied here uses the frequency spectra obtained from a STFT applied to the beamformed time-series from the FSCD to perform a binary hypothesis test. Mathematically, this is expressed as,

$$\mathcal{H}_0 : y[n] = \nu[n] \quad (4.43)$$

$$\mathcal{H}_1 : y[n] = x[n] + \nu[n]. \quad (4.44)$$

Under hypothesis \mathcal{H}_0 the vector representing the frequency spectrum ($y[n]$) is composed of complex white Gaussian noise (cWGN, $\nu[n]$) with total variance τ , and under hypothesis \mathcal{H}_1 the frequency spectrum is composed of a CRES signal ($x[n]$) with added cWGN. The dominant noise source for the FSCD is expected to be thermal Nyquist-Johnson noise, which is well approximated by a cWGN distribution. The hypothesis test is performed by calculating the ratio between the log-likelihood probability distributions for the classifier under \mathcal{H}_1 and \mathcal{H}_0 , which is the standard Neyman-Pearson approach to hypothesis testing [73]. The output of the log-likelihood ratio test is called the test statistic, which is used to assign the data as belonging to the noise or signal classes using a decision threshold.

In practice, the decision threshold is selected by finding the value of the test statistic that guarantees a tolerable rate of false positives. Given this false positive rate (FPR), one attempts to find a classifier that maximizes the true positive rate (TPR), which is the probability of correctly identifying if a piece of data contains signal or noise. Because

3250 FSCD signal classifiers will be used to evaluate the spectra of $O(10^2)$ beamforming
 3251 positions every 40.96 μ sec, there is a requirement that the signal classifiers with FPR
 3252 significantly smaller than 1% to reduce the burden placed on later stages of the CRES
 3253 reconstruction chain.

3254 4.5.0.1 Power Threshold

3255 The power threshold detection algorithm uses the maximum amplitude of the frequency
 3256 spectrum as the detection test statistic. Consider the \mathcal{H}_0 hypothesis where the signal is
 3257 pure cWGN. The performance of the power threshold can be modeled by first analyzing
 3258 a single bin in the frequency spectrum. The probability that the amplitude of a single
 3259 frequency bin falls below the decision threshold is given by the Rayleigh cumulative
 3260 distribution function (CDF),

$$\text{Ray}(x; \tau) = 1 - \exp(-|x|^2/\tau), \quad (4.45)$$

3261 where the complex value of the frequency bin is x , and τ is the cWGN variance. Because
 3262 the noise samples are independent and identically distributed (IID), the probability that
 3263 all bins in the frequency spectrum fall below the threshold is the joint CDF formed by
 3264 the product of each individual frequency bin CDF,

$$F_0(x; \tau, N_{\text{bin}}) = \text{Ray}(x; \tau)^{N_{\text{bin}}}. \quad (4.46)$$

3265 Finally, the PDF for the power threshold classifier can be obtained by differentiating
 3266 Equation 4.46.

3267 The noise variance of a beamformed frequency spectrum can be obtained directly
 3268 from the estimated noise power in a single antenna channel. The Nyquist-Johnson noise
 3269 power is given by $k_B T \Delta f$, where k_B is Boltzmann's constant, T is the system noise
 3270 temperature, and Δf is the sample rate. The beamformed noise variance is increased
 3271 by a factor of N_{ch} , where N_{ch} is the number of antennas, caused by the summation of
 3272 incoherent noise samples, however, the noise variance per frequency bin is decreased by a
 3273 factor equal to the number of samples in the STFT (N_{FFT}). The final expression for the
 3274 noise variance of the beamformed frequency spectrum is given by

$$\tau = k_B T \Delta f N_{\text{ch}} R / N_{\text{FFT}}, \quad (4.47)$$

3275 where the system impedance (R) has been used to convert from power to voltage-squared.

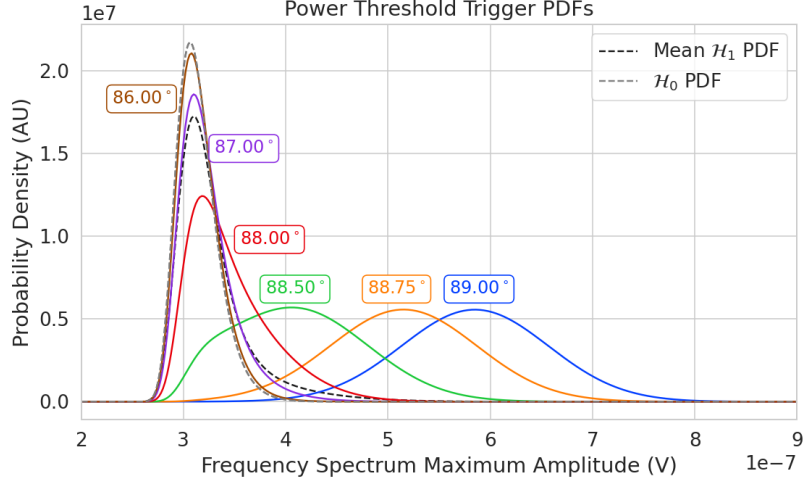


Figure 4.31. PDFs of the power threshold test statistic for CRES signals with various pitch angles as well as the PDF for the noise-only signal case. The average PDF computed for pitch angles ranging from 85.5 to 88.5° is also shown. As the pitch angle is decreased the signal PDF converges towards the noise PDF which indicates that the power threshold trigger is unable to distinguish between small pitch angle signals and noise.

3276 The probability distribution for the power threshold classifier under \mathcal{H}_1 is calculated
 3277 in a similar way, but the frequency bins that contain signal must be treated separately.
 3278 The probability that the amplitude of a frequency bin containing both signal and noise
 3279 bin falls below the decision threshold is described by a Rician CDF,

$$\text{Rice}(x; \tau, \alpha) = 1 - \int_x^\infty d|\tilde{x}| \frac{2|\tilde{x}|}{\tau} \exp\left(-\frac{|\tilde{x}|^2 + |\alpha|^2}{\tau}\right) \mathcal{I}_0\left(\frac{2|\tilde{x}||\alpha|}{\tau}\right), \quad (4.48)$$

3280 where the parameter $|\alpha|$ defines the noise-free amplitude of the signal. The CDF that
 3281 describes the probability that the entire spectrum falls below the decision threshold is
 3282 the product of both signal and noise CDFs,

$$F_1(x; \tau, \alpha, N_{\text{bin}}, N_s) = \text{Ray}(x; \tau)^{N_{\text{bin}} - N_s} \prod_{k=0}^{N_s} \text{Rice}(x; \tau, \alpha_k). \quad (4.49)$$

3283 The first half of Equation 4.49 is the contribution from the bins in the frequency spectrum
 3284 that contain only noise, and the second half is the product of the Rician CDFs for the
 3285 frequency bins that contain signal peaks with a noise-free amplitude of $|\alpha_k|$. Figure 4.31
 3286 shows plots of example PDFs under \mathcal{H}_1 and \mathcal{H}_0 .

3287 **4.5.0.2 Matched Filtering**

3288 The shape of a CRES signal in-between random scattering events with the background
 3289 gas is completely determined by the initial conditions of the electron, which implies that
 3290 it is possible to apply matched filtering as a signal detection algorithm. A matched filter
 3291 uses the shape of the known signal, which is called a template, to filter the incoming
 3292 data by computing the convolution between the signal and the data [73]. The matched
 3293 filter is the optimal detector, which means it achieves the maximum TPR for a particular
 3294 FPR, under the assumption that the signal is perfectly known and the noise is Gaussian
 3295 distributed. Since CRES signals have an unknown shape but are deterministic, the
 3296 matched filter can be applied by using simulations to generate a large number of signal
 3297 templates, called a "template bank", which spans the parameter space of possible signals.
 3298 Then at detection time, the template bank is used to identify signals by performing the
 3299 matched filter convolution for each template in an exhaustive search.

3300 CRES signals are highly periodic in nature. In such cases, it is advantageous to utilize
 3301 the convolution theorem to replace the matched filter convolution with an inner product
 3302 in the frequency-domain. Using the convolution theorem, the matched filter test statistic
 3303 is given by

$$\mathcal{T} = \max_h \left| \sum_{n=0}^{N_{\text{bin}}} h^\dagger[n] y[n] \right|, \quad (4.50)$$

3304 where $h^\dagger[n]$ is the complex conjugate of the signal template.

3305 The approach to deriving PDFs that describe the matched filter template bank will
 3306 be to first derive PDFs for \mathcal{H}_0 and \mathcal{H}_1 in the case of a single template and use these
 3307 solutions to create PDFs that describe the multi-template case. In the case when the
 3308 template bank consists of only a single template it is possible to derive an exact analytical
 3309 form for the PDF. Consider the \mathcal{H}_1 case, where the equation describing the matched
 3310 filter test statistic, also known as the matched filter score, becomes

$$\mathcal{T} = \left| \sum_{n=0}^{N_{\text{bin}}} h^\dagger[n] y[n] \right|. \quad (4.51)$$

3311 Each noisy frequency bin is a sum of signal and cWGN, which means $y[n]$ is also a
 3312 Gaussian distributed variable. Therefore, the value of the inner product between the
 3313 template and the data is also a complex Gaussian variable; and, since the matched filter
 3314 score is the magnitude of this inner product, it must follow a Rician distribution.

3315 The distribution that describes the matched filter score under \mathcal{H}_1 can be derived

3316 starting with the matched filter template equation. The matched filter template \mathbf{h} is a
3317 simulated signal (\mathbf{x}_h) with a normalization factor

$$\mathbf{h} = \frac{\mathbf{x}_h}{\sqrt{\tau|\mathbf{x}_h|^2}}, \quad (4.52)$$

3318 where τ is the noise variance. Inserting this into Equation 4.50 and expressing the data
3319 as a sum between a signal and a WGN vector yields,

$$\mathcal{T} = \frac{1}{\sqrt{\tau|\mathbf{x}_h|^2}} \left| \sum_{n=1}^{N_{\text{bin}}} x_h^\dagger[n]x[n] + \sum_{n=1}^{N_{\text{bin}}} x_h^\dagger[n]\nu[n] \right|. \quad (4.53)$$

3320 The first term is a scalar product between the signal and template vectors and the
3321 second term is a complex Gaussian distributed variable with variance one. For the
3322 purposes of identifying the statistical distribution, it is useful to rewrite the summation
3323 describing an inner product

$$\sum_{n=1}^{N_{\text{bin}}} x_h^\dagger[n]x[n] = \mathbf{x}_h \cdot \mathbf{x} = |\mathbf{x}_h \cdot \mathbf{x}|e^{i\vartheta} \leq |\mathbf{x}_h||\mathbf{x}|e^{i\vartheta}, \quad (4.54)$$

3324 the last step utilizes the Cauchy-Schawrz inequality, where equality is guaranteed when
3325 $\mathbf{x} = \mathbf{x}_h$. Instead of the inequality it is useful to define a quantity called "match" such that

$$|\mathbf{x}_h \cdot \mathbf{x}|e^{i\vartheta} = |\mathbf{x}_h||\mathbf{x}|\Gamma e^{i\vartheta}, \quad (4.55)$$

3326 where the match factor $\Gamma \in [0, 1]$. The match factor quantifies how well the template
3327 matches the signal.

3328 The fact that the second term is a random complex Gaussian variable with unity
3329 variance can be seen by noting that each of the noise samples are drawn from the complex
3330 Gaussian distribution, $\mathcal{N}(0, \tau)$. Therefore,

$$\frac{x_h^\dagger[n]}{\sqrt{\tau|\mathbf{x}_h|^2}}\nu[n] \sim \mathcal{N}\left(0, \frac{x_h^\dagger[n]x_h[n]}{|\mathbf{x}_h|^2}\right), \quad (4.56)$$

$$n = \sum_{n=1}^{N_{\text{bin}}} \frac{x_h[n]}{\sqrt{\tau|\mathbf{x}_h|^2}}\nu[n] \sim \mathcal{N}\left(0, \frac{\sum_{n=1}^{N_{\text{bin}}} x_h^\dagger[n]x_h[n]}{|\mathbf{x}_h|^2}\right) = \mathcal{N}(0, 1). \quad (4.57)$$

3331 Equation 4.53 can now be simplified

$$\mathcal{T} = \left| |\mathbf{h}| |\mathbf{x}| \Gamma e^{i\vartheta} + n \right|, \quad (4.58)$$

3332 where Equation 4.52 has been used to redefine the inner product term. The quantity
 3333 $|\mathbf{h}| |\mathbf{x}| \Gamma$ is a real number, which is the matched filter score that one would expect if the
 3334 data contained no noise. The final simplification is to define $\mathcal{T}_{\text{ideal}} = |\mathbf{h}| |\mathbf{x}| \Gamma$, from which
 3335 one obtains

$$\mathcal{T} = |\mathcal{T}_{\text{ideal}} e^{i\vartheta} + n|. \quad (4.59)$$

3336 From Equation 4.59 on can see that \mathcal{T} is simply the magnitude of a complex number
 3337 with added cWGN of variance 1, which follows the Rician distribution, therefore the
 3338 distribution that describes the matched filter score for a single template under \mathcal{H}_1 is

$$P_1(x; \mathcal{T}_{\text{ideal}}) = 2x \exp(- (x^2 + \mathcal{T}_{\text{ideal}}^2)) I_0(2x\mathcal{T}_{\text{ideal}}). \quad (4.60)$$

3339 The shape of the matched filter score distribution is controlled by the parameter $\mathcal{T}_{\text{ideal}}$,
 3340 which is effectively the value of the matched filter score if the data contained no noise.
 3341 Without noise, the data vector reduces to the signal, \mathbf{x} , in which case Equation 4.51
 3342 becomes the magnitude of an inner product between two vectors. The magnitude of an
 3343 inner product can be expressed in terms of the magnitudes of the vectors and a constant
 3344 that describes the degree of orthogonality between them. Applying this to Equation 4.51,
 3345 one obtains

$$\mathcal{T}_{\text{ideal}} = |\mathbf{h}^\dagger \cdot \mathbf{x}| = |\mathbf{h}| |\mathbf{x}| \Gamma \quad (4.61)$$

3346 where Γ describes the orthogonality between \mathbf{h} and \mathbf{x} . Γ effectively quantifies how well
 3347 the template matches the unknown signal in the data.

3348 The matched filter score PDF under \mathcal{H}_0 is readily obtained from Equation 4.60 by
 3349 setting the value of $\mathcal{T}_{\text{ideal}}$ to zero, since the data contains no signal in the noise case.
 3350 Doing this, one obtains a Rayleigh distribution,

$$P_0(x) = 2x \exp(-x^2). \quad (4.62)$$

3351 Equations 4.60 and 4.62 describe the behavior of the matched filter test statistic
 3352 under \mathcal{H}_0 and \mathcal{H}_1 for a single template. However, defining a PDF that describes the
 3353 matched filter test statistic in the case of multiple templates is in general a mathematically
 3354 intractable problem, since there is no guarantee of orthogonality between matched filter

3355 templates. This leads to correlations between the matched filter scores of different
 3356 templates, because only one sample of noise is used to compute the matched filter scores
 3357 of the template bank. In order to proceed, it is assumed that the matched filter scores for
 3358 all templates are IID variables, which allows one to ignore correlations between templates.
 3359 The overall effect of this will be an underestimate of the performance of the matched
 3360 filter by over-estimating the required number of templates and, therefore, the magnitude
 3361 of the statistical trials penalty.

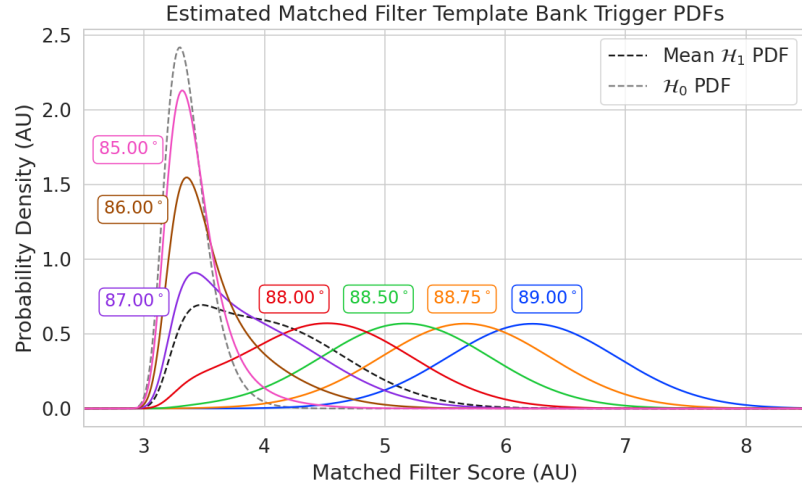


Figure 4.32. Plots of PDFs that describe the matched filter template bank test statistic for CRES signals with various pitch angles, as well as the estimated PDF for the noise only case. 10^5 matched filter templates are used and perfect match between signal and template i.e. $\Gamma_{\text{best}} = 1$ is assumed. The mean PDF includes signals ranging from $85.5 - 88.5^\circ$ in pitch angle. There is a larger distinction between the signal PDFs at small pitch angles compared to the power threshold, which indicates a higher detection efficiency for these signals.

3362 The probability that the matched filter score falls below the decision threshold under
 3363 \mathcal{H}_0 is again given by the CDF. Because of the assumption that matched filter scores from
 3364 different templates are independent, the probability that the matched filter score for all
 3365 templates falls below the threshold value is simply the joint CDF, which is

$$F_0(x) = \left(1 - e^{-x^2}\right)^{N_t}, \quad (4.63)$$

3366 where x is the matched filter score threshold and N_t is the number of templates. One
 3367 should expect that the distribution describing the maximum score of the matched filter
 3368 template bank depends on N_t , because with more templates there is a greater chance of
 3369 a random match between the template and data.

3370 The CDF that describes \mathcal{H}_1 is derived by starting with the CDF of the best matching
 3371 template, $F_{\text{best}}(x; \mathcal{T}_{\text{best}})$. Because of the orthogonality assumption, the matched filter
 3372 scores for all other templates are negligible ($\mathcal{T}_{\text{ideal}} \approx 0$). The joint CDF that describes
 3373 the total template bank is obtained by combining the distributions for all templates used
 3374 during detection. Therefore, the estimated CDF under \mathcal{H}_1 is

$$F_1(x; \mathcal{T}_{\text{best}}) = F_{\text{best}}(x; \mathcal{T}_{\text{best}}) \left(1 - e^{-x^2}\right)^{N_t}. \quad (4.64)$$

3375 Figure 4.32 shows plots of the matched filter template bank PDFs under \mathcal{H}_0 and \mathcal{H}_1 .

3376 4.5.0.3 Machine Learning

3377 The focus in this paper is on the potential of Convolutional Neural Networks (CNN)
 3378 as a machine learning based signal classifier at the trigger level. CNNs are constructed
 3379 using a series of convolutional layers, each composed of a set of filters that are convolved
 3380 with the input data. The individual convolutional filters can be viewed heuristically
 3381 as matched filter templates [?] that are learned from a set of simulated data rather
 3382 than being directly generated. This opens the possibility of finding a more efficient
 3383 representation of the matched filter templates during the training process that can
 3384 potentially reduce computational cost at inference time while retaining good classification
 3385 performance.

3386 The machine learning approach is distinct from the power threshold and matched
 3387 filtering in that there is no attempt to manually engineer a test statistic that can be
 3388 computed from the input data. Instead, a test statistic is calculated by constructing a
 3389 differentiable function that maps the complex frequency series to a binary classification
 3390 as signal or noise. The differentiable function is trained using supervised learning to
 3391 correctly perform this mapping. The test statistic for the machine learning classifier is
 3392 expressed mathematically as

$$\mathcal{T} = G(\mathbf{y}; \boldsymbol{\Omega}) \quad (4.65)$$

3393 where \mathbf{y} is the noisy data vector and $G(\mathbf{y}; \boldsymbol{\Omega})$ is the machine learning model parameterized
 3394 by the weights $\boldsymbol{\Omega}$.

3395 The CNN architecture used for this work is summarized by Table 4.1. No strategic
 3396 hyper-parameter optimization approach was implemented beyond the manual testing
 3397 of different CNN architecture variations, so this particular model is best viewed as a
 3398 proof-of-concept rather than a rigorously optimized design. Numerous model variations
 3399 were tested, some with significantly more layers and convolutions filters per layer, as

Table 4.1. A summary of the CNN model layers and parameters. The output of each 1D-Convolution and Fully Connected layer is passed through a LeakyReLU activation function and re-normalized using batch normalization before being passed to the next layer in the model. The output of the final Fully Connected layer in the model is left without activation so that the model outputs can be directly passed to the Binary Cross-entropy loss function used during training. The first layer in the network has two input channels for the real and imaginary components of the spectrum.

Layer	Type	Input Channels	Output Channels	Parameters
1	1D-Convolution	2	15	($N_{\text{kernel}} = 4$, $N_{\text{stride}} = 1$)
2	Maximum Pooling	15	15	($N_{\text{kernel}} = 4$, $N_{\text{stride}} = 4$)
3	1D-Convolution	15	20	($N_{\text{kernel}} = 4$, $N_{\text{stride}} = 1$)
4	Maximum Pooling	20	20	($N_{\text{kernel}} = 4$, $N_{\text{stride}} = 4$)
5	1D-Convolution	20	25	($N_{\text{kernel}} = 4$, $N_{\text{stride}} = 1$)
6	Maximum Pooling	25	25	($N_{\text{kernel}} = 4$, $N_{\text{stride}} = 4$)
7	Fully Connected	3200	512	NA
8	Fully Connected	512	64	NA
9	Fully Connected	64	2	NA

³⁴⁰⁰ well as others that were even smaller than the architecture in Table 4.1. Ultimately, the
³⁴⁰¹ model architecture choice was driven by the motivation to find the minimal model whose
³⁴⁰² classification performance was still comparable to the larger CNN’s tested, because of
³⁴⁰³ the importance of minimizing computational cost in real-time applications. It is possible
³⁴⁰⁴ that more sophisticated machine learning models could improve upon the classification
³⁴⁰⁵ results achieved here, but this investigation is left for future work.

³⁴⁰⁶ 4.5.1 Methods

³⁴⁰⁷ 4.5.1.1 Data Generation

³⁴⁰⁸ Simulated CRES signals were generated using the Locust simulations package [64, 81].
³⁴⁰⁹ Locust uses the separately developed Kassiopeia package [62] to calculate the magnetic
³⁴¹⁰ fields produced by a user defined set of current carrying coils along with any specified
³⁴¹¹ background magnetic fields, resulting in a magnetic trap. Next, Kassiopeia calculates the
³⁴¹² trajectory of an electron in this magnetic field starting from a set of user specified initial
³⁴¹³ conditions. The Locust software then uses the electron trajectories from Kassiopeia
³⁴¹⁴ to calculate the resulting electromagnetic fields using the Liénard-Wiechert equations,
³⁴¹⁵ and determines the voltages generated in the antenna array with the antenna transfer
³⁴¹⁶ function. Locust then simulates the down-conversion, filtering, and digitization steps
³⁴¹⁷ resulting in the simulated CRES signals for an electron.

3418 The shape of the received CRES signal is determined by the initial kinematic param-
3419 eters, including the starting position of the electron, the starting kinetic energy of the
3420 electron, and the pitch angle. The studies performed here are constrained to a single
3421 initial electron position located at $(x, y, z) = (5, 0, 0)$ mm. Two datasets are generated
3422 using this starting position by varying the initial kinetic energy and pitch angle. The
3423 first dataset consists of a two-dimensional square grid spanning an energy range from
3424 18575-18580 eV with a spacing of 0.1 eV, and pitch angles from 85.5-88.5° with a spacing
3425 of 0.001°, resulting in 153051 signals with a unique energy-pitch angle combination. This
3426 dataset is intended to represent a matched filter template bank. The upper range of pitch
3427 angles is limited because of the greater relative detection efficiency of the matched filter
3428 and neural network classifiers in this pitch angle range. The second dataset was generated
3429 by randomly sampling uniform probability distributions covering the same parameter
3430 space to produce approximately 50000 signals randomly parameterized in energy and
3431 pitch angle. This dataset provides the training and test data for the machine learning
3432 approach, and acts as a representative sample of signals to evaluate the performance of
3433 the matched filter template bank.

3434 Each signal was simulated for a duration of 40.96 μ s or 8192 samples starting at
3435 time $t = 0$ s for all simulations. This duration represents a single frequency spectrum
3436 generated by the STFT. The FSCD antenna array has sixty channels, and the output of
3437 the Locust simulations are a matrix of array snapshots with a size given by the number
3438 of channels times the event length ($N_{\text{ch}} \times N_{\text{sample}}$). The raw data from Locust is first
3439 summed using digital beamforming and converted to frequency spectra using a Fourier
3440 transform. The beamforming procedure uses the exact position and ∇B -drift correction
3441 to simplify the comparison between trigger algorithms. Many beamforming positions
3442 would be used in practice and potentially several estimates of a typical $\omega_{\nabla B}$ depending
3443 on the variation of the ∇B -drift frequency with pitch angle.

3444 **4.5.1.2 Template Number and Match Estimation**

3445 The estimated PDF for the matched filter template bank on the number of templates and
3446 the mean match (Γ_{best}). A given signal with random parameters will have a template in
3447 the filter bank that gives the highest matched filter score, therefore, the mean match
3448 ratio is obtained by averaging over the best matching templates for a representative
3449 population of test signals. Γ_{best} is a figure of merit that characterizes the performance of
3450 a template bank at signal detection. One expects that with more templates the value
3451 of Γ_{best} will increase, however, there is a point of diminishing returns at which more

3452 templates will not significantly increase match, but will still increase the likelihood of
3453 false positives. Therefore, it is desirable to use the minimum number of templates that
provide an acceptable mean value of Γ_{best} .

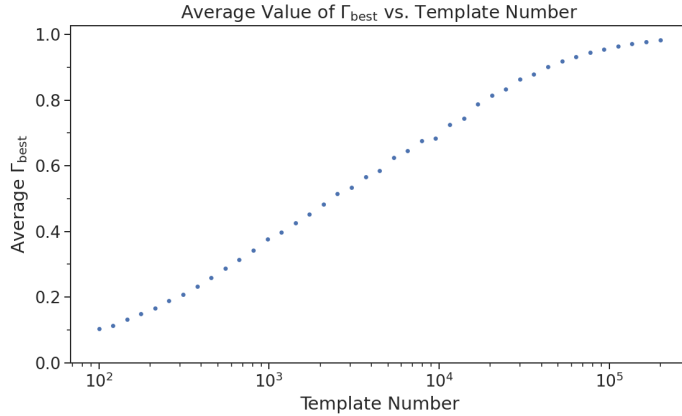


Figure 4.33. The mean match of the matched filter template bank to a test set of randomly parameterized signals as a function of the number or density of templates. The parameter space includes pitch angles from $85.5 - 88.5^\circ$ and energies from 18575 – 18580 eV.

3454
3455 To quantify the relationship between match and template number, the mean match
3456 of the random dataset to a selection of templates from the regularly spaced dataset was
3457 calculated. One sees that the average value of Γ_{best} is an exponential function of the
3458 number of templates (see Figure 4.33). Using this plot one can infer the required number
3459 of templates for the desired value of mean match.

3460 4.5.1.3 CNN Training and Data Augmentation

3461 The random dataset is split in half to create distinct training and test datasets for
3462 training the model. A randomly selected 20% of the training data is isolated for use as
3463 a validation set during the training loop. The size of the training, validation, and test
3464 datasets are tripled by appending two additional copies of the data to increase the sample
3465 size of the dataset after data augmentation. A different sample of noise is added to the
3466 simulation data during the training loop, which prevents the model from overtraining on
3467 noise features. The training and test datasets contain an equal split between signal and
3468 noise data, which are randomly shuffled after each training epoch.

3469 The Locust simulation data was augmented to make the datasets more representative
3470 of actual experiment data. As the signals are loaded for training a unique random phase
3471 shift is applied. Since the simulations are generated using the same initial axial position

3472 and cyclotron orbit phase, the randomization is an attempt to prevent overtraining on
 3473 these features. During each training epoch the data is randomly shuffled and split into
 3474 batches of 2500 signals. Each batch of signals is then circularly shifted by a random
 3475 number of frequency bins to simulate a kinetic energy shift from -75 to 20 eV, which
 3476 imitates a dataset with a larger energy range. Next, a sample of cWGN, consistent
 3477 with 10 K Nyquist-Johnson noise, is generated and added to the signal, which prevents
 3478 overtraining on noise features. As a final step, the data is renormalized by the standard
 3479 deviation of the noise so that the range of values in the data is close to $[-1, 1]$, which
 3480 ensures well-behaved back-propagation.

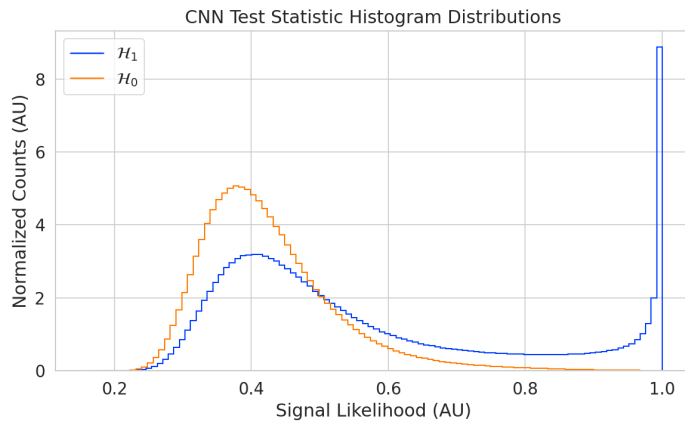


Figure 4.34. Histograms of the trained CNN model output from the test dataset. The blue histogram shows the model outputs for signal data. The oddly shaped peak near the end is the result of the softmax function mapping the long tail of the raw output distribution to the range $[0, 1]$.

3481 The Binary Cross-entropy loss function is used to compute the loss for each batch of
 3482 data, and the model weights are updated using the ADAM optimizer with a learning
 3483 rate of 5×10^{-3} . After each training epoch, the loss and classification accuracy of the
 3484 validation dataset are computed to monitor for overtraining. It was noticed that because
 3485 of the relatively high noise power and the fact that a new sample of noise was used for
 3486 each batch, it was nearly impossible to over-train the model. Typically, the loss and
 3487 classification accuracy of the model converged after a few hundred training epochs, but
 3488 the training loop was extended to 3000 epochs to attempt to achieve the best possible
 3489 performance. The training procedure generally took about 24 hrs using a single NVIDIA
 3490 V100 GPU [83].

3491 After training the model, it was used classify the test dataset and generate histograms
 3492 of the model outputs for both classes of data. The data augmentation procedure for the

3493 evaluation of the test data mirrors the training procedure without the validation split.
 3494 Since a random circular shift and a new sample of WGN is added to each batch, the
 3495 testing evaluation loop is run for 100 epochs to get a representative sample of noise and
 3496 circular shifts. The model outputs are passed through a softmax activation and then
 3497 combined into histograms (see Figure 4.34).

3498 4.5.2 Results and Discussion

3499 4.5.2.1 Trigger Classification Performance

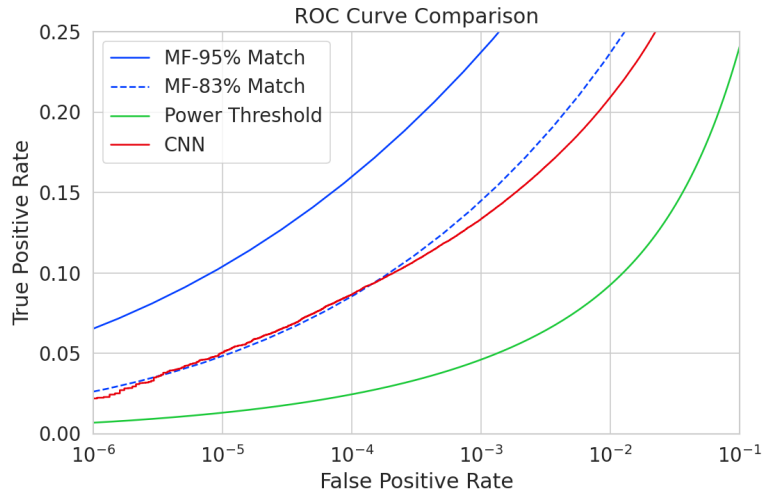


Figure 4.35. ROC curves describing the detection efficiency or true positive rates for the three signal classification algorithms examined in this paper. The matched filter (MF) and Power Threshold curves are computed analytically using the distribution functions introduced in Section 4.5, and the CNN curve is computed numerically using the classification results on the test dataset. The percent match indicated in the legend refers to the mean match of the classifier.

3500 The detection performance of the signal classifiers can be compared by computing
 3501 the receiver operating characteristic (ROC) curves (see Figure 4.35). A single ROC
 3502 curve is obtained for the matched filter and power threshold classifiers by averaging over
 3503 analytical ROC curves obtained from the distributions in Section 4.5. Two ROC curves
 3504 are calculated for the matched filter with different numbers of templates and mean match.
 3505 The ROC curve describing the CNN is obtained numerically from the histograms of the
 3506 model outputs for each signal class.

3507 The TPR of a signal classifier is equivalent to its detection efficiency, and one sees
 3508 that for the population of signals with pitch angles $< 88.5^\circ$ the power threshold has

3509 a consistently lower detection efficiency than the CNN and the matched filter. This
3510 result might have been predicted from the visualization of signal spectra in Figure 4.30,
3511 where it can be seen that a noise peak and a signal peak cannot be distinguished with
3512 high-confidence at small pitch angles. The CNN offers a significant and consistent increase
3513 in detection efficiency over the power threshold approach, with the relative improvement
3514 in detection efficiency increasing as the false positive rate decreases.

3515 If one compares the CNN to the matched filter, it can be seen that the performance of
3516 the tested network is roughly equivalent to a matched filter detector with a mean match
3517 of about 83%, which uses approximately 2×10^4 matched filter templates. The overall
3518 best detection efficiency is achieved by the matched filter classifier if a large enough
3519 template bank is used. The plot displays the ROC curve for a matched filter template
3520 bank with 95% mean match, which is achieved with approximately 10^5 templates. Since
3521 the matched filter is known to be statistically optimal for detecting a known signal in
3522 WGN, it is unsurprising that this algorithm has the highest detection efficiency.

3523 An important difference between the matched filter and CNN algorithms is that the
3524 CNN relies upon convolutions as its fundamental calculation mechanism, whereas our
3525 implementation of a matched filter utilizes an inner product. Since convolution is a
3526 translation invariant operation, the detection performance of CNN can be extended to
3527 a wider range of CRES event kinetic energies with less cost than the matched filter, a
3528 feature that is exploited during the CNN training by including circular translations of
3529 the CRES frequency spectra in the training loop. Increasing the range of detectable
3530 kinetic energies with a matched filter requires a proportional increase in the number of
3531 templates, which directly translates into increased computational and hardware costs.
3532 From a practical perspective, the detection algorithm is always limited by the available
3533 computational hardware, so estimating the relative costs is a key factor in determining
3534 their feasibility. A more detailed analysis of the relative costs of each of the detection
3535 algorithms is performed below.

3536 4.5.2.2 Computational Cost and Hardware Requirements

3537 The trade-off between better detection efficiency and computational cost is common
3538 to many signal detection problems and the FSCD is no exception. Computational
3539 costs can be related to actual hardware costs by calculating the theoretical amount of
3540 computer hardware required to implement the signal classifiers for real-time detection.
3541 The approach taken here utilizes order of magnitude estimates of the theoretical peak
3542 performance values for currently available Graphics Processing Units (GPUs) as a metric.

3543 This approach underestimates the amount of required hardware, since it is unlikely that
3544 any CRES detection algorithm could reach the theoretical peak performance of the
3545 hardware.

3546 Since the signal detection algorithms are designed to work using beamformed frequency
3547 spectra, the computational cost of beamforming combined with a fast Fourier transform
3548 (FFT) is constant for all classifiers. The beamforming grid is assumed to contain N_{bf}
3549 beamforming positions, each of which will produce a frequency spectrum containing N_{bin}
3550 after the FFT.

3551 Considering the power threshold classifier, this results in $N_{\text{bin}}N_{\text{b}}$ frequency bins
3552 that must be checked every N_{bin}/f_s seconds. The 20 cm diameter FSCD array requires
3553 $N_{\text{bf}} \approx O(10^2)$ for sufficient coverage and has a sampling frequency $f_s = 200$ MHz with a
3554 Fourier analysis window of $N_{\text{bin}} = 8192$ samples. Therefore the power threshold requires
3555 approximately $O(10^{10})$ FLOPS to check in real-time with these parameters

3556 Current generations of GPUs have peak theoretical performances in the range of
3557 $O(10^{13}) - O(10^{14})$ FLOPS [84], dependent on the required floating-point precision of
3558 the computation. Therefore, the entire computational needs of a real-time triggering
3559 system using a power threshold classifier, including digital beamforming and generation
3560 of the STFT, could be met by a single high-end GPU or a small number of less powerful
3561 GPUs. Since triggering is only one step of the full real-time signal reconstruction
3562 approach, limiting the computational cost of this stage is ideal. However, the power
3563 threshold classifier does not provide sufficient detection efficiency across the entire
3564 range of possible signals, which is the primary motivation for exploring more complicated
3565 triggering solutions.

3566 As discussed, the computational cost of the matched filter approach requires counting
3567 the number of templates that must be checked for each frequency spectra produced by
3568 the STFT. Computing the matched filter scores requires $O(N_{\text{bf}}N_tN_{\text{bin}})$ operations, since
3569 for each of the beamforming positions one must multiply N_t templates with a data vector
3570 that has length N_{bin} . The computation must be performed in a time less-than or equal
3571 to N_{bin}/f_s to keep up with the data generation rate. A 5 eV range of kinetic energies
3572 required 10^4 to 10^5 templates in order for the matched filter to exceed the performance
3573 of the CNN. The number of templates is expected to scale linearly with the total kinetic
3574 energy range of interest, therefore, 10^5 to 10^6 matched filter templates would be expected
3575 for the nominal 50 eV analysis window of the FSCD. Considering this, the estimated
3576 computational cost of the matched filter is between $O(10^{15})$ to $O(10^{16})$ FLOPS, which is
3577 $O(10^2)$ to $O(10^3)$ high-end GPUs.

3578 The computational cost of the CNN can be estimated by simply summing the compu-
3579 tational costs of the convolutions and matrix multiplications specified by the network
3580 architecture shown in Table 4.1. Each convolutional layer consists of $N_{\text{in}}N_{\text{out}}N_{\text{kernel}}L_{\text{input}}$
3581 floating-point operations, where N_{in} is the number of input channels, N_{out} is the number
3582 of output channels, N_{kernel} is the size of the convolutional kernel, and L_{input} is the length
3583 of the input vector, and the fully connected layers each contribute $N_{\text{in}}N_{\text{out}}$ operations.
3584 Summing all the neural network layers it is estimated that the CNN requires $O(10^6)$
3585 floating point operations to evaluate each frequency spectra; therefore, the total com-
3586 putational cost of the CNN trigger is value multiplied by the number of beamforming
3587 positions per the data acquisition time, which is $O(10^{13})$ FLOPS or $O(10^0)$ GPUs.

3588 Compared with the matched filter approach the CNN requires $O(100)$ to $O(1000)$
3589 fewer GPUs to implement, dependent on the exact number of templates used in the
3590 template bank. The 50 eV kinetic energy range is motivated by the application of these
3591 detection algorithms to an FSCD-like neutrino mass measurement experiment. However,
3592 if a significantly larger range of kinetic energies is required, a CNN may be the preferred
3593 detection approach despite the lower mean detection efficiency due to computational cost
3594 considerations.

3595 Additional experiments with larger CNNs, generated by increasing the depth and
3596 width of the neural network, were performed. It was observed that these changes
3597 provided minimal ($\lesssim 1\%$) improvement in the classification accuracy of the model. A
3598 potential reason for this could be the sparse nature of the signals in the frequency
3599 domain and the low SNR, which makes for a challenging dataset to learn from. Future
3600 work might investigate modifications to the neural network architecture such as sparse
3601 convolutions, which may improve the classification accuracy of the model or further
3602 reduce the computational costs of this approach. Alternatively, more complicated CNN
3603 architectures such as a ResNet [85] or VGG model [86] may provide improved classification
3604 performance over a basic CNN. An additional promising area of investigation are recurrent
3605 neural networks, which may be able to exploit the time-ordered features of the STFT for
3606 more accurate signal detection if the electron signals last for multiple Fourier transform
3607 windows.

3608 The estimate of the computational costs of the matched filter is somewhat naive if one
3609 notices that the majority of the values that make up a CRES frequency spectrum are zero
3610 (see Figure 4.30). Therefore, the majority of operations in the matched filter inner product
3611 are unnecessary, and one could instead evaluate the matched filter inner product using
3612 only the $\lesssim 10$ frequency peaks that make up the CRES signal. This optimization reduces

3613 the number of operations required to check each template by a factor of $O(100)$ to $O(1000)$,
3614 which brings the estimated computational cost of the matched filter in line with the
3615 CNN. Although this level of sparsity results in a multiplication with very low arithmetic
3616 complexity, the resulting sparse matched filter algorithm is still likely to be constrained
3617 by memory access speed rather than compute speed. Ultimately, the comparison of
3618 the relative computational and hardware costs between the matched filter and CNN
3619 will depend on the efficiency of the software implementation and hardware support for
3620 neural network and sparse matrix calculations, which will need to be determined using
3621 real-world benchmarks.

3622 **4.5.3 Conclusion**

3623 Increasing the detection efficiency and overall event rate of the CRES technique represents
3624 a key developmental path towards new scientific results and broader applications of the
3625 CRES technique. It is what motivates both the antenna array detection approach and
3626 the development of real-time signal reconstruction algorithms. The work presented here
3627 demonstrates that significant gains in the detection efficiency of the CRES technique
3628 are achievable by utilizing triggering algorithms that account for the specific shape of
3629 CRES signals in the detector. These algorithms emphasize the need for accurate and fast
3630 methods for CRES simulation, since they directly contribute to the success of matched
3631 filter methods by providing a way to generate expected signal templates and also serve
3632 as a source of training data for machine learning approaches.

3633 The down-side of these more advanced approaches to signal detection is the increase
3634 in computational resources required to implement them. However, it was shown that a
3635 CNN of minimal size was able to significantly improve detection performance above the
3636 baseline power threshold trigger algorithm with a theoretical computational cost of only
3637 $O(1)$ high-end GPU. This algorithm improves on detection performance while requiring
3638 at least a factor $O(10^2)$ less in computer relative to a matched filter template bank,
3639 which would be the classical approach to signal detection in Gaussian noise. Future work
3640 obtaining real-life benchmarks of the CNN and matched filter algorithms are required to
3641 support these conclusions, but this study has indicated that a real-time signal detection
3642 algorithm for an antenna array CRES experiment is computationally feasible without
3643 extraordinary compute power.

3644 While this work has focused on the real-time detection of CRES signals from antenna
3645 arrays, these same signal classifiers could be used in CRES experiments utilizing different
3646 detector technologies, since the same principles of signal detection will apply. For example,

3647 previous CRES measurements by the Project 8 collaboration that utilized a waveguide
3648 gas cell, could have improved their detection efficiency by employing a matched filter
3649 or neural network classifier to identify trapped electrons with pitch angles that are too
3650 small to be detected by the power threshold approach. Furthermore, alternative CRES
3651 detector technologies such as resonant cavities [41] could also see similar improvements
3652 in detection efficiency, which is of crucial importance to future efforts by the Project 8
3653 collaboration to utilize CRES to measure the neutrino mass.

Chapter 5

Antenna and Antenna Measurement System Development for the Project 8 Experiment

5.1 Introduction

The FSCD and antenna array CRES represent an innovative approach to beta-decay spectroscopy. While much can be learned from simulations about the systematics of CRES with antenna arrays, laboratory measurements and demonstrations provide critical inputs to sensitivity and simulation models, and provide a means for calibration and commissioning of the experiment. Therefore, a robust program of antenna and antenna measurement hardware development is key to the success of the FSCD and the development of antenna array CRES more broadly.

In this chapter I summarize the development of an antenna measurement system at Penn State to implement and test the techniques of antenna array CRES on the bench-top. In Section 5.2 I provide an introduction to some fundamental parameters and concepts related to antenna measurements as well as an overview of the Penn State antenna measurement system hardware. In Section 5.3 I include the manuscript of a paper [82] which details the design and characterization of a specialized antenna developed to mimic the electric fields emitted by an electron in a CRES experiment. This antenna, called the Synthetic Cyclotron Antenna (SYNCA), is intended as a calibration tool for antenna arrays developed for CRES measurements. Lastly, in Section 5.5 I summarize a set of prototype FSCD antenna array measurements with the SYNCA [44], which I use to validate the simulated performance of the antenna array and estimate systematic errors associated with the antenna array.

3678 5.2 Antenna Measurements for CRES experiments

3679 5.2.1 Antenna Parameters

3680 Antenna characterization measurements are intended to validate simulations of the
3681 antenna array performance, which ultimately informs the neutrino mass sensitivity of
3682 the experiment. In this section, I shall summarize a few fundamental concepts relating
3683 to antennas and antenna measurement, before introducing how Project 8 uses antenna
3684 measurements for the development of antenna array CRES.

3685 5.2.1.1 Radiation Patterns

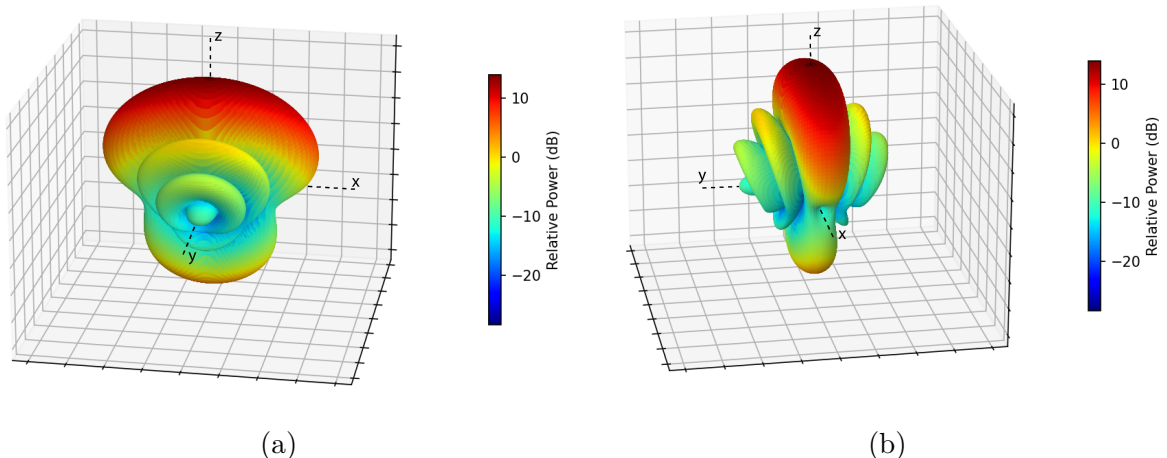


Figure 5.1. An example radiation pattern generated using HFSS simulations. The color and radial distance of the surface from the origin indicate the relative magnitude of radiation power emitted by the antenna in that direction. The primary goal of most antenna measurements is typically to measure the antenna pattern, which is used to derive many useful antenna performance parameters.

3686 Antennas are conductive structures designed to carry alternating electric currents
3687 to transmit energy in the form of EM waves [67]. Perhaps the most fundamental way
3688 to characterize an antenna, is to map out the radiated power density as a function of
3689 position, which is called the radiation pattern (see Figure 5.1). The radiation power
3690 density is obtained by calculating the time-averaged Poynting vector for all positions
3691 surrounding the antenna, which in equation form is

$$\mathbf{W}(x, y, z) = \langle \mathbf{E}(x, y, z, t) \times \mathbf{H}^*(x, y, z, t) \rangle_t, \quad (5.1)$$

3692 where $\mathbf{E}(x, y, z, t)$ and $\mathbf{H}(x, y, z, t)$ are the time-dependent electric and magnetic fields
 3693 produced by the antenna [49]. The radiation power density has units of W/m^2 and is
 3694 more typically called the energy flux density in physics applications, since it is a measure
 3695 of the amount of energy passing through a unit area over time.

3696 Because the radiation power density is a measure of power per unit area, its value
 3697 in a particular direction will depend on the distance from the antenna at which one is
 3698 measuring. This is undesirable for practical applications. A related quantity, which is
 3699 distance independent, is the energy flux per unit solid angle or radiation intensity, which
 3700 is computed directly from the radiation power density by multiplying by the squared
 3701 distance from the antenna. Specifically,

$$U = r^2 W(x, y, z), \quad (5.2)$$

3702 where r is the distance from the antenna to the field measurement point. The radiation
 3703 intensity is typically defined in regions where the Poynting vector consists only of a radial
 3704 component where it is safe to treat as a scalar quantity.

3705 5.2.1.2 Directivity and Gain

3706 Since the radiation intensity is a measure of average power per unit solid angle, it is
 3707 independent of distance and more useful as feature for antenna measurement. The
 3708 radiation intensity is directly related to antenna directivity and gain, which are common
 3709 antenna engineering figures-of-merit. Directivity is defined as the ratio between the
 3710 radiation intensity at particular point on the radiation pattern to the average radiation
 3711 intensity computed over all solid angles [67]. The equation that relates the radiation
 3712 intensity to directivity is

$$D = \frac{U}{U_0} = \frac{4\pi U}{P_{\text{rad}}}, \quad (5.3)$$

3713 where U_0 is the average radiation intensity over all solid angles, which simply the total
 3714 radiated power (P_{rad}) divided by 4π . Closely related to directivity is antenna gain, which
 3715 accounts for energy losses that occur inside then antenna when attempting to transmit
 3716 or receive a signal. The antenna gain is given by

$$G = \frac{4\pi U}{P_{\text{in}}}, \quad (5.4)$$

3717 where P_{in} is the total power delivered to the antenna. Gain can be thought of as the ratio
 3718 of the antenna's radiation intensity to that of a hypothetical isotropic, lossless radiator.

3719 The maximum values of gain and directivity exhibited by the main lobe of the antenna
 3720 pattern as well as the ratio between the gain of the main lobe and any side-lobes are
 3721 important figures-of-merit to evaluate antenna design performance.

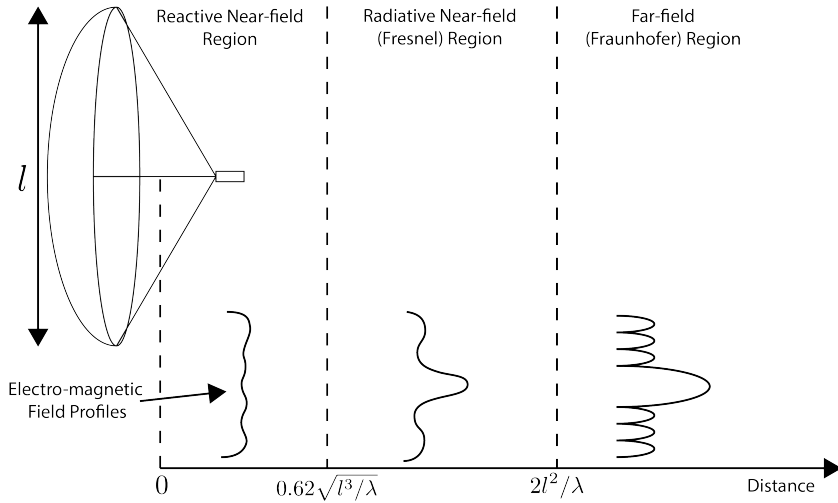


Figure 5.2. An illustration of the three field regions important for the analysis of an antenna system. Very close to the antenna the electric fields are primarily reactive so there is no radiation. If a receiving antenna were placed in this region most of the energy would be reflected back to the transmitter. Outside of the reactive near-field is the radiative near field. At these distances the antenna does radiate, but the radiation pattern is not well-defined since it changes based on the distance of the receiving antenna. It is only in the far-field region where the radiation pattern becomes constant as a function of distance, which is where the majority of antenna engineering is assumed to take place. The antenna arrays developed by Project 8 for CRES measurements operate in the radiative near-field due to the importance of limiting power loss from free-space propagation, which complicates the design of the antenna system.

3722 5.2.1.3 Far-field and Near-field

3723 Radiation patterns are well-defined only in regions where the shape of the radiation
 3724 pattern is independent of distance. The region where this approximation is valid is called
 3725 the "far-field", and in this region the EM fields from the antenna can be approximated as
 3726 spherical plane waves. A rule of thumb for antennas is that the far-field approximation
 3727 applies when the condition

$$R > \frac{2l^2}{\lambda} \quad (5.5)$$

3728 is true. In this expression, R is the distance from the antenna, l is the largest characteristic
 3729 dimension of the antenna, and λ is the wavelength of the radiation (see Figure 5.2).

3730 The region very close to the antenna is called the reactive near-field, because in this
 3731 region the reactive component of the EM field is dominant. Unlike radiative electric

fields, the reactive electric and magnetic fields are out of phase from each other by 90° , since they are caused by electrostatic and magnetostatic effects from the self-capacitance and self-inductance of the antenna. The reactive fields are unable to transfer energy a significant distance from the antenna and are thus completely negligible for most antenna applications. The limit of the reactive near-field for an electrically-large antenna is typically taken to be

$$R < 0.62\sqrt{l^3/\lambda}. \quad (5.6)$$

The unique application of antennas by Project 8 is limited by reactive near-field effects, since it defines an absolute minimum distance for detectable electrons inside the uniform cylindrical antenna array. If electrons are too close to the edge of the array than reactive near-field effects leads to a large reduction in the received power and detection efficiency. This leads to a significant volume inside the antenna array that is unsuitable for CRES lowering the volumetric efficiency of the antenna array CRES technique.

Between the reactive near-field and the far-field is the radiative near-field region. In this region the fields are primarily radiative, however, it is too close to the antenna for the spherical plane wave approximation to apply. Therefore, interference effects between EM waves emitted from different points on the antenna occur causing the shape of the radiation pattern to change as a function of distance from the antenna. Evaluating the far-field distance limit for the FSCD antennas one finds an estimated far-field distance of 43 cm, which is a factor of four larger than the radius of the antenna array designed for the experiment. Consequently, it is expected that near-field effects will influence the performance of the antenna array highlighting the importance of calibration and characterization measurements to mitigate these effects.

5.2.1.4 Polarization

The polarization of an EM wave defines the spatial orientation of the electric field oscillations. Conventionally, polarization vectors are defined in the plane perpendicular to the direction of propagation for the EM wave. For radiation moving in the radial (\hat{r}) direction the electric field can be decomposed into the orthogonal basis

$$\mathbf{E}_{\text{tot}} = E_\theta \hat{\theta} + E_\phi \hat{\phi}, \quad (5.7)$$

assuming a spherical coordinate system.

In general, one defines partial radiation patterns, directivities, and gains so that the performance of the antenna can be analyzed for the desired polarization. The radiation

³⁷⁶² pattern defined in terms of partial patterns is

$$U_{\text{tot}} = U_\phi + U_\theta, \quad (5.8)$$

³⁷⁶³ where U_ϕ and U_θ are the radiation intensities in a particular direction for the respective
³⁷⁶⁴ polarization components. Similarly, a quantity such as gain can be written in terms of
³⁷⁶⁵ partial gains,

$$G_{\text{tot}} = G_\phi + G_\theta = \frac{2\pi U_\phi}{P_{\text{in}}} + \frac{2\pi U_\theta}{P_{\text{in}}}. \quad (5.9)$$

³⁷⁶⁶ An electron performing a circular orbit in the XY-plane from the side, viewed along
³⁷⁶⁷ the X or Y axes, would be seen as performing a linear oscillation perpendicular to the
³⁷⁶⁸ viewing axis. From this picture, one would predict that the primary polarization of
³⁷⁶⁹ electric fields from CRES events is linearly polarization in the $\hat{\phi}$ direction in the XY-plane.

³⁷⁷⁰ 5.2.1.5 Antenna Factor and Effective Aperture

³⁷⁷¹ A useful way to characterize the performance of an antenna is to measure the electric
³⁷⁷² field magnitude required to produce a signal with an amplitude of one volt in the antenna
³⁷⁷³ terminals. This ratio between the magnitude of the incoming electric field and the
³⁷⁷⁴ magnitude of the signal produced by the antenna is called the antenna factor, which is
³⁷⁷⁵ written as

$$A_F = \frac{|\mathbf{E}_{\text{in}}|}{V_{\text{ant}}}, \quad (5.10)$$

³⁷⁷⁶ where A_F is the antenna factor, E_{in} is the incoming electric field, and V_{ant} is the magnitude
³⁷⁷⁷ of the voltage produced by the antenna.

³⁷⁷⁸ The antenna factor can be expressed in terms of the antenna's gain through a related
³⁷⁷⁹ quantity called the effective aperture. The effective aperture defines for a given incident
³⁷⁸⁰ radiation power density (W/m^2) the power that is received by the antenna. Therefore,
³⁷⁸¹ the effective aperture gives the equivalent area of the antenna,

$$A_{\text{eff}} = \frac{P_{\text{rec}}}{P_{\text{in}}} = \frac{\lambda^2}{4\pi} G, \quad (5.11)$$

³⁷⁸² where the received power is P_r and the total incoming power is P_{in} .

³⁷⁸³ The magnitude of the Poynting vector can be written as

$$|\mathbf{S}_{\text{in}}| = |\mathbf{E}_{\text{in}}|^2 / \eta_0, \quad (5.12)$$

3784 where η_0 is the impedance of free-space, which relates the magnitudes of the electric and
3785 magnetic fields in a vacuum, and is defined by

$$\eta_0 = \frac{|\mathbf{E}|}{|\mathbf{H}|} = \sqrt{\frac{\epsilon_0}{\mu_0}}. \quad (5.13)$$

3786 Therefore, the total received power by the antenna is

$$P_{\text{rec}} = |\mathbf{S}_{\text{in}}| A_{\text{eff}} = |\mathbf{S}_{\text{in}}| \frac{\lambda^2}{4\pi} G = \frac{|\mathbf{E}_{\text{in}}|^2 \lambda^2 G}{4\pi \eta_0}. \quad (5.14)$$

3787 To relate this to the antenna factor recall that the voltage produced by the antenna
3788 is related to the received power by

$$P_{\text{rec}} = \frac{V_{\text{ant}}^2}{Z} = \frac{|\mathbf{E}_{\text{in}}|^2}{A_{\text{F}}^2 Z}, \quad (5.15)$$

3789 where Z is the system impedance. Setting Equations 5.14 and 5.15 equal to each other,
3790 one obtains the following expression for antenna factor in terms of gain

$$A_{\text{F}} = \sqrt{\frac{4\pi\eta_0}{ZG\lambda^2}} = \frac{9.73}{\lambda\sqrt{G}}. \quad (5.16)$$

3791 The second expression in Equation 5.16 is obtained by evaluating the constant terms
3792 assuming a system impedance of 50Ω .

3793 This exercise highlights that the majority of antenna parameters that one cares
3794 to measure about an antenna can be obtained from the radiation or gain pattern of
3795 the antenna. The antenna factor is a particularly important parameter for CRES
3796 measurements due to it's relevance to antenna array simulations with the Locust software
3797 [64, 81].

3798 To compute the response of the antenna to the electric field, Locust relies upon
3799 linear time-invariant system theory, which computes the response of the antenna (i.e. the
3800 voltage time series generated by the antenna) using a convolution between the electric field
3801 time-series and the antenna impulse response. This approach is necessary for correctly
3802 modeling the antenna response to the electric field due to the broadband and non-
3803 stationary nature of the electric fields from CRES events. Since antenna measurements
3804 take place under steady-state conditions, parameters such as the radiation pattern, gain,
3805 and antenna factor are defined in the frequency domain. However, by performing an
3806 inverse Fourier transform on the antenna factor one obtains the antenna impulse response,

3807 which is used to calculate CRES signal voltages in Locust.

3808 5.2.2 Antenna Measurement Fundamentals

3809 5.2.2.1 Friis Transmission Equation

3810 The antenna factor or antenna transfer function is used to model how the antenna
3811 responds to electric fields emitted from a CRES event. Therefore, directly measuring the
3812 antenna transfer functions of the array is a key step in the commissioning and calibrating
3813 the FSCD experiment. A common approach to antenna characterization is to perform a
3814 two antenna transmit-receive measurement where an antenna with a known gain is used
to characterize the unknown gain of the antenna under test (see Figure 5.3).

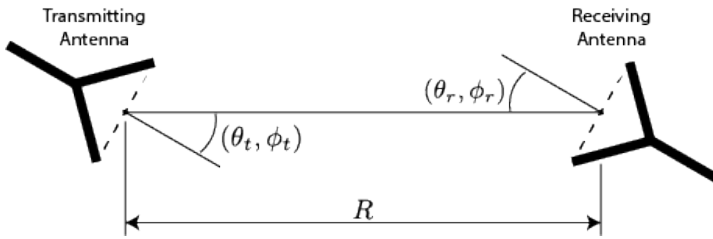


Figure 5.3. An illustration of the Friis measurement technique commonly used for antenna characterization measurements.

3815
3816 Analyzing this two antenna setup involves calculating the power received from the
3817 transmitting antenna. The received power density is expressed as a function of the
3818 antenna gain in a direction (θ_t, ϕ_t) at frequency f and distance R

$$w_t = \frac{P_t}{4\pi R^2} G_t(\theta_t, \phi_t, f), \quad (5.17)$$

3819 where the subscript t denotes the transmitting antenna, and P_t is the total power delivered
3820 to the transmitting antenna. The power density is power per unit area, so the total
3821 power delivered to the receiving antenna is the transmitted power density multiplied by
3822 the effective area of the receiving antenna

$$P_r = w_t A_{\text{eff},r} = P_t \frac{G_t(\theta_t, \phi_t, f) G_r(\theta_r, \phi_r, f) c^2}{(4\pi R f)^2}, \quad (5.18)$$

3823 where $G_r(\theta_r, \phi_r, f)$ is the gain of the receiving antenna. Equation 5.18 is called the Friis
3824 transmission equation [87], which is of fundamental importance for antenna measurements,
3825 since it allows one to measure the gain of an unknown antenna by measuring the power

3826 received from an antenna with a known gain pattern. Alternatively, if an antenna with a
 3827 known gain pattern is unavailable, two identical antennas with unknown gain patterns
 3828 can be used.

3829 **5.2.2.2 S-Parameters and Network Analyzers**

3830 It is more common to measure the ratio of the received power to the transmitted power
 3831 instead of the absolute received power

$$\frac{P_r}{P_t} = \frac{G_t(\theta_t, \phi_t, f) G_r(\theta_r, \phi_r, f) c^2}{(4\pi R f)^2}. \quad (5.19)$$

3832 This power ratio can be easily measured using a vector network analyzer (VNA), which
 3833 automates a significant fraction of the measurement process. Network analyzers are used
 3834 to measure the scattering or S-parameters of a multi-port RF device [88], which describes
 3835 how waves are scattered between the device ports. Friis antenna measurements can be
 3836 modeled as a two-port microwave device that is characterized by measuring how incident
 3837 voltage waves are transmitted or reflected (see Figure 5.4). The scattered waves (V_1^-

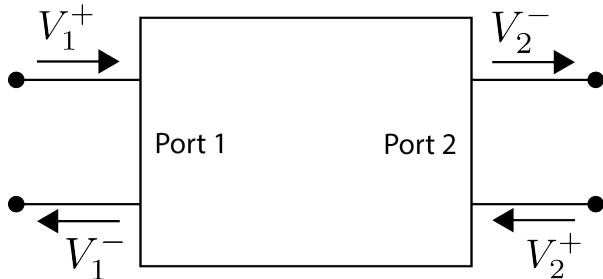


Figure 5.4. Illustration of a two-port S-parameter measurement setup. S-parameters characterize how incoming waves of voltage or power scatter off of the RF device under test. This allows you to measure important properties of the device. In particular, this framework can be used to model a two antenna radiation pattern measurement, which can be automated using a VNA.

3838 and V_2^-) can be written in terms of the incident (V_1^+ and V_2^+) waves using the scattering
 3839 matrix

$$\begin{pmatrix} V_1^- \\ V_2^- \end{pmatrix} = \begin{pmatrix} S_{11} & S_{12} \\ S_{21} & S_{22} \end{pmatrix} \begin{pmatrix} V_1^+ \\ V_2^+ \end{pmatrix}, \quad (5.20)$$

3840 where the elements of the matrix are the device S-parameters. It is assumed that,
 3841 when exciting the device from a particular port, that all other ports in the network are
 3842 terminated at the system impedance. This ensures that the incident waves from other
 3843 ports in the network are zero. Therefore, the S-parameters are the ratios between the

3844 scattered and incident waves,

$$S_{ij} = \frac{V_i^-}{V_j^+}. \quad (5.21)$$

3845 Alternatively, S-parameters can be defined as the ratio of the scattered and incident
3846 power, which is proportional to the ratio of the squared voltage waves.

3847 Returning to the antenna measurement setup, it is clear that measuring the ratio of
3848 the received to the transmitted power is equivalent to measuring the ratio of power being
3849 scattered from port 1 to port 2 in a RF network. Therefore, measuring an antenna's gain
3850 can be accomplished quite easily using a VNA to perform a two port S_{21} measurement.

3851 **5.2.2.3 Antenna Array Commissioning and Calibration Measurements**

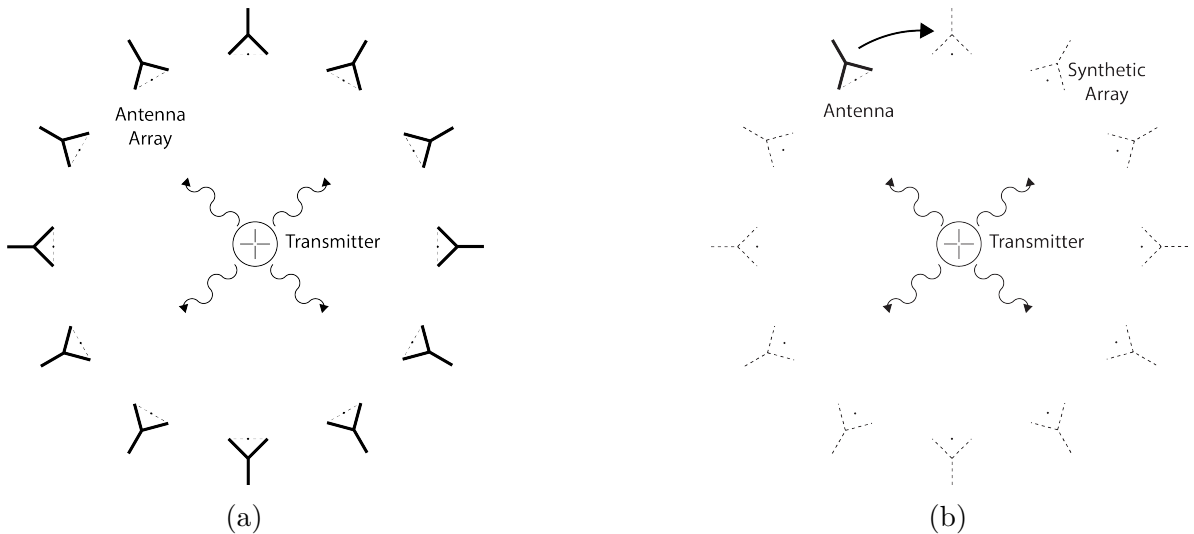


Figure 5.5. Two measurement approaches to characterizing an antenna array for CRES measurements. The full-array approach (a) requires a complete antenna array with all the associated hardware. The synthetic array approach (b) utilizes a single antenna and a set of rotation/translation stages to reposition the transmitter or the receiving antenna to synthesize the signals that would be received by the full-array. This approach reduces the cost and complexity of array measurements. A down-side of the synthetic array approach is that multi-channel effects such as reflections cannot be measured. Utilizing both the full-array and the synthetic array is a powerful way to quantify the impact of errors from the multi-channel array.

3852 Measuring the gain of each individual array element allows to predict the features of
3853 the signals received during a CRES event (see Section 5.2.1.5). However, unpredictable
3854 changes to the antenna performance can be introduced by the incorporation of the
3855 antennas into the circular array geometry, therefore, both individual antenna and full-

array characterization measurements are performed as part of the commissioning of the FSCD.

There are two main approaches to array measurements that could be used for characterization and calibration (see Figure 5.5). One approach is to construct the complete array and use a omni-directional transmitting antenna to measure the power received by each channel in the antenna array. In Section 5.3 I describe the development of an omni-directional transmitter that also mimics the radiation phase characteristics of a CRES event, which is useful because the entire array can be tested without repositioning. Alternatively, a full antenna array can be synthesized by repeatedly moving and measuring a single array element. This approach is ideal for identifying if different channels in the antenna array are affecting each other through multi-path interference by comparing the measurement results of the synthetic array to the real array.

5.2.3 The Penn State Antenna Measurement System

The development of antenna array based CRES requires the capability to test and calibrate different antenna array designs to validate the performance of the as-built antenna array before and during the experiment. With these aims in mind an antenna measurement system was developed at Penn State specifically designed to mimic the characteristics of the FSCD experiment.

The Penn State antenna measurement system utilizes a two antenna measurement configuration with a stationary reference antenna and a test antenna mounted on a set of motorized translation and rotation stages (see Figure 5.6). The antenna measurement system can be operated in two distinct modes, one focused on the characterization of the radiation patterns of prototype antennas, and the other focused on the validation of data-acquisition (DAQ) and CRES signal reconstruction techniques to bridge the gap between real measurements and simulation. In both measurement configurations, it is critical to isolate the antennas from the environment so that multi-path reflections do not negatively influence the measurement results. For this reason the measurement volume is surrounded with microwave absorber foam (AEMI AEC-1.5) specifically designed to attenuate microwave radiation near the 26 GHz measurement range of the system.

In the first measurement configuration, the reference antenna is a well-characterized horn antenna as pictured, since horn antennas have well-known and stable radiation patterns making them ideal as standard references. For characterization measurements, the test antenna represents the antenna-under-test whose pattern is being characterized. Mounting the test antenna on motorized rotation and translation stages allows for

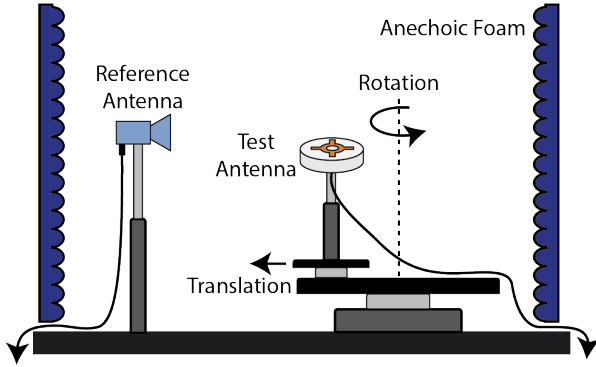


Figure 5.6. Illustration of the antenna measurement system developed for the Project 8 Collaboration. The reference and test antennas can be connected to different data acquisition configurations depending on the measurement goals. The reference antenna is typically a standard horn antenna and the test antenna is mounted on a set of translation stages for positioning. Automated translation stages allows for relatively painless data-taking enabling synthetic antenna array measurements using only a single receiving antenna. Anechoic form designed to mitigate RF reflections surrounds the setup.

3890 automation, which significantly speeds up the radiation pattern measurement process.

3891 The second measurement configuration mimics the conditions of the FSCD as it
 3892 concerns the antenna array and DAQ system. In this configuration, the reference antenna
 3893 is a prototype FSCD antenna, and the test antenna is a specially designed synthetic
 3894 cyclotron antenna (SYNCA) as picture in Figure 5.6. The SYNCA is designed such that
 3895 the radiation pattern mimics that of a CRES electron so that the signals received by the
 3896 prototype CRES array antenna mimic what is expected for a real CRES experiment.

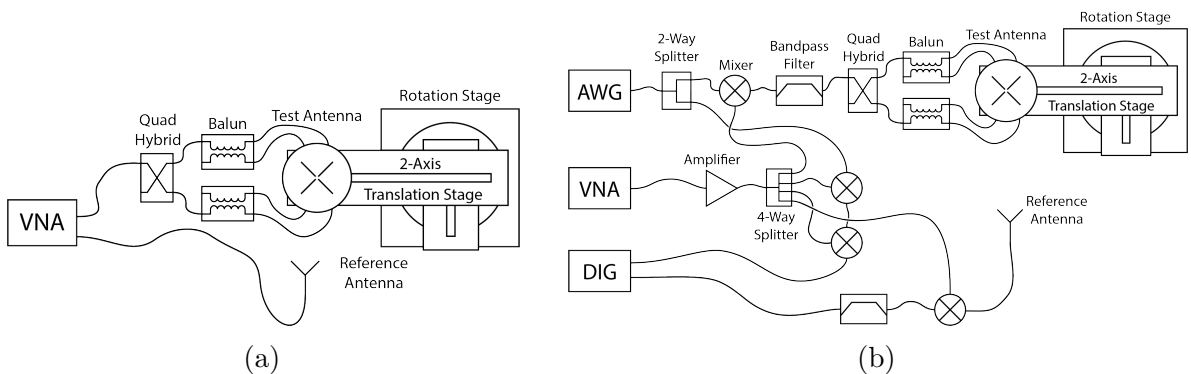


Figure 5.7. Diagrams of two measurement system configurations. Configuration (a) utilizes a VNA and is more suited to antenna characterization. Configuration (b) utilizes an AWG and VNA as a signal generation system and digitizer to collect measurement data, which is more suited to simulating CRES measurements. The transmission chain utilizes a quadrature hybrid and a pair of baluns to drive the cross-dipole variant test antenna developed for synthetic CRES measurements.

3897 Figure 5.7 shows two high-level system diagrams of the Penn State antenna measure-
3898 ment system that depict the important system components and the connections between
3899 them. The two configurations of the measurement system utilize different hardware. For
3900 characterization and radiation pattern measurements, the configuration shown in Figure
3901 5.7a is used. In this case a vector network analyzer (VNA) is used as the transmission
3902 source and data acquisition system, which is easy to calibrate over a wide range of
3903 frequencies. The configuration in 5.7b is used to mimic the FSCD experiment, since this
3904 system includes a more realistic receiver chain.

3905 The characterization configuration utilizes a network analyzer (Keysight N5222A)
3906 with two independent sources and four measurement ports as the primary measurement
3907 tool. A standard reference antenna is connected to one measurement port, and the test
3908 antenna is connected to a second port. The typical reference antenna used for these
3909 studies is a Pasternack PF9851 horn antenna. In the measurement shown, the test
3910 antenna represents a SYNCA antenna, which requires a transmission chain consisting of
3911 quadrature hybrid coupler (Marki QH-0226) connected to two baluns (Marki BAL-0026)
3912 to generate feed signals with the appropriate phases. The VNA measures the radiation
3913 pattern by performing a transmission S-parameter measurement, which can be used with
3914 the knowledge of the reference antenna's radiation pattern to determine the radiation
3915 pattern of the test antenna (see Section 5.2.1).

3916 The second configuration incorporates more hardware components to mimic the DAQ
3917 system envisioned for the FSCD experiment. The basic approach is to produce CRES-like
3918 radiation and use an antenna combined with a realistic RF receiver chain to acquire the
3919 signals. On the transmit side, an arbitrary waveform generator (AWG, RIGOL DG5252)
3920 is used to generate a waveform that mimics a CRES signal at a baseband frequency up
3921 to 250 MHz. This frequency is then up-converted to the CRES signal frequency band
3922 of 25.8 to 26.0 GHz using a mixer (Marki MM1-0832L) and a bandpass filter (K&L
3923 Microwave 3C62-25900/T200-K/K) to reject unwanted mixing components outside out
3924 of the 200 MHz CRES signal band. The local oscillator signal for mixing is provided by
3925 one of the VNA sources configured to run in a continuous wave setting. On the receive
3926 side, a prototype antenna is used to detect the radiation emitted by the test antenna,
3927 which is down-converted and filtered using the same mixer and bandpass filter as the
3928 transmission chain. Lastly, data acquisition is performed using a 14-bit ADC sampling
3929 at 500 MSa/s (CAEN DT530) to digitize the down-converted signals.

3930 In order to distribute the LO to all mixers a 4-way power splitter (MiniCircuits
3931 ZC4PD-18263-S+) along with an amplifier (Marki APM-6848) is used to drive the four

mixers used in the measurement system. A limitation of using the VNA as an LO source is that there is no control of the LO phase when a measurement is triggered by the control script, which leads to a random phase offset between acquisitions. This makes it impossible to perform synthetic array measurements, which require strict control over the starting phase of the transmitted signal. In order to monitor the random phase of the LO, a 2-way power splitter (MiniCircuits Z99SC-62-S+) is used to split the signal from the AWG between the transmission path and a LO monitoring path. The LO monitoring path consists of an up-conversion and down conversion using two mixers connected by a coaxial cable, and monitors the relative phase of the LO using a channel on the digitizer to sample this path. A phase shift in the LO will lead to a proportional phase shift in the mixed signal, which is measured and removed from the received signals.

The test antenna is mounted on a set of motorized stages, which are identical for both measurement configurations. A rotational stage (ThorLabs PRMTZ8) is used as the base layer with additional translation stages mounted on top. The rotational stage is ideal for measuring a complete azimuthal scan of the test antenna's radiation pattern as well as for moving a SYNCA antenna in circular motion to recreate the symmetry of the FSCD antenna array. On top of the rotational stage, are mounted two linear translation stages (ThorLabs MTS50-Z8 and MTS25-Z8) in a cross-wise manner so that the test antenna can be moved along two perpendicular axes. Using the linear stages in combination with the rotational stage allows one to fine-tune the positioning of the test antenna so that it can be perfectly aligned with the central axis of the array. A LabView script was developed to automate the measurement of a full 360° radiation pattern and control the measurement electronics. Data from these acquisitions is stored on university provided cloud storage.

5.3 Development of a Synthetic Cyclotron Antenna (SYNCA) for Antenna Array Calibration

This section is the manuscript of the publication [82] detailing the development of a Synthetic Cyclotron Antenna (SYNCA) for antenna array characterization measurements by the Project 8 collaboration.

5.3.1 Introduction

Neutrinos are the most abundant standard model fermions in our universe, but due to weak interaction cross-sections with other particles, neutrinos are particularly difficult to study. Consequently, many fundamental properties of neutrinos are still unknown including the absolute scale of the neutrino mass [24]. Direct, kinematic measurements of the neutrino mass are particularly valuable due to their model independent nature [37]. To date the most sensitive direct neutrino mass measurements have been performed by the KATRIN collaboration [89], which measures the molecular tritium β -decay spectrum to infer the neutrino mass. Current data from neutrino oscillation measurements [24] allow for neutrino masses significantly smaller than the design sensitivity of the KATRIN experiment; therefore, there is a need for new technologies for performing direct neutrino mass measurements to probe lower neutrino masses.

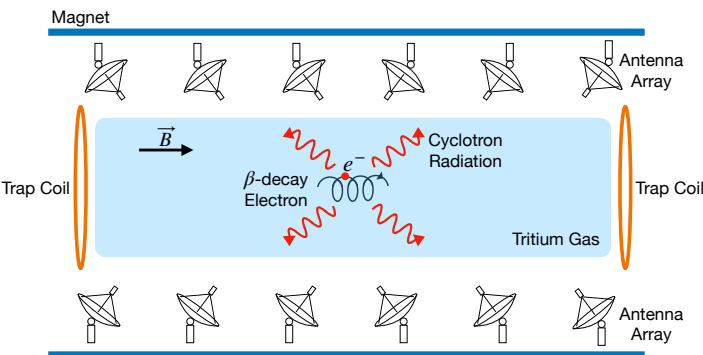


Figure 5.8. A sketch of an antenna array large-volume CRES experiment. Electrons from β -decays are confined in a magnetic field using a set of trap coils. The cyclotron radiation produced by the motion of the trapped electrons can be detected by a surrounding antenna array to determine the electron energies. Measuring the energies of many electrons produces a β -decay spectrum.

The Project 8 collaboration is developing new methods for neutrino mass measurement based on Cyclotron Radiation Emission Spectroscopy (CRES) [56, 90–92], with the goal of measuring the absolute scale of the neutrino mass with a $40 \text{ meV}/c^2$ sensitivity [?, 37]. This sensitivity goal will require the development of two separate technical capabilities. First is the development of an atomic tritium source, which avoids significant spectral broadening due to molecular final states [55]. Second is the technology for performing CRES in a multi-cubic-meter experimental volume with high combined detection and reconstruction efficiency, which is required in order to obtain sufficient event statistics near the tritium spectrum endpoint.

One approach for a large-volume CRES experiment is to use an array of antennas, which surrounds a volume of tritium gas, to detect the cyclotron radiation produced by the β -decay electrons when they are trapped in a background magnetic field using a set of magnetic trapping coils (see Figure 5.8). Project 8 has developed a conceptual experiment design to study the feasibility of this approach. The design consists of a single circular array of antennas with a radius of 10 cm and 60 independent channels positioned around the center of the magnetic trap. The motivation behind this antenna array design is to first develop an understanding of the antenna array approach to CRES with a small scale experiment before attempting to scale the technique to large volumes by using multiple antenna rings to construct the full cylindrical array. The development of the antenna array approach to CRES has largely proceeded through simulations using the Locust software package [81, 93], which is used to model the fields emitted by CRES events and predict the signals received by the surrounding antenna array. To validate these simulations, a dedicated test stand is being constructed to perform characterization measurements of the prototype antenna array developed by Project 8 (see Figure 5.9) and benchmark signal reconstruction methods using a specially designed transmitting calibration probe antenna.

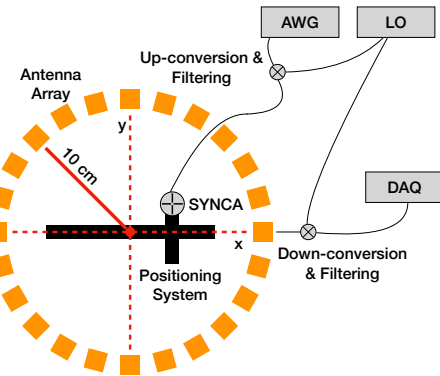


Figure 5.9. A schematic of the antenna array test stand. The circular antenna array has a radius of 10 cm with 60 independent channels (limited number shown for clarity). The test stand includes an arbitrary waveform generator (AWG), local oscillator (LO), and data acquisition (DAQ) hardware. Finally, a specialized Synthetic Cyclotron Antenna (SYNCA) is used to inject signals to test the antenna array.

We call this probe antenna the Synthetic Cyclotron Antenna or SYNCA. The SYNCA is a novel antenna design that mimics the cyclotron radiation generated by individual charged particles trapped in a magnetic field, which will be used in the antenna test stand to perform characterization measurements, simulation validation, and reconstruction benchmarking. This paper provides an overview of the design, construction, and

4004 characterization measurements of the SYNCA performed in preparation for its usage as
 4005 a transmitting calibration probe.

4006 In Section 5.3.2 we provide a description of the cyclotron radiation field characteristics
 4007 that we recreate with the SYNCA. In Section 5.3.3 we give an overview of the simulations
 4008 performed to develop an antenna design that mimics the characteristics of cyclotron
 4009 radiation. In Section 5.3.4 we outline characterization measurements to validate that
 4010 the fields generated by the SYNCA match simulation, and finally in Section 5.3.5 we
 4011 demonstrate an application of the SYNCA to test phased array reconstruction techniques
 4012 on the bench-top.

4013 5.3.2 Cyclotron Radiation Phenomenology

4014 To understand the cyclotron radiation phenomenology that the SYNCA should mimic,
 4015 we consider a charged particle moving at relativistic speed in the presence of an external
 4016 magnetic field (see Figure 5.10). In the special case we shall examine, the entirety of
 4017 the electron's momentum is directed perpendicular to the magnetic field; therefore, the
 4018 trajectory of the electron is confined to the cyclotron orbit plane. Because the momentum
 4019 vector is oriented perpendicular to the magnetic field, electrons with these trajectories
 4020 are said to have pitch angles of 90°.

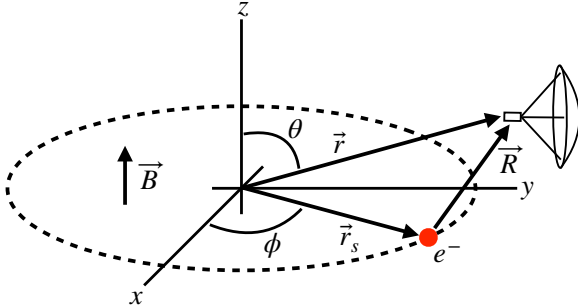


Figure 5.10. An electron (red dot) performing cyclotron motion in the x-y plane. The resulting cyclotron radiation is observed by an antenna located at the field point of interest.

4021 The cyclotron radiation fields generated by this circular trajectory are those which
 4022 we aim to reproduce with the SYNCA. We can describe the electromagnetic (EM) fields
 4023 using the Liénard-Wiechert equations [49, 81], which in non-covariant form express the
 4024 electric field as

$$\vec{E} = e \left[\frac{\hat{n} - \vec{\beta}}{\gamma^2 (1 - \vec{\beta} \cdot \hat{n})^3 |\vec{R}|^2} \right]_{tr} + \frac{e}{c} \left[\frac{\hat{n} \times [(\hat{n} - \vec{\beta}) \times \dot{\vec{\beta}}]}{(1 - \vec{\beta} \cdot \hat{n})^3 |\vec{R}|} \right]_{tr}, \quad (5.22)$$

4025 where e is the particle's charge, $\hat{n} = (\vec{r} - \vec{r}_s)/|\vec{r} - \vec{r}_s|$ is the unit vector pointing from the
 4026 electron to the field measurement point, $\vec{\beta} = \dot{\vec{r}}_s/c$ is the velocity of the particle divided
 4027 by the speed of light, and γ is the relativistic Lorentz factor. The equation is meant to
 4028 be evaluated at the retarded time as indicated by $t_r = t - |\vec{R}|/c$, which accounts for the
 4029 time delay due to the finite speed of light between the point where the field was emitted
 4030 and the point where the field is detected.

4031 We would like to simplify Equation 5.22 it at all possible. As a first step we analyze
 4032 the relative magnitudes of the electric field polarization components. Consider an electron
 4033 following a circular cyclotron orbit in a uniform magnetic field whose guiding center
 4034 is positioned at the origin of the coordinate system. The equation of motion can be
 4035 expressed as

$$\vec{r}_s = (r_c \cos \omega_c t_r) \hat{x} + (r_c \sin \omega_c t_r) \hat{y}. \quad (5.23)$$

4036 For single antenna located along the y -axis at position $\vec{r} = r_a \hat{y}$ we are interested in the
 4037 incident electric fields from the electron. The electric field is given by Equation 5.22,
 4038 which we evaluate in the regime where $r_a \gg r_c$. This limit can be justified by comparing
 4039 the radius of the cyclotron orbit for an electron with the tritium beta-spectrum endpoint
 4040 energy of 18.6 keV in a 1 T magnetic field to the typical ($r_a \simeq 100$ mm) radial position
 4041 of the receiving antenna. We find that the cyclotron orbit has a radius of 0.46 mm which
 4042 is approximately a factor of 200 smaller than the typical antenna radial position. In this
 4043 regime we can make the approximation $\vec{R} \simeq r_a \hat{y}$ and the expression for the electric field
 4044 at the antenna's position becomes

$$\vec{E} = \frac{e}{\gamma^2 r_a^2} \frac{\hat{x} \left(\frac{r_c \omega_c}{c} \sin \omega_c t_r \right) + \hat{y} \left(1 - \frac{r_c \omega_c}{c} \cos \omega_c t_r \right)}{(1 - \frac{r_c \omega_c}{c} \cos \omega_c t_r)^3} - \frac{e}{cr_a} \frac{\hat{x} \left(\frac{r_c^2 \omega_c^3}{c^2} - \frac{r_c \omega_c^2}{c} \cos \omega_c t_r \right)}{(1 - \frac{r_c \omega_c}{c} \cos \omega_c t_r)^3}. \quad (5.24)$$

4045 Since the receiving antenna is part of a circular array of antennas, it is useful to rewrite
 4046 Equation 5.24 in terms of the azimuthal ($\hat{\phi}$) and radial (\hat{r}) polarizations. Making use of
 4047 the fact that for an antenna located at $R = r_a \hat{y}$ that $\hat{\phi} = -\hat{x}$ and $\hat{r} = \hat{y}$ we find

$$\vec{E} = \hat{\phi} E_\phi + \hat{r} E_r \quad (5.25)$$

$$E_\phi = \frac{e}{(1 - \frac{r_c \omega_c}{c} \cos \omega_c t_r)^3} \left[-\frac{\frac{r_c \omega_c}{c} \sin \omega_c t_r}{\gamma^2 r_a^2} + \frac{\omega_c \left(\frac{r_c^2 \omega_c^2}{c^2} - \frac{r_c \omega_c}{c} \cos \omega_c t_r \right)}{cr_a} \right] \quad (5.26)$$

$$E_r = \frac{e \left(1 - \frac{r_c \omega_c}{c} \sin \omega_c t_r \right)}{\gamma^2 r_a^2 (1 - \frac{r_c \omega_c}{c} \cos \omega_c t_r)^3}. \quad (5.27)$$

4048 For the purposes of designing a synthetic cyclotron radiation antenna we are interested
 4049 in the dominant electric field polarization emitted by the electron. The antenna is being
 4050 designed to mimic the cyclotron radiation produced by electrons with kinetic energies of
 4051 approximately 18.6 keV in a 1 T magnetic field [55]. Since the relativistic beta factor for
 4052 an electron with this kinetic energy is $|\vec{\beta}| \simeq \frac{1}{4}$, the approximations $\gamma \simeq 1$ and $\frac{r_c \omega_c}{c} \simeq \frac{1}{4}$ are
 4053 justified. Inserting these expressions into the equations for the electric field components
 4054 above simplifies the comparison of the magnitudes of the two components. Additionally,
 4055 we compare the time-averaged magnitudes to evaluate the root mean squared electric
 4056 field ratio. The time-averaged ratio of the radial and azimuthally polarized electric fields
 4057 with the above simplifications is given by

$$\frac{\langle |E_r| \rangle}{\langle |E_\phi| \rangle} = \frac{8 - \sqrt{2}}{\left| 1 - \frac{r_a}{r_c} \frac{1-2\sqrt{2}}{8} \right|} \simeq \frac{r_c}{r_a} \frac{8(8 - \sqrt{2})}{2\sqrt{2} - 1} = 0.13, \quad (5.28)$$

4058 where we have made use of the fact that for these magnetic fields and kinetic energies
 4059 the cyclotron radius is much smaller than the radius of the antenna array.

4060 From Equation 5.28 we see that the time-averaged azimuthal polarization is larger than
 4061 the radial polarization by about a factor of 8, which makes it the dominant contribution
 4062 to the electric fields at the position of the antenna. We must also consider the directivity
 4063 of the receiving antenna which can have a gain that is disproportionately large for a
 4064 specific polarization component. Because the E_ϕ component is dominant, the receiving
 4065 antenna array is designed with an azimuthal polarization, which negates the voltages
 4066 induced in the antenna from the radially polarized fields. Therefore, we conclude that
 4067 for the purpose of designing the SYNCA antenna it is acceptable to approximate the
 4068 electric fields from Equation 5.22 as purely azimuthally or ϕ -polarized. The simplified
 4069 expression for the electric field received by an antenna becomes

$$\vec{E} = E_\phi \hat{\phi} = \frac{e^{\frac{r_c \omega_c}{c}}}{4r_a r_c} \left[\frac{\frac{r_c \omega_c}{c} - \cos \omega_c t - \frac{4r_c}{r_a} \sin \omega_c t}{(1 - \frac{r_c \omega_c}{c} \cos \omega_c t)^3} \right]_{t_r} \hat{\phi}, \quad (5.29)$$

4070 where the radius of the cyclotron orbit is called r_c , the cyclotron frequency is called ω_c ,
 4071 and the radial position of the receiving antenna is called r_a . Equation 5.29 has been
 4072 evaluated in the non-relativistic limit where $\gamma \simeq 1$, which is justified by the fact that
 4073 $|\vec{\beta}| \simeq \frac{c}{4}$ for an electron with an 18.6 keV kinetic energy in a 1 T magnetic field.

4074 This rather complicated expression can be simplified using Fourier analysis. Assuming
 4075 a background magnetic field of 1 T and a kinetic energy of 18.6 keV we calculate

4076 numerically the electric field using Equation 5.29 and apply a discrete Fourier Transform
to visualize the frequency spectrum (see Figure 5.11).

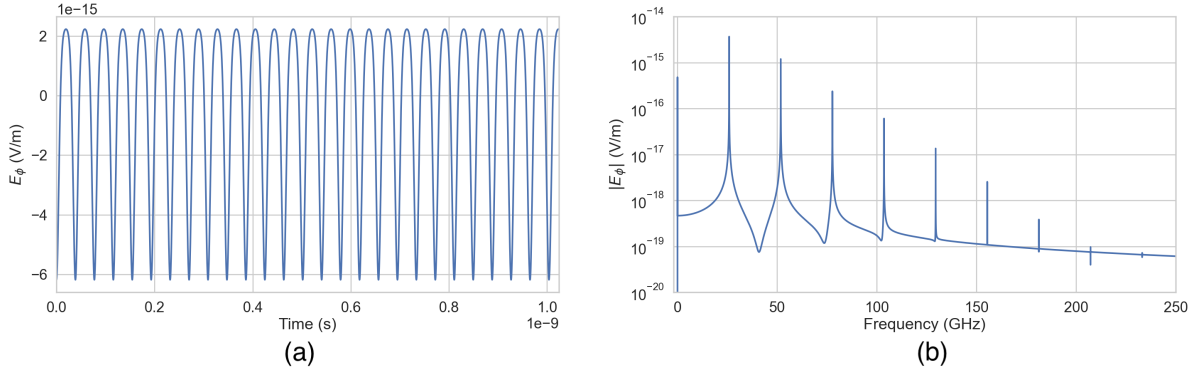


Figure 5.11. A plot of the numeric solution to Equation 5.30. The time-domain representation of the signal (a) is composed of a zero frequency term and a series of harmonics separated by the main cyclotron frequency as shown in the plot of the frequency spectrum (b). We can see that the relative amplitude of the harmonics beyond $k = 7$ are smaller than the main carrier by a factor of about 10^{-5} and are completely negligible.

4077
4078 We observe that the azimuthally polarized electric field is periodic with a base cyclotron
4079 frequency of 25.898 GHz corresponding to the highest power frequency component in
4080 Figure 5.11. The frequency spectrum reveals that the signal is composed of a constant
4081 term with zero frequency and a series of harmonics separated by 25.898 GHz. Therefore,
4082 we can represent the azimuthal electric fields from the electron as a linear combination
4083 of pure sinusoids with frequencies given by $\omega_k = k\omega_c$ ($k \in 0, 1, 2, \dots$) and amplitudes
4084 extracted from the Fourier representation. Using this representation we can transform
4085 the equation for the azimuthally polarized electric fields in Equation 5.29 into

$$E_\phi = \frac{e^{\frac{r_c \omega_c}{c}}}{4r_a r_c} \sum_{k=0}^7 A_k e^{i\omega_k t_r}, \quad (5.30)$$

4086 where we have truncated the sum over harmonics at the 7th order for completeness. The
4087 amplitudes A_k are dimensionless complex numbers, which encode the relative powers of
4088 the harmonics as well as the starting overall phase of the cyclotron radiation. Because
4089 magnitude of the relative amplitudes exponentially decreases for higher harmonics, it is
4090 usually sufficient to consider only the terms up to $k = 4$ where the relative amplitude
4091 of the harmonics has decreased from the main carrier by a factor of approximately 100.
4092 However, for completeness we include harmonics up to 7th order in Equation 5.30. The
4093 range of frequencies to which the receiving antenna array in the antenna test stand is
4094 sensitive is defined by the antenna's transfer function. The receptive bandwidth for

4095 the antennas used in the test stand is a range of frequencies with a bandwidth on the
 4096 order of a few GHz centered around the main cyclotron carrier frequency of 25.898 GHz.
 4097 Therefore, the higher order harmonics as well as the zero frequency term can be ignored
 4098 when considering only the signals that will be received by the antenna array.

4099 Considering only the 1st order harmonic term from Equation 5.30, which represents
 4100 the portion of the electric field that will be detected by the array, and evaluating this at
 4101 the retarded time we obtain the following for the ϕ -polarized electric fields

$$E_\phi \propto \cos \left(\omega_c \left(t - |\vec{R}|/c \right) - \Delta \right), \quad (5.31)$$

4102 where the arbitrary phase Δ is defined by $A_k = |A_k|e^{i\Delta}$. We are interested in the
 4103 characteristics of the amplitude of the electric field as a function of the radial distance
 4104 component ($|\vec{R}|$) of the retarded time. In particular, the maximum of E_ϕ occurs when
 4105 the argument of the cosine function is equal $n\pi$ where $n \in \{0, \pm 2, \pm 4, \dots\}$; however, the
 4106 solutions where n is negative can be discarded since they represent unphysical negative
 4107 overall phases. Applying this condition to Equation 5.31 gives a condition on the radial
 4108 position of the maximum of E_ϕ

$$\omega_c(t - |\vec{R}|/c) - \Delta = n\pi, \quad (5.32a)$$

$$|\vec{R}| = \frac{c}{\omega_c} ((\omega_c t - \Delta) - n\pi), \quad (5.32b)$$

4109 which is a function of time in the frame of the moving electron (t). Equation 5.32 can
 4110 be further simplified by noticing that the azimuthal position of the electron ($\phi_e(t)$) as a
 4111 function of time is defined by $\phi_e(t) = \omega_c t - \Delta$ which reduces Equation 5.32 to

$$|\vec{R}| = \frac{c}{\omega_c} (\phi_e(t) - n\pi). \quad (5.33)$$

4112 Equation 5.33 represents an archimedian spiral which is formed when plotting the
 4113 amplitude of E_ϕ in the x-y plane. The solution where $n = 0$ represents the leading edge
 4114 of the radiation spiral which propagates outward from the electron at the speed of light.
 4115 The additional solutions for $n > 0$ represent the persistent spiral at radii inside the
 4116 leading edge of the radiated fields that have not yet been detected by the receiver at the
 4117 current time. In Figure 5.12a we show the expected spiral pattern for the maxima of the
 4118 cyclotron radiation.

4119 In particular, we note that for the circular array geometry of the test stand, depicted
 4120 as the series of circles in Figure 5.12a, each antenna receives a linearly polarized wave

4121 with a phase offset that corresponds to the azimuthal angle for that antenna element.
 4122 Therefore, as we show in Figure 5.12b, when the relative phase of the received signal is
 4123 plotted as a function of the receiving antenna's azimuthal position the result is also an
 4124 Archimedean spiral.

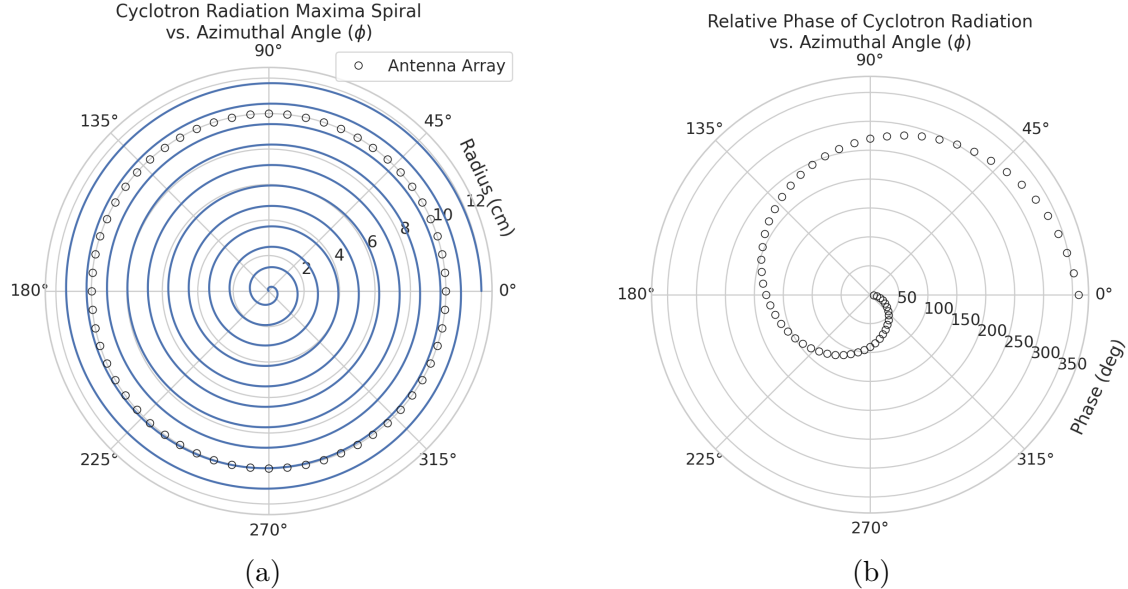


Figure 5.12. The amplitude maxima of the cyclotron radiation form an Archimedean spiral as the radiation propagates outward from the cyclotron orbit center (a). A circular antenna array located at a fixed radius from the orbit center will receive electric fields with equal magnitude in each of its channels, but the phase of the electric field incident on each array channel will be linearly out of phase from its neighbor antennas by an amount equal to the angular separation of the two channels (b).

4125 Based on these analytical calculations we can characterize the magnitude, polarization,
 4126 and phase of the signals received by the antenna array using three criteria. These criteria
 4127 are the basis of comparison for the radiation produced by the SYNCA and cyclotron
 4128 radiation emitted by electrons and will be used to evaluate the performance of antenna
 4129 designs. The criteria are:

- 4130 1. Electric fields that are ϕ -polarized near $\theta = 90^\circ$
- 4131 2. Uniform time-averaged electric field magnitudes around the circumference of a
4132 circle centered on the antenna
- 4133 3. Electric fields whose phase is equal to the azimuthal angle at the point of measure-
4134 ment plus a constant

4135 The Locust simulation package [93] can be used to directly simulate the EM fields
 4136 generated by electrons performing cyclotron motion to validate the analytical calculations.
 4137 Locust simulates the EM fields by first calculating the trajectory of the electrons in
 4138 the magnetic trap using the Kassiopeia software package [94]. The trajectory can then
 4139 be used to solve for the EM fields using the Liénard-Wiechert equations directly with
 4140 no approximations. The resulting electric field solutions drive a receiving antenna by
 4141 convolving the time-domain fields with the finite-impulse response filter of the antenna
 4142 or they can be examined directly to study the field characteristics that the SYNCA must
 4143 reproduce. In the next section we compare the radiation field patterns for electrons
 4144 simulated with Locust to patterns from a SYNCA antenna design.

4145 **5.3.3 SYNCA Simulations and Design**

4146 One potential SYNCA design is the crossed-dipole antenna [95]. A crossed-dipole antenna
 4147 consists of two dipole antennas, one of which is rotated 90° with respect to the other,
 4148 which are fed with signals that are out of phase from the opposite dipole by 90° (see
 Figure 5.13). This arrangement causes the signals fed to each arm of the dipole to be

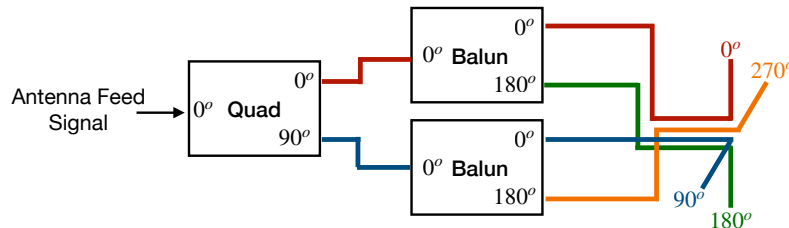


Figure 5.13. An idealized crossed-dipole antenna consists of two electric dipole antennas oriented perpendicular to each other and is fed with four signals with a quadrature phase relationship. An example antenna feed circuit is shown which is composed of a chained combination of a quadrature hybrid-coupler (Quad) and two baluns.

4149
 4150 out of phase from each of the neighboring arms by 90°, which mirrors the spatial phase
 4151 relationship of cyclotron radiation fields.

4152 A potential drawback of this design is that standard crossed-dipole antennas do not
 4153 radiate uniform electric fields near the $\theta = \pi/2$ plane. Typical crossed-dipole antennas
 4154 use dipole arm lengths equal to $\lambda/4$ or larger [95], where λ is the wavelength at the
 4155 desired operating frequency. Such large arm lengths cause the electric field magnitude
 4156 to vary significantly around the circumference of the antenna. However, making the

4157 antenna electrically small by shrinking the arm length can improve the antenna pattern
4158 uniformity.

4159 In general, the criterion for an electrically small antenna is that the largest dimension
4160 of the antenna (D) obey $D \lesssim \lambda/10$ [67]. In our application, we are attempting to mimic
4161 the cyclotron radiation emitted by electrons produced from tritium β -decay with energies
4162 near the spectrum endpoint. For a background magnetic field of 1 T, the corresponding
4163 cyclotron frequency of tritium endpoint electrons is approximately 26 GHz. Therefore, the
4164 electrically small condition would require that the largest dimension of the crossed-dipole
4165 antenna be smaller than 1.2 mm.

4166 A crossed-dipole antenna with an overall size of 1.2 mm is challenging to fabricate due
4167 to the small dimensions of the dipole arms that, in practice, are fragile and unsuitable
4168 for use as a calibration probe. To mitigate some of the challenges with the fabrication
4169 of such a small antenna, a variant crossed-dipole antenna design using printed circuit
4170 board (PCB) technology (see Figure 5.14) was developed in partnership with an antenna
prototyping company, Field Theory Consulting ¹.

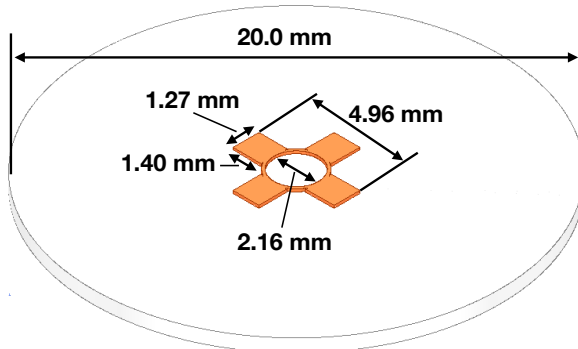


Figure 5.14. A model of the PCB crossed-dipole antenna with dimensions. The design has an inside diameter of 2.16 mm for the central circular trace, which is 0.13 mm wide. The dipole arms each have a width of 1.27 mm and protrude beyond the circular trace by 1.40 mm, which gives an overall width of 4.96 mm for the length of the antenna PCB trace from end-to-end. The overall size of the antenna is 20.0 mm the majority of which is the PCB dielectric material. This design was observed in simulation to maintain the field characteristics of the idealized crossed-dipole while being simpler to fabricate due to the increased size of the antenna.

4171
4172 The PCB crossed-dipole design uses four rectangular pads to represent the dipole arms,
4173 which are connected by a thin circular trace. The circular trace both adds mechanical
4174 stability to the antenna and improves the azimuthal uniformity of the electric fields
4175 compared to a more standard crossed-dipole geometry. Furthermore, the circular trace

¹<https://fieldtheoryinc.com/>

4176 allows for a greater separation between dipole arms than standard crossed-dipoles, which
 4177 is required to accommodate the coaxial connections to each pad. The pads each contain
 4178 a through-hole solder joint to connect coaxial transmission lines using hand soldering.
 4179 The antenna PCB has no ground plane on the bottom layer as this was observed in
 4180 simulation to significantly distort the radiation pattern in the plane of the PCB. The
 4181 only ground planes present in the model are the outer conductors of the four coaxial
 4182 transmission lines which feed the antenna. These are left unterminated on the bottom of
 4183 the PCB dielectric material.

4184 The antenna design development utilized a combination of Locust electron simula-
 4185 tions and antenna simulations using ANSYS HFSS [68], a commercial finite-element
 4186 electromagnetic simulation software. Two antenna designs were simulated: an idealized
 4187 electrically small crossed-dipole antenna with an arm length of 0.40 mm and an arm
 4188 separation of 0.05 mm, as well as a PCB crossed-dipole antenna with the dimensions
 4189 shown in Figure 5.14. Plotting the magnitude of the electric fields generated by the
 4190 antennas across a 10 cm square located in the same plane as the respective antennas
 4191 reveals the expected cyclotron spiral pattern (see Figure 5.15) which closely matches
 4192 the prediction for simulated electrons. The spiral pattern demonstrates that the electric
 4193 fields have the appropriate phases to mimic cyclotron radiation, which fulfills SYNCA
 criterion 3 identified in Section 5.3.2.

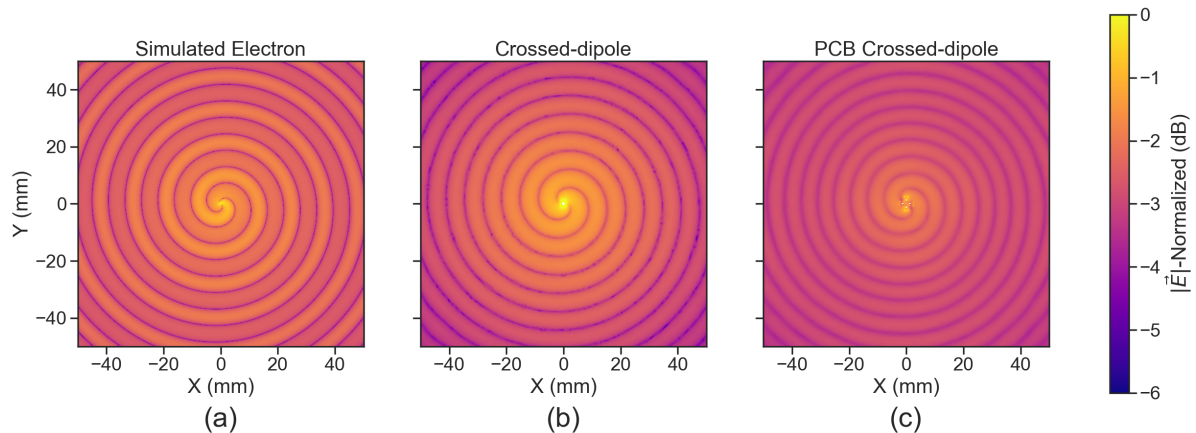


Figure 5.15. A comparison of the electric field magnitudes, normalized by the maximum value of the electric field in each simulation, plotted on a 10 cm square to visualize the Archimedean spirals formed by the electron (a), the crossed-dipole antenna (b), and a PCB crossed-dipole antenna (c). The matching patterns indicate that the electric fields have similar phase characteristics. These images were generated using Locust simulations for the electron and ANSYS HFSS for both antennas.

4194

4195 As we can see from Figure 5.16, the crossed-dipole antenna, which uses an idealized

4196 geometry, exhibits good agreement with simulation. The antenna has a maximum
 4197 deviation from a simulated electron of approximately 0.5 dB in the total electric field, 1
 4198 dB for the ϕ -polarized electric field and 1 dB for the θ -polarized electric field.

4199 In comparison, the pattern of the PCB crossed-dipole antenna, because the simulation
 4200 incorporates the geometry of the coax transmission lines, exhibits some distortion from
 4201 the idealized cross-dipole simulations. The vertically oriented ground planes of the coax
 4202 lines introduce more θ -polarized electric fields than are observed for simulated electrons
 4203 near $\theta = 90^\circ$. The significant θ -polarized field minimum is still present but shifted
 to approximately $\theta = 65^\circ$. The θ -polarized field deviations of the PCB crossed-dipole

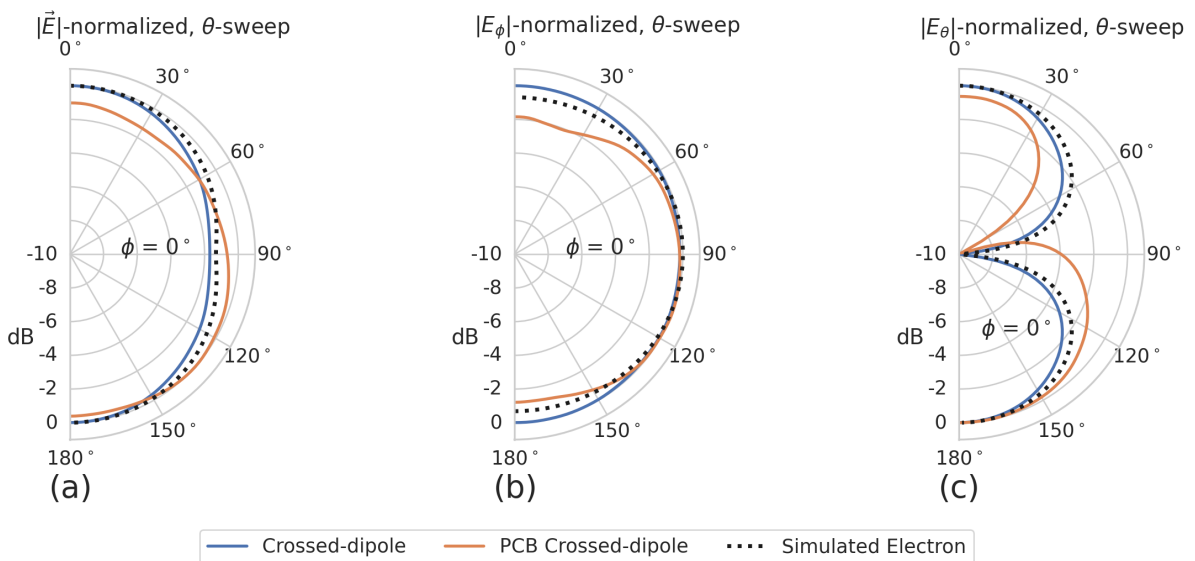


Figure 5.16. A comparison of the normalized electric field magnitudes for the ideal crossed-dipole, PCB crossed-dipole, and a simulated electron as a function of the polar angle (θ). (a) Shows the total electric field, (b) shows the ϕ -polarized electric field component, and (c) shows the θ -polarized electric field component. These images were generated using Locust simulations for the electron and ANSYS HFSS for both antennas.

4204
 4205 antenna should not greatly impact the performance of the antenna because the receiving
 4206 antenna array is primarily ϕ -polarized. Therefore deviations in the θ -polarized fields
 4207 will be suppressed due to the polarization mismatch. More importantly, the ϕ -polarized
 4208 electric field pattern generated by the PCB crossed-dipole closely matches simulated
 4209 electrons across the polar angle range of $50^\circ < \theta < 150^\circ$. In this region the PCB crossed-
 4210 dipole differs by less than 0.5 dB from simulated electrons. This range greatly exceeds
 4211 the beamwidth of the receiving antenna array which is designed to be most sensitive
 4212 to fields produced near $\theta = 90^\circ$. Therefore, we conclude that the PCB crossed-dipole
 4213 antenna generates a ϕ -polarized radiation pattern that fulfills SYNCA criterion 1 from

4214 Section 5.3.2.

4215 The final SYNCA criterion is related to the uniformity of the electric fields when
4216 measured azimuthally around the antenna. As we saw for real electrons in Section 5.3.2
4217 it is expected that the magnitude of the electric field be completely uniform as a function
4218 of the azimuthal angle due to the symmetry of the cyclotron orbit. In Figure 5.17 we plot
4219 the total electric field as a function of azimuthal angle for an electron, the crossed-dipole
antenna, and the PCB crossed-dipole antenna. The crossed-dipole antenna exhibits

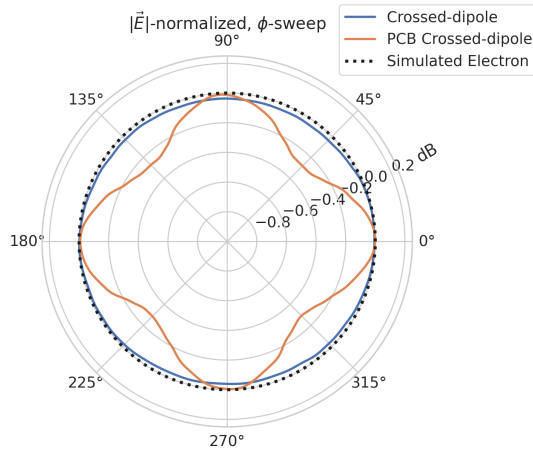


Figure 5.17. A comparison of the normalized electric field magnitudes for the crossed-dipole, PCB crossed-dipole, and a simulated electron as a function of the azimuthal angle (ϕ) evaluated at $\theta = 90^\circ$. This image was generated using Locust simulations for the electron and ANSYS HFSS for both antennas.

4220
4221 perfect uniformity around the azimuthal angle, whereas the PCB crossed-dipole has a
4222 small periodic deviation with a maximum difference of 0.3 dB caused by the coaxial
4223 transmission lines below the PCB. Such a small deviation from uniformity is acceptable
4224 since it is smaller than the expected variation in uniformity caused by imperfections in
4225 the antenna fabrication process, which modifies the antenna shape in an uncontrolled
4226 manner by introducing solder blobs with a typical size of a few tenths of a millimeter on
4227 the dipole arms (see Figure 5.18). Additionally, the SYNCA will be separately calibrated
4228 to account for azimuthal differences in the electric field magnitude. Therefore we see
4229 from the simulated performance of the PCB crossed-dipole antenna that this antenna
4230 design meets all three of the SYNCA criteria.

4231 **5.3.4 Characterization of the SYNCA**

4232 Two SYNCAs were manufactured using the PCB crossed-dipole design (see Figure 5.18).
4233 The antenna PCB (Matrix Circuit Board Materials, MEGTRON 6) is connected to

4234 four 2.92 mm coaxial connectors (Fairview Microwave, SC5843) using semi-rigid coax
 4235 (Fairview Microwave, FMBC002), which also physically support the antenna PCB. The
 4236 antenna PCB consists only of two layers which correspond to the copper antenna trace
 4237 and the PCB dielectric. Each coax line is connected to the associated dipole arm using
 4238 through-hole soldering and phase matched to ensure that the electrical length of each
 4239 of the transmission lines is identical at the operating frequency. The antenna PCB is
 4240 further reinforced using custom cut polystyrene foam blocks, which have an electrical
 4241 permittivity nearly identical to air. A custom 3D printed mount is included at the base
 4242 of the antenna to support the coax connectors and to provide a sturdy mounting base.

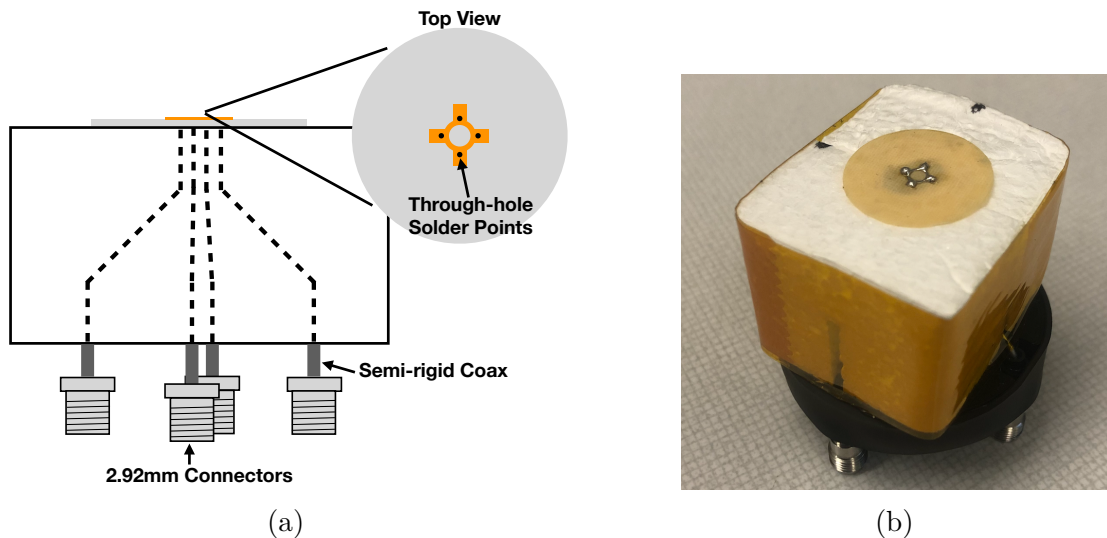


Figure 5.18. (a) A cartoon schematic which highlights the routing of the semi-rigid coax transmission lines. (b) A photograph of a SYNCA constructed using the modified crossed-dipole PCB antenna design. Visible in the photograph of the SYNCA are four blobs of solder which are an artifact of the SYNCA’s hand-soldered construction. These solder blobs are the most significant deviation from the SYNCA design shown in Figure 5.14 and are responsible for a significant fraction of the irregularities seen in the antenna pattern.

4243 Characterization measurements were performed using a Vector Network Analyzer
 4244 (VNA) to measure the electric field magnitude and phase radiated by the SYNCA to
 4245 verify the radiation pattern (see Figure 5.19). The VNA is connected to the SYNCA
 4246 at one port through a hybrid-coupler whose outputs are connected to two baluns to
 4247 generate the signals with the appropriate phases to feed the SYNCA (see Figure 5.13).
 4248 The other port of the VNA is connected to a single reference horn antenna that serves
 4249 as a field probe. To position the SYNCA, a combination of translation and rotation
 4250 stages are used to characterize the antenna’s fields across the entire radiation pattern

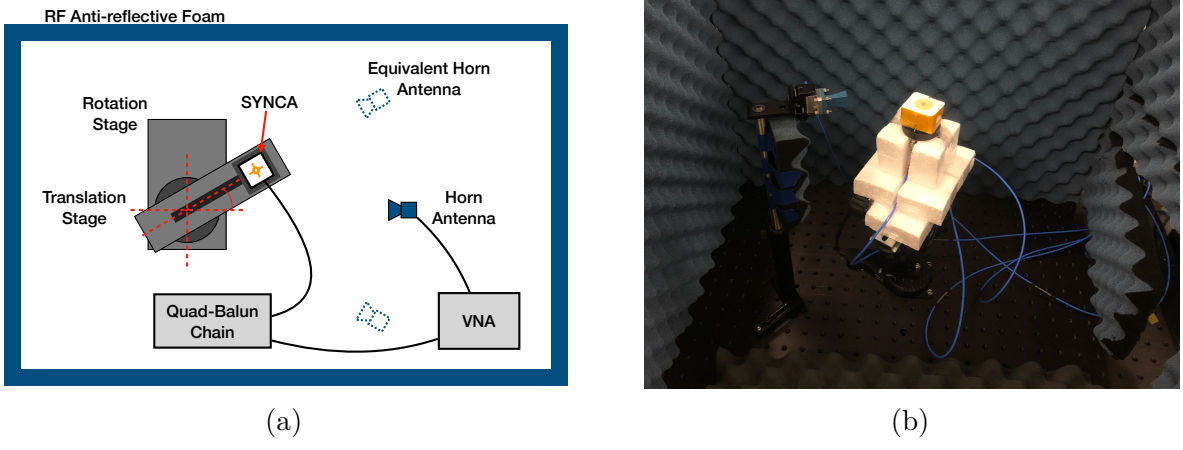


Figure 5.19. A schematic of the VNA characterization measurements (a). This setup allows for antenna gain and phase measurements across a full 360° of azimuthal angles using a motorized rotation stage and control of the radial position of the SYNCA using a translation stage. A photo of the setup in the lab is shown in (b).

4251 circumference. This measurement scheme is equivalent to measuring the fields generated
 4252 by the SYNCA using a full circular array of probe antennas.

4253 The antenna measurement space is surrounded by RF anti-reflective foam to isolate
 4254 the measurements from the lab environment (see Figure 5.19b) and remaining reflections
 4255 are removed using the VNA’s time-gating feature. The SYNCA is affixed to the stages
 4256 by a custom RF transparent mount made of polystyrene foam. The coaxial cables deliver
 4257 the antenna feed signals generated by the VNA to the SYNCA while still allowing
 4258 unrestricted rotation. The horn antenna probe is nominally positioned in the plane
 4259 formed by the antenna PCB ($\theta = 90^\circ$ or $z = 0$ mm) at a distance of 10 cm from the
 4260 SYNCA, to match the expected position of the antenna array relative to the SYNCA in
 4261 the antenna array test stand. The horn antenna can be manually raised or lowered to
 4262 different relative vertical positions to characterize the radiation pattern at different polar
 4263 angles.

4264 Several 360° scans were performed with probe vertical offsets of -10.0 mm, -5.0 mm,
 4265 0.0 mm, 5.0 mm, and 10.0 mm relative to the antenna PCB plane. These probe offsets
 4266 cover a 2 cm wide vertical region centered on the SYNCA PCB, approximately equal to
 4267 ± 6 degrees of polar angle. The measurements show that the SYNCA is generating fields
 4268 with nearly isotropic magnitude across the probed region. The standard deviation of the
 4269 electric field magnitude measured around the antenna circumference is approximately
 4270 2.9 dB for a typical rotational scan. The presence of a significant pattern null is noted

4271 near 45° (see Figure 5.20), which we attribute to small imperfections in the antenna
 4272 PCB that could be introduced from the hand soldered terminations connecting the coax
 4273 cables to the antenna. There is no significant difference in the radiation pattern when
 4274 measured across the 2 cm vertical range. The measured relative phases closely follow
 4275 the expectation for an electron, being linear with the measurement rotation angle and
 4276 forming the expected spiral pattern. Other than the small phase imperfections there is
 4277 a slight sinusoidal bias to the phase data, which we determined is the result of a small
 4278 ($\lesssim 1$ mm) offset of the antenna's phase center from the rotation axis of the automated
 4279 stages.

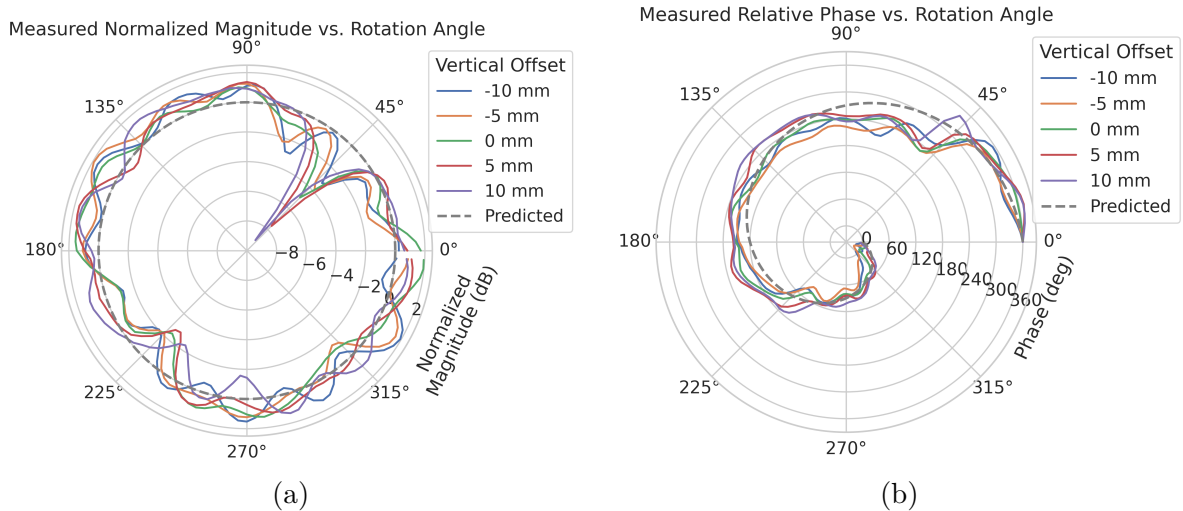


Figure 5.20. Linear interpolations of the measured electric field magnitude (a) and phase (b). The data was acquired using a VNA at 120 points spaced by 3 degrees from 0 to 357 degrees of azimuthal angle. The different color lines indicate the vertical offset of the horn antenna relative to the SYNCA PCB and the dashed line shows the expected shape from electron simulations. No significant difference in the antenna pattern is observed for the measured vertical offsets.

4280 The characterization measurements confirm the simulated performance of the SYNCA.
 4281 As expected the fields generated by the antenna are nearly isotropic in magnitude, ϕ -
 4282 polarized, and are linearly out of phase around the circumference of the antenna as
 4283 predicted for cyclotron radiation in Section 5.3.2. Small imperfections in the magnitude
 4284 and phase of the antenna are expected, particularly at the antenna's high operating
 4285 frequency of 26 GHz where small geometric changes can have significant impacts on
 4286 electrical properties. However, calibration through careful characterization measurements
 4287 can be used to remove the majority of these pattern imperfections, including the relatively
 4288 large pattern null near 45° , which will allow for the usage of the SYNCA as a test source

4289 for free-space CRES experiments utilizing antenna arrays. In the next section we use the
 4290 VNA measurements obtained here as a calibration for signal reconstruction using digital
 4291 beamforming.

4292 5.3.5 Beamforming Measurements with the SYNCA

4293 Digital beamforming is a standard technique for signal reconstruction using a phased
 4294 array [96]. The SYNCA, since it exhibits the same cyclotron phases as a trapped electron,
 4295 can be used to perform simulated CRES digital beamforming reconstruction experiments
 4296 on the bench-top without the need for the magnet, cryogenics, and vacuum systems
 4297 required by a full CRES experiment. The fields received by the individual elements
 4298 of the antenna array will have phases dependent on the spatial position of the source
 4299 relative to the antennas. Therefore, a simple summation of the received signals will fail
 4300 to reconstruct the signal due to destructive interference between the individual channels
 4301 in the array. However, applying a phase shift associated with the source's spatial position
 4302 removes phase differences and results in a constructive summation of the channel signals
 4303 (see Figure 5.21). We can summarize the digital beamforming operation succinctly using
 4304 the following equation

$$y[t_n] = \sum_{m=0}^{N-1} x_m[t_n] A_m e^{i\phi_m}, \quad (5.34)$$

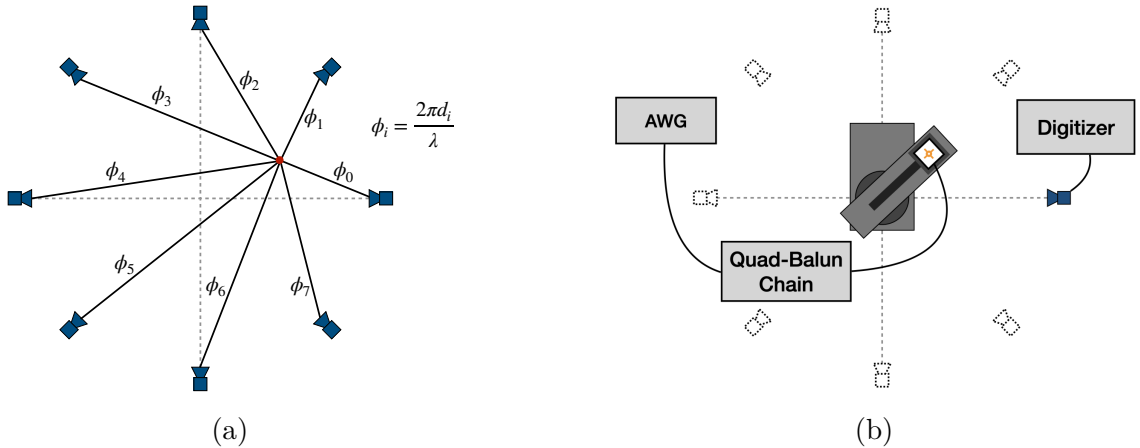


Figure 5.21. (a) A depiction of the relative phase differences for signals received by a circular antenna array from an isotropic source. The phases correspond to a unique spatial position.
 (b) A schematic of the setup used to perform digital beamforming.

4305 where $y[t_n]$ represents the summed array signal at time t_n , $x_m[t_n]$ is the signal received
 4306 by channel m at time t_n , ϕ_m is the phase shift applied to the signal received at channel
 4307 m , and A_m is an amplitude weighting factor that accounts for the different signal power
 4308 received by individual channels. By changing the digital beamforming phases, the point
 4309 of constructive interference can be scanned across the sensitive region of the array to
 4310 search for the location of a radiating source, which is identified as the point of maximum
 4311 summed signal power above a specified threshold. The digital beamforming phases consist
 4312 of two components,

$$\phi_m = 2\pi d_m / \lambda + \theta_m, \quad (5.35)$$

4313 where d_m is the distance from the m -th array element to the source, and θ_m is the
 4314 relative angle between the source position and the m -th antenna. The first component is
 4315 the standard digital beamforming phase that corresponds to the spatial position of the
 4316 source, and the second component is the cyclotron phase that corresponds to the relative
 4317 azimuthal phase offset.

4318 With a small modification to the hardware used to characterize the SYNCA (see
 4319 Figure 5.19), we can perform a digital beamforming reconstruction of a synthetic CRES
 4320 event. By replacing the VNA with an arbitrary waveform generator (AWG), the SYNCA
 4321 can be used to generate cyclotron radiation with an arbitrary signal structure, which
 4322 can then be detected by digitizing the signals received by the horn antenna. Rotational
 4323 symmetry allows us to use the rotational stage of the positioning system to rotate the
 4324 SYNCA to recreate the signals that would have been received by a complete circular
 4325 array of antennas.

4326 Using this setup, signals from a 60 channel circular array of equally spaced horn
 4327 antennas were generated with the SYNCA positioned 10 mm off the central array axis,
 4328 reconstructed using digital beamforming, and compared to Locust simulation (see Figure
 4329 5.22). When the cyclotron spiral phases are not used, which is equivalent to setting θ_m
 4330 in Equation 5.35 to zero, the SYNCA's position is reconstructed as a relatively faint ring
 4331 as predicted by simulation. However, when the appropriate cyclotron phases are used
 4332 during the beamforming procedure, both the simulated electron and the SYNCA appear
 4333 as a single peak of high relative power corresponding to the source position. Therefore,
 4334 we observe good agreement between the simulated and SYNCA reconstructions. While it
 4335 may seem that for the case with no cyclotron phase corrections the ring reconstructs the
 4336 position of the electron as effectively as beamforming with the cyclotron phase corrections,
 4337 it is important to note that the simulations and measurements were generated without a
 4338 realistic level of thermal noise. The larger maxima region and lower signal power, which

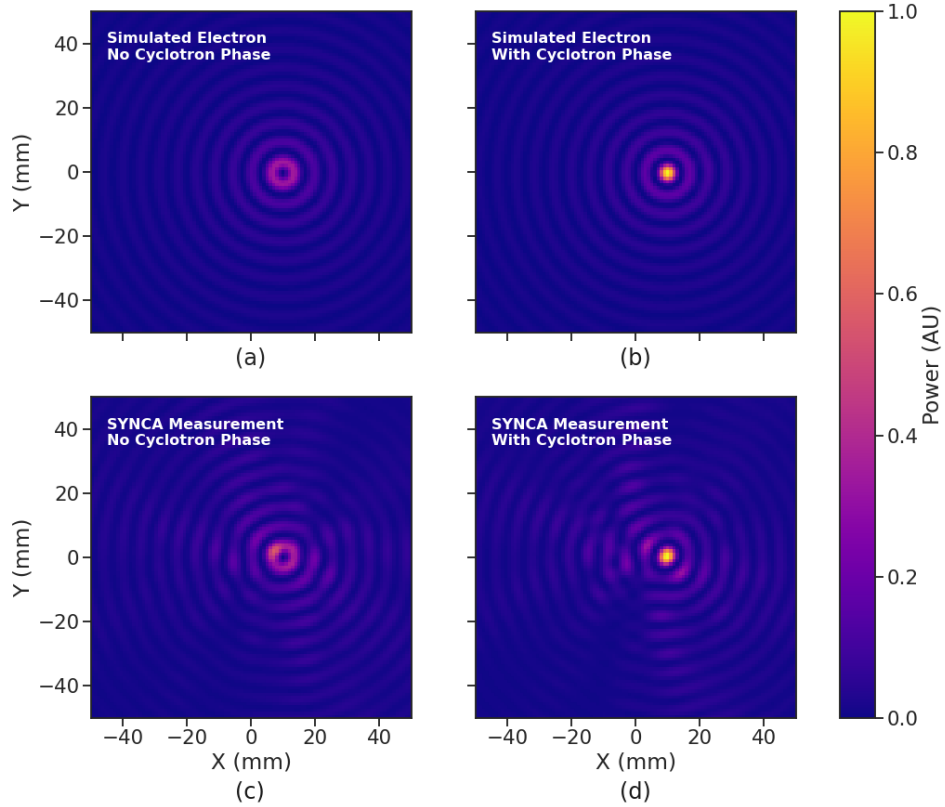


Figure 5.22. Digital beamforming maps generated using a simulated 60 channel array and electron simulated using the Locust package. (a) and (b) show the beamforming maps for simulated electrons without the cyclotron spiral phases and with the cyclotron spiral phases respectively. (c) and (d) show the beamforming maps produced from SYNCA measurements. We observe good agreement between simulated electrons and the SYNCA measurements.

4339 occurs without the cyclotron phase corrections, significantly reduce the probability of
 4340 detecting an electron in a realistic noise background.

4341 To bound the beamforming capabilities of the synthetic array of horn antennas, we
 4342 performed a series of beamforming reconstructions where the SYNCA was progressively
 4343 moved off the central axis of the array (see Figure 5.23). To extract an estimate of the
 4344 position of the SYNCA using the digital beamforming image we apply a 2-dimensional
 4345 (2D) Gaussian fit to the image data and extract the estimated centroid value. We find
 4346 that the synthetic horn antenna array reconstructs the position of the SYNCA with a
 4347 1σ -error of 0.3 mm with no apparent trend across the 30 mm measurement range. This
 4348 reconstruction error is an order of magnitude larger than mean fit position uncertainty
 4349 of 0.02 mm indicating that systematic effects related to the SYNCA positioning system
 4350 could be contributing additional uncertainty to the measurements. Note that the current

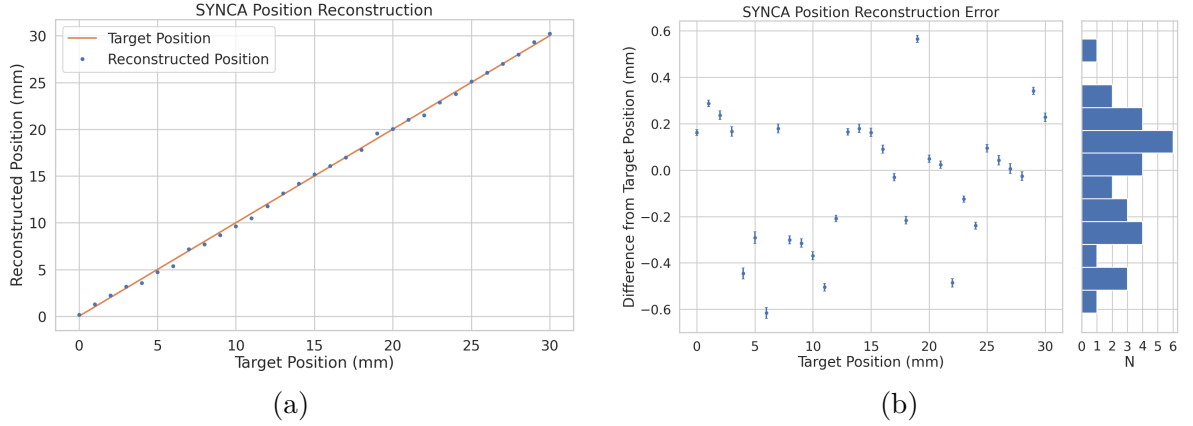


Figure 5.23. A plot of the SYNCA’s reconstructed position using the synthesized horn-antenna array and digital beamforming. (a) Shows the reconstructed position of the SYNCA compared with the target position indicated by the positioning system readout. (b) Shows the reconstruction error, which is the difference between the target and reconstructed positions. The error bars in (b) are the uncertainty in the mean position of the 2D Gaussian used to fit the digital beamforming reconstruction peak obtained from the fit covariance matrix. The mean fit position uncertainty of 0.02 mm is an order of magnitude smaller than the typical reconstruction error of 0.3 mm obtained by calculating the standard deviation of the difference between the reconstructed and target position.

4351 mean reconstruction error of 0.3 mm is a factor of 20 smaller than the full width at half
 4352 maximum of the digital beamforming peak (6 mm), which could be interpreted as a naive
 4353 estimate of the position reconstruction performance of this technique. Because these
 4354 measurements are intended as a proof-of-principle demonstration, we do not investigate
 4355 potential sources of systematic errors further; however, we expect that a similar and
 4356 more thorough investigation will be performed using the Project 8 antenna array test
 4357 stand, where typical reconstruction errors can be used to estimate the energy resolution
 4358 limits of antenna array designs.

4359 5.3.6 Conclusions

4360 In this paper we have introduced the SYNCA, which is a novel antenna design that
 4361 emits radiation that mimics the unique properties of the cyclotron radiation generated by
 4362 charged particles moving in a magnetic field. The characterization measurements of the
 4363 SYNCA validated the simulated performance of the PCB crossed-dipole antenna design.
 4364 Additionally, the SYNCA was used to estimate the position reconstruction capabilities
 4365 of a synthesized array of horn antennas and experimentally reproduced the simulated
 4366 digital beamforming reconstruction of electrons.

4367 While the SYNCA performs well, there exist discrepancies in the phase and magnitude
4368 of the radiation pattern compared to the simulated SYNCA design that are related to
4369 the small geometric differences in the soldered connections. Future design iterations that
4370 replace the soldered connections with a fully surface mount design could improve the
4371 radiation pattern at the cost of some complexity and expense. Furthermore, improving
4372 the design of the antenna PCB and mounting system would allow the antenna to be
4373 inserted into a cryogenic and vacuum environment where in-situ antenna measurement
4374 calibrations could be performed.

4375 The discrepancies in the radiation pattern and phases exhibited by the as-built
4376 SYNCA should not greatly impact its performance as a calibration probe. Both magni-
4377 tude and phase variations can be accounted by applying the SYNCA characterization
4378 measurements as a calibration to the data collected by the antenna array test stand. The
4379 separate calibration of the SYNCA radiation does not impact the primary goals for the
4380 antenna array test stand which are array calibration and signal reconstruction algorithm
4381 performance characterization, because it can be performed with standard reference horn
4382 antennas with well understood characteristics.

4383 The SYNCA antenna technology advances the CRES technique by providing a
4384 mechanism to characterize free-space antenna arrays for CRES measurements without
4385 the need for a magnet and cryogenics system, which would be required for calibration
4386 using electron sources. Both the Project 8 collaboration as well as future collaborations
4387 which are developing antenna array based CRES experiments can make use of SYNCA
4388 antennas as an important component of their calibration and commissioning phases.

4389 **5.4 SYNCA Development Discussion**

4390 A crossed-dipole antenna (see Figure 5.24) was identified early on as a candidate SYNCA
4391 design. The crossed-dipole is a circularly polarized antenna, consequently, the electric
4392 fields measured in the plane of the dipole antenna exhibit the same relative phase offsets
4393 as a 90° electron in a magnetic trap. This is explained in greater detail in Section 5.3.
4394 These phase offsets were measured with the first rudimentary crossed-dipole prototype
4395 manufactured from coaxial cables with the insulation and shield stripped away.

4396 Because the SYNCA is ultimately a calibration tool, it is desireable that the antenna
4397 have a well-characterized and robust antenna pattern. Therefore, manufacturing a
4398 SYNCA using the stripped wire method shown in Figure 5.24 is infeasible. Studies of
4399 crossed-dipole antennas manufactured out of printed circuit boards were performed using

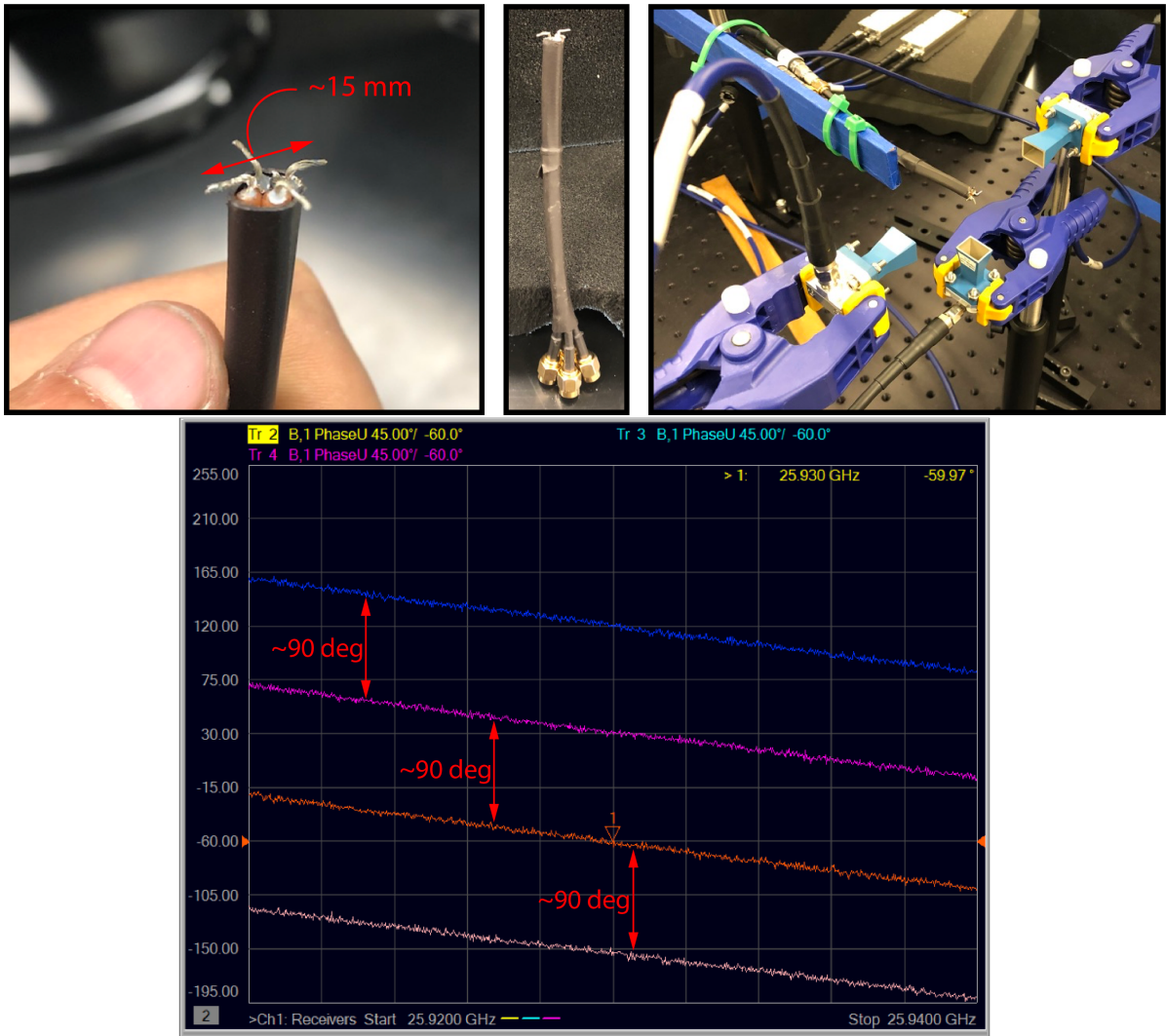


Figure 5.24. Images of an early prototype crossed-dipole antenna manufactured by hand and the first measurement setup. The antenna was constructed by hand using four stripped coaxial cables. The antenna was connected to one port of the VNA, and the remaining three ports on the VNA were connected to horn antenna arranged with 90 deg offsets around the crossed-dipole. The measured unwrapped S-parameter phases exhibit the desired relative phase behavior for a SYNCA. These early measurements were the first laboratory proof-of-principle for the crossed-dipole SYNCA.

4400 HFSS to identify an antenna design that imitated an electron, while being more robust
 4401 and simpler to manufacture (see Figure 5.25).

4402 Identifying a design that was robust, manufacturable, and matched the electric fields
 4403 of a trapped electron proved to be a non-trivial task. The primary factor driving the
 4404 difficulty was the high operating frequency of the antenna (26 GHz) combined with
 4405 the requirement that the antenna be electrically-small. An antenna that is electrically-

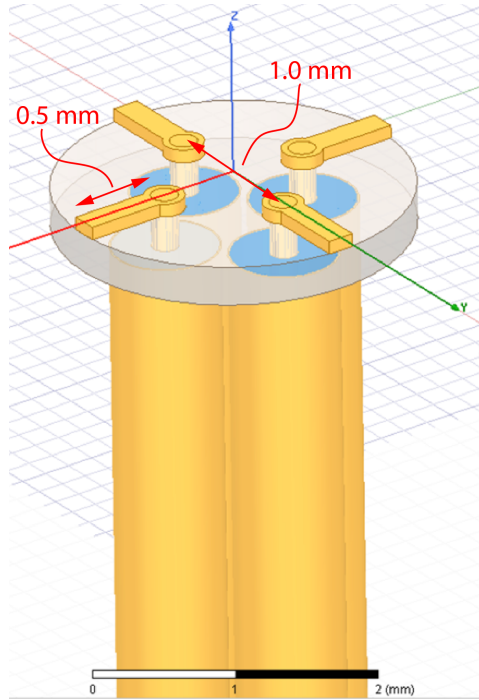


Figure 5.25. An early iteration of a crossed-dipole SYNCA antenna simulated in HFSS. The antenna is electrically small at 26 GHz, which requires dipole arms on the order of 1 mm long. This design is limited by the minimum achievable distance between the dipole arms caused by the available diameters of coaxial cables. The assumed termination scheme for the coaxial cables to the antenna is hand-soldering, which introduces random variation in the antenna pattern from the inevitable blobs of solder left on the surface of the PCB.

4406 small at 26 GHz has a largest dimension on the order of 1 mm, which poses significant
 4407 manufacturability challenges given the limited available budget for SYCNA fabrication.

4408 One of the key limitations with the small size requirements is the diameter of the
 4409 coaxial cables needed to feed the crossed-dipole antenna. The smallest commonly available
 4410 rigid coaxial cables available on the market have diameters of approximately 0.5 mm,
 4411 which limited the spacing between dipole arms to a minimum of about 1 mm. The
 4412 crossed-dipole antenna performs better as a SYNCA if the dipole arm separation is
 4413 significantly less than the operating wavelength. Therefore, the high operating frequency
 4414 ultimately limited how well the SYNCA could mimic an electron. If the desired cyclotron
 4415 frequency was lowered by an order of magnitude to approximately 3 GHz a significantly
 4416 higher quality SYNCA could be manufactured at lower cost.

4417 The decision to use coaxial transmission lines terminated on the antenna PCB with a
 4418 hand-soldered connection was driven primarily to limit the costs of SYNCA development
 4419 and contributed to the observable variations in the SYNCA's gain and phase patterns.

4420 A second iteration of the SYNCA design that minimized hand-soldering by using surface-
4421 mount components could significantly reduce variations in the antenna pattern. The
4422 major drawback in the development of a surface-mount SYNCA is the cost, and given the
4423 transition to a cavity based design for Phase IV, such a design was never investigated.

4424 **5.5 FSCD Antenna Array Measurements with the SYNCA**

4425 **5.5.1 Introduction**

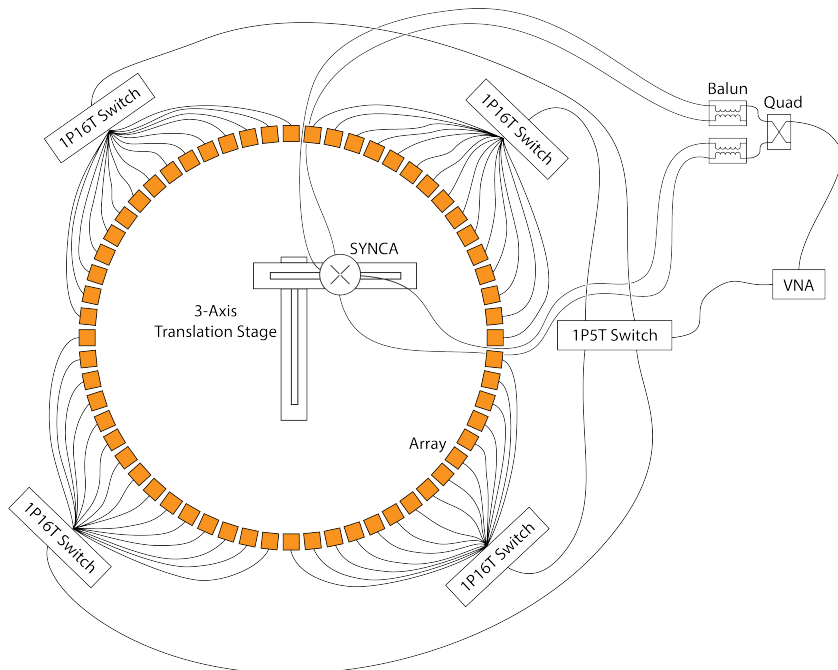


Figure 5.26. A diagram of the array measurement system used to test the prototype FSCD antenna array. A VNA is used as the primary measurement tool, which is connected to the array through a series of switches. The other port of the VNA connects to the SYNCA through the quad-balun chain used to provide the SYNCA feed signals. During measurements the SYNCA is positioned inside the center of the antenna array and translated to different radial and axial positions using a 3-axis manual translation stage setup.

4426 Using the SYNCA it is possible perform full-array measurements of prototype versions
4427 of the FSCD antenna array with a realistic cyclotron radiation source (see Figure 5.26).
4428 The goal is to compare the measured power received to FSCD simulations as a function
4429 of the radial and axial position of the SYNCA source. These measurements are intended
4430 to validate the antenna research and development by Project 8, which has been driven
4431 primarily by simulations with Locust [64] and CRESana (see Section 4.2.3), and identify

any discrepancies with these simulations tools. This knowledge will provide confidence in the simulations necessary for the analysis of the sensitivity of larger antenna array based CRES experiment designs to the neutrino mass.

As shown in Section 5.3, the SYNCA has some radiation pattern imperfections that complicate the comparison between measurement and simulation data. One way to disentangle the effects of these imperfections is to perform an additional set of measurements using a synthetic antenna array setup along with the SYNCA antenna. Since the synthetic array setup uses only a single array antenna, the data should be free of errors associated with individual antenna differences and multi-path interference, which are two error sources being tested with the full-array setup. By comparing the synthetic array data to the FSCD array data and to simulation data one can evaluate the significance of these effects relative to the errors introduced by SYNCA imperfections.

5.5.2 Measurement Setups

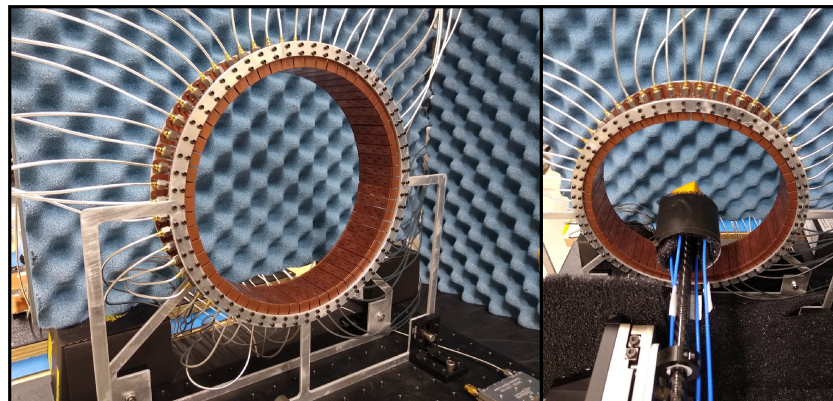
5.5.2.1 FSCD Array Setup

The antenna design that composes the array is the 5-slot waveguide antenna developed for the FSCD experiment (see Figure 5.27a). The antenna is 5 cm long and is constructed out of WR-34 waveguide with a 2.92 mm coax connector located at the center of the antenna. Copper flanges located on both ends of the antenna are used to mount the antenna in the array support structure. The antennas are supported by two circular steel brackets that can be bolted to both ends of the waveguide to construct the circular array (see Figure 5.27b). The antenna array consists of sixty identical waveguide antennas with a radius of 10 cm. The array is mounted perpendicular to an optical breadboard surface using a pair of the steel brackets, which provide sufficient space for the coaxial cable connections and allows for easy positioning of the SYNCA antenna. The SYNCA is mounted on the end of a carbon fiber rod attached to a set of manual translation stages, which are used to move the SYNCA antenna to different positions inside the array (see Figure 5.27c). The stages allow for independent motion in three different axes and can position the SYNCA at radial distances up to 5 cm from the center.

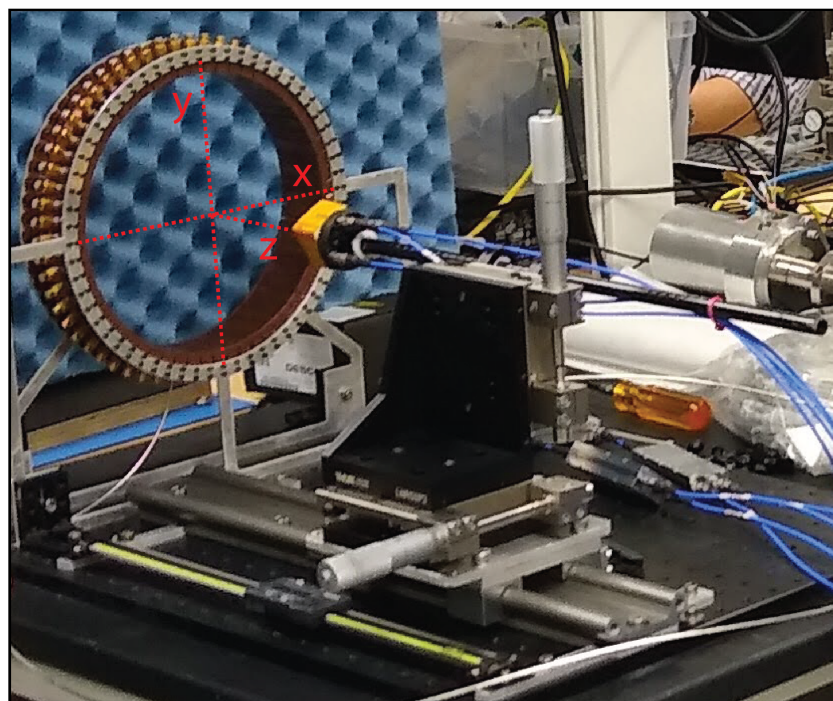
Data acquisition is accomplished using a two-port VNA in combination with a series of microwave switches that allow the VNA to connect to each channel in the array . The first port of the VNA is connected to the quad-balun chain used to feed the SYNCA (see Section 5.3), and the second port of the VNA connects to a 1P5T microwave switch. The 1P5T switch is connected to four separate 1P16T switch boards that connect directly



(a)



(b)



(c)

Figure 5.27. Photos of the prototype FSCD antenna (a), the FSCD array and SYNCA (b), and the translation stages and coordinate system used to position the SYNCA (c).

4465 to the array. The data acquisition is controlled by a python script running on a lab
4466 computer, which is connected to the VNA and an Arduino board programmed to control
4467 the microwave switches. The script uses the switches to iteratively connect each of the
4468 antennas in the array to the VNA. The VNA is configured to load a specific calibration
4469 file for each antenna channel and performs the measurements of all available S-parameters.
4470 The separate calibration files is an attempt to remove phase and magnitude errors caused
4471 by different propagation through the RF switches. Array measurements were performed
4472 for the set of SYNCA positions consisting of radial (x-axis) positions from 0 to 50 mm
4473 in 5 mm steps and axial (z-axis) positions from 0 to 50 mm in 5 mm steps resulting in
4474 121 array measurements. At each SYNCA position the two-port S-parameter matrix
4475 is measured using a linear frequency sweep from 25.1 to 26.1 GHz with 101 discrete
4476 frequencies.

4477 5.5.2.2 Synthetic Array Setup

4478 A photograph of the setup used to perform the synthetic array measurements is shown
4479 in Figure 5.28. A difference between this setup and the FSCD array setup is that the
4480 synthetic array measurements were performed with a waveform generator and digitizer
4481 instead of a VNA. The electronics configuration is identical to the diagram in Figure
4482 5.7b. Despite the differences, one is still able to compare the measured phases of the
4483 synthetic array and the relative magnitude of the power, since the digitized signal power
4484 is directly proportional to S21.

4485 The arbitrary waveform generator in the setup is configured to produce a 64 MHz
4486 sine wave signal that is up-converted to 25.864 GHz using a mixer and the VNA source.
4487 This signal is passed through a bandpass filter and fed to the SYNCA quad-balun chain.
4488 A single FSCD antenna is positioned 10 cm from the SYNCA and aligned vertically so
4489 that the center of the 5-slot waveguide is in the plane of the SYNCA PCB (see Figure
4490 5.28). This position corresponds to $z = 0$ in Figure 5.27c. The SYNCA is rotated
4491 in three degree steps to synthesize an antenna array with 120 channels. This channel
4492 count is more than could physically fit in a 10 cm radius array, but there is no cost to
4493 over-sampling. The signals from the FSCD antenna are down-converted using the second
4494 mixer connected to the VNA source before being digitized at 250 MHz and saved to
4495 disk. Several synthetic array measurement scans were performed by using the linear
4496 translation stage to change the radial position of the SYNCA. In total eight scans were
4497 taken from 0 to 35 mm using a radial position step size of 5 mm.

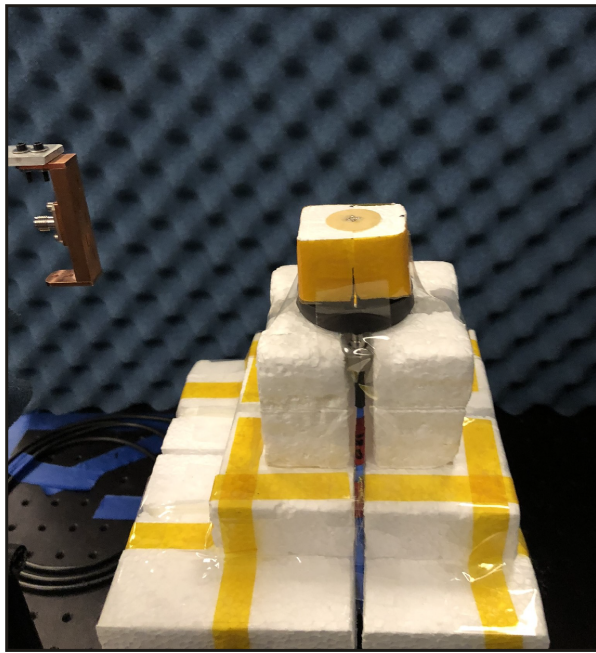


Figure 5.28. A photo of the FSCD antenna and the SYNCA in the synthetic array measurement setup at Penn State.

4498 5.5.3 Simulations, Analysis, and Results

4499 The Locust and CRESana simulation packages utilize the antenna transfer functions
4500 to calculate the power that would be received by each antenna from a CRES electron.
4501 The equivalent quantity in the measurement setup is the S21 matrix element, which
4502 indicates the ratio of the power received by an antenna in the array to the amount of
4503 power delivered to the SYNCA. Therefore, the analysis focuses on comparing the relative
4504 magnitudes and phase of the S21 parameters measured by the VNA as a function of the
4505 array channel and the SYNCA position. Additionally, a beamforming reconstruction
4506 using the S21 data is done to evaluate how the summed power and beamforming images
4507 change as a function of the position of the SYNCA.

4508 5.5.3.1 Simulations

4509 Simulations for the FSCD array measurements were performed using CRESana, which
4510 performs analytical calculations of the EM-fields produced by an electron at the position
4511 of the antennas. At each sampled time CRESana computes the electric field vector at the
4512 antenna positions, which is projected onto the antenna polarization axis to obtain the
4513 co-polar electric field. The magnitude of the co-polar electric field is then multiplied by
4514 a flat antenna transfer function to calculate the corresponding voltage signal. CRESana

4515 simulations exploit the flat transfer functions of the FSCD antennas, which allows the
 4516 electric field to be multiplied by the antenna transfer function rather than performing
 4517 the full FIR calculation. These calculations produce a voltage time-series for each of the
 4518 antennas in the array that can be compared to the laboratory measurements.

4519 CRESana was configured to simulate a 90° electron in a constant background magnetic
 4520 field of ≈ 0.958 T with a kinetic energy of 18.6 keV. These parameters were chosen
 4521 in order to mimic a CRES event near the tritium beta-decay spectrum endpoint in
 4522 the FSCD experiment. The constant background magnetic field guarantees that the
 4523 guiding center of the electron is stationary across the duration of the simulation which is
 4524 consistent with the SYNCA in the laboratory measurements. Simulations were performed
 4525 with the electron's guiding center at radial positions from 0 to 45 mm in steps of 1 mm
 4526 and axial positions from 0 to 30 mm in steps of 1 mm. The simulations generated time
 4527 series consisting of 8192 samples at 200 MHz for the sixty channel FSCD antenna array
 4528 geometry.

4529 5.5.3.2 Phase Analysis

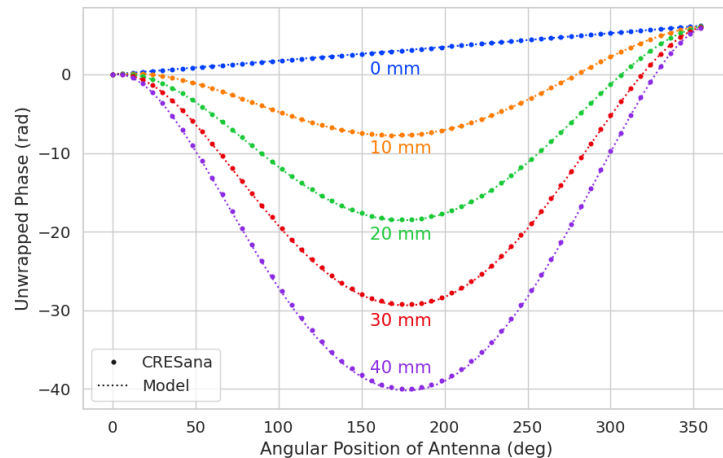


Figure 5.29. The unwrapped phases of signals received by the FSCD antenna array from an electron with a 90° pitch angle located in the plane of the antenna array. The data points indicated the phases extracted from simulation and the dashed lines show the model predictions.

4530 Correct modeling of the signal phases is fundamental to reconstruction for both
 4531 beamforming and matched filter approaches. The beamforming reconstruction relies on
 4532 a signal phase model developed from Locust simulations, which allows one to predict the
 4533 relative signal phases for a specific magnetic trap and electron position. The equation

4534 for the model is

$$\phi_{ij}(t) = \frac{2\pi d_{ij}(t)}{\lambda} + \theta_{ij}(t), \quad (5.36)$$

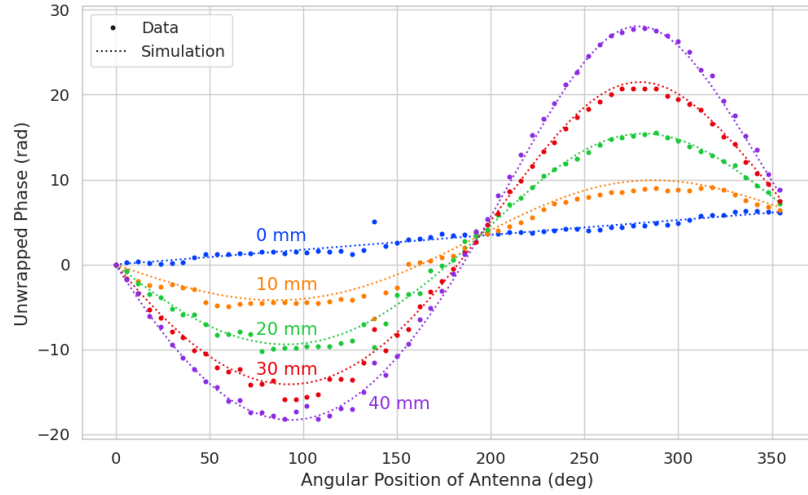
4535 where $d_{ij}(t)$ is distance between the assumed electron position and the antenna position,
4536 and $\theta_{ij}(t)$ is the angular separation between the electron and antenna positions. For
4537 details on the components of the phase model see Section 5.3.2. In Figure 5.29 I compare
4538 the phases predicted by Equation 5.36 to phases extracted from CRESana simulations of
4539 an electron located in the plane of the antenna array at a series of radial positions. One
4540 observes excellent agreement between the model and simulation.

4541 The measured signal phases from the FSCD array and synthetic array are shown
4542 in Figures 5.30a and 5.30b compared to the signal phase model. The axial position of
4543 the SYNCA in both plots is $z = 0$ mm, such that the plane of the PCB is aligned with
4544 the center of the FSCD antenna. The data shown in Figure 5.30a corresponds to the
4545 S-parameters measured at 25.80 GHz which is the frequency closest to the one used in
4546 the synthetic array setup. The different slope and sinusoidal phases exhibited by Figure
4547 5.30a and 5.30b reflects differences in the coordinate system for each setup. In general,
4548 the phase model predicts the large scale features of the phases well, but there are some
4549 small scale deviations or errors from the phase model that do not appear to be present
4550 in simulation.

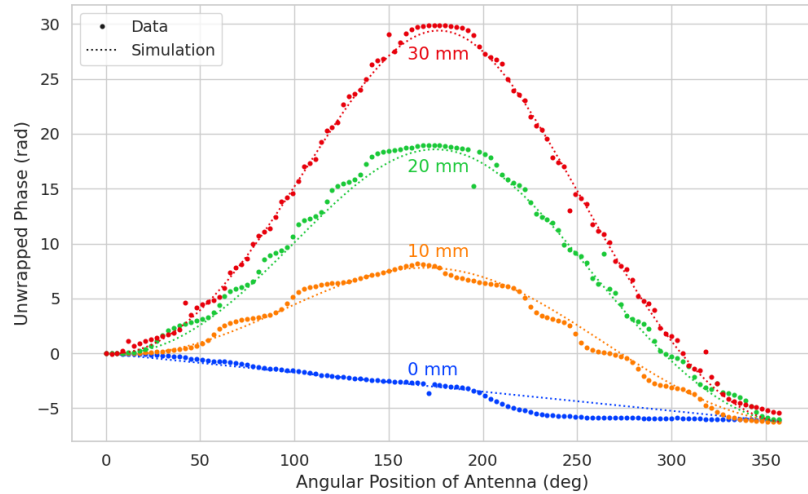
4551 A comparison of the phase errors, which are the difference between measurement and
4552 model is shown in Figure 5.31. The FSCD array data is referred to as the JUGAAD
4553 data in the plot legend, which is an alternative name for the FSCD array setup.

4554 The phase error at $R = 0$ in Figure 5.31 forms a smooth curve, with the exception of
4555 an outlier data point caused by a bug in the data acquisition script. One can attribute
4556 the observed phase error at this position to imperfections in the antenna pattern of the
4557 SYNCA. As the SYNCA is moved away from $R = 0$ mm one observes that the phase
4558 error exhibits oscillations whose frequency increases as a function of the radial position
4559 of the SYNCA. These oscillations have the appearance of a diffraction pattern, which
4560 is particularly clear for the radii ≥ 15 mm, due to the bilateral symmetry of the phase
4561 error peaks around 180° .

4562 One can observe a higher average variance in the phase errors measured for the FSCD
4563 array compared to the synthetic array. This is best seen by comparing the curves at
4564 $R \leq 15$ mm where the smooth synthetic array curves are distinct from the relatively
4565 noisy FSCD array errors. The extra noise in the FSCD array is most likely caused by
4566 differences in the radiation patterns of the antennas that make up the array as well as
4567 differences in the transmission lines through the switch network that introduce additional



(a)



(b)

Figure 5.30. Plots of the measured unwrapped phases from the FSCD array (a) and the synthetic array (b) compared to the model predictions for a series of radial positions. The different phases of the sinusoidal phase oscillations in the two plots reflects differences in the coordinate systems of the measurements.

phase errors into the measurement. Since the synthetic array measurements use only a single antenna, these extra error terms are not present, which explains the relatively smoother phase error curves. Despite the extra phase errors in the FSCD array, it is still possible to observe a similar phase error oscillation effect as the SYNCA is moved away from $R = 0$ mm.

The diffraction pattern exhibited by the phase error oscillations is more easily observed

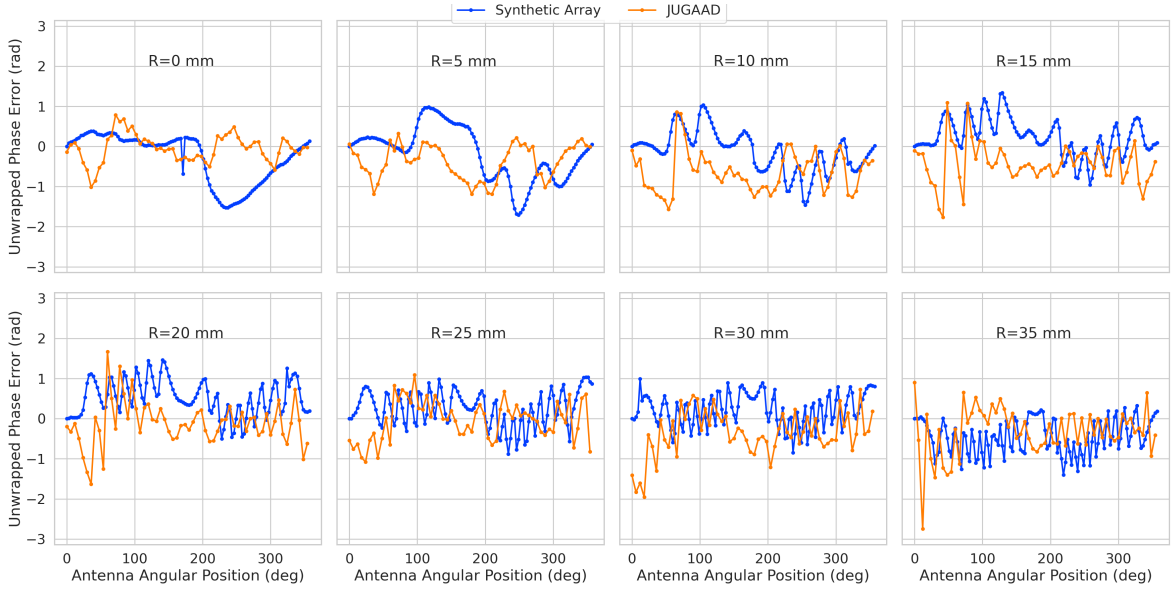
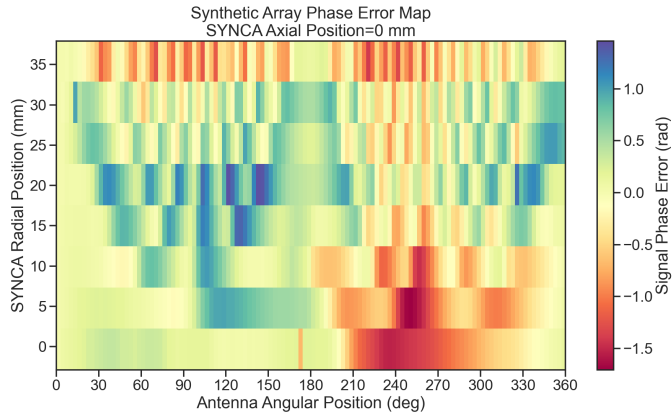


Figure 5.31. The phase errors between the measurement and model for the synthetic array (blue) and the FSCD array (orange) for a series of radial positions. The label JUGAAD refers to an alternative name for the FSCD array setup. As the SYNCA is translated off-axis phase errors with progressively higher oscillation frequency enter into the measurements.

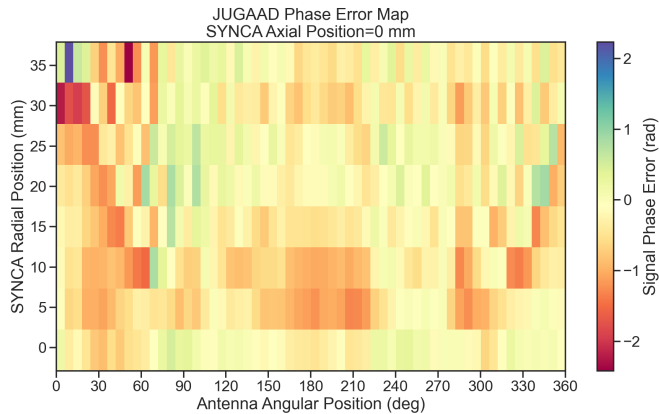
4574 by plotting the phase errors in a two-dimensional map, which is done in Figures 5.32a and
 4575 5.32b. For the synthetic array data ones observes a relatively clear diffraction pattern
 4576 that emerges as the SYNCA is moved radially. The bilateral symmetry of the diffraction
 4577 patterns is due to the bilateral symmetry of the circular synthetic array around the
 4578 translation axis of the SYNCA. A similar pattern is also visible in the FSCD array data,
 4579 although, it is obscured by the additional phase error that results from the multi-channel
 4580 array.

4581 The physical origin of the phase error diffraction pattern is attributed to interference
 4582 effects arising from path-length differences between the individual slots in the FSCD
 4583 antenna and the SYNCA transmitter. Since measurements are being performed in the
 4584 radiative near-field of the FSCD antenna, the path length differences between the slots
 4585 introduces a significant change in the summation of the signals that occurs inside the
 4586 waveguide, which causes the radiation pattern of the antenna to change as a function of
 4587 distance. Therefore, when the SYNCA is positioned off-axis the different path-lengths
 4588 from the SYNCA to each antenna results in different radiation patterns leading to the
 4589 observed diffraction pattern.

4590 This near-field effect is not present in simulations, because in order to simplify the
 4591 calculations it is assumed that the far-field approximation can be applied to the FSCD



(a)



(b)

Figure 5.32. Two dimensional plots of the phase errors for the synthetic array (a) and the FSCD (JUGAAD) array (b). In both plots there is evidence of a similar diffraction pattern with bilateral symmetry, but the FSCD array measurements have an additional phase error contribution from the different antennas and paths through the switch network.

antennas. This means that the radiation pattern and antenna transfer functions are independent of the distance between the transmitter and the receiving antenna. In principle, the near-field effects can be accounted for with a more detailed simulation of the FSCD antennas either in CRESana or Locust, which would result in an additional term in the beamforming phase model. However, this would increase the computational intensity of the simulation software. In the next section I briefly discuss the impact of these near-field effects on the measured magnitude of the signals.

4599 5.5.3.3 Magnitude Analysis

4600 Exactly as for the signal phase, one can use simulations to construct a model that
4601 describes the magnitude of the signals received by each channel in the antenna array.
4602 By examining the results of simulations or by analyzing the Liénard-Wiechert equation
4603 one can show that radiation pattern from a 90° pitch angle electron in a magnetic field
4604 is omni-directional. Therefore the relative magnitudes of the signals received by each
4605 channel will be determined by the free-space power loss, which is proportional to the
4606 inverse distance between the assumed electron position and the antenna.

4607 A consequence of this is that the signals produced in the array for electrons off the
4608 central axis will have larger amplitudes for the antennas closer to the electron compared
4609 to those which are further away. The amplitudes of the signals received by the array
from an electron located at a series of radial positions are shown in Figure 5.33.

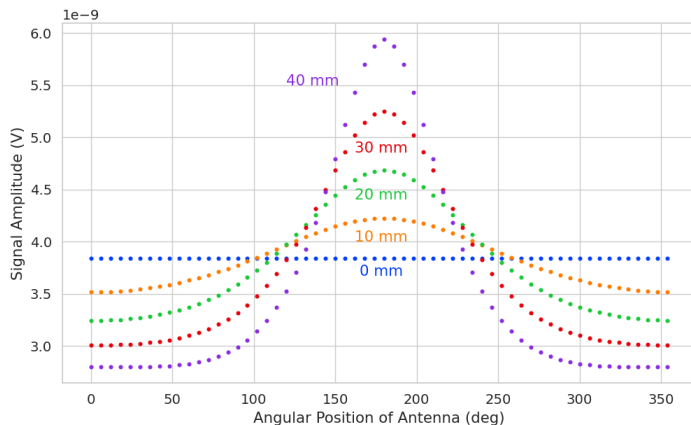


Figure 5.33. The amplitude of the signals from CRESana for the FSCD array from a 90° electron. As the electron is moved from $R = 0$ the signals begin to have unequal amplitudes depending on the distance from the electron to the antenna.

4610
4611 One expects to see a similar trend in the signal magnitudes in both the FSCD and
4612 synthetic arrays. The normalized signal magnitudes extracted from the full and synthetic
4613 array setups for a series of radial SYNCA positions are shown in Figure 5.34. The data
4614 corresponds to a SYNCA axial position of $z = 0$ mm and at a frequency 25.86 GHz. One
4615 complication is that the radiation pattern of the SYNCA is not perfectly omni-directional,
4616 which causes the measured magnitudes at $R = 0$ mm to diverge from the perfectly flat
4617 behavior exhibited by electrons.

4618 As the SYNCA is moved off-axis one observes a similar increase in the number of
4619 magnitude peaks in the synthetic array data that one would expect from a diffraction

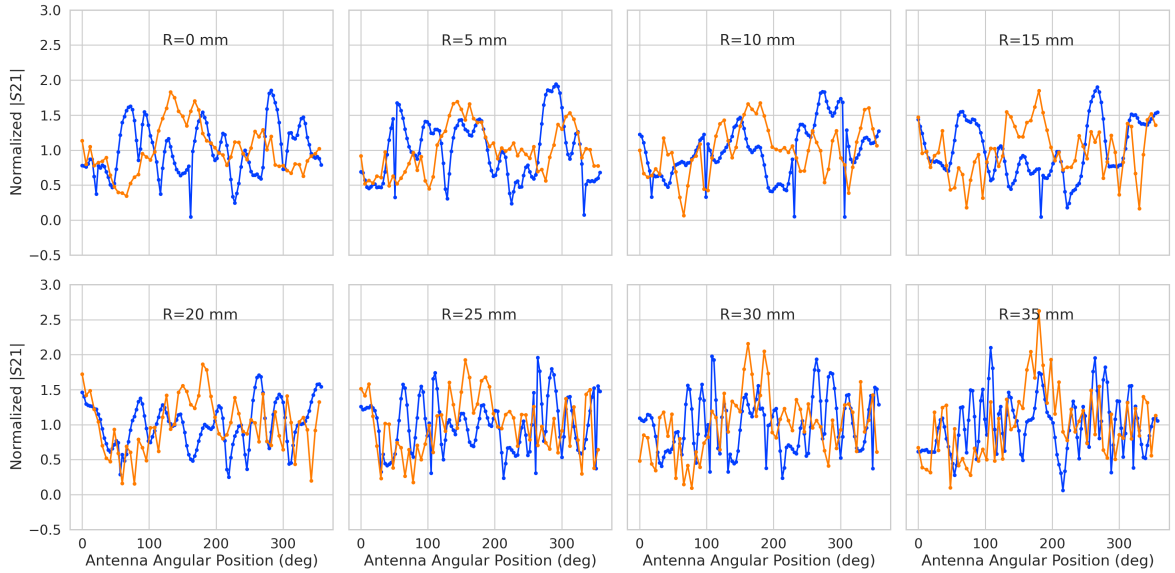
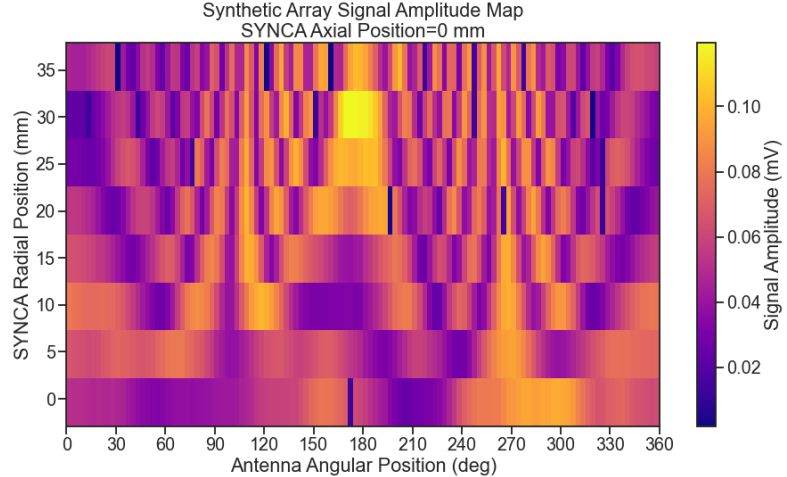


Figure 5.34. The normalized magnitudes of the S21 parameters measured in the FSCD (orange) and synthetic array (blue) setups. The dominant observed behavior as a function of radius is the increase in the number of magnitude peaks, which was noted in the phase error curves. There does not appear to be a strong change in the relative amplitude of a group of antennas as predicted by CRESana.

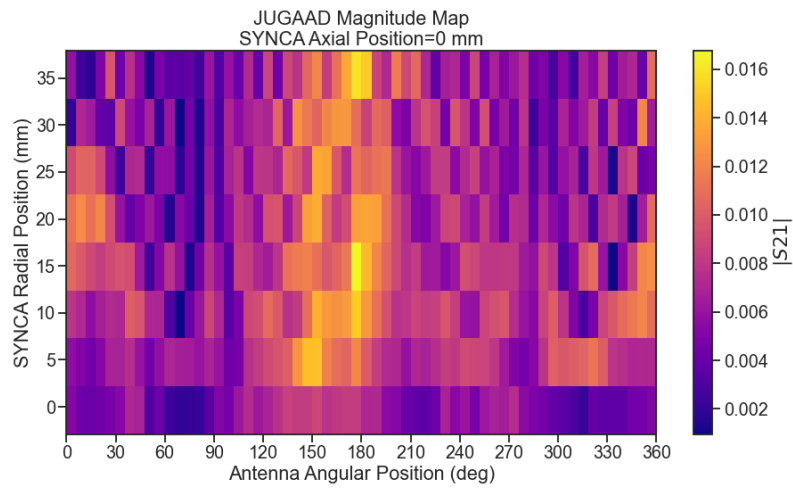
pattern, although this trend is not as stark compared to the phase data. Noticeably, there does not appear to be a set of channels with disproportionately larger amplitude at large R , which would be expected based on the trends from CRESana.

Comparing the magnitudes of the synthetic array to the FSCD array in Figure 5.34, one observes a similar amount of variability in the magnitudes at $R = 0$ mm, although there is potentially more small scale error in the magnitude curve caused by channel differences in the FSCD array. A similar trend is seen in the number of magnitude error peaks in the FSCD array data to the synthetic array data, which mirrors the diffraction effect observed in the phase data. The diffraction effect can be visualized more clearly by plotting a similar two-dimensional map of the magnitudes (see Figure 5.35).

The fact that one observes a similar diffraction pattern in the signal magnitudes as a function the SYNCA position reinforces the conclusions from the phase analysis that near-field effects are having a significant impact on the radiation pattern of the FSCD array. These near-field effects lead to changes in the magnitude and phase of the radiation pattern of the FSCD antenna as a function of distance. If left uncorrected these errors reduce detection efficiency by causing power loss in the beamforming or matched filter reconstruction due to phase mismatch. I explore the impact of these phase and



(a)



(b) The two-dimensional maps showing the diffractive pattern exhibited by the FSCD and synthetic array signal magnitudes.

Figure 5.35.

4637 magnitude errors on beamforming in the next section.

4638 5.5.3.4 Beamforming Characterization

4639 Errors in the signal magnitudes and phases lead to errors in signal reconstruction. For
 4640 example, a matched filter reconstruction requires accurate knowledge of the signals in
 4641 each channel to achieve optimal performance. Uncorrected errors leads to mismatches
 4642 between the template and signal, which reduces detection efficiency and introduces
 4643 uncertainty in the parameter estimation. In this section, I analyze the beamformed

4644 signal amplitude as a function of the position of the SYNCA to quantify the impact of
 4645 the phase and magnitude errors on signal reconstruction. Because of the imperfections
 4646 in the SYNCA source, it is inappropriate to directly compare the beamformed signal
 4647 amplitude of the FSCD array or synthetic array. Such a comparison would not allow
 4648 one to disentangle losses that occur because of the antenna array from those that occur
 4649 because of the source. Therefore, I focus on comparing the beamforming of the FSCD
 4650 array to the synthetic array.

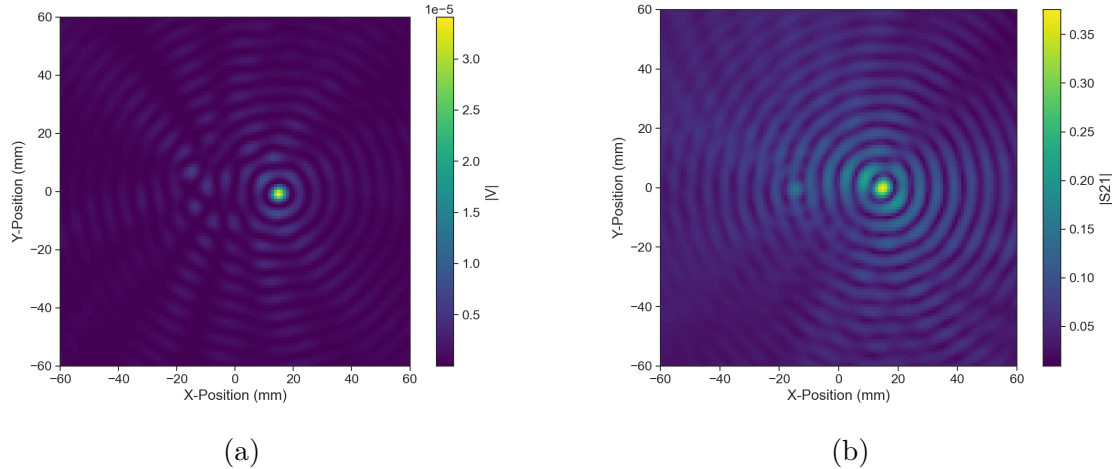


Figure 5.36. Beamforming images from the synthetic array (a) and FSCD array (b) setups with the SYNCA positioned 15 mm off the central axis. In both images, there is a clear maxima that corresponds to the true SYNCA position. However, in the FSCD array there is an additional faint peak located at the opposite position of the beamforming maximum. This additional peak is the mirror of the true peak and is the result of reflections between antennas in the FSCD array.

4651 The first method of comparison is to analyze the images generated by applying the
 4652 beamforming reconstruction specified in Section 4.3.1 to the FSCD and synthetic array
 4653 data (see Figure 5.36). The beamforming grid consisting of a square 121×121 grid
 4654 spanning a range of -60-mm to 60 mm in the x and y dimensions. The beamforming
 4655 images formed from the synthetic array produces a three-dimensional matrix where each
 4656 grid position contains a summed time series. A single beamforming image is formed from
 4657 this data matrix by taking the mean over the time dimension. In the case of the FSCD
 4658 array, the VNA generates frequency domain data such that each grid position contains a
 4659 summed frequency series produced by the VNA sweep. For this data a single image is
 4660 formed by averaging in the frequency domain.

4661 There is a clear difference between the synthetic and FSCD array beamforming images,
 4662 which is the additional faint beamforming maxima located directly opposite the maxima

4663 corresponding to the SYNCA position. The images in Figure 5.36 were generated with
 4664 data collected at a SYNCA radial position of 15 mm, which agrees well with the observed
 4665 beamforming maximum in both images. The faint beamforming peak is located directly
 4666 opposite of the true beamforming maximum similar to a mirror image. Therefore, the
 4667 origin of this additional feature appears to be reflections between the two sides of the
 4668 circular antenna array that are not present for the synthetic array since only a single
 4669 physical antenna is used.

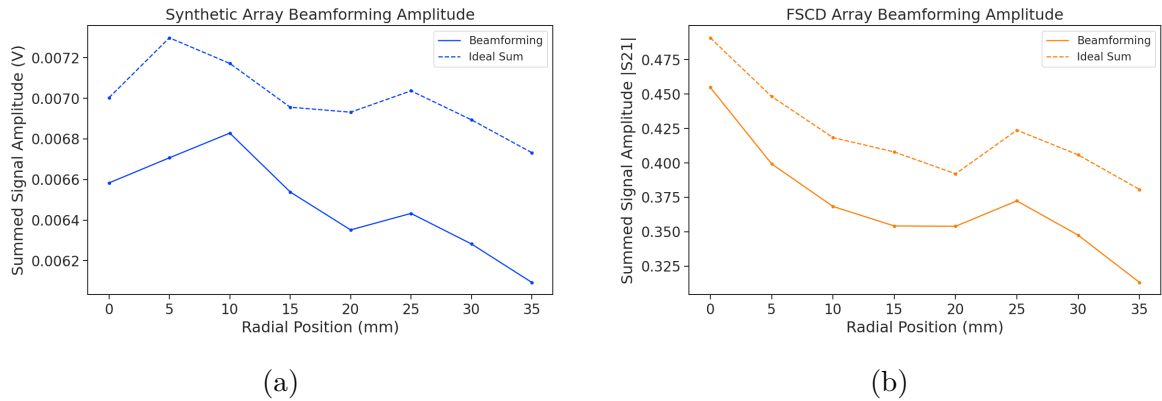


Figure 5.37. A comparison of the maximum signal amplitude obtained by beamforming to the signal amplitude obtained with an ideal summation as a function of the radial position of the SYNCA. The amplitudes for the synthetic array are shown in (a) and the FSCD array are shown in (b). In both setups, the signal amplitudes obtained from beamforming are smaller than the signal amplitude that could be attained with the ideal summation without phase mismatch.

4670 From the beamforming images the maximum amplitude is extracted, which can be
 4671 plotted as a function of the radial position of the SYNCA (see Figure 5.37). The phase
 4672 errors observed in the FSCD and synthetic arrays leads to power loss at the beamforming
 4673 stage due to phase mismatches between the signals at different channels. This power loss
 4674 can be quantified by comparing the signal amplitude obtained from beamforming to the
 4675 amplitude which would be obtained from an ideal summation. The ideal summation is
 4676 performed by phase shifting each array channel to an identical phase and then summing.
 4677 The comparison between the beamforming and ideal sums is shown in Figure 5.37,
 4678 where it is seen that the synthetic and FSCD arrays experience power losses from the
 4679 beamforming summation.

4680 The beamforming power loss can be quantified using the ratio of the beamforming to
 4681 ideal signal amplitudes. Computing this ratio as a function of SYNCA radial position
 4682 radius for the FSCD and synthetic arrays, it is found that the FSCD array has a uniformly
 4683 smaller beamforming amplitude ratio, which means that the FSCD array has a larger

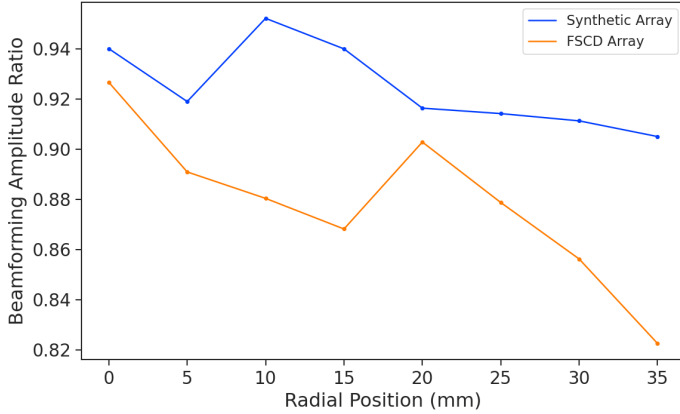


Figure 5.38. The ratio of the beamforming signal amplitude to the ideal signal amplitude for the FSCD and synthetic arrays. The FSCD array has a larger power loss from phase error compared to the synthetic array which indicates that calibration errors associated with the multiple channels as well as reflections are impacting the signal reconstruction.

beamforming power loss (see Figure 5.38). The primary contributions to the beamforming power loss in the synthetic array are phase errors from the SYNCA and phase errors from the FSCD antenna near-field. Both of these phase errors contribute to beamforming losses in the FSCD array, but there are clearly additional phase errors in the FSCD array measurements contributing to the smaller ratio. Two potential error sources include phase differences in the different antenna channels that could not be corrected by calibration as well as reflections between antennas in the array. The total effect of these additional phase errors is to reduce the beamforming amplitude ratio by about 5% from the beamforming ratio of the synthetic array. Therefore, it is estimated that if no effort is made to correct these phase errors in an FSCD-like experiment, then one would expect approximately a 10% total signal amplitude loss from a beamforming signal reconstruction.

5.5.4 Conclusions

The estimated power loss of a beamforming reconstruction obtained from this analysis provides valuable inputs to sensitivity calculations of a FSCD-like antenna array experiment to measure the neutrino mass, since it helps to bound systematic uncertainties from the antenna array and reconstruction pipeline. This power loss lowers the estimated detection efficiency of the experiment since some of the signal power is lost due to improper combining between channels and also increases the uncertainty in the electron's kinetic energy by contributing to errors in the estimation of the electron's cyclotron frequency.

4704 If these reconstruction losses prove unacceptable there are steps that can be taken
4705 to mitigate their effects. Some examples include the development of a more accurate
4706 antenna simulation approach that can reproduce the observed near-field interference
4707 patterns of the FSCD antennas and the implementation of a calibration approach that
4708 allows for the relative phase delays of the array to be measured without changing or
4709 disconnecting the antenna array configuration.

4710 **Chapter 6 |**

4711 **Development of Resonant Cavities for Large**

4712 **Volume CRES Measurements**

4713 **6.1 Introduction**

4714 The cavity approach was originally an alternative CRES measurement technology under
4715 consideration by the Project 8 collaboration for the Phase IV experiment. After pursuing
4716 an antenna array based CRES demonstrator design for several years, the increasing costs
4717 and complexity of the antenna arrays led to a reconsideration of the baseline technology
4718 for the ultimate CRES experiment planned by Project 8. Currently, a cavity based CRES
4719 experiment is the preferred technology choice for future experiments by the Project 8
4720 collaboration including the Phase IV experiment.

4721 In this chapter I provide a brief summary of resonant cavities and sketch out the key
4722 features of a cavity based CRES experiment. In Section 6.2 I provide a brief introduction
4723 to cylindrical resonant cavities and the solutions for the electromagnetic fields in the
4724 cavity volume.

4725 In Section 6.3 I describe the main components of a cavity based CRES experiment,
4726 including the background and trap magnets, cavity geometry and design, and cavity
4727 coupling considerations. I also discuss some relevant trade-offs between an antenna array
4728 and cavity CRES experiment, and highlight some reasons for the transition of Project 8
4729 to the development of a cavity based experiment.

4730 Finally, in Sections 6.4 and 6.5, I present the design and development of an open
4731 mode-filtered cavity that could be used in a cavity based CRES experiment with atomic
4732 tritium. The results of the cavity simulations are confirmed by laboratory measurements
4733 of a proof-of-principle prototype that demonstrates key features of the design.

6.2 Cylindrical Resonant Cavities

Resonant cavities are sealed conductive containers, which allows one to describe the electromagnetic (EM) fields contained in the cavity volume as a superposition of resonant modes [88]. The field shapes of the resonant modes are determined by Maxwell's equations and the boundary conditions enforced by the cavity geometry. Of interest to Project 8 for CRES measurements are cylindrical cavities due to their ease of construction and integration with atom and electron trapping magnets.

6.2.1 General Field Solutions

Consider a long segment of conducting material with a cylindrical cross-section (see Figure 6.1). A geometry such as this can be used as a waveguide transmission line to transfer EM energy from point to point, or, if conducting shorts are inserted on both ends of the cylinder, the waveguide becomes a resonant cavity.

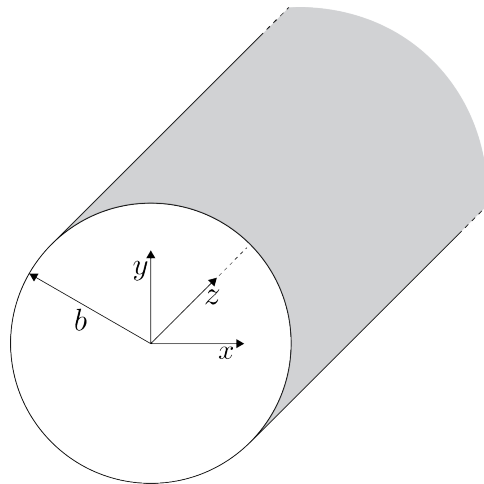


Figure 6.1. Geometry of a cylindrical waveguide with radius b .

The fields allowed inside a cylindrical cavity are determined by the boundary conditions of the cylindrical geometry. The general approach to solving the fields begins by assuming solutions to Maxwell's equations of the form

$$\mathbf{E}(x, y, z) = (\mathbf{e}(x, y) + \hat{z}e_z(x, y))e^{-i\beta z}, \quad (6.1)$$

$$\mathbf{H}(x, y, z) = (\mathbf{h}(x, y) + \hat{z}h_z(x, y))e^{-i\beta z}. \quad (6.2)$$

The solutions assume a harmonic time dependence of the form $e^{i\omega t}$ and propagation

4750 along the positive z-axis. The functions $\mathbf{e}(x, y)$ and $\mathbf{h}(x, y)$ represent the transverse
 4751 (\hat{x}, \hat{y}) components of the electric and magnetic fields respectively, and $e_z(x, y)$, $h_z(x, y)$
 4752 represent the longitudinal components. The version of Maxwell's equations in the case
 4753 where there are no source terms can be written as a pair of coupled differential equations,

$$\nabla \times \mathbf{E} = -i\omega\mu\mathbf{H}, \quad (6.3)$$

$$\nabla \times \mathbf{H} = i\omega\epsilon\mathbf{E}, \quad (6.4)$$

4754 where ϵ and μ are the permittivity and permeability of the material inside the waveguide
 4755 or cavity. Using the field solutions from Equations 6.1 and 6.2 one can solve for the
 4756 transverse components of the fields in terms of the longitudinal fields. Because cylindrical
 4757 cavities are of interest, it is advantageous to write the field solutions in cylindrical
 4758 coordinates. After performing this transformation, the set of four equations for the
 4759 transverse field components are

$$H_\rho = \frac{i}{k_c^2} \left(\frac{\omega\epsilon}{\rho} \frac{\partial E_z}{\partial\phi} - \beta \frac{\partial H_z}{\partial\rho} \right), \quad (6.5)$$

$$H_\phi = \frac{-i}{k_c^2} \left(\omega\epsilon \frac{\partial E_z}{\partial\rho} + \frac{\beta}{\rho} \frac{\partial H_z}{\partial\phi} \right), \quad (6.6)$$

$$E_\rho = \frac{-i}{k_c^2} \left(\beta \frac{\partial E_z}{\partial\rho} + \frac{\omega\mu}{\rho} \frac{\partial H_z}{\partial\phi} \right), \quad (6.7)$$

$$E_\phi = \frac{i}{k_c^2} \left(\frac{-\beta}{\rho} \frac{\partial E_z}{\partial\phi} + \omega\mu \frac{\partial H_z}{\partial\rho} \right), \quad (6.8)$$

4760 where k_c is the cutoff wavenumber defined by $k_c^2 = k^2 - \beta^2$ with $k = \omega\sqrt{\mu\epsilon}$ being the
 4761 wavenumber of the EM radiation.

4762 This set of equations can be used to solve for a variety of different modes, which can
 4763 be obtained by setting conditions on E_z and H_z . For cylindrical cavities two types of
 4764 modes are allowed, which correspond to solutions where $E_z = 0$ and $H_z = 0$ respectively.

4765 6.2.2 TE and TM Modes

4766 The TE family of modes corresponds to the case where $E_z = 0$. This implies that H_z is
 4767 a solution to the Helmholtz wave equation

$$(\nabla^2 + k^2)H_z = 0. \quad (6.9)$$

4768 For solutions of the form $H_z(\rho, \phi, z) = h_z(\rho, \phi)e^{-i\beta z}$, Equation 6.9 can be solved using
 4769 the standard technique of separation of variables. Rather than reproduce the derivation
 4770 here I shall simply quote the solutions for the transverse fields [88], which are

$$H_\rho = \frac{-i\beta}{k_{c_{nm}}} (A \sin n\phi + B \cos n\phi) J'_n(k_{c_{nm}}\rho) e^{-i\beta_{nm}z}, \quad (6.10)$$

$$H_\phi = \frac{-i\beta n}{k_{c_{nm}}^2 \rho} (A \cos n\phi - B \sin n\phi) J_n(k_{c_{nm}}\rho) e^{-i\beta_{nm}z}, \quad (6.11)$$

$$E_\rho = \frac{-i\omega\mu n}{k_{c_{nm}}^2 \rho} (A \cos n\phi - B \sin n\phi) J_n(k_{c_{nm}}\rho) e^{-i\beta_{nm}z}, \quad (6.12)$$

$$E_\phi = \frac{i\omega\mu}{k_{c_{nm}}} (A \sin n\phi + B \cos n\phi) J'_n(k_{c_{nm}}\rho) e^{-i\beta_{nm}z}. \quad (6.13)$$

4771 One observes that the solutions have a periodic dependence on ϕ , and radial profiles
 4772 given by the Bessel functions of the first kind. The integer indices n and m arise from
 4773 continuity conditions on the EM fields in the azimuthal and radial directions. For the
 4774 TE modes, the indices range from $n \geq 0$ and $m \geq 1$. $k_{c_{nm}}$ is the cutoff wavenumber for
 4775 the TE_{nm} mode given by

$$k_{c_{nm}} = \frac{p'_{nm}}{b}, \quad (6.14)$$

4776 where b is the radius of the cavity or waveguide and p'_{nm} is the m -th root of the derivative
 4777 of the n -th order Bessel function (see Table 6.1).

Table 6.1. A table of the values of p'_{nm} .

n	p'_{n1}	p'_{n2}	p'_{n3}
0	3.832	7.016	10.174
1	1.841	5.331	8.536
2	3.054	6.706	9.970

4778 The TM mode family corresponds to the case where $H_z = 0$, and $(\nabla^2 + k^2)E_z = 0$.
 4779 Again, solutions are assumed of the form $E_z(\rho, \phi, z) = e_z(\rho, \phi)e^{-i\beta z}$, for which the general
 4780 form of the solutions is the same as for the TE modes. However, the different boundary
 4781 conditions for the TM modes results in particular solutions with a different form, which I
 4782 shall quote here without derivation. The transverse fields of the TM modes are given by

$$H_\rho = \frac{-i\omega\epsilon n}{k_{c_{nm}}^2 \rho} (A \cos n\phi - B \sin n\phi) J_n(k_{c_{nm}}\rho) e^{-i\beta_{nm}z}, \quad (6.15)$$

$$H_\phi = \frac{-i\omega\epsilon}{k_{c_{nm}}} (A \sin n\phi + B \cos n\phi) J'_n(k_{c_{nm}}\rho) e^{-i\beta_{nm}z} \quad (6.16)$$

$$E_\rho = \frac{-i\beta}{k_{c_{nm}}} (A \sin n\phi + B \cos n\phi) J'_n(k_{c_{nm}}\rho) e^{-i\beta_{nm}z}, \quad (6.17)$$

$$E_\phi = \frac{-i\beta n}{k_{c_{nm}}^2 \rho} (A \cos n\phi - B \sin n\phi) J_n(k_{c_{nm}}\rho) e^{-i\beta_{nm}z}, \quad (6.18)$$

⁴⁷⁸³ which one may notice are the same solutions as the TE modes with H and E flipped.
⁴⁷⁸⁴ The cutoff wavenumber for the TM modes is given by, $k_{c_{nm}} = p_{nm}/b$, where the values of
⁴⁷⁸⁵ p_{nm} correspond to the m -th zero of the n -th order Bessel function (see Table 6.2).

Table 6.2. A table of the values of p_{nm} .

n	p_{n1}	p_{n2}	p_{n3}
0	2.405	5.520	8.654
1	3.832	7.016	10.174
2	5.135	8.417	11.620

⁴⁷⁸⁶ 6.2.3 Resonant Frequencies of a Cylindrical Cavity

⁴⁷⁸⁷ A cylindrical cavity is constructed by taking a section of cylindrical waveguide and
⁴⁷⁸⁸ shorting both ends with conductive material. This means that the electric fields inside a
⁴⁷⁸⁹ cylindrical cavity are exactly those derived in Section 6.2.2 with the additional condition
that the electric fields must go to zero at $z = 0$ and $z = L$ (see Figure 6.2).

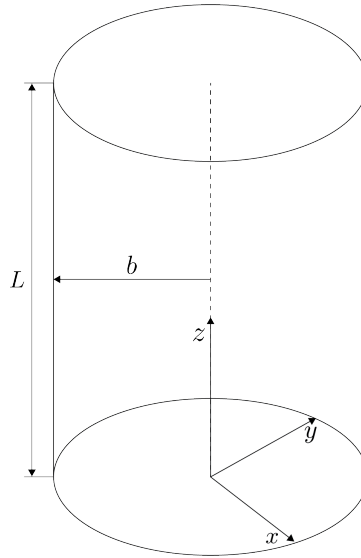


Figure 6.2. The geometry of a cylindrical cavity with length L and radius b .

₄₇₉₁ The transverse electric field solutions for a cylindrical waveguide are of the form

$$\mathbf{E}(\rho, \phi, z) = \mathbf{e}(\rho, \phi) (A_+ e^{-i\beta_{nm}z} + A_- e^{i\beta_{nm}z}), \quad (6.19)$$

₄₇₉₂ where A_+ and A_- are arbitrary amplitudes of forward and backward propagating waves.

₄₇₉₃ In order to enforce that \mathbf{E} is zero at both ends of the cavity it is required that

$$\beta_{nm}L = 2\pi\ell, \quad (6.20)$$

₄₇₉₄ where $\ell = 0, 1, 2, 3, \dots$. Using this constraint on the propagation constant one can solve

₄₇₉₅ for the resonant frequencies of the TE_{nml} and the TM_{nml} modes in a cylindrical cavity.

₄₇₉₆ For the TE modes the resonant frequencies are

$$f_{nml} = \frac{c}{2\pi\sqrt{\mu_r\epsilon_r}} \sqrt{\left(\frac{p'_{nm}}{b}\right)^2 + \left(\frac{\ell\pi}{L}\right)^2}, \quad (6.21)$$

₄₇₉₇ and the frequencies of the TM modes are

$$f_{nml} = \frac{c}{2\pi\sqrt{\mu_r\epsilon_r}} \sqrt{\left(\frac{p_{nm}}{b}\right)^2 + \left(\frac{\ell\pi}{L}\right)^2}. \quad (6.22)$$

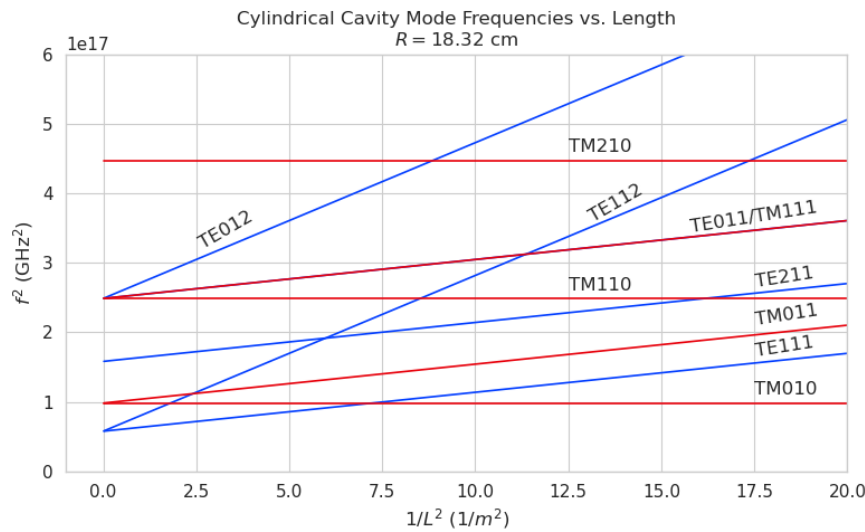


Figure 6.3. Relation of mode frequency to cavity length for a cylindrical cavity with a radius of 18.32 cm.

4798 6.2.4 Cavity Q-factors

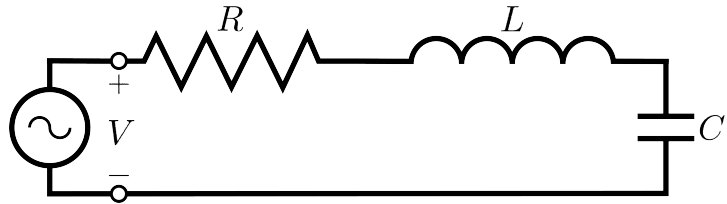


Figure 6.4. A series RLC circuit.

4799 The resonant behavior of cylindrical cavities can be modeled as a series RLC circuit
 4800 (see figure 6.4). The input impedance of the circuit can be obtained by applying
 4801 Kirchhoff's laws to calculate the impedance of the equivalent circuit. For a series RLC
 4802 circuit the input impedance is

$$Z_{\text{in}} = \left(\frac{1}{R} + \frac{1}{i\omega L} + i\omega C \right). \quad (6.23)$$

4803 The resistance in the circuit represents all sources of loss in the cavity, which is primarily
 4804 caused by the finite conductivity of the cavity walls. The inductor and capacitor represent
 4805 the energy stored in the cavity in the form of electric and magnetic fields. If the circuit
 4806 is being driven by an external power source the input power can be written in terms of
 4807 the circuit input impedance and the source voltage

$$P_{\text{in}} = \frac{1}{2} Z_{\text{in}} |I|^2 = \frac{1}{2} |I|^2 \left(\frac{1}{R} + \frac{1}{i\omega L} + i\omega C \right). \quad (6.24)$$

4808 The resistor introduces a loss into the system with a power given by

$$P_{\text{loss}} = \frac{1}{2} |I|^2 R, \quad (6.25)$$

4809 and the capacitor and inductor store energies given by

$$W_e = \frac{1}{4} \frac{|I|^2}{\omega^2 C}, \quad (6.26)$$

$$W_m = \frac{1}{4} |I|^2 L, \quad (6.27)$$

4810 respectively. Using these expressions the input power and input impedance can be written

4811 in terms of the lost power and stored energy

$$P_{\text{in}} = P_{\text{loss}} + 2i\omega(W_m - W_e), \quad (6.28)$$

$$Z_{\text{in}} = \frac{P_{\text{loss}} + 2i\omega(W_m - W_e)}{\frac{1}{2}|I|^2}. \quad (6.29)$$

4812 The condition for resonance in the RLC circuit is that the stored magnetic energy
4813 is equal to the stored electric energy ($W_e = W_m$). When this occurs $Z_{\text{in}} = R$, which is a
4814 purely real impedance, and $P_{\text{in}} = P_{\text{loss}}$. The resonant frequency of the circuit can be
4815 determined from the condition $W_e = W_m$ from which one finds that

$$\omega_0 = \frac{1}{\sqrt{LC}}. \quad (6.30)$$

4816 An important performance parameter for any resonant system is the Q-factor, which
4817 quantifies the quality of the resonator as the ratio of the stored energy multiplied by the
4818 resonant frequency to the average energy lost per second. For the series RLC circuit, the
4819 Q-factor is given by the expression

$$Q_0 = \omega \frac{W_e + W_m}{P_{\text{loss}}} = \frac{1}{\omega_0 RC}, \quad (6.31)$$

4820 from which one observes that as the resistance of the RLC circuit is decreased the quality
4821 factor of the resonator increases. From the perspective of cylindrical cavities this implies
4822 that as one decreases the resistance of the cavity walls it is expected that the Q-factor of
4823 the cavity should increase, which is indeed the case. In certain applications where a high
4824 Q is desireable it is possible to manufacture a cavity out of superconducting materials in
4825 order to minimize the power losses of the system.

4826 The Q-factor of the resonator also determines with bandwidth (BW) of the system. A
4827 cavity with a high Q-factor will resonant with a smaller range of frequencies than a cavity
4828 with a low Q-factor. To see this examine the behavior of the RLC circuit when driven by
4829 frequencies near the resonance. For a frequency $\omega = \omega_0 + \Delta\omega$, where $\Delta\omega = \omega - \omega_0 \ll \omega_0$,
4830 the input impedance can be written as

$$Z_{\text{in}} = R + i\omega L \left(\frac{\omega^2 - \omega_0^2}{\omega^2} \right), \quad (6.32)$$

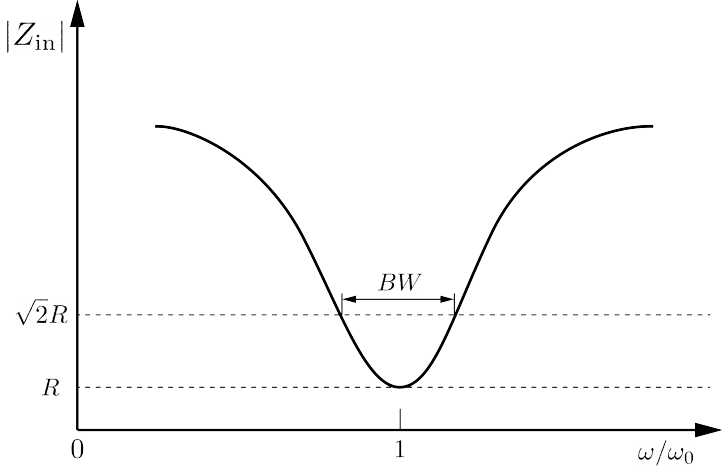


Figure 6.5. Illustration of the behavior of the input impedance of the series RLC circuit as a function of the driving frequency. The BW is proportion to the width of the resonance, which is inversely proportional to Q.

4831 and by expanding $(\omega^2 - \omega_0^2)/\omega^2$ to first order in $\Delta\omega$, one obtains

$$Z_{\text{in}} \approx R + i \frac{2RQ_0\Delta\omega}{\omega_0}. \quad (6.33)$$

4832 Therefore, the magnitude of the input impedance near the resonance is given by

$$|Z_{\text{in}}| = R \sqrt{1 + 4Q_0^2 \frac{\Delta\omega^2}{\omega^2}}, \quad (6.34)$$

4833 from which it is seen that for the series RLC circuit the input impedance is minimized
 4834 at the resonant frequency, which corresponds to the maximum input power (see Figure
 4835 6.5). The half-power BW is the range of frequencies over which the input power drops to
 4836 half the input power on resonance. This occurs when $|Z_{\text{in}}| = \sqrt{2}R$, which corresponds to
 4837 $\Delta\omega/\omega = \text{BW}/2$. Using Equation 6.34 one can find that

$$2R^2 = R^2(1 + Q_0^2\text{BW}^2), \quad (6.35)$$

4838 which implies

$$\text{BW} = \frac{1}{Q_0} \quad (6.36)$$

4839 It is important to emphasize that the Q-factor defined here, Q_0 , is technically the
 4840 unloaded Q. It reflects the quality of the cavity or resonant circuit without the influence
 4841 of any external circuitry. In practice, however, a cavity is invariably coupled to an

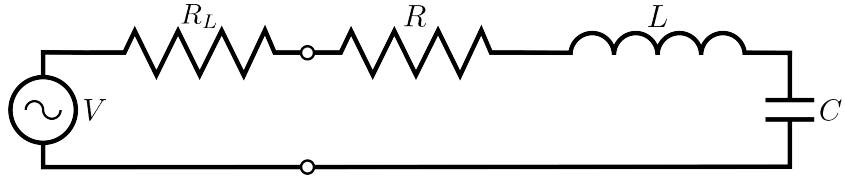


Figure 6.6. A series RLC circuit coupled to an external circuit with input impedance R_L .

4842 external circuit to drive a cavity resonance or to measure the energy of a resonant mode.
 4843 Coupling a cavity to an external circuit changes the Q by loading the equivalent cavity
 4844 RLC circuit (see Figure 6.6). The Q-factor of the cavity when it is loaded by an external
 4845 circuit is called the loaded Q, which is the quantity that one actually measures when
 4846 exciting a resonance in the cavity. Using the series RLC circuit model one can see that
 4847 the load resistor in Figure 6.6 will add in series with the resistor in the circuit for a total
 4848 equivalent resistance of $R + R_L$. Therefore, the loaded Q is given by

$$Q_L = \frac{1}{\omega_0(R + R_L)C}, \quad (6.37)$$

4849 from which one observes that the loaded Q is always less than the intrinsic Q of the
 4850 cavity.

4851 The amount of coupling that is desireable depends on the specific application of
 4852 the resonator. If one wants a resonator that is particular frequency selective than it
 4853 makes sense to limit the amount of coupling to the cavity to maintain a small BW,
 4854 alternatively, if a larger BW is need one can increase the cavity coupling by tuning the
 4855 input impedance of the external circuit. The critical point, where maximum power is
 4856 transferred between the cavity and the external circuit, occurs when the input impedance
 4857 of the cavity matches the input impedance of the external transmission line. For the
 4858 series RLC circuit on resonance, this matching condition corresponds to

$$Z_0 = Z_{in} = R, \quad (6.38)$$

4859 where Z_0 is the impedance of the transmission line. The loaded Q at this critical point
 4860 is, therefore,

$$Q_L = \frac{1}{2\omega_0 Z_0 C} = \frac{Q_0}{2}. \quad (6.39)$$

4861 One can described the degree of coupling between the cavity and an external circuit by

⁴⁸⁶² defining a coupling factor, g , such that,

$$g = \frac{Q_0}{Q_L} - 1. \quad (6.40)$$

⁴⁸⁶³ When $g = 1$ then $Q_L = Q_0/2$, and the cavity is said to be critically coupled. If
⁴⁸⁶⁴ $Q_L < Q_0/2$, then the cavity is undercoupled to the transmission line, corresponding to
⁴⁸⁶⁵ $g < 1$. Alternatively, if $Q_L > Q_0/2$, then $g > 1$, and the cavity is overcoupled to the
⁴⁸⁶⁶ transmission line. Various specialized circuits can be used to tune the input impedance
⁴⁸⁶⁷ of the external circuit as seen by the cavity to achieve a wide range of different coupling
⁴⁸⁶⁸ factors based on the desired application of the cavity.

⁴⁸⁶⁹ 6.3 The Cavity Approach to CRES

⁴⁸⁷⁰ 6.3.1 A Sketch of a Molecular Tritium Cavity CRES Experiment

⁴⁸⁷¹ Resonant cavities can be used to perform CRES measurements, and they represent the
⁴⁸⁷² current preferred technology by the Project 8 collaboration. The basic approach to a
⁴⁸⁷³ neutrino mass measurement using a resonant cavity and molecular tritium beta-decay
source is illustrated by Figure 6.7.

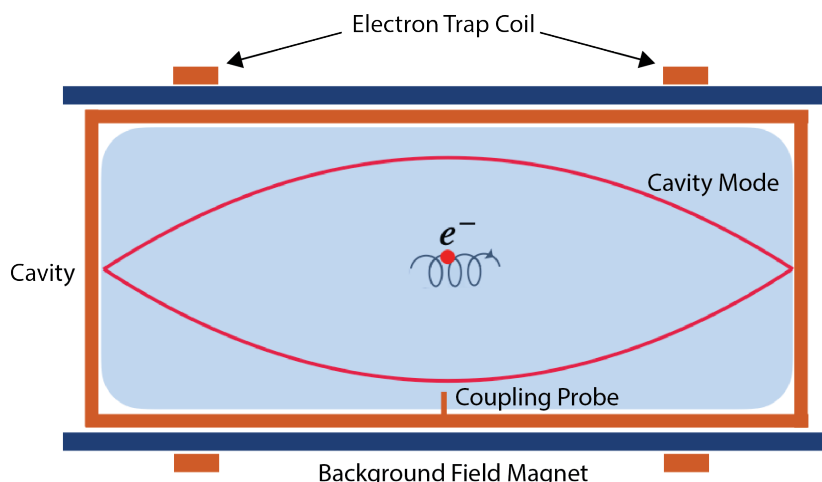


Figure 6.7. A cartoon depiction of a cavity CRES experiment. A metallic cavity filled with tritium gas is inserted into a uniform background magnetic field to perform CRES measurements. Electrons from beta-decays inside the cavity can be trapped and used to excite a resonant mode(s). By coupling to the cavity mode with a suitable probe one can measure the cyclotron frequency of the electron and perform CRES.

⁴⁸⁷⁴

4875 At the core of the experiment is a large resonant cavity filled with tritium gas. The
4876 filled cavity is then placed in a uniform magnetic field provided by a primary magnet,
4877 which provides the background magnetic field. The value of the background magnetic field
4878 sets the range of cyclotron frequencies for electrons emitted near the tritium spectrum
4879 endpoint. When a beta-decay electron is produced in the cavity it is trapped using a set
4880 of magnetic pinch coils that keep electrons inside the cavity volume.

4881 Electrons trapped inside the cavity do not radiate in the same way as electrons
4882 in free-space. Effectively, the same boundary conditions that were used to derive the
4883 resonant modes of a cylindrical cavity in Section 6.2 apply to the radiation of the electron
4884 as well. The coupling of an electron performing cyclotron motion in a cavity has been
4885 studied in detail for measurements of the electron’s magnetic moment [97–99]. If an
4886 electron is emitted with a kinetic energy that corresponds to a cyclotron frequency that
4887 matches a resonant frequency of the cavity, then energy radiated by the electron excites
4888 a corresponding resonance in the cavity. The strength of the electron’s coupling to the
4889 cavity is given to first order by the dot product between the electrons trajectory and
4890 the electric field vector of the resonant mode. Additional effects, such as the Purcell
4891 enhancement [100], alter the emitted power from the free-space Larmor equation [50]. If
4892 an electron is moving with a cyclotron frequency that is far from any resonant modes
4893 in the cavity, then radiation from the electron is suppressed. One can interpret this
4894 somewhat surprising effect as the metallic walls of the cavity reflecting the radiated
4895 energy back to the electron.

4896 Detecting an electron in the cavity is accomplished by coupling the cavity to an
4897 external transmission line that leads to an amplifier and RF receiver chain [101]. The
4898 coupling of the cavity resonance to the amplifier occurs through a coupling probe or
4899 aperture designed to read-out the excitation of the mode(s) excited by the electron. For
4900 CRES measurements, the placement of a wire antenna coupling probe inside the cavity
4901 volume leads to unacceptable losses of tritium atoms due to recombination to molecular
4902 tritium on the antenna surface, therefore, apertures are the preferred coupling method
4903 for cavity CRES experiments.

4904 One of the attractive features of the CRES technique for neutrino mass measurement
4905 is the gain in statistics that comes from the differential nature of the tritium spectrum
4906 measurement. Initially, this seems incompatible with cavities, due to the narrow reso-
4907 nances of cavity modes giving relatively small bandwidth. However, by intentionally
4908 over-coupling to a single cavity mode one can achieve bandwidths of a few 10’s of MHz
4909 (see Section 6.2), which is sufficient for a measurement of the tritium spectrum endpoint

4910 region.

4911 **6.3.2 Magnetic Field, Cavity Geometry, and Resonant Modes**

4912 **Magnetic Field and Volume Scaling**

4913 For a CRES experiment, cylindrical cavities are a natural choice since they match
4914 the geometry of standard solenoid magnets, which are needed in order to produce the
4915 background magnetic field for CRES measurements. Furthermore, the cylindrical shape is
4916 compatible with a Halbach array, which is the leading choice of atom trapping technology
4917 for future atomic tritium experiments by the Project 8 collaboration. Cylindrical
4918 cavities also benefit from well-established machining practices that are able to achieve
4919 high geometric precision at large lengths scales. More exotic cavity designs are under-
4920 consideration and there are on-going efforts to investigate the potential advantages these
4921 may have over the standard cylindrical geometry.

4922 As shown in Section 6.2, the physical dimensions of the cavity are directly coupled to
4923 the resonant frequencies of the cavity. This dependency links the size of the cavity to
4924 the magnitude of the background magnetic field, because the magnetic field determines
4925 the cyclotron frequencies of trapped electrons. Specifically, as the size of the cavity is
4926 increased to accommodate larger volumes of tritium gas, the frequencies of the resonant
4927 modes decrease proportionally. This requires that the magnetic field also decrease in
4928 order to maintain coupling between electrons and the desired cavity mode.

4929 The required cavity size is ultimately determined by the required statistics in the
4930 tritium spectrum endpoint region. Because the gas density must be kept below a certain
4931 level to ensure that electrons have sufficient time to radiate before scattering, larger
4932 volumes become the only way to achieve higher event statistics. To achieve the sensitivity
4933 goals of Phase III and IV cavity volumes on the order of several cubic-meters are required,
4934 which pushes one towards frequencies in the range of 100's of MHz.

4935 **Single-mode Cavity CRES**

4936 It is tempting to consider maintaining a high magnetic field, while still increasing the size
4937 of the cavity, in order to increase the radiated power from trapped electrons for better
4938 SNR. However, if one were to maintain the same magnetic field while increasing the
4939 size of the cavity, the electrons would begin to couple to higher order modes with more
4940 complicated transverse geometries. The danger with this approach is that a complicated
4941 mode structure could introduce systematic errors into the CRES signals. Example

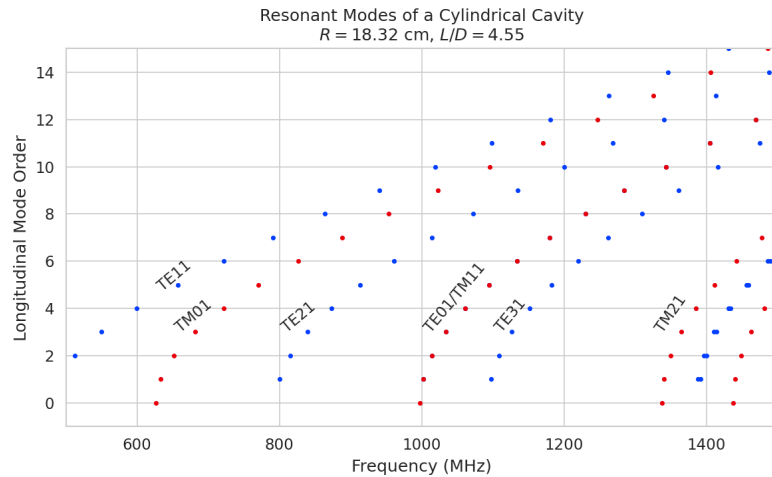
4942 systematics include unpredicted mode hybridization or changes in the mode shapes from
4943 imperfections in the cavity construction, which would prevent reconstruction of the
4944 electron's starting kinetic energies with adequate resolution. For this reason, it is ideal
4945 to operate with magnetic fields that give cyclotron frequencies near the fundamental
4946 frequency of the cavity, where the mode structure is relatively simple (see Figure 6.8).
4947 In this frequency region it is possible to perform CRES by coupling to only a single
4948 resonant mode, however, it is currently an open question if a single mode measurement
4949 will provide enough information about an individual electron's position to reconstruct
4950 the full event. Regardless, developing a solid understanding of the CRES phenomenology
4951 when an electron is coupling to a single mode will be a necessary step towards a future
4952 multi-mode cavity experiment.

4953 Considerations for Resonant Mode Selection

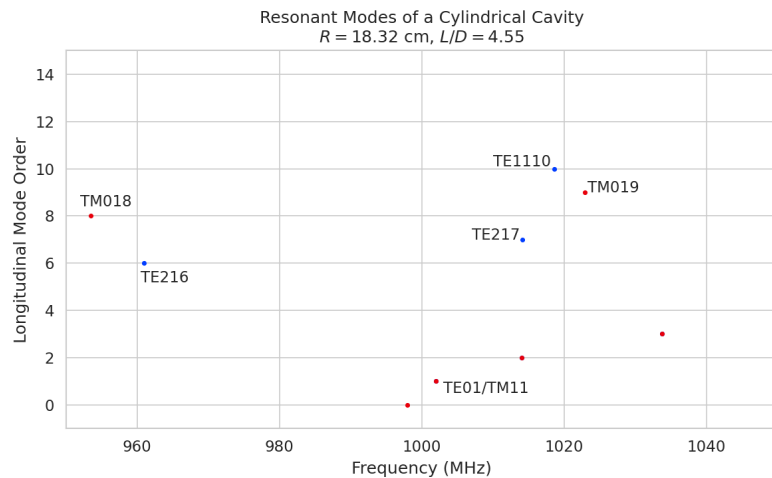
4954 A single-mode cavity experiment begs the question, which resonant mode is best for
4955 CRES measurements? There is an immediate bias towards low order TE_{nm} and TM_{nm}
4956 modes due to the multi-mode considerations discussed above. Additionally, there is a
4957 preference towards modes with longitudinal index $\ell = 1$ with a single antinode along the
4958 vertical axis of the cylindrical cavity. The reason for this is that there is a phase change
4959 in the electric fields between antinodes that leads to modulation effects that destroy the
4960 carrier frequency signal information.

4961 A second consideration for mode selection is the volumetric efficiency of the mode.
4962 Volumetric efficiency can be thought of as an integral over the volume of the cavity
4963 weighted by the relative amplitude of the mode. From the perspective of simply maximiz-
4964 ing the volume useable for CRES measurements this integral would be as close to unity
4965 as possible. However, there is a requirement to reconstruct the position of the electrons
4966 inside the cavity volume so that the local magnetic fields can be used to convert the
4967 measured cyclotron frequency to a kinetic energy. With a single mode this necessarily
4968 requires a variable transverse mode amplitude, which lowers the volumetric efficiency, so
4969 that position of the electron in the cavity can be estimated from the average amplitude
4970 of the CRES signal. Longitudinal indices of $\ell = 1$ have an advantage in volumetric
4971 efficiency over higher order ℓ modes, since there are only two longitudinal nodes, one at
4972 each end of the cavity. Therefore, the average coupling strength of trapped electrons as
4973 they oscillate axially is higher for $\ell = 1$ modes.

4974 The longitudinal variation in the mode strength is ultimately critical for achieving the
4975 energy resolution required for neutrino mass measurements. Correcting for the change in



(a)



(b)

Figure 6.8. Examples of the resonant mode frequencies of a cylindrical cavity. This cavity has a radius of 18.32 cm and a length to diameter ratio of 4.55.

4976 the average magnetic fields experienced by electrons with different pitch angles requires
 4977 that information on the axial motion of the electron be encoded into the CRES signal.
 4978 The longitudinal variation in the mode amplitude leads to amplitude modulation of the
 4979 CRES signal with a frequency proportional to the electron's pitch angle.

4980 An additional factor for mode selection is the intrinsic or unloaded Q of the mode. In
 4981 terms of SNR it is advantageous to use a mode with a very high Q_0 , which is then highly
 4982 overcoupled to achieve the necessary bandwidth to cover the tritium endpoint spectrum.
 4983 This scheme leads to a decoupling of the physical cavity temperature from the effective
 4984 noise temperature after the amplifier, which allows us to achieve adequate SNR without

4985 the requirement of cooling the entire cavity to single Kelvin temperatures.

4986 An example of a resonant mode that exhibits these traits is the TE₀₁₁ mode. At present
4987 the TE₀₁₁ mode is the preferred resonance for a single-mode cavity CRES experiment
4988 by the Project 8 collaboration. TE₀₁₁ is a low order mode located in a region relatively
4989 far from other cavity modes. Furthermore, the separation of the TE₀₁₁ mode can be
4990 improved by various mode-filtering techniques discussed in Section 6.4.2 below. TE₀₁₁
4991 consists of a single longitudinal antinode that can provide pitch angle information in the
4992 form of amplitude modulation, and has an electric field with a radial profile given by the
4993 J'_0 Bessel function allowing for radial position estimation. Lastly, the TE₀₁₁ mode has a
4994 relatively high intrinsic Q compared to nearby modes, which helps with SNR. Unloaded
4995 Q's greater than 80000 are achievable for a 1 GHz TE₀₁₁ resonance using a copper walled
4996 cavity.

4997 **6.3.3 Trade-offs Between the Antenna and Cavity Approaches**

4998 The choice between cavities and antennas for large-scale CRES measurements is not
4999 without trade-offs. Both the antenna array and cavity approaches are relatively immature
5000 techniques, at present there are no known obstacles that would prevent either approach
5001 from being used for a large scale neutrino mass experiment. The preference for cavities
5002 is largely driven by important practical considerations that could make a cavity based
5003 experiment significantly cheaper than an antenna experiment of similar size and scope.
5004 However, the switch to cavities also introduces new challenges less relevant to the
5005 antenna array, which must be solved in order for Project 8 to achieve its neutrino mass
5006 measurement goals.

5007 One of the major relative drawbacks of the antenna array approach is the size and
5008 complexity of the data-acquisition system. A large-scale antenna array experiment
5009 requires $O(100)$ antennas independently digitized at rates of $O(10)$ to $O(100)$ MHz. Since
5010 there is insufficient information in a single antenna channel to detect or reconstruct the
5011 CRES signal, the entire array output must be processed during the signal reconstruction.
5012 Because data storage becomes an issue with these data volumes, there is a real-time
5013 signal reconstruction requirement that allows one to detect CRES signals buried in the
5014 thermal noise. As discussed in Section 4.4, the computational cost of these real-time
5015 detection algorithms are potentially quite large for even a small scale antenna array
5016 experiment. However, the operating principle of a cavity experiment allows the CRES
5017 signal to be detected using only a single read-out channel digitized at rates of $O(10)$ MHz,
5018 which reduces the cost of the data acquisition system by many orders of magnitude.

5019 From an engineering perspective, the simple geometry and thin-walls of a cylindrical
5020 cavity are simpler to interface with the cryogenic and magnetic subsystems needed for a
5021 CRES experiment. Whereas, the antenna array requires careful design and engineering
5022 to accommodate the antenna array and receiver electronics in proximity to the trapping
5023 magnets. Additionally, due to near-field interference effects, the antenna array is unable
5024 to reconstruct CRES events within the reactive near-field distance of the antennas.
5025 Because atom trapping requirements require magnetic fields which correspond to cyclotron
5026 frequencies for endpoint electrons less than 1 GHz, the required stand-off distance leads to
5027 a significant loss in useable experiment volume, necessitating larger and more expensive
5028 magnets.

5029 Another advantage to the cavity approach is the relatively compact sideband structure,
5030 which is a result of the low modulation index for cavity CRES signals. The axial motion
5031 in an antenna array experiment leads to frequency modulation and sidebands. The shape
5032 of the sideband structure is determined by the modulation index, $h = \frac{\Delta f}{f_a}$, where Δf
5033 is the size of the frequency deviation and f_a is the axial frequency. The large electron
5034 traps required for a cubic-meter-scale experiment leads to high modulation indices, which
5035 causes the signal spectrum to be made up of numerous low power sidebands that make
5036 reconstruction and detection challenging. This behavior was observed in simulations
5037 of the FSCD in which carrier power decreased with pitch angle due to the increase in
5038 modulation index (see Figure 4.30). For cavities, however, the modulation index remains
5039 near $h = 1$ even for very long magnetic traps due to the high phase velocity in cavities
5040 relative to the axial velocity of the electron. This results in an almost ideal spectrum
5041 shape that has a strong carrier frequency with a few sidebands whose relative amplitudes
5042 encode pitch angle information.

5043 A downside of the cavity approach is the apparent difficulty of estimating the position
5044 of the electron using only the coupling of the electron to a single mode. The amplitude of
5045 the TE₀₁₁ mode is completely independent of the azimuthal coordinate, therefore, position
5046 reconstruction using the TE₀₁₁ mode is only able to estimate the radial position of the
5047 electron. This position degeneracy may lead to magnetic field uniformity requirements
5048 that are too challenging to meet due to mechanical uncertainties in cavity and magnet
5049 construction, as well as uncertainties caused by nuisance external magnetic fields such
5050 as the Earth's field and magnetic fields from building materials. A multi-mode cavity
5051 experiment may provide a way to extract more precise information on the position of
5052 the electron by analyzing the coupling of the electron to several modes that overlap in
5053 different ways.

5054 **6.4 Single-mode Resonant Cavity Design and Simulations**

5055 The single-mode cylindrical cavities envisioned for the Phase III and IV experiments must
5056 be carefully engineered in order to measure the neutrino mass with the desired sensitivity.
5057 In this section I summarize some simulation studies performed to analyze early design
5058 concepts for a single-mode cavity. The primary tool for these investigations was Ansys
5059 HFSS, which was also used for the development of the SYNCA antenna described in
5060 Section 5.3.

5061 **6.4.1 Open Cylindrical Cavities with Coaxial Terminations**

5062 **Design Concept**

5063 A basic cavity design question relevant to Project 8's ultimate goal of an atomic tritium
5064 CRES experiment is how to build a cavity that can be efficiently filled with atomic
5065 tritium. To keep the rate of atom loss from recombination on surfaces it is ideal if the
5066 ends of the cylindrical cavity are as open as possible so that tritium atoms can flow
5067 inside unimpeded. Additionally, one of the primary calibration techniques planned for
5068 future CRES experiments involves CRES measurements using electrons injected from
5069 an electron gun source, which also requires an opening at the cavity end. Cylindrical
5070 cavities with open ends can be manufactured, however, the intrinsic Q-factors of these
5071 cavities are orders of magnitude less than their sealed counterparts, which reduces the
5072 signal-to-noise ratio when that cavity is used for CRES measurement.

5073 Cylindrical cavities with mostly open ends that also exhibit Q values for the $TE_{01\ell}$
5074 modes similar to sealed cavities can be built by using coaxial endcaps to terminate the
5075 cavity. Cavities of this type have been manufactured for specialized applications related
5076 to the measurements of the dielectric constants of liquefied gasses (see Figure 6.9) [3, 4].
5077 This cavity design leaves the ends of the cavity wide open, but retains high Q-values for
5078 the $TE_{01\ell}$ modes due to the coaxial endcap, which are designed to perfectly reflect the
5079 electric fields of $TE_{01\ell}$ modes. Coupling to the $TE_{01\ell}$ mode is achieved via an aperture
5080 located at the center of the cavity wall.

5081 A cavity similar to Figure 6.9 is a candidate design for the future CRES experiments
5082 by Project 8, since it appears to elegantly solve many practical issues that arise when
5083 combining cavity CRES and atomic tritium. The coaxial endcaps leave significant regions
5084 of the cavity ends completely open, which allows for the entrance of atomic tritium as
5085 well as the pumping away of molecular tritium that has recombined on the cavity walls.

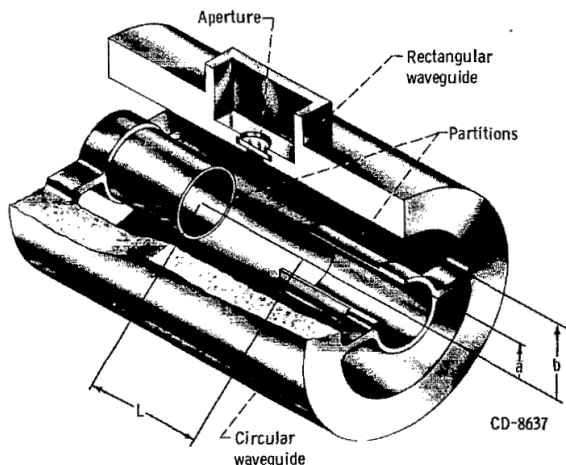


Figure 6.9. An image of an open cavity with coaxial terminations used for dielectric constant measurements. Figure from [3].

5086 These open ends are achieved while preserving the high Q-values of the $\text{TE}_{01\ell}$ modes,
 5087 which is important for extracting as much signal power from the electron as possible. In
 5088 subsequent sections this cavity design will be analyzed in more detail, primarily by using
 5089 HFSS simulations to analyze the resonant mode structure of this cavity geometry.

5090 **Coaxial Terminator Constraints**

5091 The reason that coaxial endcaps can be used to achieve high Q-values for the $\text{TE}_{01\ell}$
 5092 modes is that the electric fields for these modes are purely azimuthally polarized (see
 5093 Equations 6.12 and 6.13). Therefore, the boundary conditions that require the electric
 5094 field to go to zero at the cavity ends can be supplied using a coaxial partition of the
 5095 correct radius (see Figure 6.10). Because the cylindrical shape enforced by the partition
 5096 does not match the boundary conditions of other cavity modes, these terminations also
 5097 significantly suppress the Q-factors of non- $\text{TE}_{01\ell}$ modes, which is potentially beneficial
 5098 for a single-mode cavity CRES experiment.

5099 The correct radius of the cylindrical partition is derived by setting up the boundary
 5100 value problem in Figure 6.10, and analyzing the reflection and transmission coefficients
 5101 for waves incident on the coaxial terminators. The basic problem is to identify the radius
 5102 a where the reflection coefficient for the $\text{TE}_{01\ell}$ modes becomes equal to 1. One can show
 5103 that if the coaxial partitions are made sufficiently long relative to the wavelength of the
 5104 TE_{01} modes than perfect reflection can be achieved. This derivation is quite lengthy
 5105 and complex and is presented in full in [4]. Here, I shall simply explain the resulting

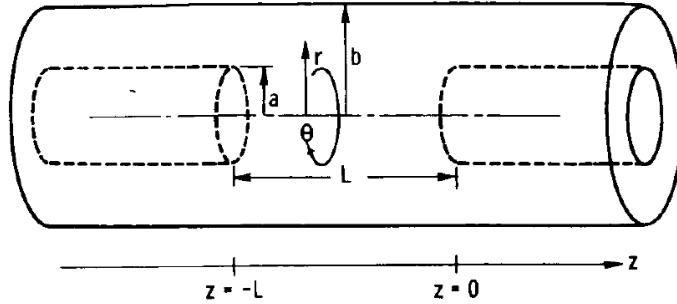


Figure 6.10. The simplified geometry of an open cavity with coaxial terminations. Figure from [4].

5106 conditions on the partition radius for perfect reflection.

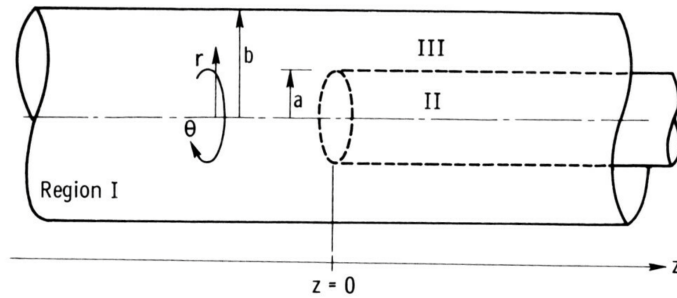


Figure 6.11. Electric field regions for the open cavity boundary value problem. Figure from [4].

5107 The open cavity boundary value problem is solved by expressing the forms of the
 5108 electric fields in the different regions of the cavity and requiring that the electric fields are
 5109 continuous. There are effectively three distinct regions in the open cavity corresponding
 5110 to the central cavity volume, the inner coaxial volume, and the outer coaxial volume (see
 5111 Figure 6.11).

5112 In Region I, the boundary conditions are those of a cylindrical waveguide, and it
 5113 is required that E_ϕ for the TE_{0m} modes go to zero at the cavity wall ($r = b$). This
 5114 necessitates $J'_{0m}(k_{c0m}b) = 0$. A solution for the radius a is desired such that the TE_{01}
 5115 mode propagates, but other TE_{0m} modes are below the cutoff frequency for the circular
 5116 waveguide. This is equivalent to requiring

$$3.832 < k_{c0m}b < 7.016, \quad (6.41)$$

5117 where the numbers 3.832 and 7.016 correspond to the first and second zeros of the Bessel
 5118 function (see Table 6.1).

In Region II the boundary conditions are those of a cylindrical waveguide, but with a smaller radius. The condition that $E_\phi = 0$ at the cylindrical partition radius is that $J'_{0m}(k_{c0m}a) = 0$. To ensure perfect reflection, all modes in Region 1 of the cavity must be below the cutoff frequency of the circular waveguide formed by the inner volume of the coaxial terminator. Therefore, solutions where the condition

$$k_{c0m}a < 3.832, \quad (6.42)$$

is true are required.

Finally, in Region III the boundary condition are those of a coaxial waveguide. One needs to guarantee that $E_\phi = 0$ at both $r = b$ and $r = a$, which involves finding the eigenvalues of the following equation

$$J'_0(k_{c0m}a)Y'_0(k_{c0m}b) - J'_0(k_{c0m}b)Y'_0(k_{c0m}a) = 0, \quad (6.43)$$

where Y'_0 the zeroth-order derivatives of the Bessel function of the second kind. The solutions to this equation depend on the value of the ratio b/a . The approximate solution is given by

$$\delta_n a \simeq \frac{n\pi}{b/a - 1}, \quad (6.44)$$

where δ_n are eigenvalues of Equation 6.43. Similar to Region II, solutions for which the TE₀₁ modes of Region I are below the cutoff frequency of Region III are needed. Therefore, it is required that

$$k_{c0m} < \delta_1. \quad (6.45)$$

In general, one has some freedom in specifying the value of b/a . A value typically used in practice is $b/a = 2.082$, which corresponds to positioning the radius of the cylindrical partition at the maxima of the TE₀₁ electrical fields.

Using the constraints from the three field regions one can develop a coaxial terminator that acts as a virtual perfectly conducting surface for the TE₀₁ modes. The only required inputs are the desired frequency of the TE₀₁₁ mode and a choice for the value of b/a .

6.4.2 Mode Filtering

The general case of an electron coupling to a resonant cavity is complicated. This is because cavities contain an infinite number of resonant modes, which for higher order modes, have couplings to the electron with a complex spatial dependence. The danger is

5144 that improper modeling of the electron's coupling to the cavity can lead to systematic
5145 errors in the CRES measurements that prevent a high-resolution measurement of the
5146 electron's kinetic energy. This in part drives the preference for a single-mode cavity
5147 experiment that uses only the electron's coupling to the TE₀₁₁ mode to perform CRES,
5148 assuming that sufficient information on the electron's position can be obtained with a
5149 single mode.

5150 The TE₀₁₁ mode is in a region where there are relatively few other modes to which
5151 the electron could couple(see Figure 6.8). However, one can see that the frequency of
5152 the TE₀₁₁ is perfectly degenerate with the TM₁₁₁ mode, which means that electrons will
5153 inevitably couple to both modes if they have the correct cyclotron frequency.

5154 The magnitude of the impact of the electron coupling to both TE₀₁₁ and TM₁₁₁ is
5155 currently unknown. To first order an electron coupling to more both modes will lose more
5156 energy overtime, which can be measured by observing the frequency chirp rate of the
5157 signal. This effect may be small enough to be negligible or simple enough to model that
5158 the cavity can be treated as an effective single-mode cavity. Alternatively, the one could
5159 consider devising a coupling scheme that is sensitive to both the TE₀₁₁ and the TM₁₁₁
5160 modes. By measuring the coupling of the electron to both modes more information on
5161 the position of the electron could be obtained, which could improve the position and
5162 energy resolution of the CRES measurements.

5163 A different approach is the mode filtering approach, which seeks to obtain a single
5164 TE₀₁₁ mode cavity using perturbations to the cavity walls that selectively impede the
5165 TM modes, while leaving the TE modes mostly unperturbed. The type of perturbations
5166 required can be determined by visualizing the surface currents induced in the cavity
5167 walls by each type of mode (see Figure 6.12). By definition, all TM have electric fields
5168 directed along the vertical axis of the cylindrical cavity, which means that perturbations
5169 that impede currents in this direction will modify TM resonances. On the other hand,
5170 the TE₀₁ modes induce azimuthal currents in the cavity walls, therefore, it is possible to
5171 break the degeneracy between TE₀₁ and TM₁₁ using a cavity perturbation that impedes
5172 axial currents, but does not affect the flow of azimuthal currents.

5173 Figure 6.12 shows two cavity design concepts that achieve this selective current
5174 perturbation. The resistive approach inserts a series of thin dielectric rings into the walls
5175 of the cavity that introduces a resistive and capacitive impedance to the longitudinal
5176 currents, while leaving azimuthal current paths intact. Cavities of this type with high
5177 TE₀₁ Q's have also been constructed by tightly wrapping a thin, dielectric coated wire
5178 around a mold to form the cavity wall. An alternative method is to introduce an inductive

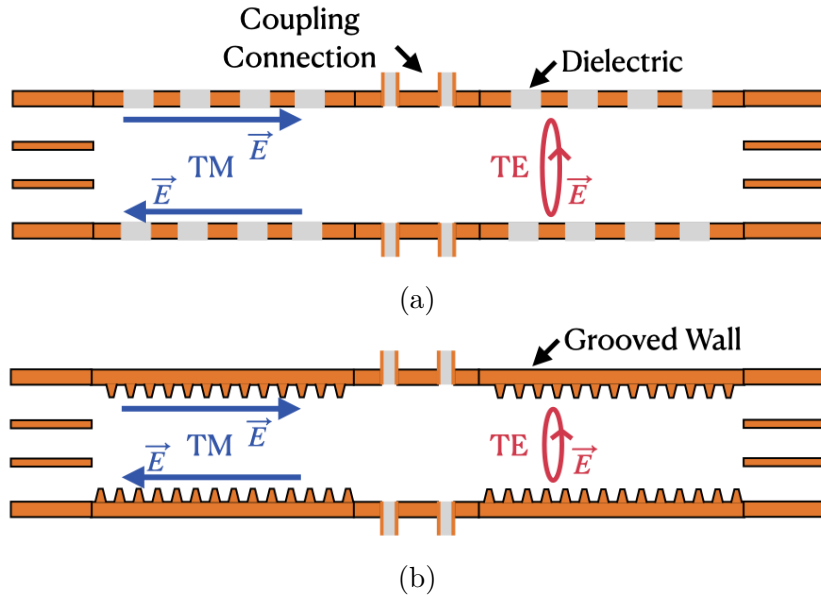


Figure 6.12. Two mode filtering concepts to break the degeneracy of TE_{01} and TM_{11} modes. The resistive approach uses dielectric materials to impede currents that travel vertically along the cavity while leaving azimuthal currents unperturbed. An alternative approach is to impede the currents using grooves cut into the cavity wall, which achieve the same effect with an inductive impedance.

5179 impedance by cutting grooves or a thread pattern on the inside wall of the cavity. For
 5180 reasons of manufacturability and compatibility with tritium the grooved cavity approach
 5181 is the preferred method for mode-filtered cavity construction by Project 8.

5182 **6.4.3 Simulations of Open, Mode-filtered Cavities**

5183 A candidate design for a single TE_{011} mode CRES experiment is a cavity that utilizes
 5184 the coaxial terminations combined with a mode-filtering wall. The first step towards
 5185 validating that a cavity that combines these two design features will operate as expected
 5186 is a thorough simulation effort for which finite element method (FEM) simulation software
 5187 is invaluable. The primary tool for electromagnetic FEM calculations inside Project 8 is
 5188 Ansys HFSS, which has a robust and well-established eigenmode solver that can identify
 5189 the resonant frequencies and associated Q-factors for given structure.

5190 Four variations of a cavity design with a ~ 1 GHz TE_{011} resonance were implemented
 5191 in HFSS (see Figure 6.13). The four designs include a standard cylindrical cavity, an
 5192 open cavity with smooth walls, an open cavity with resistive walls, and an open cavity
 5193 with grooved walls. The relevant design parameters are summarized in Table 6.3. All
 5194 cavities were simulated using copper walls and filled with a vacuum dielectric. The

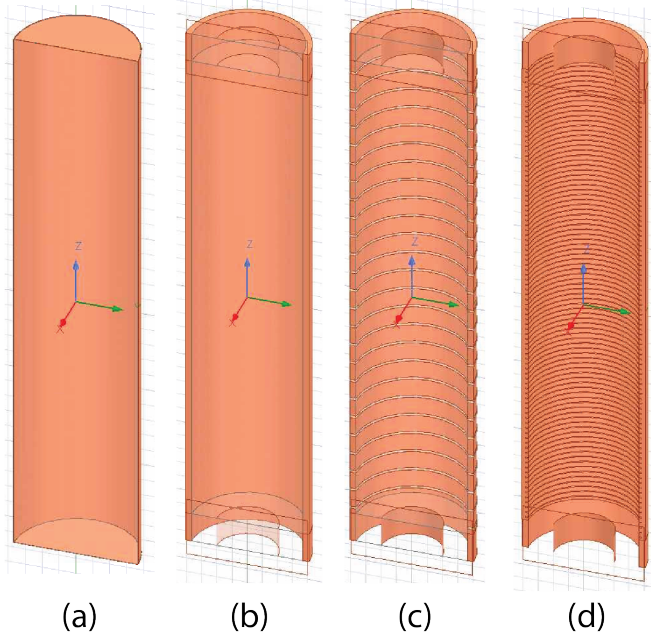


Figure 6.13. Four cavity design variations. (a) is a standard sealed cylindrical cavity, (b) is an open cavity with smooth walls, (c) is an open cavity with resistive walls, and (d) is an open cavity with grooved walls. The main cavity and coaxial terminator parameter are identical for all four cavities.

5195 identities of the resonant modes found by HFSS were validated by visual inspection of
 5196 the electric and magnetic field patterns and by comparison to analytical calculations of
 5197 the mode frequencies.

Table 6.3. A table of cavity design parameters used for HFSS simulations.

Name	Qty.	Unit	Description
D_{cav}	326.4	mm	Cavity diameter
L_{cav}	1668.0	mm	Cavity length
D_{term}	200.2	mm	Inner diameter of coaxial terminator
L_{term}	100.0	mm	Terminator length
l_{die}	8.3	mm	Dielectric spacer thickness
Δl_{die}	66.7	mm	Distance between dielectric spacers
l_{groove}	3.0	mm	Groove height
d_{groove}	9.0	mm	Groove depth
Δl_{groove}	18.3	mm	Distance between grooves

5198 The results of the HFSS simulations validate our predictions of the resonant behavior
 5199 of an open, mode-filtered cavity developed in the preceding sections (see Figure 6.14) One
 5200 can see that for a standard cavity the TE_{01} and the TM_{11} are degenerate in frequency
 5201 with relatively high Q-factors. The open-ended cavity preserves the high Q-factors of

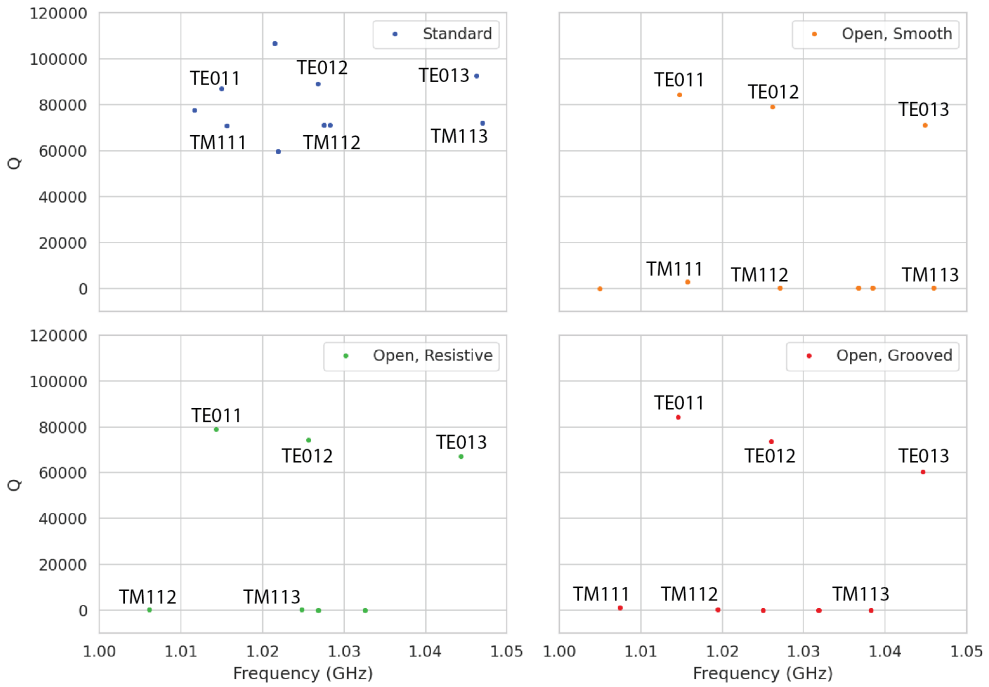


Figure 6.14. The frequencies and Q-factors of the resonant modes identified by HFSS for the cavity variations shown in Figure 6.13. The fully-sealed cavity with smooth walls has several high-Q modes near the TE_{011} resonance. Introducing the open-termination preserves the Q-factors of the $TE_{01\ell}$ modes and suppresses the Q-factors of the modes whose boundary conditions do not match the cylindrical partition. Both the resistive and grooved wall perturbations shift the resonant frequencies of the TM modes away from the TE_{011} mode. By properly tuning the geometry of the grooves or the resistive spacers several MHz of frequency separation can be achieved.

the TE_{01} modes, while the other modes, since their boundary conditions do not match the coaxial geometry, have their Q-factors suppressed. One can see that the effect of the resistive and inductive mode-filtering schemes is to effectively shift the resonant frequencies of the TM_{11} modes below those of the associated TE_{01} modes, which breaks the degeneracy. Optimization of the dielectric spacer or groove parameters can ensure that the TE_{011} mode is isolated from other modes by $O(10)$ MHz, which provides sufficient bandwidth for a measurement of the tritium spectrum endpoint.

Further optimization of the cavity design requires a more detailed cavity simulation that includes the cavity coupling mechanism as well as other geometry modifications required for integration into the magnetic and tritium gas subsystems. Perhaps more important is the development of the capability to simulate the interaction of electrons with the cavity so that simulated CRES signals can be generated using cavities designed for CRES measurements. Simulated CRES signals can then be used to estimate the

5215 neutrino mass sensitivity of the experiment, which allows for the optimization of the cavity
5216 design towards the configuration that provides the best measurement of the neutrino
5217 mass.

5218 **6.5 Single-mode Resonant Cavity Measurements**

5219 Measurement test stands play an important role in the research and development process
5220 that cannot be replaced by simulations. For example, constructing a prototype CRES
5221 cavity forces one to consider important practical issues such as manufacturability and
5222 machine tolerances that may require modifications to the design. Furthermore, by
5223 comparing laboratory measurements of a real cavity to simulations, one can quantify
5224 the impact of imperfections and real-life measurement systematics, which allows for
5225 more accurate sensitivity estimates of the experiment. Lastly, the development of these
5226 prototypes helps to build the necessary experience and expertise within the collaboration
5227 required for more complicated experiments to succeed.

5228 In this spirit a prototype cavity was constructed to demonstrate the open, mode-
5229 filtered cavity concept explored in the previous sections. The primary goal of the
5230 measurements was to validate that an open, mode-filtered cavity suppressed the TM_{11}
5231 modes as predicted by HFSS simulations.

5232 **6.5.1 Cavities and Setup**

5233 Two rudimentary, cavities were constructed using segments of copper pipe available from
5234 McMaster-Carr (see Figure 6.15). The design consists of copper pipes of two diameters.
5235 The larger diameter pipe forms the main cavity wall and the smaller diameter pipe is
5236 used to create a coaxial termination. The diameter of the outer pipe was chosen to
5237 produce a TE_{011} resonance of approximately 6 GHz, while the diameter of the smaller
5238 pipe was selected based on the open termination criteria introduced in Section 6.4.1. The
5239 approximate diameters and lengths of the copper pipe are summarized in Table 6.4.

5240 Coupling to the cavity was achieved using a hand-formable segment of coaxial cable
5241 stripped at one end to form a loop antenna. This was inserted into a small hole located
5242 at the center of the main cavity wall. The coaxial terminators were supported inside the
5243 main cavity by carving a spacer from polystyrene foam (styrofoam) so that they could
5244 be easily inserted into the cavity and repositioned. The dielectric constant of styrofoam
5245 is quite close to air at microwave frequencies so this is expected to have minimal impact

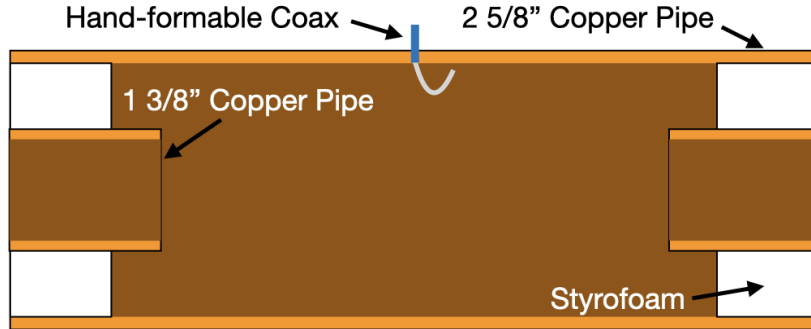


Figure 6.15. A cartoon depicting the design of the open-ended cavity prototype designed to operate at approximately 6 GHz. The main cavity wall was composed of a single copper pipe. A mode-filtered version of this cavity was constructed by

5246 on the resonant properties of the cavity.

Table 6.4. A table of parameters describing the cavity prototypes. Certain values such as the cavity length and the distance between dielectric spacers are approximate due to variation in the machining of the copper. In particular, the filtered cavity was constructed from conducting copper segments that varied in size from 1.50" to 1.85".

Name	Qty.	Unit	Description
D_{cav}	2.625	in	Cavity diameter
L_{cav}	≈ 13	in	Cavity length
D_{term}	1.375	in	Inner diameter of coaxial terminator
L_{term}	1.575	in	Terminator length
l_{die}	0.75	in	Dielectric spacer thickness
Δl_{die}	≈ 1.50 to 1.85	in	Distance between dielectric spacers

5247 The actual length of the cavity is given by the distance between the inner edges of the
 5248 coaxial terminations. The length of the outer section of pipe that forms the main wall of
 5249 the cavity is approximately 16" in length which leads to a cavity length of $\approx 13"$ when
 5250 both terminators are inserted in the cavity. Because the terminators were not rigidly
 5251 mounted this distance is only approximate, however, the uncertain length of the cavity
 5252 will not prevent us from validating the open cavity design.

5253 Along with the smooth-walled open cavity a resistively mode-filtered cavity was
 5254 constructed by creating dielectric spacers out of segments of clear PVC pipe (see Figure
 5255 6.16). The spacers were machined such that the conductive segments of the cavity would
 5256 be separated by 0.75" when the cavity was fully assembled. Due to variations in the
 5257 lengths of the copper segments that make up the cavity wall the distance between spacers
 5258 has significant variation with average value of about 1.7". Eight total spacers were used
 5259 to build the cavity, which when assembled was approximately 16" in total length similar

to the non-filtered cavity.

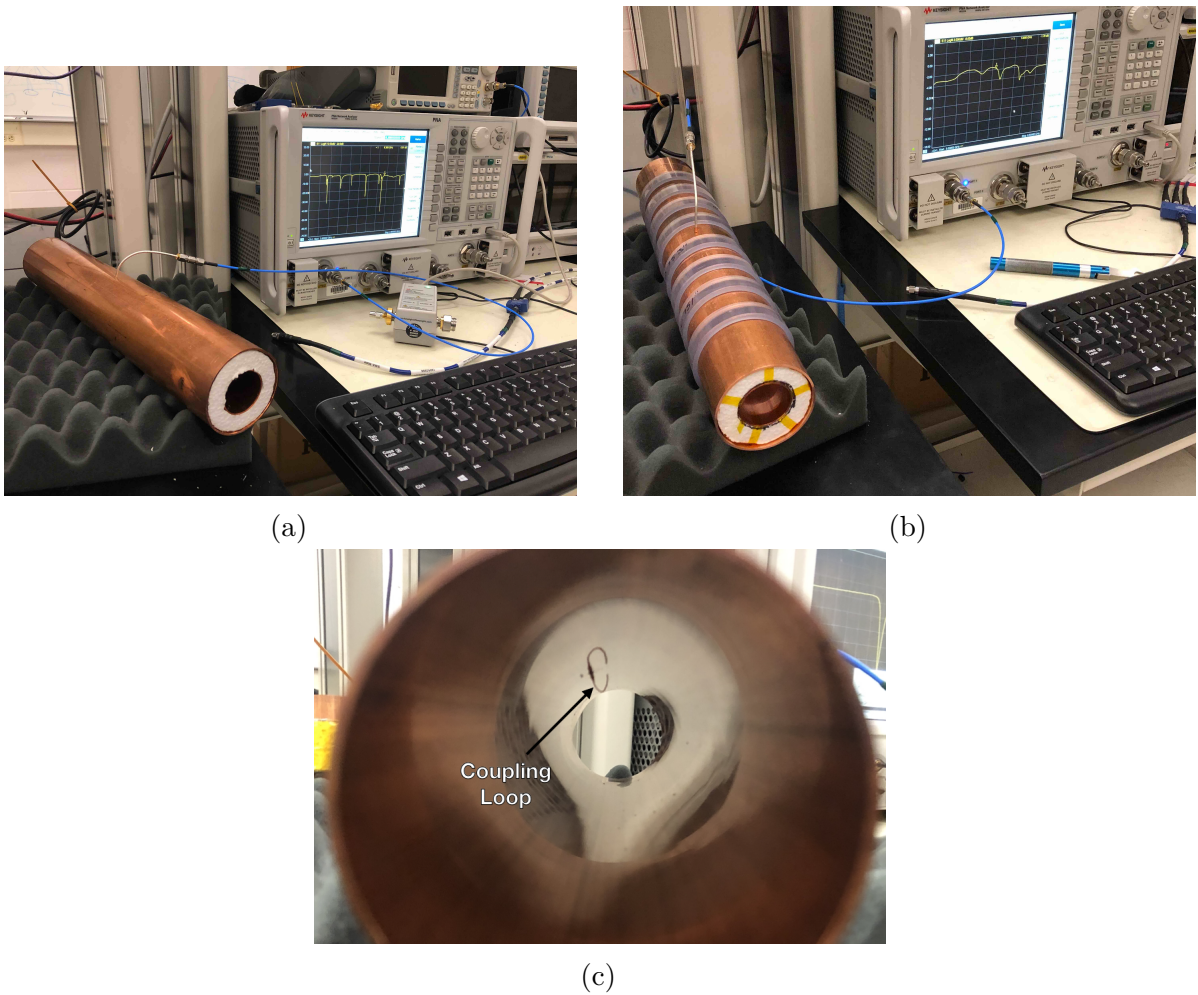


Figure 6.16. Images depicting the measurement of the filtered and non-filtered open cavities using the VNA. The coupling loop in the figure is shown in the TE orientation.

5260

5261 Measurements of both cavities were performed using a VNA connected to the cavity
 5262 coupling probe (see Figure 6.16). By measuring the return loss over a range of frequencies
 5263 one can measure the frequencies and relative Q-factors of the resonant modes in the
 5264 cavity. Due to the opposite polarity of the electric fields for the TE and TM modes,
 5265 the loop coupling probe must be rotated 90° to change the polarity of the loop antenna.
 5266 When the antenna is oriented such that the loop opening faces the ends of the cavity, it
 5267 couples primarily to the TE modes which have magnetic fields directed along the long
 5268 axis of the cavity (see Figure 6.16). If the coupling loop is turned by 90° from where
 5269 it is shown in the image then it will couple to the TM modes which have azimuthally
 5270 directed magnetic fields. In this way both the TE and TM resonances can be measured

5271 independently.

5272 6.5.2 Results and Discussion

5273 The primary analysis for the prototype cavities involved a simple visualization of the
5274 return loss as measured by the VNA and a comparison between the filtered and non-
5275 filtered variations. Since the resonances measured by the VNA are not labeled, there is
5276 an uncertainty about the true identities of the modes measured by the VNA. To resolve
5277 this I performed a simulation of the simplest possible cavity that could be created from
5278 the prototype components, which is a fully open cavity created by removing the coaxial
5279 inserts. The fully-open cavity with the as-built dimensions was simulated in HFSS to get
5280 estimates on the positions of the TE₀₁₁ and TM₁₁₁ modes (see Figure 6.17).

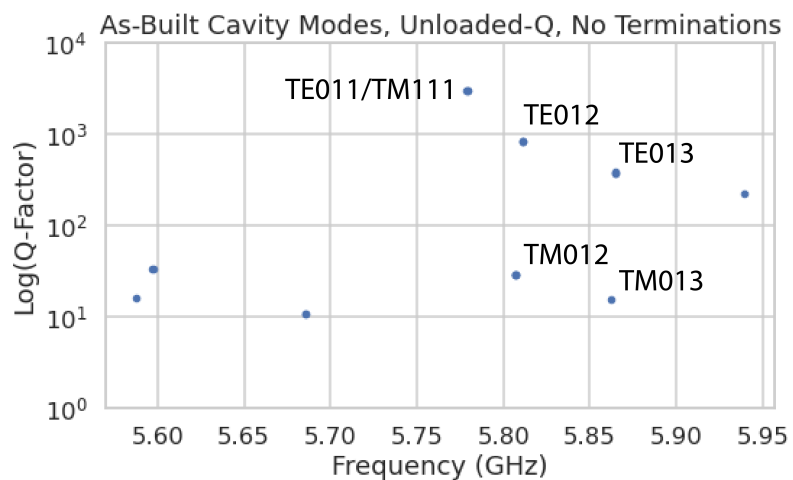


Figure 6.17. HFSS simulation results for a the as-built cavity with the coaxial terminators removed. The TE₀₁₁/TM₁₁₁ frequency is approximately 5.78 GHz.

5281 Simulation of the fully open cavity shows that the TE₀₁₁/TM₁₁₁ modes have a
5282 frequency of approximately 5.78 GHz in the fully open cavity. If the frequency of this
5283 mode is compared to the measurements of the fitered and non-filtered cavities with the
5284 terminators removed one can easily identify the TE₀₁₁ mode at approximately 5.75 GHz
5285 (see Figure 6.18).

5286 Both variations of the non-filtered cavities one sees that the TE₀₁₁ mode is degenerate
5287 in frequency with what appears to be a doublet of TM modes located at the TM₁₁₁
5288 frequency position. This doublet is actually the TM₁₁₁ mode, which has two polarizations
5289 with opposite polarizations. Because the pipe used to construct the cavity is not perfectly

5290 round, the frequency degeneracy between the two polarizations is broken resulting in the doublet peaks.

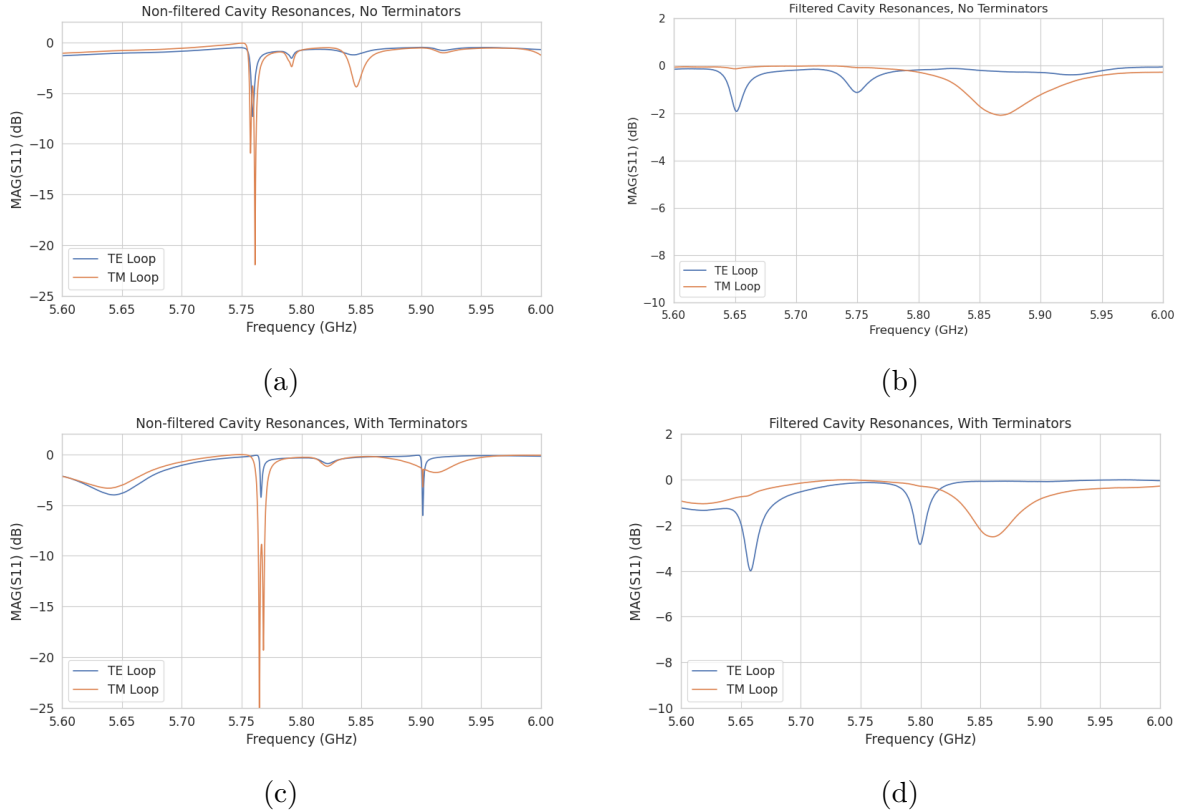


Figure 6.18. Measurements of the filtered and non-filtered prototype cavities acquired with the VNA.

5291
 5292 The S-parameter plot for the filtered cavity without terminators has an isolated TE
 5293 resonance at 5.65 GHz, associated with the TE_{011} mode. The frequency of this mode
 5294 is lower than the non-filtered cavity due to a difference in the overall lengths of the
 5295 cavities. An obvious difference between the filtered and non-filtered cavities is that
 5296 there is no TM_{111} doublet at the TE_{011} frequency. This is what one would expect if
 5297 the mode-filtering was suppressing the TM modes. There appears to be a noticeable
 5298 difference in the Q of the TE_{011} resonance between non-filtered and filtered variations as
 5299 indicated by the increased resonance depth for the filtered cavity. Overall, the Q-factors
 5300 of the filtered cavity appear significantly smaller than the non-filtered cavity due to the
 5301 increase in resonance width. This is likely caused by the relatively large widths of the
 5302 dielectric spacers, which are partially impeding the TE modes.

5303 One can see from these cavity measurements that, in principle, resistive mode-filtering
 5304 can be used to separate the TE_{011} resonance from the degenerate TM_{111} modes in

5305 combination with the open cavity endcaps. This finding agrees with the expectations
5306 from HFSS, which should provide confidence that the eigenmode solver is correctly
5307 modeling the behavior of the cavity. Although I did not perform a similar study using
5308 a cavity with grooved walls it is expected that the resonant mode structure would be
5309 similar to the cavity studied here.

5310 While this prototype cavity is a good first step, several deficiencies prevent this setup
5311 from providing more than qualitative information to the design of cavities for CRES. This
5312 includes the rudimentary approach to cavity coupling using a stripped coax antenna and
5313 the inability to map the field density in the cavity volume. Improvements in these areas
5314 are required so that measurements from a real cavity can provide useful information to
5315 cavity CRES simulations that will ultimately inform neutrino mass sensitivity estimates.

5316 Future work with prototype cavities must include an improved cavity coupling scheme,
5317 which is robust and compatible with atomic tritium. Since the cavity will ultimately
5318 be filled with atomic tritium, a coupling antenna cannot be used due to the losses of
5319 atomic tritium caused by recombination on the antenna surfaces. Possible non-invasive
5320 coupling schemes include aperture coupling, where the cavity is coupled to an external
5321 waveguide structure through an aperture, or a split-ring coupling approach, where the
5322 center segment of the cylindrical cavity wall is replaced an isolated conductive ring with
5323 a small vertical slit. The aperture coupling approach is a standard coupling scheme [88]
5324 used in a wide range of applications, but at low frequencies the size of the external
5325 waveguide conflicts with design of the atom trapping magnet and cryogenics system.
5326 The split-ring approach could potentially be coupled to a small coaxial transmission line
5327 which is more compatible with the rest of the experiment design. A challenge is achieving
5328 adequate coupling through impedance tuning, which is a focus of current research.

5329 The robustness of the coupling mechanism is relevant due to the difficulty in modeling
5330 its effect on the cavity modes. Small changes in geometry can have a large influence on
5331 the coupling and hence the performance of the cavity, therefore, correctly modeling the
5332 cavity coupling is critical for accurate CRES simulations. Coupling schemes that rely
5333 on connections to coaxial lines are potentially at a disadvantage in this regard due to
5334 the affect of soldering imperfections or unintended bends in the coax on the coupling.
5335 Future work will identify a coupling scheme for the cavity compatible with the neutrino
5336 mass goals of Project 8.

5337 Imperfections in the geometry of a real cavity will necessarily distort the resonant
5338 modes away from simulation predictions. This will change the coupling of an electron
5339 to the cavity and thus change the expected signal structure. Ultimately, this effect will

5340 limit the achievable energy resolution of the experiment unless the differences between
5341 simulation and a real cavity can be sufficiently characterized and calibrated. One possible
5342 approach to this is to utilize a "bead puller" system [102] to strategically perturb the
5343 cavity by moving a conductive bead through the cavity volume. The small perturbation
5344 caused by the bead affects the phase of the cavity resonances proportional to the total
5345 magnitude of the electric field at that position, so by moving the bead through the
5346 cavity volume the total electric field can be mapped and compared to simulation. This
5347 information can provide bounds on the relative perturbations to the cavity mode structure
5348 from real-life imperfections compared to the idealized cavity in HFSS.

5349 **Chapter 7 |**

5350 **Conclusion and Future Prospects**

5351 In this dissertation I have discussed research and development efforts towards the
5352 development of a scalable CRES measurement technology that can be used to build a
5353 CRES experiment at cubic-meter scales with sensitivity to neutrino masses of 40 meV.
5354 The primary contributions of my dissertation are the development and analysis of signal
5355 reconstruction algorithms for an antenna array based CRES experiment [103], which leads
5356 to estimates of the neutrino mass sensitivity; the development of a synthetic cyclotron
5357 radiation antenna (SYNCA) [82], which allowed for laboratory validation of antenna
5358 array CRES simulation models [44]; and the development of an open-ended cavity design
5359 compatible with atomic tritium for a cavity based CRES experiment. A measurable
5360 impact of this work is the transition of the Project 8 collaboration's experimental plan
5361 from an antenna array based approach to a cavity based approach, where my work played
5362 a key role in demonstrating the significantly higher cost and complexity of the antenna
5363 array experiment.

5364 The transition from antenna arrays to cavities requires a new set of demonstrator
5365 experiments to make incremental progress towards a 40 meV measurement of the neutrino
5366 mass. At the time of writing, the near-term plan of Project 8 is to design and construct a
5367 small-scale cavity CRES experiment utilizing the 1 T magnet installed in the UW-Seattle.
5368 This cavity is designed to have a TE011 resonance with a frequency of about 26 GHz with
5369 a length-to-diameter ratio that mimics the larger cavities intended for the pilot-scale and
5370 Phase IV experiments. The goal of this experiment is to demonstrate cavity CRES as
5371 well as validate models of CRES systematics using electrons from ^{83m}Kr and an electron
5372 gun. Though the primary goal is demonstration, near-term physics measurements are
5373 available in the form of high-resolution measurements of the ^{83m}Kr conversion spectrum
5374 of interest to the KATRIN collaboration.

5375 Furthermore, Project 8 is currently constructing a low-frequency CRES setup located
5376 at Yale University to better understand the principles of cavity based CRES at lower

5377 magnetic fields. The Low, UHF Cavity Krypton Experiment at Yale (LUCKEY) is
5378 a 1.5 GHz cavity CRES experiment the will use conversion electrons from ^{83m}Kr to
5379 perform CRES measurements at the lowest frequencies ever attempted with the technique.
5380 LUCKEY will validate frequency scaling models developed by Project 8 and will pave
5381 the way for the future Low-Frequency Apparatus (LFA), which will be a larger, 1 GHz
5382 cavity CRES experiment that includes a molecular tritium source. The target for the
5383 LFA is a measurement of the neutrino mass with a sensitivity of approximately 0.2 eV,
5384 which will build towards the atomic pilot-scale CRES experiment.

5385 In parallel to the development of cavity CRES is the development of the atomic
5386 tritium source. Recent demonstrations of the production of atomic hydrogen are excellent
5387 steps towards the atomic tritium production needed for the pilot-scale experiment. One
5388 area of future study includes the development of a more detailed understanding of the
5389 efficiency of atomic hydrogen production. Near-term plans include the development
5390 of a magnetic, evaporatively cooled beamline, as well as the prototyping of a Halbach
5391 array atoms trap. Nearly all the components of the atomic tritium system will require
5392 demonstration before the complete system can be built. The long-term goal of the
5393 atomic tritium work is to construct a full atomic tritium prototype that demonstrates
5394 the production, cooling, trapping, and recycling of tritium at the rates needed for the
5395 pilot-scale experiment.

5396 More broadly, the long-term goal of the Project 8 collaboration is to fully develop
5397 both the atomic tritium and cavity CRES technologies so that both can be combined in
5398 a pilot-scale CRES experiment. It is envisioned that this process will take approximately
5399 10 years for both atomic tritium and cavity CRES. After these developments comes
5400 the pilot-scale experiment which will be the first CRES experiment that simultaneously
5401 demonstrates all the required technologies for Phase IV. Scaling to Phase IV with cavity
5402 CRES will require the construction of multiple copies (approximately 10) of the pilot-scale
5403 experiment to obtain sufficient statistics for 40 meV sensitivity.

5404 Development of the CRES experimental technique by Project 8 has led to new
5405 experiments utilizing the CRES technique for basic physics research, such as the ^6He -
5406 CRES collaboration [104], and has also found applications as a new approach to x-ray
5407 spectroscopy [105]. Recently, a new experimental effort called CRESDA has begun in
5408 the UK to develop new quantum technologies applied to CRES measurements for the
5409 neutrino mass [106]. This flourishing of new experimental efforts based on the CRES
5410 technique is likely to continue as Project 8 continues to develop the technique towards
5411 its neutrino mass measurement goal.

Bibliography

- [1] CAHN, R. N., D. A. DWYER, S. J. FREEDMAN, W. C. HAXTON, R. W. KADEL, Y. G. KOLOMENSKY, K. B. LUK, P. McDONALD, G. D. OREBI GANN, and A. W. P. POON (2013) “White Paper: Measuring the Neutrino Mass Hierarchy,” in *Snowmass 2013: Snowmass on the Mississippi*, 1307.5487.
- [2] AGOSTINI, M., G. BENATO, and J. DETWILER (2017) “Discovery probability of next-generation neutrinoless double- β decay experiments,” *Phys. Rev. D*, **96**(5), p. 053001, 1705.02996.
- [3] WENGER, N. C. and J. SMETANA (1972) “Hydrogen Density Measurements Using an Open-Ended Microwave Cavity,” *IEEE Transactions on Instrumentation and Measurement*, **21**(2), pp. 105–114.
- [4] WENGER, N. (1967) “Resonant Frequency of Open-Ended Cylindrical Cavity,” *IEEE Transactions on Microwave Theory and Techniques*, **15**(6), pp. 334–340.
- [5] DAS, A. and T. FERBEL (2003) *Introduction to Nuclear and Particle Physics*, World Scientific.
- [6] CURIE, P. (1898) “Sur une nouvelle substance fortement radioactive, contenue dans la pechblende,” *Comptes rendus de l’Academie des Sciences, Paris*, **127**, pp. 1215–1217.
- [7] RUTHERFORD, E. (1899) “Uranium radiation and the electrical conduction produced by it,” *Philos. Mag.*, **47**, p. 109.
URL <https://cds.cern.ch/record/261896>
- [8] GERWARD, L. (1999) “Paul Villard and his Discovery of Gamma Rays,” *Physics in Perspective*, **1**, pp. 367–383.
- [9] BECQUEREL, H. (1900) “Deviation du rayonnement du radium dans un champ électrique,” *C.R.*, **130**, pp. 809–815.
- [10] D.Sc., E. R. M. and F. S. B.A. (1902) “XLI. The cause and nature of radioactivity.—Part I,” *The London, Edinburgh, and Dublin Philosophical Magazine and Journal of Science*, **4**(21), pp. 370–396, <https://doi.org/10.1080/14786440209462856>.
URL <https://doi.org/10.1080/14786440209462856>

- 5442 [11] CHADWICK, J. (1914) *Intensitätsverteilung im magnetischen Spektrum der β -*
5443 *Strahlen von Radium B+C*, Druck von Friedr. Vieweg und Sohn.
5444 URL <https://books.google.com/books?id=8s8UmQEACAAJ>
- 5445 [12] BROWN, L. M. (1978) “The idea of the neutrino,” *Physics Today*, **31**(9).
- 5446 [13] PAULI, W. (1978) “Dear radioactive ladies and gentlemen,” *Phys. Today*, **31N9**,
5447 p. 27.
- 5448 [14] AMALDI, E. (1984) “From the discovery of the neutron to the discovery of nuclear
5449 fission,” *Physics Reports*, **111**(1), pp. 1–331.
5450 URL <https://www.sciencedirect.com/science/article/pii/037015738490214X>
- 5452 [15] CHADWICK, J. (1932) “The existence of a neutron,” *Proceedings of the Royal
5453 Society of London. Series A, Containing Papers of a Mathematical and Physical
5454 Character*, **136**(830), pp. 692–708, <https://royalsocietypublishing.org/doi/pdf/10.1098/rspa.1932.0112>.
5455 URL <https://royalsocietypublishing.org/doi/abs/10.1098/rspa.1932.0112>.
- 5456 [16] WILSON, F. L. (1968) “Fermi’s Theory of Beta Decay,” *American Journal of
5457 Physics*, **36**(12), pp. 1150–1160, https://pubs.aip.org/aapt/ajp/article-pdf/36/12/1150/11891052/1150_1_online.pdf.
5460 URL <https://doi.org/10.1119/1.1974382>
- 5462 [17] CRANE, H. R. and J. HALPERN (1938) “New Experimental Evidence for the
5463 Existence of a Neutrino,” *Phys. Rev.*, **53**, pp. 789–794.
5464 URL <https://link.aps.org/doi/10.1103/PhysRev.53.789>
- 5466 [18] COWAN, C. L., F. REINES, F. B. HARRISON, H. W. KRUSE, and A. D.
5467 MC GUIRE (1956) “Detection of the Free Neutrino: a Confirmation,” *Science*,
5468 **124**(3212), pp. 103–104, <https://www.science.org/doi/pdf/10.1126/science.124.3212.103>.
5469 URL <https://www.science.org/doi/abs/10.1126/science.124.3212.103>
- 5470 [19] ANICIN, I. V. (2005) “The Neutrino - Its Past, Present and Future,” *arXiv e-prints*,
5471 physics/0503172, physics/0503172.
- 5472 [20] DAVIS, R. (2003) “Nobel Lecture: A half-century with solar neutrinos,” *Rev. Mod.
5473 Phys.*, **75**, pp. 985–994.
- 5474 [21] McDONALD, A. B. ET AL. (2002) “Direct evidence for neutrino flavor transfor-
5475 mation from neutral-current interactions in SNO,” *AIP Conf. Proc.*, **646**(1), pp.
5476 43–58.
- 5477 [22] FUKUDA, Y. ET AL. (1998) “Evidence for oscillation of atmospheric neutrinos,”
5478 *Phys. Rev. Lett.*, **81**, pp. 1562–1567, hep-ex/9807003.

- 5479 [23] GIGANTI, C., S. LAVIGNAC, and M. ZITO (2018) “Neutrino oscillations: The rise
 5480 of the PMNS paradigm,” *Prog. Part. Nucl. Phys.*, **98**, pp. 1–54, 1710.00715.
- 5481 [24] WORKMAN, R. L. and OTHERS (2022) “Review of Particle Physics,” *PTEP*, **2022**,
 5482 p. 083C01.
- 5483 [25] AN, F. ET AL. (2016) “Neutrino Physics with JUNO,” *J. Phys. G*, **43**(3), p. 030401,
 5484 1507.05613.
- 5485 [26] BIAN, J. ET AL. (2022) “Hyper-Kamiokande Experiment: A Snowmass White
 5486 Paper,” in *Snowmass 2021*, 2203.02029.
- 5487 [27] ABI, B. ET AL. (2020) “Long-baseline neutrino oscillation physics potential of the
 5488 DUNE experiment,” *Eur. Phys. J. C*, **80**(10), p. 978, 2006.16043.
- 5489 [28] ZUBER, K. (2020) *Neutrino Physics*, CRC Press.
- 5490 [29] XING, Z. Z. and S. ZHOU (2011) *Neutrinos in Particle Physics, Astronomy and*
 5491 *Cosmology*, Springer.
- 5492 [30] MOHAPATRA, R. N. ET AL. (2007) “Theory of neutrinos: A White paper,” *Rept.
 5493 Prog. Phys.*, **70**, pp. 1757–1867, hep-ph/0510213.
- 5494 [31] DE GOUVÉA, A. (2016) “Neutrino Mass Models,” *Ann. Rev. Nucl. Part. Sci.*, **66**,
 5495 pp. 197–217.
- 5496 [32] WONG, Y. Y. Y. (2011) “Neutrino mass in cosmology: status and prospects,”
 5497 *Ann. Rev. Nucl. Part. Sci.*, **61**, pp. 69–98, 1111.1436.
- 5498 [33] ADE, P. A. R. ET AL. (2016) “Planck 2015 results. XIII. Cosmological parameters,”
 5499 *Astron. Astrophys.*, **594**, p. A13, 1502.01589.
- 5500 [34] CARLSTROM, J. ET AL. (2019) “CMB-S4,” in *Bulletin of the American Astronomical Society*, vol. 51, p. 209, 1908.01062.
- 5502 [35] ELLIOTT, S. R. and P. VOGEL (2002) “Double beta decay,” *Ann. Rev. Nucl. Part.
 5503 Sci.*, **52**, pp. 115–151, hep-ph/0202264.
- 5504 [36] DOLINSKI, M. J., A. W. P. POON, and W. RODEJOHANN (2019) “Neutrinoless
 5505 Double-Beta Decay: Status and Prospects,” *Ann. Rev. Nucl. Part. Sci.*, **69**, pp.
 5506 219–251, 1902.04097.
- 5507 [37] FORMAGGIO, J. A., A. L. C. DE GOUVÉA, and R. G. H. ROBERTSON (2021)
 5508 “Direct measurements of neutrino mass,” *Physics Reports*, **914**, pp. 1–54, direct
 5509 measurements of neutrino mass.
 5510 URL [https://www.sciencedirect.com/science/article/pii/
 5511 S0370157321000636](https://www.sciencedirect.com/science/article/pii/S0370157321000636)

- 5512 [38] AKER, M. ET AL. (2022) “New Constraint on the Local Relic Neutrino Background
 5513 Overdensity with the First KATRIN Data Runs,” *Phys. Rev. Lett.*, **129**(1), p.
 5514 011806, 2202.04587.
- 5515 [39] FORMAGGIO, J. A., A. L. C. DE GOUVÊA, and R. G. H. ROBERTSON (2021)
 5516 “Direct Measurements of Neutrino Mass,” *Phys. Rept.*, **914**, pp. 1–54, 2102.00594.
- 5517 [40] MONREAL, B. and J. A. FORMAGGIO (2009) “Relativistic cyclotron radiation
 5518 detection of tritium decay electrons as a new technique for measuring the neutrino
 5519 mass,” *Phys. Rev. D*, **80**, p. 051301.
 5520 URL <https://link.aps.org/doi/10.1103/PhysRevD.80.051301>
- 5521 [41] ESFAHANI, A. A. ET AL. (2022) “The Project 8 Neutrino Mass Experiment,”
 5522 2203.07349.
- 5523 [42] ——— (2023) “Cyclotron Radiation Emission Spectroscopy of Electrons from
 5524 Tritium Beta Decay and ^{83m}Kr Internal Conversion,” 2303.12055.
- 5525 [43] ——— (2023) “Tritium Beta Spectrum and Neutrino Mass Limit from Cyclotron
 5526 Radiation Emission Spectroscopy,” 2212.05048.
- 5527 [44] “Antenna Arrays for Physics Measurements with Large-scale CRES Detectors,” *In
 5528 preparation*.
- 5529 [45] NICHOLSON, T. ET AL. (2015) “Systematic evaluation of an atomic clock at 2 x
 5530 10-18 total uncertainty,” *Nature Communications*, **6**(6896).
- 5531 [46] HÄNSCH, T. W. (2006) “Nobel Lecture: Passion for precision,” *Rev. Mod. Phys.*,
 5532 **78**, pp. 1297–1309.
 5533 URL <https://link.aps.org/doi/10.1103/RevModPhys.78.1297>
- 5534 [47] GABOR, D. (1946) “Theory of communication. Part 1: The analysis of information,”
 5535 *Journal of the Institution of Electrical Engineers-part III: radio and communication
 5536 engineering*, **93**(26), pp. 429–441.
- 5537 [48] ESFAHANI ASHTARI, A. ET AL. (2022) “Viterbi decoding of CRES signals in
 5538 Project 8,” *New J. Phys.*, **24**(5), p. 053013, 2112.05265.
- 5539 [49] JACKSON, J. D. (1999) *Classical electrodynamics*, 3rd ed., Wiley, New York, NY.
 5540 URL <http://cdsweb.cern.ch/record/490457>
- 5541 [50] F.R.S., J. L. D. (1897) “LXIII. On the theory of the magnetic influence on
 5542 spectra; and on the radiation from moving ions,” *The London, Edinburgh, and
 5543 Dublin Philosophical Magazine and Journal of Science*, **44**(271), pp. 503–512,
 5544 <https://doi.org/10.1080/14786449708621095>.
 5545 URL <https://doi.org/10.1080/14786449708621095>

- 5546 [51] ESFAHANI, A. A. ET AL. (2022) “The Project 8 Neutrino Mass Experiment,” in
 5547 *2022 Snowmass Summer Study*, 2203.07349.
- 5548 [52] KRAUS, C. ET AL. (2005) “Final results from phase II of the Mainz neutrino mass
 5549 search in tritium beta decay,” *Eur. Phys. J. C*, **40**, pp. 447–468, [hep-ex/0412056](#).
- 5550 [53] ASEEV, V. N. ET AL. (2011) “An upper limit on electron antineutrino mass from
 5551 Troitsk experiment,” *Phys. Rev. D*, **84**, p. 112003, [1108.5034](#).
- 5552 [54] SAENZ, A., S. JONSELL, and P. FROELICH (2000) “Improved Molecular Final-
 5553 State Distribution of HeT+ for the β -Decay Process of T2,” *Phys. Rev. Lett.*, **84**(2),
 5554 p. 242.
- 5555 [55] BODINE, L. I., D. S. PARNO, and R. G. H. ROBERTSON (2015) “Assessment
 5556 of molecular effects on neutrino mass measurements from tritium β decay,” *Phys.
 5557 Rev. C*, **91**(3), p. 035505, [1502.03497](#).
- 5558 [56] ASNER, D. M. ET AL. (2015) “Single electron detection and spectroscopy via
 5559 relativistic cyclotron radiation,” *Phys. Rev. Lett.*, **114**(16), p. 162501, [1408.5362](#).
- 5560 [57] VÉNOS, D., J. SENTKERESTIOVÁ, O. DRAGOUN, M. SLEZÁK, M. RYŠAVÝ, and
 5561 A. ŠPALEK (2018) “Properties of 83mKr conversion electrons and their use in the
 5562 KATRIN experiment,” *JINST*, **13**(02), p. T02012.
- 5563 [58] LAGENDIJK, A., I. F. SILVERA, and B. J. VERHAAR (1986) “Spin exchange and
 5564 dipolar relaxation rates in atomic hydrogen: Lifetimes in magnetic traps,” *Phys.
 5565 Rev. B*, **33**, pp. 626–628.
 5566 URL <https://link.aps.org/doi/10.1103/PhysRevB.33.626>
- 5567 [59] SILVERA, I. and J. WALRAVEN (1986) “Spin-polarized atomic hydrogen,” *Prog.
 5568 Low Temp. Phys.*, **X**, pp. 139–370.
- 5569 [60] PRITCHARD, D. E. (1983) “Cooling Neutral Atoms in a Magnetic Trap for Precision
 5570 Spectroscopy,” *Phys. Rev. Lett.*, **51**, pp. 1336–1339.
 5571 URL <https://link.aps.org/doi/10.1103/PhysRevLett.51.1336>
- 5572 [61] HALBACH, K. (1980) “Design of permanent multipole magnets with oriented rare
 5573 earth cobalt material,” *Nuclear Instruments and Methods*, **169**(1), pp. 1–10.
 5574 URL <https://www.sciencedirect.com/science/article/pii/0029554X80900944>
- 5576 [62] FURSE, D. ET AL. (2017) “Kassiopeia: a modern, extensible C++ particle tracking
 5577 package,” *New Journal of Physics*, **19**(5), p. 053012.
 5578 URL <https://doi.org/10.1088/1367-2630/aa6950>
- 5579 [63] ESFAHANI, A. A. ET AL. (2019) “Electron radiated power in cyclotron radiation
 5580 emission spectroscopy experiments,” *Phys. Rev. C*, **99**, p. 055501.
 5581 URL <https://link.aps.org/doi/10.1103/PhysRevC.99.055501>

- 5582 [64] ASHTARI ESFAHANI, A. ET AL. (2019) “Locust: C++ software for simulation of
 5583 RF detection,” *New J. Phys.*, **21**, p. 113051, 1907.11124.
- 5584 [65] WIECHERT, E. (1901) “Elektrodynamische Elementargesetze,” .
 5585 URL <https://doi.org/10.1002/andp.19013090403>
- 5586 [66] LIÉARD, A. (1898) “Champ électrique et Magnétique,” *Léclairage électrique*, **16**(27-
 5587 29).
- 5588 [67] BALANIS, C. (2015) *Antenna Theory: Analysis and Design*, Wiley.
 5589 URL <https://books.google.com/books?id=PTFcCwAAQBAJ>
- 5590 [68] <https://www.ansys.com/products/electronics/ansys-hfss>.
- 5591 [69] https://en.wikipedia.org/wiki/Linear_time-invariant_system.
- 5592 [70] NYQUIST, H. (1928) “Certain Topics in Telegraph Transmission Theory,” *Transactions of the American Institute of Electrical Engineers*, **47**(2), pp. 617–644.
- 5594 [71] BRUN, R. and F. RADEMAKERS (1997) “ROOT: An object oriented data analysis
 5595 framework,” *Nucl. Instrum. Meth. A*, **389**, pp. 81–86.
- 5596 [72] ASHTARI ESFAHANI, A. ET AL. (2021) “Bayesian analysis of a future β decay
 5597 experiment’s sensitivity to neutrino mass scale and ordering,” *Phys. Rev. C*, **103**,
 5598 p. 065501.
 5599 URL <https://link.aps.org/doi/10.1103/PhysRevC.103.065501>
- 5600 [73] KAY, S. (1998) *Fundamentals of Statistical Signal Processing: Detection Theory*,
 5601 *Volume II*, Pearson.
- 5602 [74] NEYMAN, J. and E. PEARSON (1933) “On the problem of the the most efficient
 5603 tests of statistical hypotheses,” *Phil. Trans. R. Soc. Lond. A*, **231**.
- 5604 [75] STUMPF, M. (2018) *Electromagnetic Reciprocity in Antenna Theory*, Wiley.
- 5605 [76] BISHOP, C. (2016) *Pattern Recognition and Machine Learning*, Springer.
- 5606 [77] PLEHN, T., A. BUTTER, B. DILLON, and C. KRAUSE (2022) “Modern Machine
 5607 Learning for LHC Physicists,” 2211.01421.
- 5608 [78] GEORGE, D. and E. A. HUERTA (2018) “Deep Learning for Real-time Gravitational
 5609 Wave Detection and Parameter Estimation: Results with Advanced LIGO Data,”
 5610 *Phys. Lett. B*, **778**, pp. 64–70, 1711.03121.
- 5611 [79] GABBARD, H., C. MESSENGER, I. S. HENG, F. TONOLINI, and R. MURRAY-
 5612 SMITH (2022) “Bayesian parameter estimation using conditional variational au-
 5613 toencoders for gravitational-wave astronomy,” *Nature Phys.*, **18**(1), pp. 112–117,
 5614 1909.06296.

- 5615 [80] REIMANN, R. (2022) “Project 8: R&D for a next-generation neutrino mass experi-
 5616 ment,” *PoS, PANIC2021*, p. 283.
- 5617 [81] BUZINSKY, N. (2021) *Statistical Signal Processing and Detector Optimization in
 5618 Project 8*, Ph.D. thesis, Massachusetts Institute of Technology.
- 5619 [82] ESFAHANI, A. A. ET AL. (2023) “SYNCA: A Synthetic Cyclotron Antenna for
 5620 the Project 8 Collaboration,” *Journal of Instrumentation*, **18**(01), p. P01034.
 5621 URL <https://dx.doi.org/10.1088/1748-0221/18/01/P01034>
- 5622 [83] <https://www.nvidia.com/en-us/data-center/v100/>.
- 5623 [84] <https://www.nvidia.com/en-us/data-center/h100/>.
- 5624 [85] HE, K., X. ZHANG, S. REN, and J. SUN (2016) “Deep Residual Learning for
 5625 Image Recognition,” in *2016 IEEE Conference on Computer Vision and Pattern
 5626 Recognition (CVPR)*, pp. 770–778.
- 5627 [86] SIMONYAN, K. and A. ZISSERMAN (2015) “Very Deep Convolutional Networks
 5628 for Large-Scale Image Recognition,” in *3rd International Conference on Learning
 5629 Representations, ICLR 2015, San Diego, CA, USA, May 7-9, 2015, Conference
 5630 Track Proceedings* (Y. Bengio and Y. LeCun, eds.).
 5631 URL <http://arxiv.org/abs/1409.1556>
- 5632 [87] FRIIS, H. (1946) “A Note on a Simple Transmission Formula,” *Proceedings of the
 5633 IRE*, **34**(5), pp. 254–256.
- 5634 [88] POZAR, D. M. (2005) *Microwave engineering*; 3rd ed., Wiley, Hoboken, NJ.
 5635 URL <https://cds.cern.ch/record/882338>
- 5636 [89] AKER, M. ET AL. (2022) “Direct neutrino-mass measurement with sub-electronvolt
 5637 sensitivity,” *Nature Physics*, **18**(2), pp. 160–166.
 5638 URL <https://doi.org/10.1038/s41567-021-01463-1>
- 5639 [90] MONREAL, B. and J. A. FORMAGGIO (2009) “Relativistic Cyclotron Radiation
 5640 Detection of Tritium Decay Electrons as a New Technique for Measuring the
 5641 Neutrino Mass,” *Phys. Rev. D*, **80**, p. 051301, 0904.2860.
- 5642 [91] ASHTARI ESFAHANI, A. ET AL. (2017) “Determining the neutrino mass with
 5643 cyclotron radiation emission spectroscopy—Project 8,” *J. Phys. G*, **44**(5), p. 054004,
 5644 1703.02037.
- 5645 [92] ESFAHANI, A. A. ET AL. (2022) “The Project 8 Neutrino Mass Experiment,” in
 5646 *2022 Snowmass Summer Study*, 2203.07349.
- 5647 [93] ASHTARI ESFAHANI, A. ET AL. (2019) “Locust: C++ software for simulation of
 5648 RF detection,” *New Journal of Physics*, **21**(11), p. 113051.
 5649 URL <https://doi.org/10.1088/1367-2630/ab550d>

- 5650 [94] FURSE, D. ET AL. (2017) “Kassiopeia: a modern, extensible C++ particle tracking
 5651 package,” *New Journal of Physics*, **19**(5), p. 053012.
 5652 URL <https://doi.org/10.1088/1367-2630/aa6950>
- 5653 [95] BALANIS, C. (2011) *Modern Antenna Handbook*, Wiley.
 5654 URL <https://books.google.com/books?id=UYpV8L8GNCwC>
- 5655 [96] WIRTH, W. (2001) *Radar Techniques Using Array Antennas*, Institution of Engi-
 5656 neering and Technology.
 5657 URL <https://books.google.com/books?id=ALht42gkzLsC>
- 5658 [97] BROWN, L. S., G. GABRIELSE, K. HELMERSON, and J. TAN (1985) “Cyclotron
 5659 motion in a microwave cavity: Lifetime and frequency shifts,” *Phys. Rev. A*, **32**,
 5660 pp. 3204–3218.
 5661 URL <https://link.aps.org/doi/10.1103/PhysRevA.32.3204>
- 5662 [98] HANNEKE, D., S. FOGWELL HOOGERHEIDE, and G. GABRIELSE (2011) “Cavity
 5663 control of a single-electron quantum cyclotron: Measuring the electron magnetic
 5664 moment,” *Phys. Rev. A*, **83**, p. 052122.
 5665 URL <https://link.aps.org/doi/10.1103/PhysRevA.83.052122>
- 5666 [99] HANNEKE, D. A. (2007) *Cavity control in a single-electron quantum cyclotron: an
 5667 improved measurement of the electron magnetic moment*, Ph.D. thesis, Harvard U.
- 5668 [100] PURCELL, E. (1946) “Spontaneous Emission Probabilities at Radio Frequencies,”
 5669 *Phys. Rev.*, **69**, pp. 674–674.
 5670 URL <https://link.aps.org/doi/10.1103/PhysRev.69.674>
- 5671 [101] MOSKOWITZ, B. E. and J. ROGERS (1988) “ANALYSIS OF A MICROWAVE
 5672 CAVITY DETECTOR COUPLED TO A NOISY AMPLIFIER,” *Nucl. Instrum.
 5673 Meth. A*, **264**, pp. 445–452.
- 5674 [102] RAPIDIS, N. M. (2018) “Application of the Bead Perturbation Technique to a
 5675 Study of a Tunable 5 GHz Annular Cavity,” *Springer Proc. Phys.*, **211**, pp. 45–51,
 5676 1708.04276.
- 5677 [103] “Real-time Signal Detection for Cyclotron Radiation Emission Spectroscopy Mea-
 5678 surements using Antenna Arrays,” *In preparation*.
- 5679 [104] BYRON, W. ET AL. (2022) “First observation of cyclotron radiation from MeV-scale
 5680 e^{pm} following nuclear beta decay,” 2209.02870.
- 5681 [105] KAZKAZ, K. and N. WOOLLETT (2021) “Using Cyclotron Radiation Emission
 5682 for Ultra-high Resolution X-Ray Spectroscopy,” *New J. Phys.*, **23**(3), p. 033043,
 5683 1911.05869.
- 5684 [106] CANNING, J. A. L., F. F. DEPPISCH, and W. PEI (2023) “Sensitivity of future
 5685 tritium decay experiments to New Physics,” *JHEP*, **03**, p. 144, 2212.06106.

5686

Vita

5687

Andrew Douglas Ziegler

5688

Education

5689

- Doctor of Philosophy, Physics, The Pennsylvania State University, University Park, Pennsylvania, USA, 2023
- Bachelor of Science, Physics, The University of Minnesota, Minneapolis, Minnesota, USA, 2017

5690

5691

Selected Publications

5692

- Astari Esfahani, A. et al. (2023) "Antenna Arrays for CRES-based Neutrino Mass Measurement", *Phys. Rev. C*, In preparation.
- Astari Esfahani, A. et al. (2023) "Real-time Signal Detection for Cyclotron Radiation Emission Spectroscopy Measurements using Antenna Arrays", *Journal of Instrumentation*, In preparation.
- Astari Esfahani, A. et al. (2023) "Tritium Beta Spectrum and Neutrino Mass Limit from cyclotron Radiation Emission Spectroscopy", *Phys. Rev. Lett.*, Accepted.
- Astari Esfahani, A. et al. (2022) "SYNCA: A Synthetic Cyclotron Antenna for the Project 8 Collaboration", *Journal of Instrumentation*, **18**(01).

5693

Selected Presentations

5694

- *New Developments in the CRES Technique for Neutrino Mass Measurement*, Invited Talk, Fall 2022 Meeting of the APS Division of Nuclear Physics, New Orleans, Louisiana, USA, 2022
- *Signal Detection Algorithms for Phase III of the Project 8 Experiment*, Contributed Talk, APS April Meeting 2022, New York, New York, USA, 2022
- *Synthetic Electron Antenna for Calibrating the Project 8 Neutrino Mass Experiment*, Contributed Talk, Fall 2021 Meeting of the APS Division of Nuclear Physics, Virtual, 2021

5695

5696

5697

5698

5699

5700

5701

5702

5703

5704

5705

5706

5707

5708

5709

5710

5711